Faculty of Science and Engineering

Seismic Inversion Applications and Laboratory Measurements to Identify High TOC Shale

Yazeed Khalid Altowairqi

This thesis is presented for the Degree of

Doctor of Philosophy

Of

Curtin University

June 2015

Declaration

To the best of my knowledge and belief this thesis contains no material previously published by any other persons except where due acknowledgment has been made. This thesis also contains no material which has been accepted for the award of any other degree or diploma in any university.

Yazeed Khalid Altowairqi

Signature: Yazeed

Date: 25-06-2015

Abstract

This study investigates the seismic response of organic-rich shale in-situ conditions. The aim is to understand the interrelationship between rock properties and elastic properties, as well as the main factors that affect the full elastic tensor and resultant anisotropy of organic shale. The mechanical and dynamic elastic properties of shale are not well understood as there have been investigations of well-preserved shale samples.

This thesis focus of using two different approaches: seismic inversion applications and multi-attribute analysis, as well as laboratory measurements of natural and synthetic shale samples. Firstly, different approaches of seismic inversion and multi-attribute analysis were conducted by combining 3D seismic data with log data to predict the TOC content. This study shows that Acoustic Impedance (AI) decreases linearly with increasing Total Organic Carbon (TOC) content in shale formations. By cross-plotting the AI derived from seismic data against the measured TOC content, it became possible to map TOC variations directly from 3D seismic data for the northern Perth Basin, Western Australia. This study provides a methodology that has a potential to detect sweet spots within shale formations by incorporating the rock physics relationships into inversion multi-attributes seismic analysis.

Secondly, natural and synthetic shale samples were used during the laboratory measurements to understand their elastic properties. The natural shale samples were selected based on the TOC content, allowing the influence of TOC content on the elastic properties to be studied. A total of 40 synthetic shale samples were manufactured with different mineral compositions and TOC percentages. A mixture of clay and non-clay minerals was compressed with organic matter under high pressure inside a steel core holder only in the axial direction, to produce an anisotropic media and the layering of the shale within each sample. Ultrasonic transducer arrays were used to measure the independent wave velocities, which were used to calculate the elastic properties. The study of the synthetic shale samples presents equations that allow us to estimate the TOC content shale using compressional and shear wave velocities and density.

The other objective of this study was to investigate the AVO response on organic and inorganic shale formations using well-log data and then comparing the results to the

experimental studies by measuring the AVO ray on organic and inorganic synthetic shale samples. The AVO effects were measured under increasing pressure with different fluid types present at the reflection boundary, using a True Triaxial Stress Cell (TTSC) to apply both axial and confining pressure on the samples. The study presents a new method of measuring AVO ray in-situ conditions, with different fluid types and TOC, which helps to understand the amplitude background trend of the shale formation.

This study shows that the gas shale sweet spots (brittle shale) are characterised by high TOC and relatively high AI, as well as low Lambda-Rho (LR) and high Mu-Rho (MR) values, which is found in the base of the organic rich Hovea Member in the Perth Basin. Also, this study indicates that the TOC contents of natural shale and synthetic shale samples have significant influences on their elastic properties. The results indicated that P and S-wave velocities vary depending on the isotropic stress conditions, with respect to the fabric and TOC contents. Careful manufacturing of synthetic shales increases the understanding of natural organic rich shales. This allowed us to deduce and propose appropriate methodologies that can be used for seismic exploration of organic rich shales. Finally, the AVO modelling from well-log data shows that the amplitude increases when the offset correspondingly increases for the organic shale layers. The laboratory results of two synthetic shale samples demonstrate that amplitude is related to offset under isotropic stress conditions with respect to the TOC content and different fluid media. It is shown that isotropic stress can significantly impact the amplitude. Generally, the trend of the amplitude values increase smoothly as the pressure is increased for each fluid media, and then drops suddenly when closely the highest pressures (refracted point) are reached; the refracted point are different depending on the fluid media. The amplitude is also higher for the organic sample as compared to the inorganic sample.

Parts of this thesis have been published or accepted for publishing in the following journals and conference articles:

- Altowairqi, Y., R. Rezaee, B. Evans, and M. Urosevic, 2015, Shale elastic property relationship as a function of total organic carbon content using synthetic samples: Journal of Petroleum Science and Engineering, 2015. (Accepted).

- Altowairqi, Y., R. Rezaee, B. Evans, and M. Urosevic, 2015, A quantitative application of seismic inversion and multi-attribute analysis based on rock physics linear relationships to identify high TOC shale: a case study from Perth Basin, Western Australia: Interpretation SEG, 2015. (Accepted).

- Altowairqi, Y., R. Rezaee, B. Evans, and M. Urosevic, 2015, Shale elastic property relationship as a function of total organic carbon content using synthetic samples: 3rd International Workshop on Rock Physics, 2015.

- Altowairqi, Y., R. Rezaee, B. Evans, and M. Urosevic, 2015, Measuring Elastic Properties to determine the influence of TOC on Synthetic Shale Samples: ASEG Extended Abstracts, 2015(1), 1-5.

- Altowairqi, Y., R. Rezaee, and M. Urosevic, 2014, Quantitative application of post stack inversion of organic-rich based on rock physics linear relationship and 3D seismic data, Perth Basin, Western Australia: Australian Petroleum Production and Exploration Association Extended Abstracts, 2014.

- Altowairqi, Y., R. Rezaee, and M. Urosevic, 2013, Seismic Inversion Applications and Laboratory Measurements to Identify High TOC Shale Formations: SEG Workshop on The Role of Geoscience in Unlocking Unconventional reservoirs, 2013.

- Altowairqi, Y., R. Rezaee, M. Urosevic, and C. Delle Piane, 2013, Measuring ultrasonic characterisation to determine the impact of TOC and the stress field on shale gas anisotropy: Australian Petroleum Production and Exploration Association Journal, 2013 (53).

Acknowledgements

First and foremost, I wish to thank my supervisor Professor Reza Rezaee. I am grateful for his continual guidance and knowledge, which has provided the energy and support for me to push through the difficulties during my PhD research. I remember him using the phrase “make your hands dirty”, to motivate me to create synthetic samples in the laboratory.

I am also very thankful to my co-supervisor, Professor Brian Evans, for his recommendations and comments during my PhD study especially with the data analysis and experimental designs. I am grateful to him, for allowing me to use his laboratory equipment.

I wish also to convey my appreciation to him for his continuous assistance in editing my written work. I am also very grateful to Assoc. Professor Milovan Urosevic for his valuable feedback, particularly with the seismic inversion. I wish to convey appreciation to Dr. Claudio Delle Piane for continuously helping in the measurement of the ultrasonic wave of shale sample in CSIRO. I would like to convey special thanks and appreciation to Mr. Glenn Reid for his constant support during the laboratory work. I wish to thank Mr. Robert Verstandig for editing my thesis according to the standards of the Institute of Professional Editing.

I am thankful to Allah for all opportunities that I have had. I am especially thankful to my family, especially my mother, father and brothers for their support and prayers that helped me a lot during my study. The final and most significant acknowledgement must be given to my wife and son for their long suffering patience while I was studying; without their help and unwavering support, this study would not have been done.

Table of Contents

List of Figures

List of Tables

List of Abbreviations and Acronyms

List of Acronyms

m	Meter
ms	Millisecond
ml/ min	Millilitre per minute
wt%	Weight percent
Pa	Pascal
Psi	Per square inch
ΔlogR	Separation between resistivity and sonic
Tmax	Thermal maturation level determined by Rock-Eval pyrolysis

List of Abbreviations

AI	Acoustic Impedance
AVO	Amplitude versus Offset
AWE	Australian Worldwide Exploration
DMP	Department of Mining and Petroleum
DT	Sonic transit time
EIA	Energy Information Administration
EI	Elastic Impedance
HI	Hydrogen Index
HTI	Horizontal Transverse Isotropy
LMR	Lambda-Mu-Rho
QFP	Quartz, Feldspar, Pyrite
SEM	Scanning Electron Microscopy
SI	Shear Impedance
tcf	Trillion Cubic Feet
TI	Transverse Isotropy
TOC	Total Organic Carbon
TTST	True Triaxial Stress Cell
VTI	Vertical Transverse Isotropy
XRD	X Ray Diffraction

Chapter 1. Introduction

1.1 Introduction to gas shale

Gas shale is becoming an increasingly important exploration and production target in many countries as a new energy source for the future. Gas shale is a fine-grained, organic-rich sedimentary rock that is recognised to store natural gas trapped inside nano-sized pores. Gas can be absorbed on the surface of organic compounds contained within the shale (Boyer et al., 2006). Shale source rock is the foundation for hydrocarbon accumulation (Magoon and Dow, 1994; Johnson et al., 2003; Yang et al., 2004) and may be characterised by: (1) the maturity of organic matter, (2) the type of gas generated and stored in the reservoir, (3) the total organic carbon (TOC) content of the strata and (4) the permeability and porosity of the reservoir (Rokosh et al., 2009). Shales are generally recognised as anisotropic; an anisotropic rock fabric can cause seismic anisotropy — the layered micro structure of clay particles that leads to the anisotropy of shale (Hornby et al., 1994; Bayuk et al., 2007; Sarout and Guéguen, 2008). Such unconventional natural gas deposits are challenging to characterise, due to the organised distribution of platy clay minerals (Altowairqi et al, 2013; Zhu et al, 2011) and compliant organic materials (Vernik and Nur, 1992; Vernik and Liu, 1997; Sondergeld et al, 2000; Vernik and Milovac, 2011). Organic shale (High TOC content) is usually characterised by low velocity, relatively low density and strong velocity anisotropy (Vernik and Nur, 1992; Vernik and Liu, 1997). The intrinsic anisotropy increases with rising TOC (Tutuncu, 2010). Gas shale formations share properties include heterogeneity, low-permeability and matrix porosity (Vernik and Milovac, 2011). Organic shale is typically required to have a high TOC in order to be able to generate gas (Close et al., 2010). However, the difficulty of gas shale has required researchers to try and understand the controls on unconventional resources, such as geology, geophysics, petrophysics, geomechanics and rock physics (Close et al., 2010).

To become familiar with the seismic responses of the gas shales, rock physics relationships and seismic inversions are important. These are constrained by the rock properties and physical characteristics, when applying prestack and poststack seismic inversion (Sena et al., 2011) for the prediction in-situ rock parameters, such as

acoustic and shear impedances, TOC, mineral composition, rock strength, stress fields and elastic properties (Zhu et al., 2011).

Elastic properties, estimated from laboratory measurements or from seismic inversions, are useful in the calibration of seismic and acoustic studies of rock samples. Seismic waves within the shale anisotropy travel with different speeds in directions parallel to the bedding as well as perpendicular to the bedding (Brevik et al., 2007; Chesnokov et al., 2010; Lebedev et al., 2011). The laboratory measurement requires a good understanding of symmetry and orientation of the principal axes (Sondergeld and Rai, 2011). "Vertical transverse isotropy (VTI) and horizontal transverse isotropy (HTI) are key components of the solution. VTI is significant to the interval velocity calculation for the initial model building in the pre-stack inversion process and pore pressure. Any change in VTI heterogeneity values (even small values) produce measurable velocity changes. HTI plays an important role in differential stress analyses" (Sena et al., 2011). In this project, general rock physics studies and seismic modelling/inversion workflow have been used, similar to Zhu et al., 2011 to understand the gas shale properties by using field data and core shale samples (Figure 1-1).

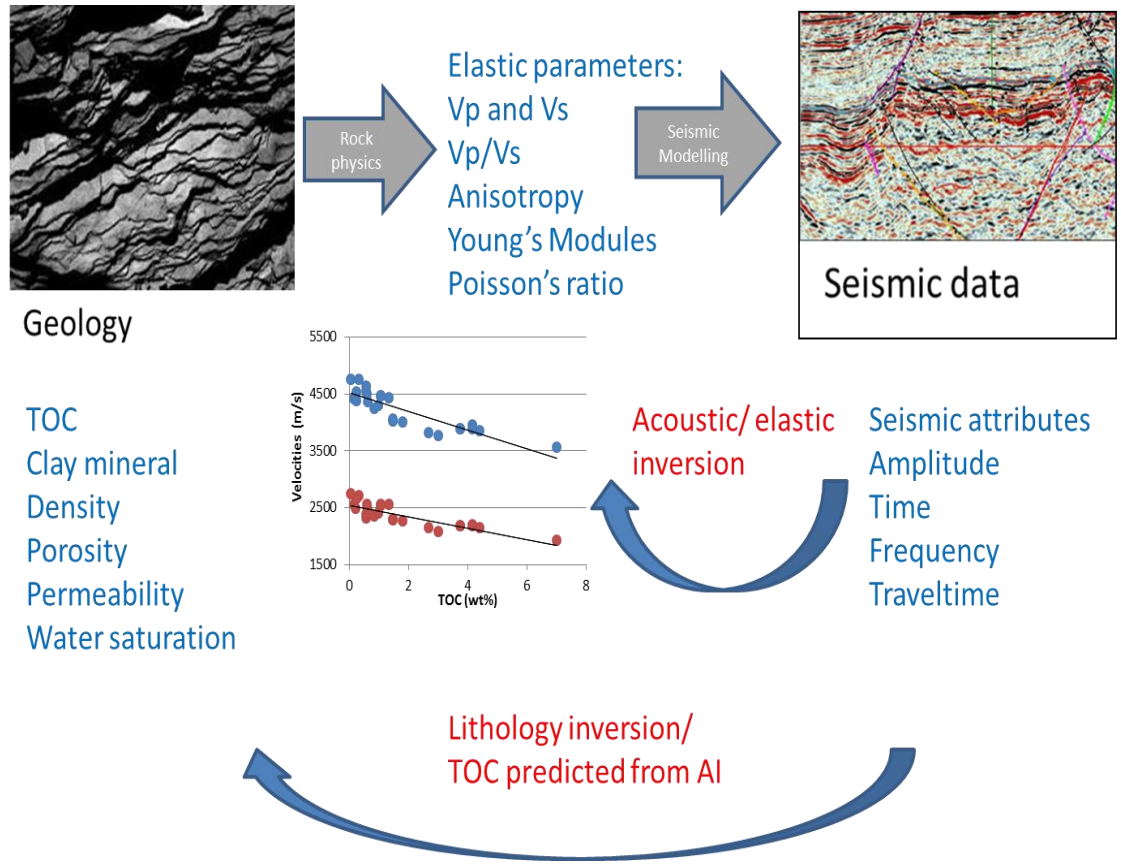

Figure 1-1: A general workflow of gas shale studies based on the rock physics and seismic modelling/ inversion (Modified from Zhu et al., 2011).

1.2 Gas shale resources in the Perth Basin

The Perth Basin is located in the south-west of Western Australia and aligned approximately north-south as shown in Figure 1-2. The basin comprises a sequence of northerly striking sub-basins, troughs and uplifts. It covers an area of about 45,000 km^2 onshore and 55,000 km^2 offshore and comprises a number of conventional oil and gas fields (Song & Cawood, 2000). It is an established petroleum province with more than 300 drilled wells. The main exploration activity was onshore, specifically in the north of the Perth Basin. An estimation of the amount of 'technically recoverable' gas shale resources in Australia is approximately 396 trillion cubic feet (Tcf). In particular, there is a total of 288 Tcf of risked recoverable gas shale estimated in Western Australia (WA) gas reserves, according to the US Energy Information Administration (US EIA). This estimation means that WA holds the fifth largest reserve of gas shale in the world. WA is also considered to have the greatest potential for gas shale production in the future and currently provides gas to the Perth

market via two pipelines (Triche, 2012). The main source rock for gas shale in the Perth Basin is the Lower Triassic Basal Kockatea Shale, especially at the base of the formation (the Hovea Member), which is richer in the TOC than the overlying part (Thomas and Barber, 2004). Tupper (1992) explained that the thickness of the Kockatea Shale varies throughout the northern Perth Basin from about 200 m in the north to a maximum of 1100 m. The TOC content ranges from 0.5 – 4 wt%. Another source interval in the Permian is the Carynginia Formation, which shows good organic richness with TOC values of more than 2 wt%, with depositional thickness at a fairly constant 300 m (Tupper, 1992; Thomas and Barber, 2004).

Figure 1-2: Western Australian map with Perth Basin shows the gas shale resources (after Volk et al., 2004).

1.3 Rock physics and the seismic response of gas shale

Rock physics is one of the most important studies used in direct hydrocarbon indication, reservoir characterisation and monitoring. It provides a bridge for field measurements, such as log and seismic data, to reservoir rock and fluid properties and a common base for geoscientists and reservoir engineers to communicate (Han, 2002). Rock physics links geological rock properties (mineralogy, porosity, grain configuration and different fluids) to seismic responses (elastic properties, velocities, impedances and the Vp/Vs ratio) (Mavko et al., 2009; Wang, 2001). "Therefore, it is necessary to study how the rock properties are influenced by compaction during burial. How compositional processes influence sediments will vary depending on the original composition sediment texture (clay type/ amount, grain size, sorting, the type and maturity of organic matter), which often varies significantly in different depositional systems (e.g., fluvial, shallow marine, deep marine)" (Storvoll and Brevik, 2008).

Seismic reflections depend on the contrasts of the elastic properties; each elastic property depends on a number of rock parameters such as porosity, mineralogy, pore fluid, differential pressure and the TOC (Figure 1-3). "It also requires all wave-propagation effects, sampling, as well as noise issues, have to be calculated properly to provide an accurate translation of the elastic properties (velocity and/or impedance) into reservoir properties" (Singleton and Keirstead, 2011; Singleton, 2008 and 2009).

Rock physics relationships also provide unique mappings and cross-plotting of elastic properties to reservoir properties. Therefore, seismic reservoir characterisation requires simultaneously linking point-based rock physics relationships to band-limited seismic data and statistical methods, to account for the ambiguous relationships between elastic and reservoir properties (Spikes, 2008).

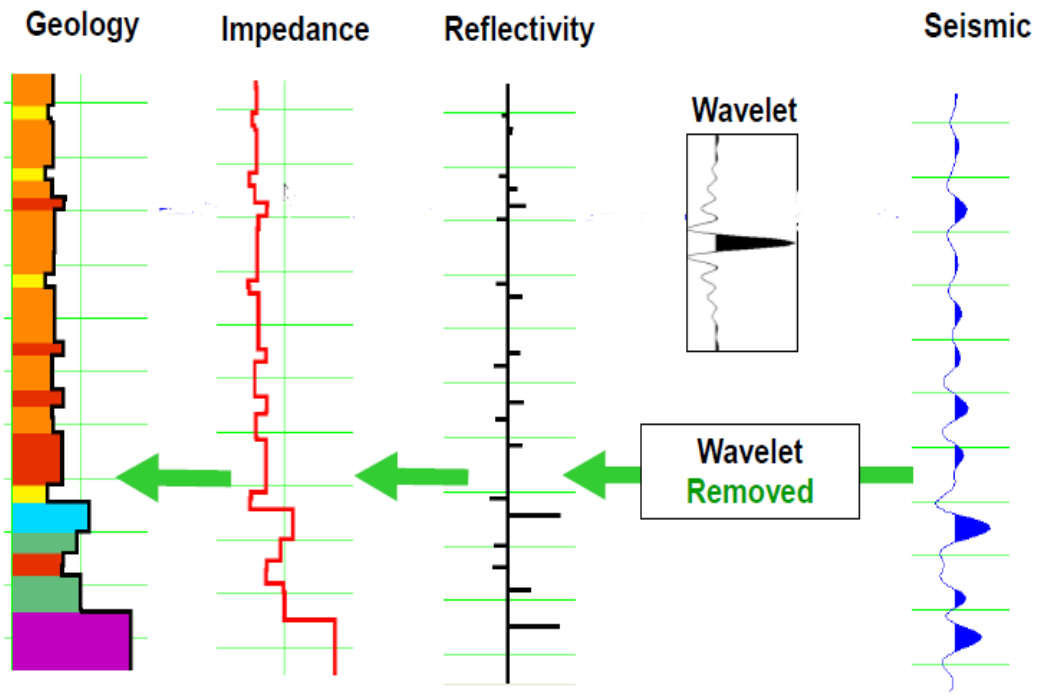

Figure 1-3: Inversion workflow (Geology to Seismic) (after CGG Veritas Strata Workshop, 2012).

Seismic inversion applications can be classified according to the type of seismic data (inversion of poststack or prestack data). Post-stack inversion seismic data is used to extract AI, which can be used to help detect discontinuities and structural trends that may influence drilling or production. On the other hand, prestack inversion plays an important role in the detection of gas shale properties and is a more effective tool, especially when used to predict the sweet spots that are likely to have a high TOC content and good gas storage. Imaging sweet spots using 3D seismic data requires AVO modelling, analysis and inversion, which allows the physical properties of the reservoir to be predicted. The inverted data (acoustic impedance, shear impedance, Vp/ Vs ratio, and density) can be transferred into the elastic properties including Poisson's ratio, Young's modulus, lambda (λ) and mu (μ). These elastic properties are used as the main controls and affect the seismic responses in gas shale.

Seismic multi-attribute analysis can be used to determine the hydrocarbon sweet spots and predict lithology, porosity, elastic properties and resistivity distributions during gas shale exploration (Ogiesoda and Eastwood, 2013). Gupta et al. (2013) used a seismic multi-attribute to identify different lithofacies containing variable

quantities of the TOC, as well as quartz, which controls the brittleness in shale formation. In addition, the LMR approach and AVO responses are supportive tools, (the shale is assumed as isotropic shale), that can be used for gas shale analysis by using the rock physics trends. The resulting seismic inversion data can then be used to predict changes in reservoir properties, such as porosity, lithology and stiffness of the rock (Perez et al., 2012). This approach helps identify the optimal location for infill drilling and potential hydraulic fracture areas by finding the location and the distribution of the hydrocarbon accumulation so that the gas shale resources can be extracted more efficiently.

1.4 Ultrasonic Characterisation

Ultrasonic characterisation is one of the most important keys used in direct hydrocarbon indication. However, it is challenging to characterise unconventional natural gas reservoirs because the elastic properties of shale rock vary significantly within and across such reservoirs, due to various mineral composition and anisotropy parameters exhibited by these organic rich shales (Zhu et al., 2011). Presently, our understanding of their dynamic and elastic behaviour is very limited due to the low volume of variable organic shale samples available, as well as the amount of time taken to test low-permeability samples. Experiments involving organic shale core samples can be found in a limited number of publications (Altowairqi et al., 2013; Dewhurst et al., 1998; Dewhurst and Siggins, 2006; Dewhurst et al., 2011; Delle-Piane et al., 2011). Indeed, many ultrasonic wave velocity measurements of gas shale core samples have been conducted without controlling the stress conditions, which is critical if the intent is to relate velocities to influences in effective stress conditions (Dewhurst and Siggins, 2006).

One of the difficulties of studying the elastic properties is that organic-rich shales are chemically and mechanically unstable, due to the organised distribution of platy clay minerals (Zhu et al., 2011) and compliant organic materials (Vernik and Nur, 1992; Vernik and Liu, 1997; Sondergeld et al., 2000; Vernik and Milovac, 2011). There are propositions in the literature that it is not only the amount of organic content influencing the anisotropy in organic rich shale, but also the maturity of the shale (Sone, 2012). Moreover, difficulties in testing the elastic properties of gas shale arise due to their small grain and low permeability (Horsrud et al., 1998; Prasad et al., 2009).

Limited laboratory experiments of the full elastic tensor and resultant anisotropy of organic shale, which take into account factors including porosity, smectite, kerogen content and micro fractures, have been described in the literature (Altowairqi et al., 2013; Dewhurst and Siggins, 2006; Vernik and Liu, 1997; Hornby, 1998). Therefore, it is difficult to account for all the factors affecting the velocity and anisotropy of a natural shale sample under in-situ conditions. In particular, factors including stress state, stress history, clay mineral content, and the TOC content are not widely reported (Altowairqi et al., 2015(A); Bohacs et al., 2005; Passey et al., 2010). Control of laboratory tests on well-characterised shale samples under in-situ stress and stress conditions can aid the investigation of the impact of these factors on organic shale velocity and anisotropic response (Tutuncu, 2010).

In this study, presents a laboratory experiment that investigates the influence of the TOC content, stress and clay mineral on wave velocities using natural shale core samples from the Perth Basin. The expected results of these laboratory experiments are that the velocities should increase with the stress levels and decrease as the TOC percentage increases. In addition, other factors including clay minerals, porosity and density have an influence on the elastic wave velocities of organic shale (Altowariqi et al., 2013).

Furthermore, such experiments in testing natural shale sample are difficult to control in terms of all the factors that affect the elastic properties of the shale samples and are also dependent on the sample quality. In contrast, synthetic shale samples provide us with the opportunity to conduct investigations in a fully-controlled environment where variability of parameters is controlled by the user. Core samples with known percentages of clay minerals, non-clay minerals and the TOC content under variable and/or in-situ stress conditions can thus be manufactured (Altowairqi et al., 2015) Such a system allows us to study the contribution of each of the factors independently. The process of creating the synthetic sample is much quicker as compared to the real rock, which is compacted over a long period of time.

1.5 Research Objectives

The main issue is that the seismic properties of high TOC shale remain poorly understood. Therefore, predictions of the seismic response from a rock system remain challenging. The main objective here is to apply different applications of

seismic inversion and multi-attribute analysis through acoustic and shear impedance analysis. This approach will help to identify and map spatial distributions of the organic rich shales in the Perth Basin. The second objective in this project is to investigate the ultrasonic response of gas shale samples recovered from different wells in the Perth Basin, with changing isotropic stress conditions. Specifically, the influence of the TOC content on gas shale samples and the resultant impact on elastic wave velocities and their anisotropy are evaluated using laboratory measurements. The third objective of the research described here is to investigate the influence of variable TOC and clay minerals on the elastic properties of synthetic shale with and without stress conditioning. More than 40 synthetic shale samples with similar mineral compositions (but different TOC percentages) were manufactured under typical geological stress conditions resembling those found in the field. Specifically, the influence on the TOC of gas shale synthetic samples and the resultant impact on elastic wave velocities are investigated. This approach enables us to estimate the organic material richness of potential gas shale reservoirs using well-log or seismic data. The fourth objective is to measure the AVO effect on organic and inorganic shale samples using well-log and seismic data and then comparing the results to experimental studies by measuring the AVO rays from different synthetic shale samples.

1.6 Research Methodology

As previously mentioned, this research focuses on the influence of TOC on the elastic properties of gas shale. This subject is tackled using two different approaches: seismic inversion applications and the multi-attribute analysis, as well as laboratory measurement of natural and synthetic gas shale samples. Furthermore, the results obtained from both approaches are compared with the theoretical predictions. Different approaches of seismic inversion and multi-attribute analysis are conducted by combining 3D seismic data with logs data to determine hydrocarbon sweet spots within shale formations in the northern Perth Basin. This approach will help to identify and map spatial distributions of the organic rich shale. Rock physics relationships help us identify the relationship between the TOC and AI. This study shows that the AI values decreases nonlinearly with an increasing TOC content in gas shale formations. By cross-plotting the AI derived from seismic data values

against TOC, it became possible to map TOC variations directly from 3D seismic data.

The second objective is to measure the ultrasonic waves and the elastic properties of natural and synthetic gas shale samples. Six core samples with different percentages of TOC were recovered from shale formations in the Arrowsmith-2 and Redback-2 wells in the Perth Basin. Moreover, 40 synthetic shale samples with different mineral compositions and TOC percentages were also created under isotropic stressed and unstressed conditions for our investigations. Ultrasonic transducers were used to measure body-wave velocities, which were then used to calculate the elastic properties in different shale samples. The results demonstrate that P- and S-wave velocities vary under isotropic stress conditions with respect to the TOC and clay mineral content. The last study via laboratory measurement is to understand the AVO response of organic shale, which shows that the amplitude is greater when the offset increases for the organic shale layer in field data. The laboratory results of the two synthetic shale block samples with different TOC content demonstrate that the amplitude is related to offset, under isotropic stress conditions, with respect to the TOC and different fluids media.

1.7 Research Significance

This study presents results from new concepts and methodologies for the modelling and characterisation of gas shale reservoirs in the Perth Basin. A better understanding of gas shale properties would help in several geological or geophysical areas such as the TOC and rock-strength estimation, the impact of the TOC and clay minerals, anisotropy quantification for improved seismic imaging, borehole geophysics and seal evaluation.

Seismic inversion applications and attributes analysis by using the rock physics relationships help to determine hydrocarbon sweet spots within shale formations in the northern Perth Basin. This approach helps us identify and map spatial distributions of the organic rich shale. In the laboratory measurements, the results of the ultrasonic waves of both real and synthetic shale samples indicate that the TOC content has a significant impact on the elastic properties of gas shale. This approach enables us to estimate the organic material richness of potential gas shale reservoirs using well-log or seismic data.

A brief description of the significance of this research is given below:

- The estimation of brittle shale using the LMR approach with 3D seismic and well-log data is used to predict the change in reservoir properties such as lithology and stiffness of the rock; which is useful in identifying the optimal location for infill drilling for hydraulic facture actions.
- A triaxle testing rig (new equipment from CSIRO) was used to measure ultrasonic waves and elastic properties of different core shale samples.
- A total of 40 synthetic shale samples were manufactured under typical geological stress conditions with similar mineral compositions but different TOC percentages resembling those found in the field. Each synthetic sample was formed under high pressure (7000 psi) using a true triaxial loading. The ultrasonic waves were examined with varying stress levels using a core holder. This study presents equations that allowed us to estimate the organic material richness of potential gas shale reservoirs using compressional and shear wave velocities and density.
- The AVO responses of organic and inorganic synthetic samples were measured under increasing pressure with different fluid types present at the reflection boundary, using TTSC to apply both axial and confining pressure in the samples. The study presents a new method of measuring AVO ray in-situ condition, with different fluid types and TOC, which helps us to understand the amplitude background trend of the shale formation.

1.8 Thesis Structure

The previous sections in this chapter introduced the gas shale properties and gas shale resources in the Perth Basin. Also, the seismic response based on rock physics relationships and the ultrasonic characterisations were briefly discussed. Furthermore, the main objectives, methodology and significance of this study were briefly explained.

Chapter 2 contains a broad review of the geology of the Perth Basin. Regional geology, structure, stratigraphy and potential gas shale formation studies are reviewed here. The chapter then focuses mainly on the shale formations properties and fault structures in the Perth Basin, which helps map the TOC profile in the area.

Chapter 3 begins with the methodology of rock physics linear relationships with and the TOC and continues with to seismic inversion and multi-attribute analysis, which discusses the workflow of the seismic inversion applications that were applied in this study. This chapter also addresses the theoretical aspects of ultrasonic measurement and characterisations that can be used to understand the effect of TOC on gas shale samples. Afterwards, it explains the steps and the method of manufacture of synthetic gas shale samples.

Chapter 4 discusses the results of the seismic inversion and multi-attribute analysis used to identify high TOC shale using 3D seismic data. First, this chapter clarifies the database of the Denison 3D seismic and well-log data located in the north Perth Basin, including the geophysical interpretation of the seismic section. It then describes the crossplot analysis, including the TOC content variation and the AI and obtains a linear relationship between P- and S-waves from shale formation to estimate S-wave velocities for all the wells that only had P-wave velocities, and then apply it as assumption for S-impedance inversion. This is followed by a rock physics relationship study on shale. The third part of this chapter discuss the results and analysis of the first objective of this study, which starts by applying poststack seismic inversion to produce AI values and then applying AVO modelling and analysis on an organic shale formation in the area to identify the hydrocarbon resources. The application of prestack inversion on both near and far-offsets is then described, followed by the discussion of the TOC prediction using two multi-attribute analyses. The last part of this section discusses the estimation of brittleness of shale formations in this area using the LMR approach.

The experimental results are presented in Chapter 5 and the effect of the TOC and clay minerals on the elastic properties of gas shale using real and synthetic shale samples are discussed. The first part of this chapter explains the ultrasonic measurement of natural gas shale core samples, including the shale composition and microstructure of gas shale formations, the physical properties, the results, analysis and the discussion. The second part describes the ultrasonic measurement of the synthetic shale samples that have been created, including the mineral compositions and microstructure of those shales. The physical properties, results, analysis as well as the influences of clay minerals and TOC on those synthetic shales are also

described here. The end of this section explains the practical applications to field data.

Chapter 6 describes the AVO response of organic shale based on laboratory testing, starting with AVO modelling and the analysis of organic and inorganic shale formations in the Perth Basin. It then explains the methods and the steps involved in creating synthetic block samples. The third section describes the AVO setup, which is used for this test. The last part of this chapter discusses the results and analysis for both organic and inorganic shale measurements and the comparison of those measurements.

Chapter 7 presents discussion and conclusions of this study. A number of recommendations are presented for further study in this area.

Chapter 2. Geology of the Perth Basin

2.1 Regional geology

The Perth Basin is an extended trending trough along the divergent margins of Australia and Greater India formed during the Palaeozoic and Mesozoic periods. The Basin is located in the south-west of Western Australia and aligns approximately north-south. Approximately half of the Basin is located onshore covering an area of approximately 45,000 km^2 and extends from the south coast of Western Australia to near the Murchison River, a distance of about 750 kilometres (Song and Cawood, 2000; Mory and Lasky, 1996). The eastern boundary of the Basin, which extends offshore to the continental-oceanic boundary, is defined by the Darling Fault. "The Perth Basin is divided from the Yilgarn Craton by the Darling Fault in the east and extends west to the continental edge of the Indian Ocean crust" (Mory and lasky, 1996).

The total thicknesses of sediments in the Perth Basin is up to 15,000 m and were formed during the Silurian to Pleistocene with an extreme phase of deposition starting from the Early Permian through to the Late Jurassic (Song and Cawood, 2000). The depositional environmental structure of the sediments is from glacial to marine and fluvial. The main exploration source of gas shale in the northern Perth Basin has been the late Permian sequence immediately below the regional marine Kockatea Shale. Overall, the tectonic style of the Basin is organised by a general north to north-western to south to south-eastern faulting with a secondary west to east fault system. The onshore section displays a series of well-defined terraces and troughs as a result of predominantly tensional tectonic activities (Harris et al., 1994).

2.2 Structure

The Perth Basin has been matured on complex structural styles, which were developed during the continental break-up. The structural fundamentals in the Basin consist of extension-related plannar and strike-slip deformation listric faults, transfer zones and some structures linked to the Basin inversion (Harris et al., 1994). The complex structural styles in the Basin are a result of the Jurassic to earliest Cretaceous extension and transtension through the breakup of Gondwana. There are two main rifting phases, which have been recognised in both the onshore and

offshore parts of the Basin, within the Permian and Jurassic to the earliest Cretaceous (Harris et al., 1994). The strike of normal faults in the Basin is between 310° and 360° and expresses the overall northerly strike, which characterises the Basin and its elevation. The main hydrocarbon traps in the Perth Basin related with this period of the deformation, as well as the rollover anticlines, are proven exploration locations (Crostella, 1995).

The main depositions in the north of the Perth Basin are the Dandaragan Trough and the Vlaming Sub-basin. The Dandaragan Trough is an extended north-south oriented half-graben, restricted by the Darling and Urella faults to the east and making up a considerable part of the onshore Perth Basin north of Perth (Mory and Lasky, 1996). The Mountain Bridge Fault defines the boundary between the Dongara Saddle and a series of terraces along the western flank of the Dandaragan Trough. There are a series of terraces slopes that extend into the Dandaragan Trough south of the Allanooka Fault and east of the Mountain Bridge and Beagle Faults. The Beharra Springs Terrace is located between the Mountain Bridge Fault and the Beharra Springs Fault. The Redback Terrace is situated in the hanging wall of the Beharra Springs Fault.

The normal faults within the Perth Basin are grouped into two types, namely the planar and listric normal faults. The planar normal faults in the Basin such as Urella, Muchea and Darling faults have complicated structures with a long history of movements and reactivations, extending back to the Precambrian and also define the eastern boundary of the Basin (Harris et al., 1994). These faults are planar with sedimentary formations in the interpreted seismic reflection section and they dip approximately 60° – 70° to the west. “The delineation of the dip in these structures is more obvious in the northern Perth Basin where thin sedimentary succession is found” (Song and Cawood, 2000). The Busselton and Dunsborough faults delineate as rift faults controlling the western boundary; those faults lie within the Bunbury Trough, found in the southern Perth Basin (Song and Cawood, 2000). The listric normal faults in the Basin occur as both bounding features and with troughs. For example, the Mountain Bridge defines the western margin of the north Dandaragan Trough and is shown in the interpreted seismic section as a continuous down-dip decline to a dip angle of about 65° near the top of the section to 20° at the sedimentary basement cover. A rollover anticline has developed in the Mountain

Bridge Fault hanging wall and includes the oil accumulation in the Yardarino oil field (Song and Cawood, 2000).

2.3 Stratigraphy

The sedimentation deposited into the north of the Perth Basin (Figure 2-1) started as early as the Late Ordovician to the Silurian (Cadman et al., 1994). In a structural low adjacent to the uplifted Precambrian basement, the fluviatile Tumblagooda Sandstone was laid down. In the Early Permian, the initial phases of rifting were established with a north-south trending trough along the axis of the Basin. "This trough was first filled to the north with a coarse, tillitic boulder conglomerate (Nangetty Formation). This was followed by the marine shale (Holmwood Shale), before regression in the Artinskian saw the deposition of shallow marine sands, which was followed by a fluviatile and the paludal coal measure sequence". These are commonly known as the Irwin River Coal Measures and cover a vast area to the north of the Basin (Playford et al., 1976; Cadman et al., 1994). With the return of shallow marine conditions in the Late Artinskian, siltstones shales and carbonates were deposited with thin sandstone interbeds — the Carynginia Formation (Song and Cawood, 2000).

After an uplift in the Late Permian, the eroded material from the Artinskian (284 to 290 Ma) and other older sequences spread westward in an alluvial fan from the Darling Fault and into the north of Perth Basin (Wagina Sandstone). The sediment supply was mainly from the uplifted areas to the east and northeast of the fault with minimal supplies from the Northampton Block and eastern flank of Beagle Ridge. At the start of the Triassic, the rifting that had commenced in the Late Palaeozoic had produced a sequence of echelon rifts with shallow basement highs in the north of the Basin. The rise of the sea level at this period resulted in a region of marine transgression to the northern Perth Basin. Further subsidence, related with great movements on the Darling and Urella Faults in the Early Triassic, led to the deposition of the Kockatea Shale (a transgressive marine sequence of organic black shale, siltstone and fine sandstone) over a wider part of the northern Perth Basin. To the south, continental sedimentation, known as the Sabina Sandstone, continued in the Bunbury Trough and gradually spread northwards until the Middle Triassic times when fluviatile sedimentation appeared throughout a wide percentage of the Basin

(the Lesueur Sandstone). The Darling and Urella Fault movements were clearly developing from the Middle Triassic to the Middle Neocomian times (Playford et al., 1976).

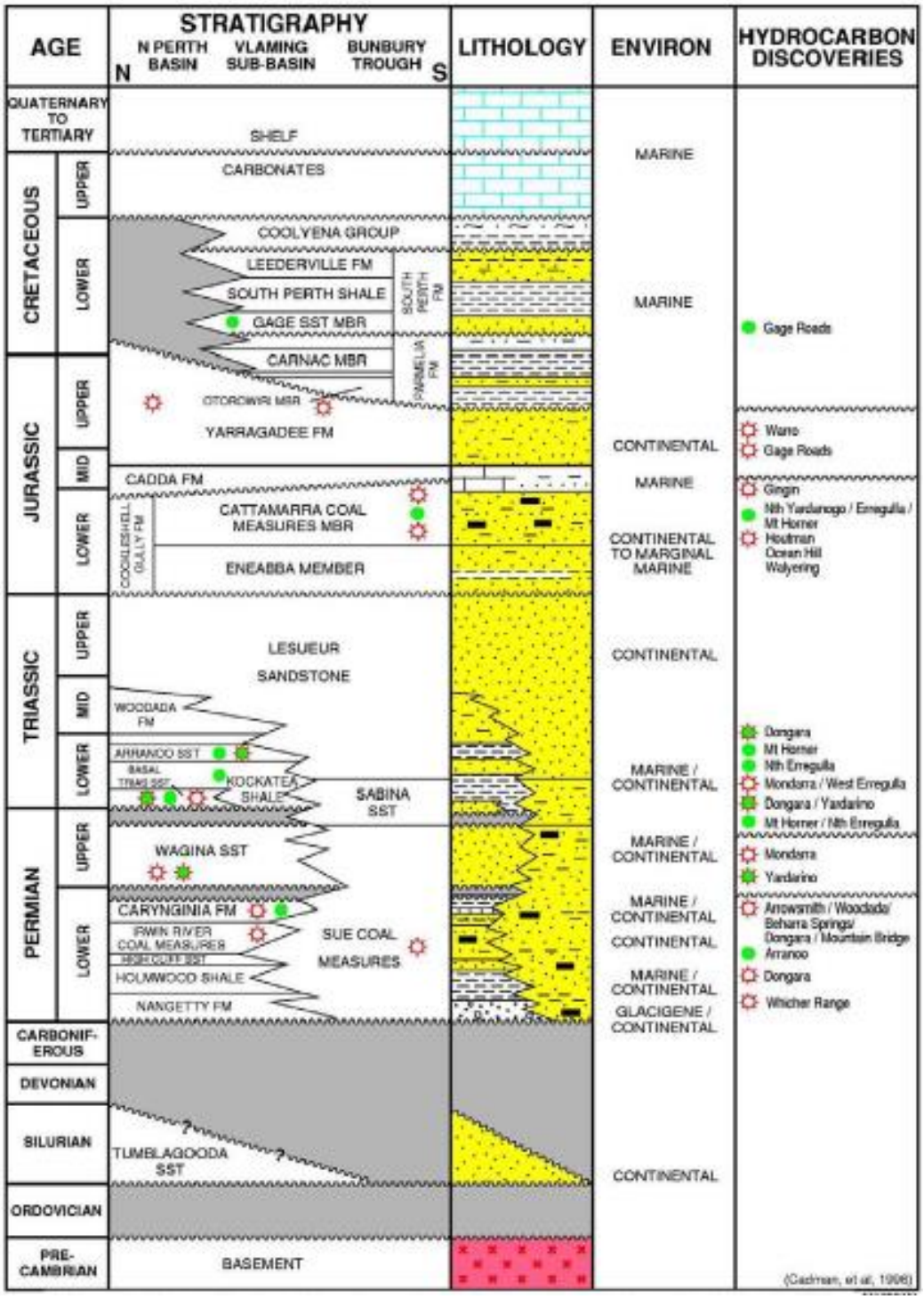

Figure 2-1: Stratigraphy of the northern Perth Basin (after the Cadman., 1994).

2.4 Potential gas shale formations

The Perth Basin has several fields already discovered, that have a potential for gas shale formation, the source rocks of those gas are the Kockatea Shale, the Carynginia Formation and the Irwin River Coal Measures. In 2010, the Woodada Deep-1 well was the first well drilled by the Australian Worldwide Exploration (AWE), as a target for gas shale resource in the Perth Basin. AWE also tested the Kockatea Shale from the Redback-2 and the Redback South-2 wells in 2011. In addition, the Arrowsmith-2 well was drilled to test the gas shale resources in the Kockatea Shale, the Carynginia Formations and the Irwin River Coal Measures (Western Australia Department of Mines and Petroleum, 2014 (DMP)). Our study covers the interesting potential gas shale formations of north Perth basin, which are associated with different 3D seismic surveys in the area. There are more than four areas of interest that have the potential to be future gas fields (Figure 2-2), with the most important being the Beharra Springs, which is located in the south of the seismic survey. This is followed by the Dongara gas field in the north of the surveyed area. The Hovea and Mondarra gas reserves are also main gas fields in the Perth Basin and are located in the centre of the seismic survey. The main gas source rock in this area is found in the basal marine facies of the Lower Triassic Kockatea shale, with the most important reservoirs in the Upper Permian and Jurassic sandstone. Other gas source rocks found in the Perth Basin include the Carynginia Formation and the Lower Permian Irwin River Coal Measures (Boreham et al., 2001 a, b).

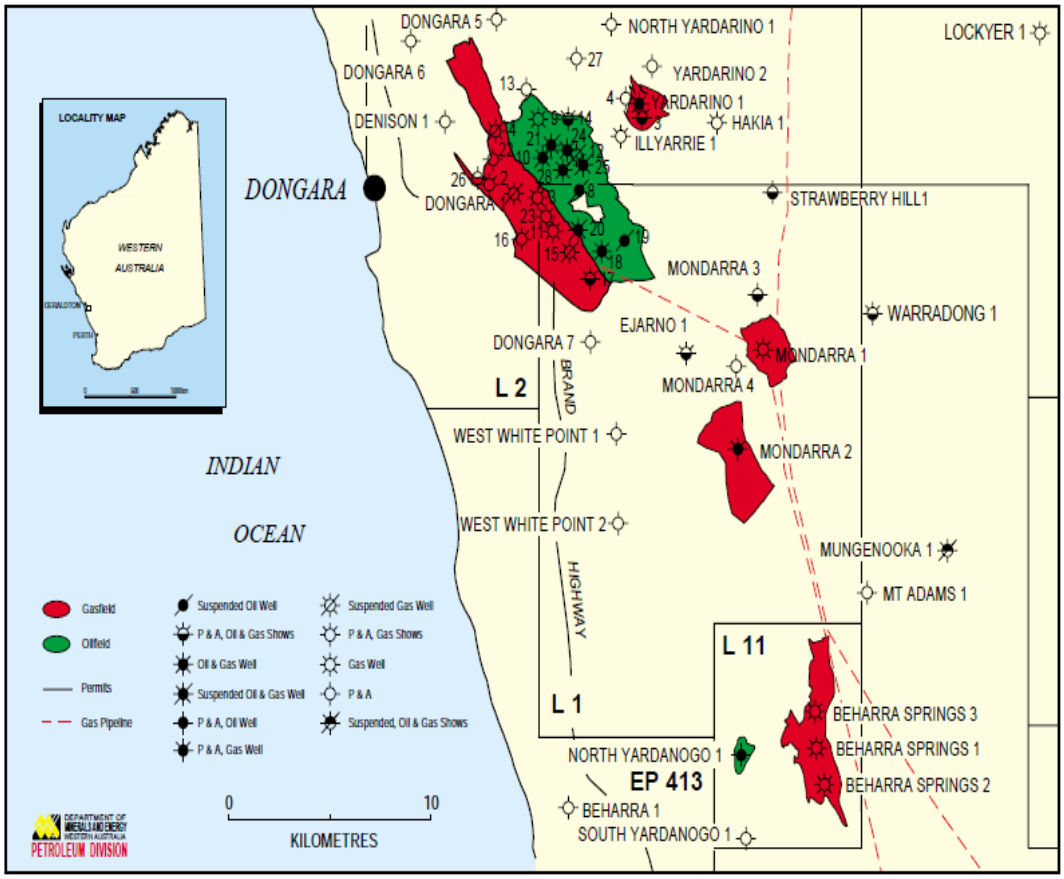

Figure 2-2: Perth Basin map shows gas shale potential in after (Owad-Jones and Ellis, 2000).

2.5 Hydrocarbon shows (Source Rock in the Perth Basin)

2.5.1 Kockatea Shale

Petroleum accumulations in the Perth Basin are supposedly to the originated from the Permian, Lower Triassic and Jurassic strata. The main Permian and Triassic source rock of the Lower Triassic Kockatea Shale in the northern Perth Basin has been shown to have the most potential for hydrocarbon condensates (Thomas and Barber, 2004). The Kockatea Shale consisting of inter-bedded sandstone, limestone, shale and siltstone widespread throughout most of the northern Perth Basin (Millheim, 1972). Tupper (1992) documented that the Kockatea Shale is thickly developed throughout the northern Perth Basin varying from about 200 m in the north to a maximum thickness of 1100 m. The TOC content ranges from 0.5 – 5%. The TOC content is greatest at the base of the Kockatea Shale, decreasing upward with an

accompanying change from hydrogen rich to hydrogen poor kerogens. The base of the Kockatea Shale ("hot shale") is the main source interval. The Hovea Member at the base of the Kockatea Shale contains fossiliferous and organic-rich shale, commonly 1 – 5 % TOC associated with hydrogen index HI 300 mg HC/g TOC, which is representative of the rich hydrocarbon source rock (Redback Well Completion Report, 2011).

2.5.1 Carynginia Formation

The Carynginia Formation in the Perth Basin indicates a good organic richness with TOC values of more than 1% and low hydrogen index (HI) values of less than 100 mg HC/g TOC. The gas shale source potential of the Carynginia Formation is related to the Carynginia Shale Unit that is defined as dark brown black, as well as inconsistently micaceous and carbonaceous, with a fairly constant depositional thickness of 300 m across the Basin (Tupper, 1992; Thomas and Barber, 2004). The overlying Carynginia Limestone Unit is dominated by clean limestone and sandstone with negligible mudstone. The authors also added that the timing of gas generation from the Carynginia Formation is broadly similar to the underlying Irwin River Coal Measures. Peak gas generation in the Dandaragan Trough area took place in the mid to late Jurassic. On the Cadda Shelf, the generation began in the latest Permian and continued to the Early Cretaceous. Gas is the most likely hydrocarbon type generated from the Carynginia Shale Unit, given its kerogen type and current maturity. The existence of an earlier phase of oil generation appears to be unlikely given the distribution of hydrocarbons discovered in the Basin to date. Migrating upwards from the sequence into the Carynginia Limestone Unit, the Wagina and the Basal Triassic Sandstone is straightforward where these reservoir conduits are developed. Elsewhere expulsion from the Carynginia Shale will necessitate vertical migration up faults to higher stratigraphic levels. Intraformational traps within the Carynginia Shale are unlikely due to the low sandstone and limestone content. The Carynginia Shale directly beneath the Woodada and Beharra Springs Fields is not sufficiently mature for significant gas generation. Therefore the gas was probably sourced from the down faulted Permian section located immediately to the east of these fields.

2.6 Shale composition

The samples used in our study to investigate the composition of shales in the Perth Basin from both the Kockatea Shale and the Carynginia formations come from different wells in the Perth Basin. The mineralogy and geochemical analysis data were determined and provided by the DMP. The composition of the whole rock mineralogy for different wells and shale formations in the Perth Basin is displayed in a ternary plot in Figure 2-3. It contains 12 samples come from three different wells (Redback-2, Redback-1 and Arrowsmith-2) of Kockatea Shale. Quartz, Feldspar and Pyrite (QFP) are abundant in three samples (comprising of 13 – 55%, by weight). Quartz is the highest content among the non-clay mineral in eight samples which comprised 8 – 40% by weight. Quantitative whole rock analysis results showed that the clay minerals with kerogen collectively made up between 30 and 72% of the samples. Illite/mica ranks the highest content among the clay minerals in the 12 samples, which account for 16 – 30% by weight. The second highest content of clay minerals is illite/ semectite with 11 – 26%, by weight. Carbonate in those samples had around 1–52% by weight.

The ternary plot shows also 48 samples from five different wells (the Arrowsmith-2, the Woodada-2, the Jingemia-5, the Freshwater point-1 and the Dongara-23), taken from the Carynginia Formation. QFP are abundant in the three samples (comprising of 15 – 85% by weight). Quartz is the highest content among the non-clay minerals which comprised 15 – 55% by weight. Quantitative whole rock analysis results showed that the clay minerals plus kerogen collectively made up between 20 and 70% by weight. Illite/mica ranks the highest content among the clay minerals in the 48 samples, which comprised 5 - 25% by weight. The second highest content of clay minerals is illite/semectite with 6 – 20% by weight. Carbonate in those samples was around 2 - 15% by weight.

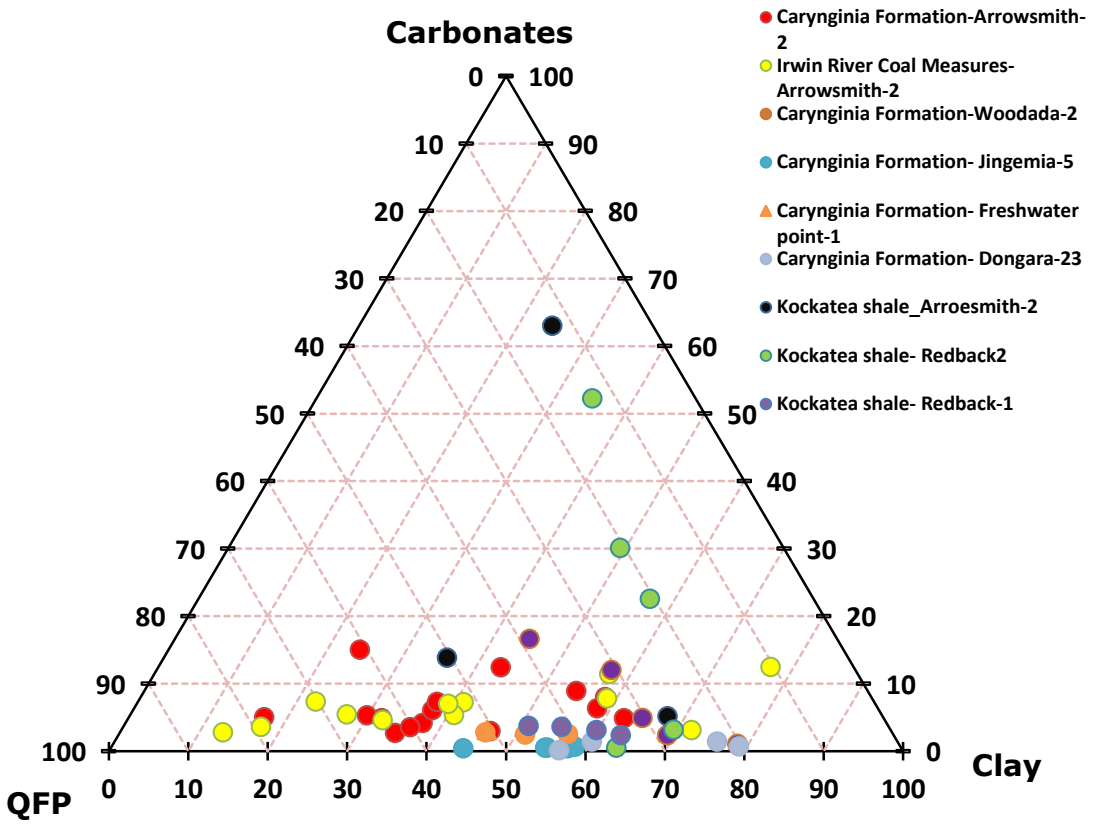

Figure 2-3: Ternary plot is representation of the sample material compositions for different shale formation, (most of the data are from the DMP and Origin Energy LTD, Shale reservoir evaluation report)**.**

Chapter 3. Methodology

3.1 Seismic inversion applications and analysis

The workflow plays a key role during unconventional used different seismic inversion approaches. Poststack inversion and attributes are used to map discontinuities and structural trends that may influence the drilling or production processes. Unconventional natural gas reservoirs are challenging to characterise due to the elastic properties of shale rock, which can vary significantly within and across the reservoir due to variable mineral compositions exhibited by the organic rich shale (Zhu et al., 2011). Therefore, the role of seismic in gas shale has become a more effective tool in predicting the sweet spots that are likely to have high TOC content and good gas storage. In addition, based on the relation between the petrophysical and elastic rock properties obtained from the interpretation of measured well-log data, the reservoir properties can be predicted. Recently, many independent methodologies have become well known within the spectrum of the 2D and 3D seismic interpretation approaches: multi-dimensional attribute analysis, neural networks, AVO analysis, as well as prestack and poststack inversions. While each of these approaches has different benefits and weaknesses, the applicability of any particular technique depends first on the available data and geological tasks (Filippova and Alabushin, 2011).

3.1.1 Model-based inversion and multi-attribute analysis

Seismic inversion helps to analyse the elastic properties of shale formations by extracting the analysis of reflection coefficients at acoustic interfaces (Avseth et al., 2005). Poststack (model-based) inversion is used to generate the AI volume and involves interpreted horizons to guide the interpolation process. This requires a series of steps to be followed after loading the well and 3D seismic data and picking the horizon. The first step in our objective is to apply poststack inversion to estimate the TOC content by performing model-based AI inversion. This identifies the zones of low AI and pertinent rock properties, such as the TOC, porosity, elastic properties and V_{clay}, using seismic multi-attribute analysis. Those rock properties are used as external attributes, together with other trace attributes to perform seismic multi-

attribute analysis to predict TOC. The workflow of seismic inversion is shown in Figure 3-1 as follows: (1) Find a relationship between the TOC content and the AI of shale formation, to convert the AI values to the TOC percentage. This information can be obtained using well-log data and laboratory experiments with samples cored from the well bore. Together with the seismic data, all of this information can be used to understand the entire dimension of the reservoir, providing valuable quantitative estimation of the TOC content (Zhu et al., 2011).

Rock physics studies of organic shale have shown that the AI, which is the product of compressional velocity (P-wave velocity) and density, decreases when the TOC is increased. The correlations between the TOC content and the AI can be used to map variations in TOC profiles with well-calibration by cross-plotting the AI and TOC content and predict the TOC content from that correlation; (2) The seismic interpretation and picking the horizons of the target formations; (3) The check-shot-calibrated time/ depth conversion and edited well-data logs are used to extract wavelets around each well; (4) Well to seismic tie until the best correlation is obtained, by extracting wavelets using statistical wavelet and well data; (5) Build the initial model and run the inversion analysis; (6) Select optimal seismic attributes.

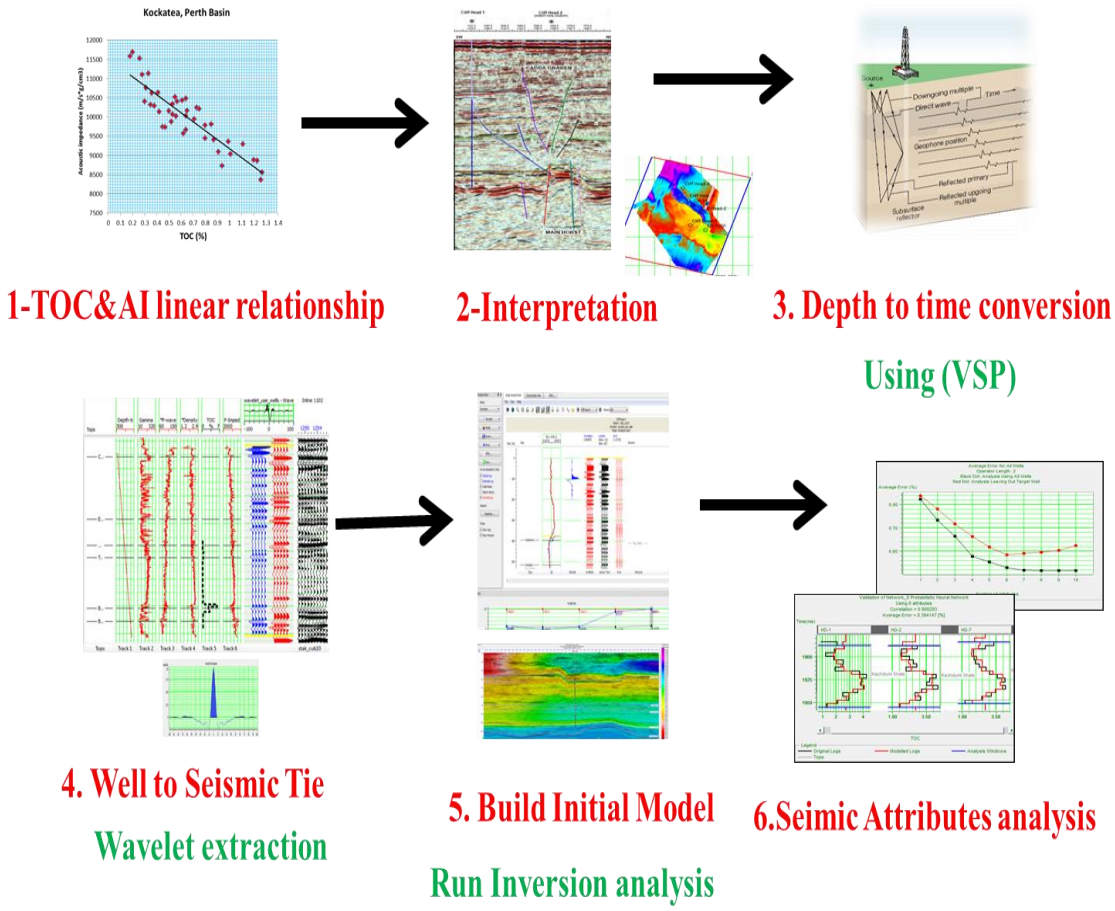

Figure 3-1: Workflow of poststack seismic inversion.

3.1.2 AVO analysis and modelling

To better understand the rock properties of organic shales from the target reservoir interval, it is important to understand the AVO analysis and response of the organic gas shale. The AVO response is dependent on the elastic properties, P- and S-wave velocities, and density in a porous reservoir rock. The change in effective velocities and density due to the TOC and other minerals impact the AVO response of the organic shale formation. Synthetic CDP gathers were modelled using log and 3D seismic data to understand the AVO responses for different cases. The first case relates to organic rich TOC (5%wt) in shale formations, while the second relates to inorganic TOC shale formations (≈ 0%wt). There are three main methods used for the modelling process namely by Zoeppritz equation, Aki-Richards equation and the elastic wave equation. In this project, we have used the elastic wave methods developed by Kennet (1980).

Several steps are involved when applying the AVO modelling after the well-log data (P-wave, S-wave and density) and the seismic data are selected: extract a wavelet, tie the well and optimise the depth-time relationship between well and seismic and then compare the synthetic result to the stacked offset. The first step is to extract the wavelet using two basic methods, which are either statistical or by using the wells. The statistical methods use the seismic data only to extract the wavelet; the amplitude spectrum estimation is from the seismic data, but the assumption about the phase is required. The other method uses the well data; the estimation of the amplitude and phase spectra of the wavelet is good, but the wells need to be correlated before use. The second step is to correlate the well and extract the wavelet using the wells. The next step is to identify scenarios. This step helps to identify the geological conditions of the model. This option can also apply to different scenarios with different fluid combinations within the target reservoir. The last step is to create synthetics; different methods can be used from the three algorithms (Zoeppritz, Aki-Richards and Elastic wave) to calculate the synthetics. Different options can be chosen from the type of synthetics (Offset or Angle), the quantity of the offset as well as the location of the near and far offsets. Elastic waves can model a wider range of all the effect offsets, such as multiples and converted waves. This method is more accurate than the Zoeppritz modelling, but it can be more sensitive to log editing issues.

3.1.3 Elastic Impedance Inversion for near- and far-offset

Elastic Impedance (EI) was used in this project to extend and exploit the study of the AVO response of the organic shale formations in the seismic data. EI inversion is used to generate EI volumes for both near- and far- offsets, which provide a reliable framework to invert non-zero offset seismic data; the same goes for as AI with zero offset. The amplitudes of different offsets are rated to the change in AI. This can be tied to well-log using synthetics based on AI poststack inversion and using the same AI poststack inversion workflow. EI is a function of P-wave velocity, S-wave velocity and density, with application of the incidence angle. The theory of EI is introduced from Aki and Richard's approximation to the linearization of Zoeppritz Equations as show below in Equations 3-1 and 3-2. In all the cases of EI inversion, note when the angle is 0°, the EI is equal to AI (Connolly, 1999) as shows in Equation 3-3. Different angles were tested on volumes for both near and far offsets

(5° , 7.5° , 12.5° , 15° , 22.5° *and* 30°) and the angle of 5° was used for the near offset, while 30° was used for the far offset.

$$EI(\theta) = V_P^{(1+\sin^2\theta)} V_S^{(-8K\sin^2\theta)} \rho^{(1-4K\sin^2\theta)}, \quad \text{Equation 3-1}$$

$$\text{Where } K = \left(\frac{V_S}{V_P}\right)^2 \quad \text{Equation 3-2}$$

$$EI(\theta = 0^{\circ}) = AI = \rho V_P \quad \text{Equation 3-3}$$

EI inversion involves a series of steps to be followed, similar to the AI inversion by using the poststack inversion algorithms. The only difference is in the setup for the elastic inversion for building the initial model and the setup for the EI equation based on using 30 wells to control the model.

3.1.4 Lambda-Mu-Rho (LMR) approach used for gas shale

The LMR approach is one of the most important tools used for gas shale analysis as i assumed the shale is isotropic. It uses the rock physics trends, which allow the seismic inversion data to be used to predict changes in reservoir properties such as porosity, lithology and stiffness or fracability of the rock (Perez et al., 2012).

In the physical meaning, the lambda (λ) is a measure of the incompressibility and is sensitive to the pore fluid, where mu (μ) is a measure of shear rigidity, which is sensitive to the rock matrix (Goodway et al., 1997). LMR uses the following definitions as shown in Equation 3-4 and 3-5:

$$\lambda\rho = Ip^2 - 2Is^2 \quad \text{Equation 3-4}$$

$$\mu\rho = Is^2 \quad \text{Equation 3-5}$$

The crossplots of Lambda-Rho (LR) versus Mu-Rho (MR) are most beneficial when defining the fundamental properties of gas shale, similar to other fundamental conventional interpretation templates such as I_P versus V_P/V_S , or I_P versus Poisson's ratio. Goodway et al. (2006, 2010) and Perez et al. (2011) developed LMR

interpretation templates for interpreting the seismic inversion data of gas shale based on the rock physics trends (Figure 3-2). The compressional of LR and MR logs (which are calculated from measured compressional and shear sonic logs, together with the density log) show a graphic correlation between these geophysical parameters and more traditional petrophysical properties. These correlations allow the seismic inversion data to predict the change in reservoir properties. In this project, LMR template has been used to define the sweet spot of gas shale in the Perth Basin, using two different analyses; the first is LR versus MR displayed with mineral companions to define the clay-rich or quartz-rich within our shale formation. The shale described in this study varies in mineral composition from 60/ 40% quartz/clay to 30/ 70% in quartz/clay respectively, while the porosity is about 0% - 12%. The change in the rock composition is linked directly to the brittleness of the rock with the quartz-rich begin described as brittle, while the clay-rich is ductile. The second is LR versus MR displayed with TOC, Young's modulus and Poisson's ratio to define the brittle organic shale. The definition of a sweet spot in the reservoir zone is characterised by low LR and higher MR values.

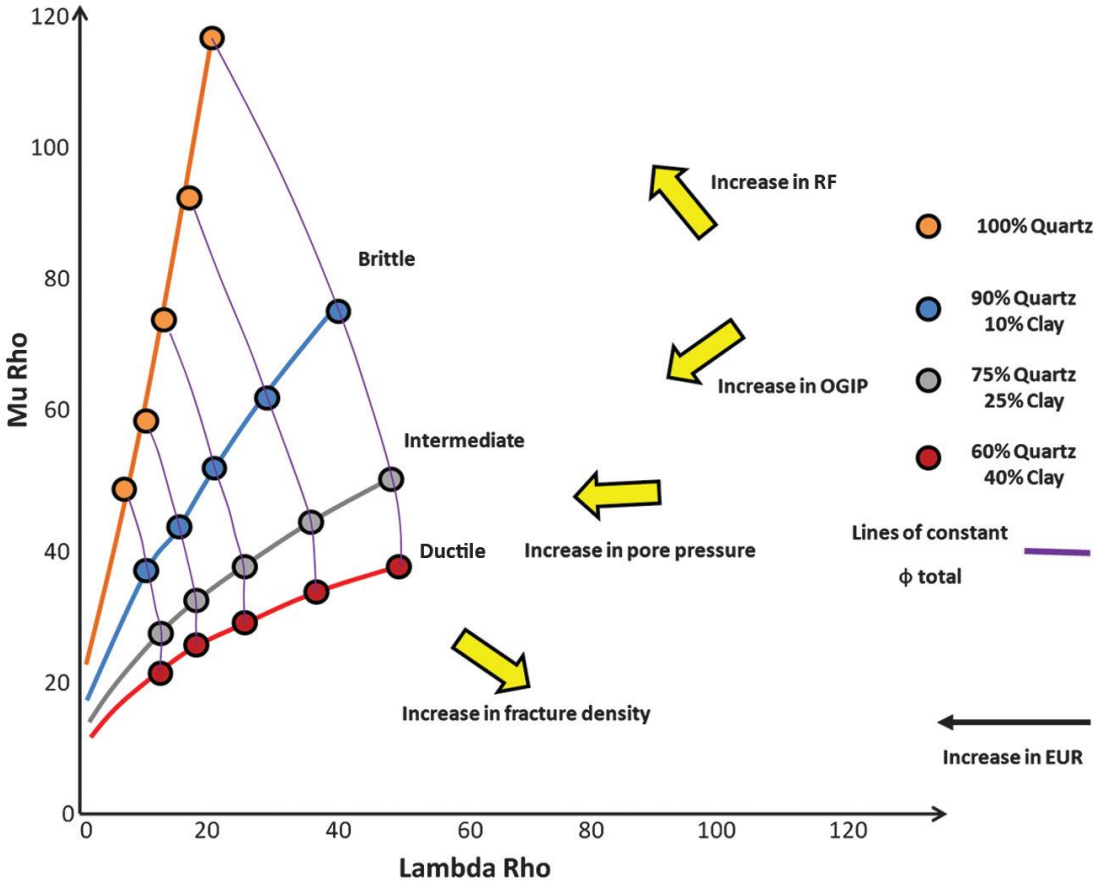

Figure 3-2: Crossplots of LR versus MR based on a heuristic rock physics template, which was developed by Perez et al. (2011) to interpret seismic, well-log and core samples in gas shale (after Alzate and Devegowda, 2013).

3.2 Ultrasonic measurement

The laboratory experiment is needed to understand the gas shale properties more thoroughly via core gas shale samples, which will support our study of the seismic inversion. In this study, the laboratory experiments presented help us to understand the effects of the TOC content, clay mineral and stress, as well as lithology on wave velocities using natural shale core samples from the Perth Basin. This experiment will also try to account for all the factors affecting the velocity and anisotropy of a natural shale sample. In particular, factors including stress state, stress history, clay mineral content and TOC content are taken into account. Indeed, in the second part of this study synthetic shale core samples with known percentages of clay mineral, non-clay mineral and the TOC content under variable and/or in-situ stress conditions were produced. Such a system enabled us to study the contribution of each of the factors independently. The objective of this part of the study was to investigate the

effect of variable TOC content on elastic properties of synthetic shale with and without stress conditioning. Most of the presented methodology and results are published in an international journal (Altowairqi et al., 2013) and some are published as conference papers in different international conferences (Altowairqi et al., 2015, (A); Altowairqi et al., 2015, (B)).

3.2.1 Terminology

In this section, a mean effective stress, defined as *1/3 (σ'1+2σ'3),* is used as a standard triaxial test. An in-depth discussion of this test has been written by Dewhurst and Siggins (2006). Hooke's law describes the mechanical behaviour of a linear elastic body; the law states that for such a body, stress and strain can be related through a fourth–order tensor Cijkl (Mavko et al., 1998). An anisotropy elastic rock displaying vertical transverse, isotropy (VTI) is given in a Cartesian coordinate, as shown in Equation 3-6.

$$\begin{bmatrix}\sigma_{xx}\\ \sigma_{yy}\\ \sigma_{zz}\\ \sigma_{xy}\\ \sigma_{xz}\\ \sigma_{zy}\end{bmatrix}=\begin{bmatrix}C_{11} & C_{12} & C_{13} & 0 & 0 & 0\\ 0 & C_{11} & C_{13} & 0 & 0 & 0\\ 0 & 0 & C_{33} & 0 & 0 & 0\\ 0 & 0 & 0 & C_{44} & 0 & 0\\ 0 & 0 & 0 & 0 & C_{44} & 0\\ 0 & 0 & 0 & 0 & 0 & C_{66}\end{bmatrix}\begin{bmatrix}\varepsilon_{xx}\\ \varepsilon_{yy}\\ \varepsilon_{zz}\\ \varepsilon_{xy}\\ \varepsilon_{xz}\\ \varepsilon_{zy}\end{bmatrix} \quad \text{Equation 3-6}$$

"From the matrix, Z lies along the symmetry axis, the elastic stiffness coefficients (*Cij*), *σxx, yy, zz* are the normal stresses; σzx, yz, xy are the shear stresses; ε*xx*, *yy*, *zz* are the normal strains and εzx, yz, xy are the shear strains" (Dewhurst and Siggins 2006). Velocities and elastic constants are connected via the following Equations (3-7) to (3-11) posted from Dewhurst and Siggins (2006):

$$C_{11} = \rho V_{ph}^2, \;\; V_{ph} = (C_{11}/\rho)^{1/2} \quad \text{Equation 3-7}$$

$$C_{33} = \rho V_{pv}^2, \;\; V_{pv} = (C_{33}/\rho)^{1/2} \quad \text{Equation 3-8}$$

$$C_{44} = \rho V_{s1}^2, \;\; V_{s1} = (C_{44}/\rho)^{1/2} \quad \text{Equation 3-9}$$

$$C_{66} = \rho V_{sh}^2,\ V_{sh} = [(C_{11} - C_{12})/2\rho]^{1/2} \quad \text{Equation 3-10}$$

$$C_{13} = -C_{44} + [(C_{11} + C_{44} - 2\rho V_{p45}^2)(C_{33} + C_{44} - 2\rho V_{p45}^2)]^{1/2} \quad \text{Equation 3-11}$$

"Where V_{pv} is the P-wave that travels normal to the bedding plane, V_{ph} is the P-wave propagate parallel to the bedding, qV_{p45} is the quasi-P-wave propagating at 45° to the bedding, V_{s1} is the wave propagating normal to the bedding with particle motion parallel to the bedding, V_{sh} is the S-wave that travels parallel to the bedding with particle motion parallel to the bedding and ρ is the bulk density of the sample" (Delle-Piane et al., 2011).

The anisotropy factors ε, γ and δ are calculated based on Thomsen (1986) as shown in Equations 3-12 to 3-14 below:

$$\varepsilon = (C_{11} - C_{33})/2C_{33} \quad \text{Equation 3-12}$$

$$\gamma = (C_{11} - C_{33})/2C_{33} \quad \text{Equation 3-13}$$

$$\delta = \frac{(C_{13} + C_{44})^2 - (C_{33} - C_{44})^2}{2C_{33}(C_{33} - C_{44})} \quad \text{Equation 3-14}$$

In the ultrasonic wave measurement, the isotropic stress state was applied equally in all directions. The shale was cut parallel to the bedding as it was presumed to be transversely isotopic (TI) and all the three principal stresses were presumed to be equal.

Due to the fine-grained nature of the organic shales and their challenging characteristics, it is important to use the new methods and equipment from CSIRO to ensure that the samples are measured in-situ reservoir conditions (Prasad et al., 2009). This is important to avoid the desiccation of the organic shales after coring, which would cause the shale to fracture, inducing large capillary stresses and changing the particle orientation and pore-size distribution (Tutunce, 2010; Dewhurst et al., 2011). The shale samples used in this research are from the Arrowsmith–2 and Redback-2 wells, taken at different depth intervals and TOCs (0.23%, 1.8% and 3.03%). The samples were cylindrical (about 75 mm in length and around 38 mm in diameter) and offcuts from those samples were used to measure porosity,

composition and grain density. It was necessary to obtain proprietary information before testing the samples and this information includes the depth, age and the TOC content of the samples.

3.2.2 Equipment setup of testing gas shale core samples

In this research, equipment from CSIRO was used such that it allows an understanding of the physical properties of shale under well-constrained laboratory conditions. The equipment used for testing the organic shale core samples, includes of high stiffness load frames, triaxial cell, simulating natural in-situ conditions and examining the changes in the physical properties of the rock (Figure 3-3). "The rig provides an independent control of pore pressure, confining pressure and axial load to the operational upper limits of 70 MPa, 70 MPa and 400 MPa respectively" (Dewhurst and Siggins, 2006). All three principal stresses can be applied on samples of 38 mm in diameter. All of the tests were measured at normal room temperature, data logging and pump control were based on a LabVIEW program. Additional details on this equipment can be found in Dewhurst and Siggins (2006) and Delle Piane et al. (2011).

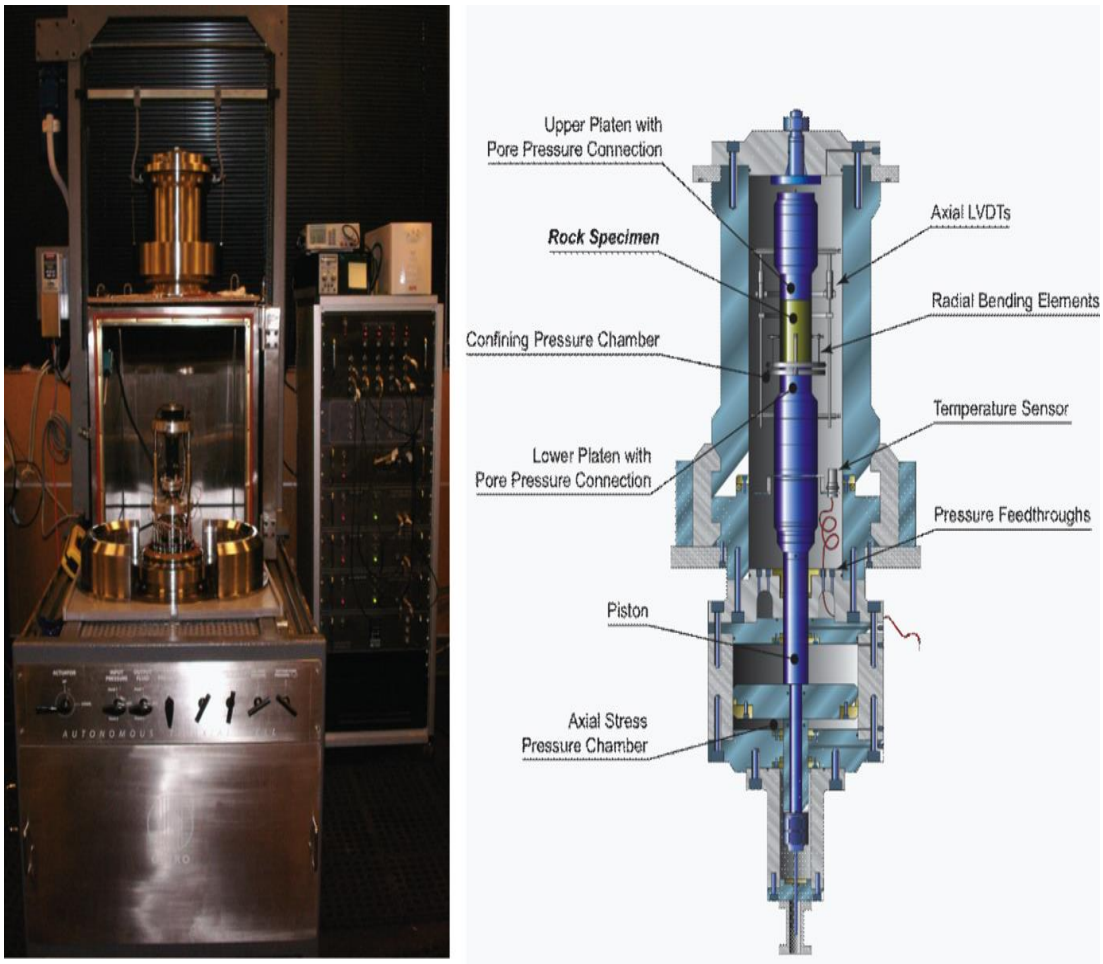

Figure 3-3: Triaxial testing equipment with ultrasonic setup located in the CSIRO Rock Mechanical Lab.

One of the most popular methods to shale characterisation is to assume symmetry, extracting the oriented plugs and measuring the elastic velocity consistent to specific elastic constants. "Transverse isotropy (TI) symmetry needs to extract the vertical, horizontal and 45°core plugs with respect to the bedding and measurement of the P- and S-wave velocities to calculate five required elastic constants" (Mavko et al., 2009). Seismic wave velocities in any direction can be obtained from the combinations of stiffness tensor elements (Ciz and Shapiro, 2009; Sarout et al., 2006; Sayers, 2005). However, this experimental configuration (Figure 3-4), which is the same as that described by Dewhurst and Siggins (2006), was used in this research in order to make all measurements for the determination of the elastic tensor on a single core plug; rather than using a few core plugs cut at different angles to the principal axes to calculate anisotropy (Hornby, 1998). "By assuming the shale is a TI medium, the extraction of five independent elastic coefficients (to provide a full description of its elastic responses and the symmetry plane of such coincides with the fabric/bedding plane), is required" (Dewhurst et al., 2011).

The end platens house one MHz, PZT-5H piezo-ceramic P- and S-wave element that measures the ultrasonic wave velocities down the core axis. Furthermore, radial P and S-wave transducers are attached to the membrane to measure the velocity crossing the core diameter. Also, a couple of P-wave elements are directly attached to the sample surface transmit and receive pulses at 45° to the core axis (Delle Piane et al., 2011). Examples of waveforms for the five independent wave velocities measured with the ultrasonic transducer array are shown in Figure 3-5.

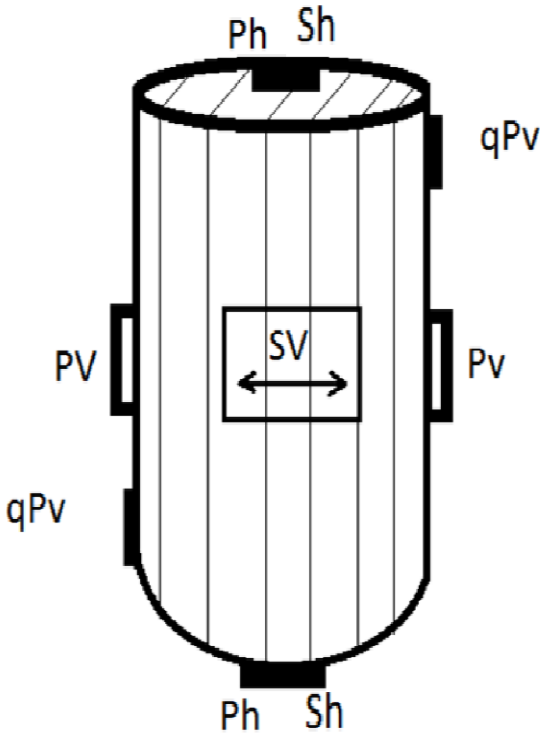

Figure 3-4: Experimental configuration of ultrasonic measurements.

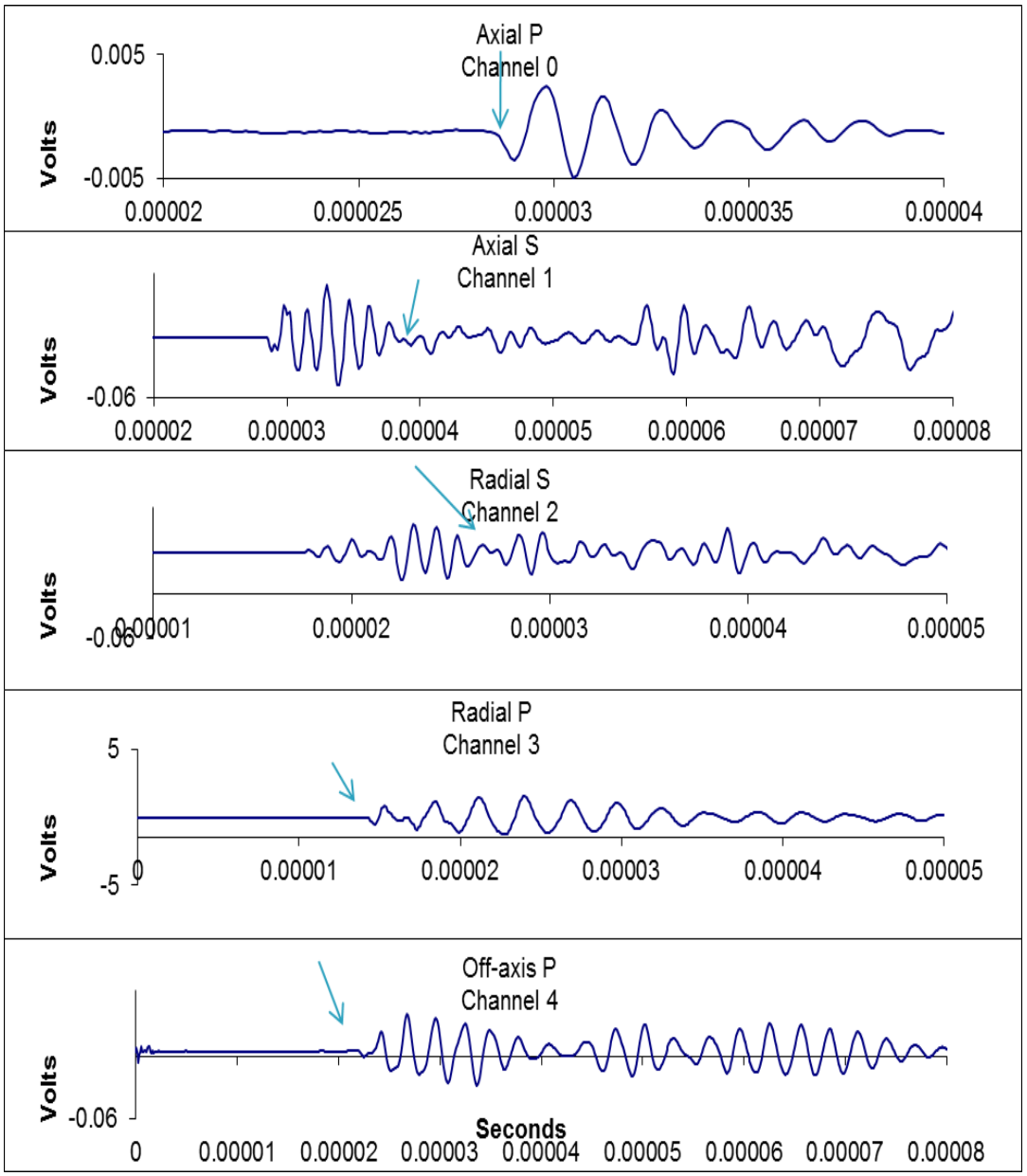

Figure 3-5: Plots showing five independent elastic coefficients measured. The arrows show the first arrival picks for P-wave and the picks of S-wave.

3.2.3 Synthetic shale preparation

Synthetic samples were prepared with predefined properties to enable systematic investigations of their elastic properties as a function of the TOC content and some other factors such as mineral composition. Having highly controlled environmental conditions enables us to investigate the effect of the TOC content and clay minerals

on the elastic characterisation of shale under different reservoir stress conditions in a more quantitative and accurate way.

As such measurements are rare; the impact of the organic matter on the shale elasticity has not been well understood. Most reports have been about manufacturing synthetic sandstone samples by different methods (Sherlock and Siggins, 2003). In this work, a number of synthetic shale samples were made using clay, quartz and calcite with different TOC percentages.

Zhu et al. (2011) noted that gas shales usually consisted of different types of minerals such as clay, quartz, calcite, dolomite and pyrite, which normally form intricate and perhaps an anisotropic matrix of rocks. In this study, we created more than 40 shale samples after a series of systematic trials with different methods to get representative synthetic shale samples. In this study, a method was developed to manufacture synthetic shale samples, having the correct weight to the density ratio and the best mix of minerals to produce a (consistent media). The target of making a mix of minerals consistent is that to make sure all the different types of minerals are mixed well and equal around the sample. To achieve this, a mixture of clay and non-clay minerals was compressed with organic matter under high pressure inside a steel core holder (only in the axial direction) to produce an anisotropic media within each sample. The composition of synthetic shale samples used in our test had the same composition of a typical gas shale formation in the Arrowsmith-2 and Redback-2 wells in the Perth Basin (Well Completion Report- Arrowsmith-2, 2011; Well Completion Report- Redback-2, 2011).

Several steps and equipment were involved in creating a single sample. Each synthetic sample was formed under a high pressure using a hydraulic compressor, to produce a simulated core shown in Figure 3-6. A hydraulic compressor contains the control system and digital displays, which can help to control a force at a constant rate or pressure. Almost 7000 psi (48 MPa) of hydraulic pressure was applied by an oil driven hydraulic pump.

The first stage of preparing the samples is to mix an amount of material (fine powder) using a mixer machine for several hours until it becomes consistent (homogeneous). The mix is composed of 45% clay minerals (kaolinite), 40% non-clay minerals (quartz), and 15% cement with some water. Organic matter is added to

the mixer minerals with different percentages for each sample. Petrographic analysis results for the organic material used indicate a mixture of vitrinite (71%), semi-fusinte (13%) and some other minor components. The density of the organic material is about 1.4 g/cc.

The second stage is to add water to the mixed minerals and to compact them within a steel cylinder frame (10.2 cm in length and 3.8 cm in diameter). The steel cylinder with the materials inside is placed from the top between several steel blocks and a solid cylinder (designed with different lengths but with the same diameter of 3.6 cm); to compress the minerals inside the steel cylinder, using a hydraulic pressure jack, all of which are placed within a hydraulic compressor. Pressure is applied at a constant flow rate of hydraulic oil (3 mL/min) until the pressure reaches 7000 psi (48 MPa). The samples' final bulk density and porosity are in the range of 2.0 - 2.4 g/cc and 20 - 30% respectively. All the samples are tested ultrasonically to obtain the elastic properties.

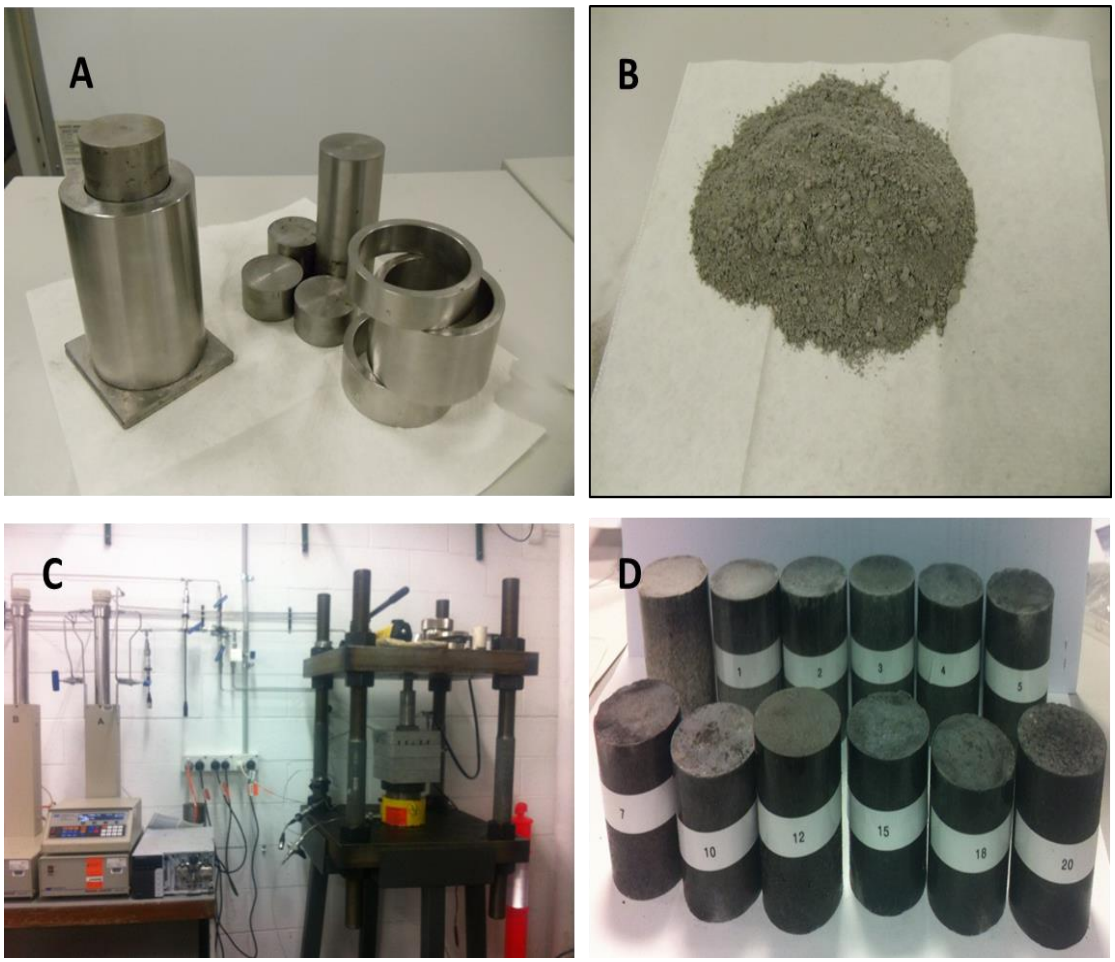

Figure 3-6: (A) Steel cylinder casts designed for high pressure use. (B) The mineral mix as a fine powder. (C) Hydraulic compressor with different steel blocks and hydraulic pressure jack used to create synthetic shale. (D) Synthetic shale core samples with different percentages of the TOC contents from 0 to 20%.

3.2.4 Equipment setup for testing synthetic shale core samples

We chose our experimental technique to investigate the variations of P- and S-wave velocities as a function of the TOC content or of the clay mineral for 40 samples under varying stress levels. The experiment is typically set up involving 1 MHz transducers. Initially we measured ultrasonic velocities at both atmospheric pressure and elevated confining pressures of up to 6000 psi (41 MPa). This core holder (Figure 3-7) contains a high pressure triaxial cell, with the ability for independent control of the stresses to operational upper limits of 7500 psi (52 MPa) for all the principal stresses, while independently exerting pore pressure of up to 3200 psi (22

MPa). All of the tests were measured at normal room temperature (around 23°C); data logging and pump control are based on the LabVIEW program.

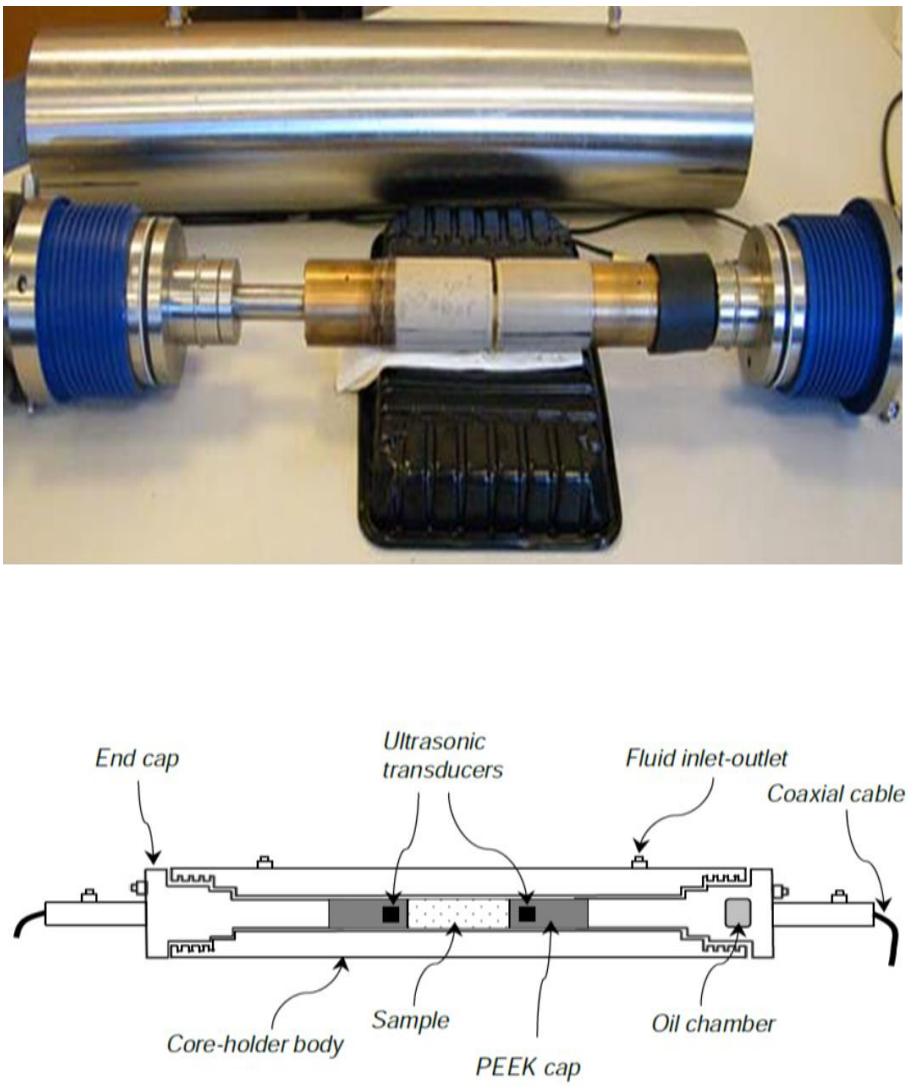

Figure 3-7: View and schematic of core holder which was used for testing the ultrasonic wave velocities under stress.

An example of the P- and S-wave velocities of each independently recorded waveform is shown in Figure 3-8. While P-wave arrivals are clean, the S-waves are less easy to pick at low confining pressure. High confining pressure helps to improve and pick the S-wave arrival. Arrival time picks are based on first breaks. Standard geophysical methods are used to improve those picks. Each signal is recorded and vertically stacked 20 times to improve the signal and to reduce the noise. It is noted that the picking errors decrease with rising stress levels. The errors in the S-wave velocities are approximately 6% at lower stress levels. P-wave errors are small at all

stress levels used in this research. SV-wave velocity is smaller than SH-wave velocity for each sample.

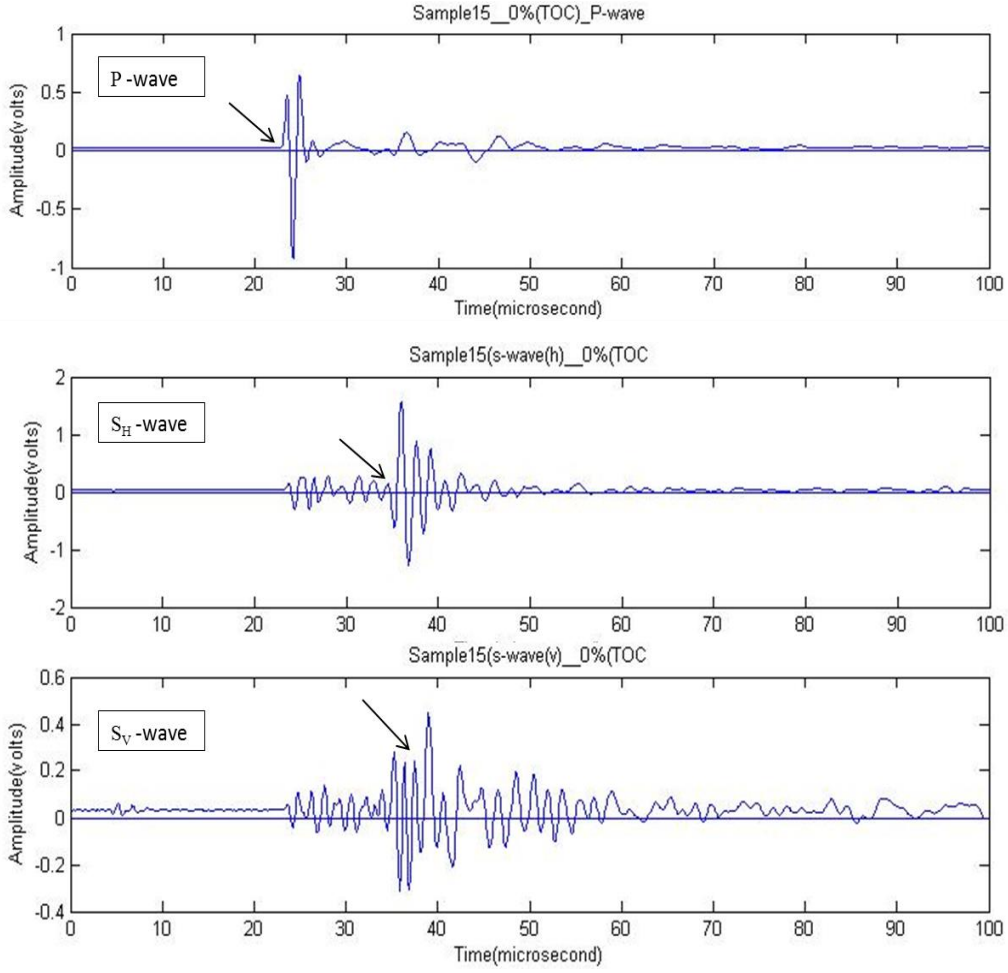

Figure 3-8: An example of the P-wave, SH-wave and SV-wave velocities of each independently recorded waveform.

Chapter 4. Seismic inversion and multi-attribute analysis to identify high TOC shale

A key objective in this chapter is to predict the TOC percentage from the seismic AI using the rock physics linear relationships equation between the TOC and AI for the Kockatea Shale and the Carynginia Formation. Different approaches of seismic inversion and multi-attribute analysis were conducted by combining 3D seismic data with log data. Also, the AVO analysis and modelling were applied to study the impact of the TOC content on the AVO response. The relationship between the LMR approach and the elastic properties are applied to predict brittle shale in our study. Some of the presented results have already been published (Altowairqi et al., 2013). In this chapter all the results are presented for the Kockatea Shale Formation, while some of the key findings for the Carynginia Formation. The complete results of the Carynginia Formation are provided in Appendix 1. Also, Appendix 2 presents the result of the 3D Marian Seismic inversion from the Cliff Head filed which is located west of the Perth Basin.

4.1 Database of Denison 3D seismic and well-log data

The Denison survey is located onshore in the north of the Perth Basin, WA (Figure 4-1). In 2004, a 3D seismic survey was conducted by Terrex Seismic (Veritas DGC Asia pacific LTD 2006). The survey covered 367.17 km^2. The data were acquired using cross-spread acquisition techniques with a vibrator source and 1,152 receivers. The source and receivers were spaced at 40 m intervals and the acquired data were binned in packets of 20 by 20 m. The dataset was processed using a 3D prestack time migration (Veritas DGC Asia pacific LTD 2006). In the study area, more than 92 wells were used in the seismic interpretation to pick the target formations. Only 20 control wells were used to build the poststack and prestack inversion. Most of the control wells had the requisite log suites (i.e. gamma ray, sonic, density, resistivity, neutron porosity, etc.). Only two wells had shear sonic, which was used when testing the gas shale resources in the Kockatea Shale and the Carynginia Formation. We have estimated S-wave velocities for all the wells by finding a linear relationship between the P-wave and the S-wave for both shale formations for the two wells that had shear sonic logs (Figures 4-2 (A) and (B)), the estimation of S-wave (as

assumption) will help to apply S-Impedance, AVO modelling, analysis and inversion, as we as the LMR approach.

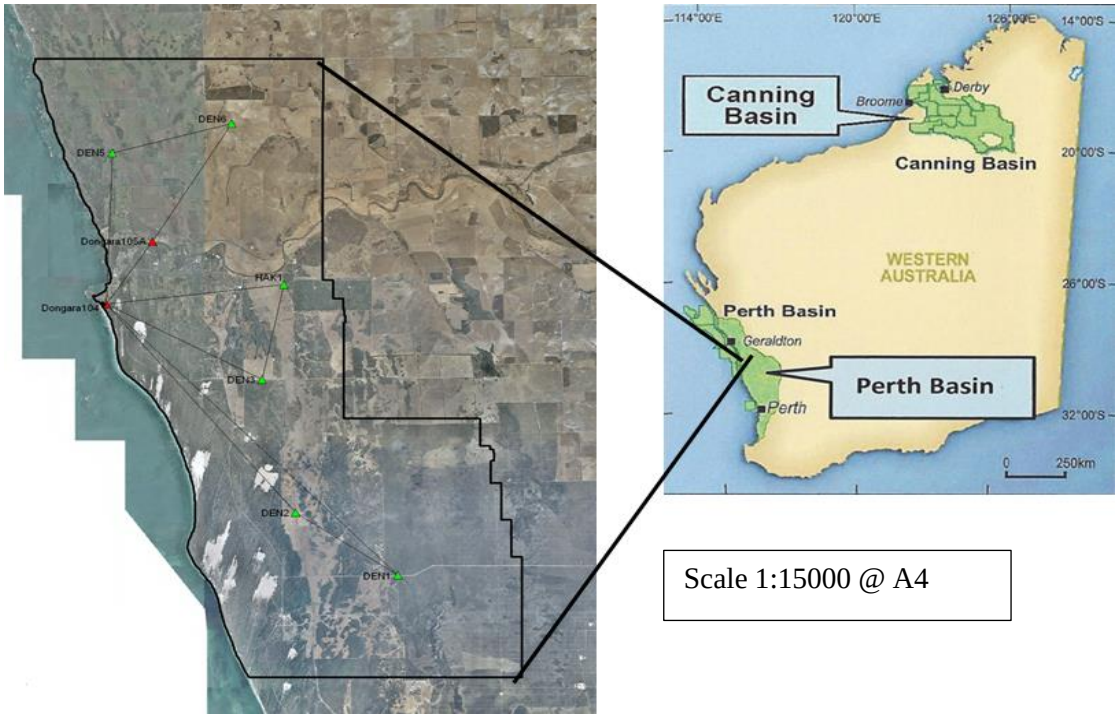

Figure 4-1: Denison 3D survey map in the northern Perth Basin (after Veritas DGC Asia pacific LTD, 2006).

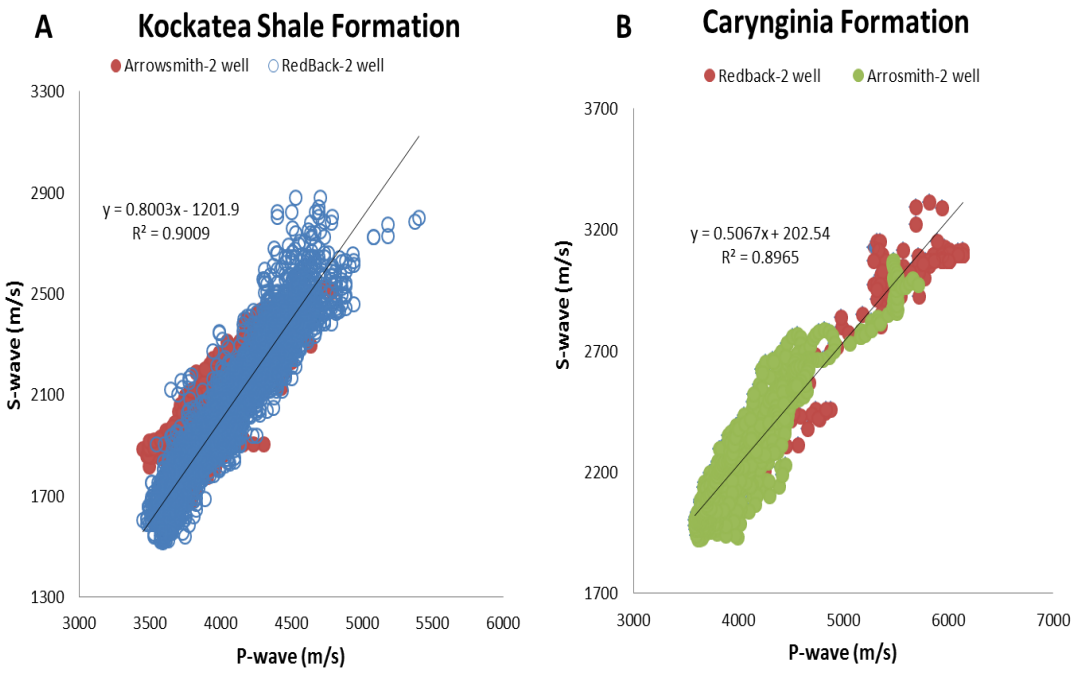

Figure 4-2: The estimated S-wave from P-wave linear relationship for (A) the Kockatea Shale and (B) the Carynginia Formation.

In total, five horizons were interpreted including the Kockatea Shale, Hovea Member, the shale formation at the base of Dongara Sandstone and the base of the Carynginia Formation (Figures 4-3 (A) and (B)). The seismic survey covers a large area and includes more than four gas fields of interest. The most important one is the Beharra Springs, which is located in the south of the seismic survey. This is followed by the Dongara Gas Field in the north of the survey. The Hovea and Mondarra gas reserves are also significant gas fields in the Perth Basin and are located in the centre of the seismic survey. The main gas sources in this area are found in the Kockatea Shale, the Carynginia Formation and the Lower Permian Irwin River Coal Measures (Boreham et al., 2001 a, b).

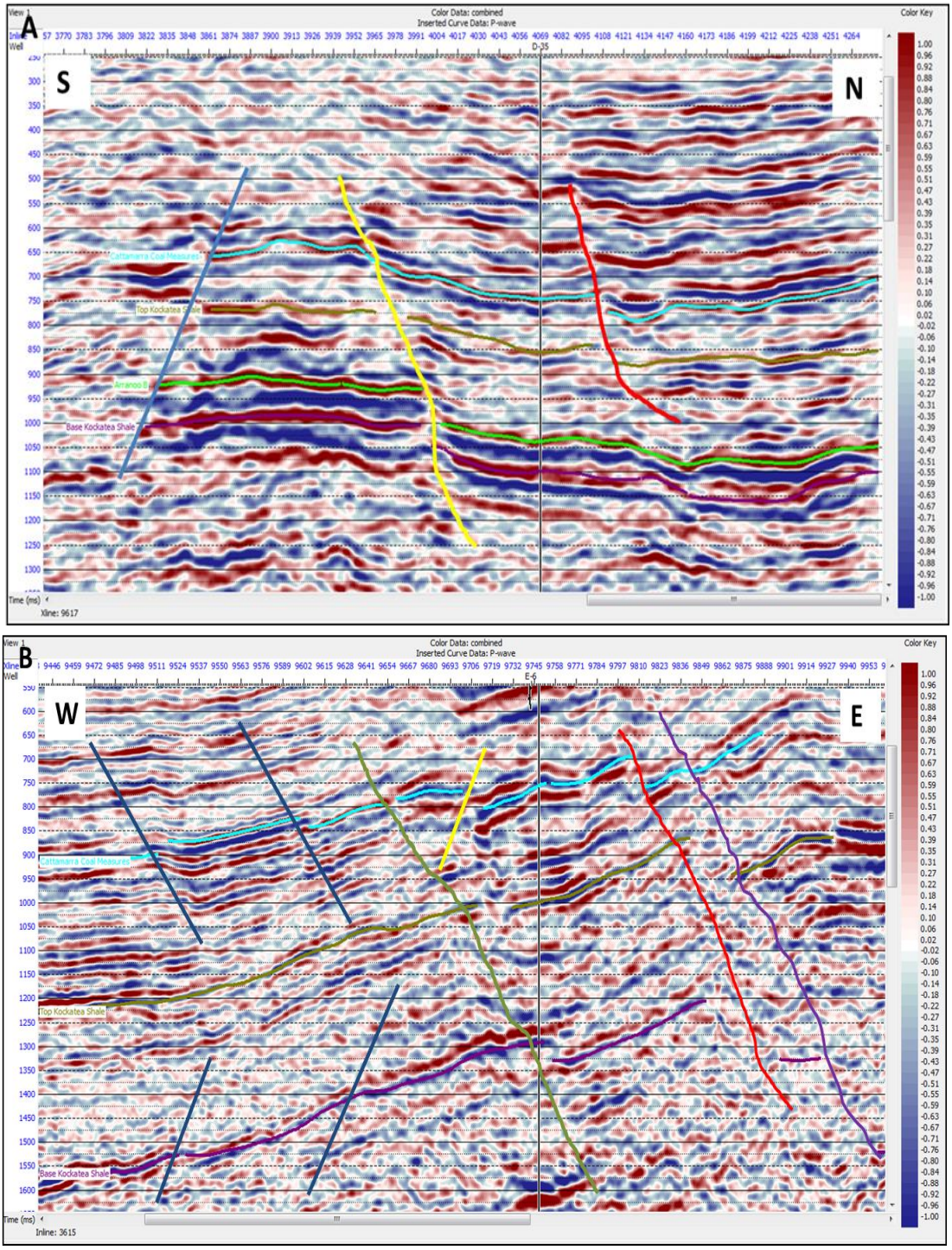

Figure 4-3: Seismic cross sections showing six horizons with complex faulting interpreted. (A) Example of the Dongara Gas Field with a strongly faulted northwest-trending anticline, bounded to the east by the north-south Mountain Bridge Fault. (B) Example of a complex structure as a result of interaction between the northerly Mountain Bridge Fault and the north-westerly trending fault system.

4.2 Cross-plot analysis

4.2.1 TOC content variations and acoustic impedance

TOC is a main attribute of organic shales and is a measure of the organic richness present in gas shales (Ross and Bustin, 2009). A good understanding of the influence of rock and pore fluid properties on seismic waves is needed characterise of a subsurface hydrocarbon reservoirs based on seismic data (Sena et al., 2011). Many rock physics studies of gas shales described in the literature have shown that the Acoustic Impedance (AI), the product of compressional velocity and density, drops with high TOC content (Altowairqi et al., 2013; Zhu et al., 2011). "This provides the top and base of the source rock reflections, which have characteristically negative and positive high amplitude, respectively, and dim with an increasing reflection angle" (Loseth et al., 2012).

The TOC content data in the Carynginia Formation and Kockatea Shale in the Perth Basin were from the Rock-Eval pyrolysis. All required data for the selected wells are provided by the DMP. Based on 65 samples collected from 15 wells at depths of 870 – 4,000 m, the TOC present in the Kockatea Shale varies from 0.3 to 5 wt% (Figure 4-4 (A)). Based on 55 samples from depths of 1,180–3,659 m from 8 wells, the TOC present in the Carynginia ranges from 0.4 to approximately 4 wt% (Figure 4-4 (B)). There is a good correlation between the TOC and the AI for both the Kockatea Shale and the Carynginia Formation.

We used the TOC obtained by using the linear Equations 4-1 and 4-2 as shown below, between the measured TOC content and the AI for both formations. These correlations are applied to all wells, and used to map variations in the TOC profiles with well-calibration by converting seismic AI data to TOC content.

$$TOC\ (wt\%) = -0.0015 * AI\left(\frac{m}{s} * \frac{g}{cc}\right) + 16.086 \text{ (Kockatea Shale)} \qquad \text{Equation 4-1}$$

$$TOC\ (wt\%) = -0.0007 * AI\left(\frac{m}{s} * \frac{g}{cc}\right) + 8.762 \text{ (Carynginia Formations)} \qquad \text{Equation 4-2}$$

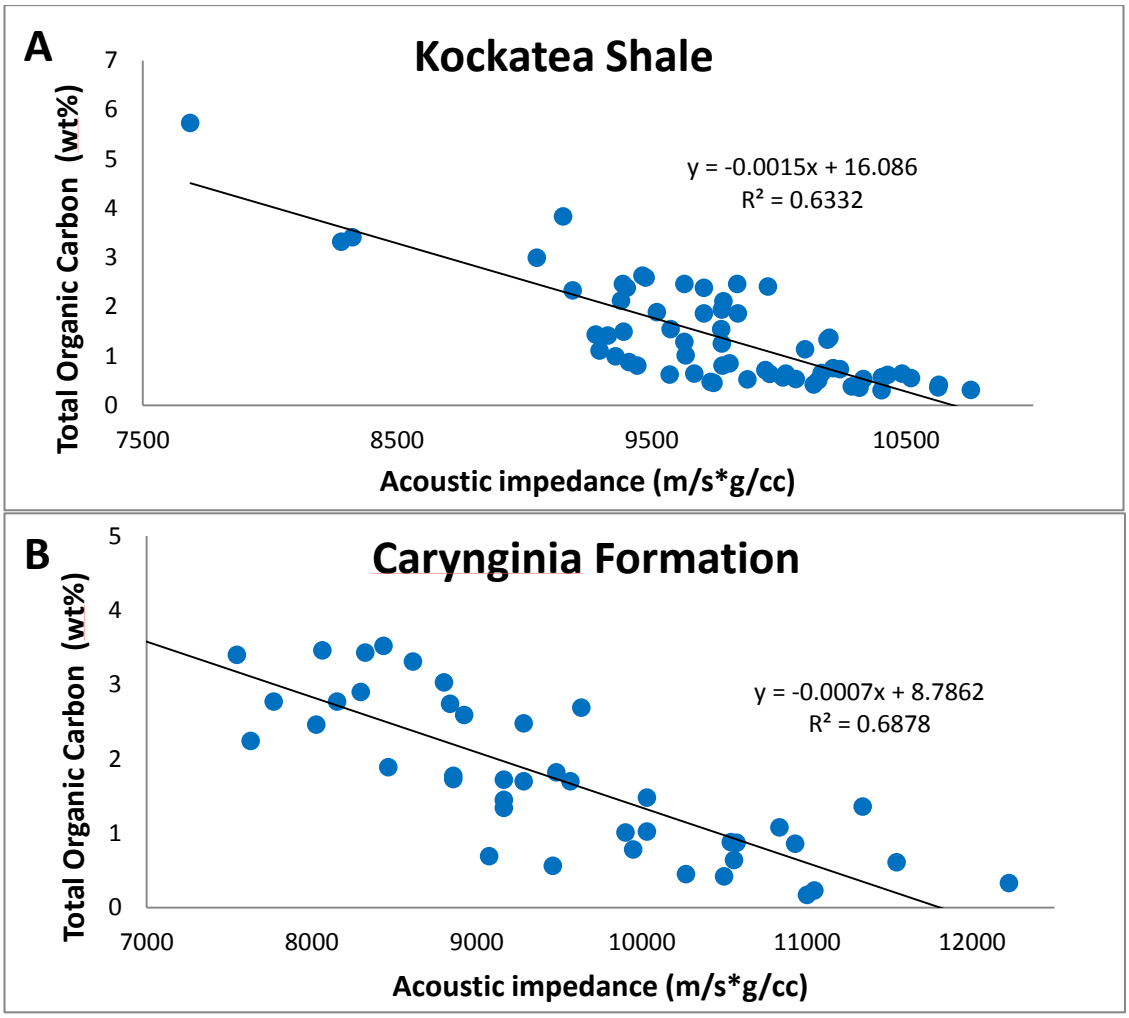

Figure 4-4: Relationship between the measured TOC content and AI in (A) Kockatea Shale and (B) Carynginia Formations.

Moreover, the Passey's methods were applied to see the difference between both methods. The TOC variations were computed of calibrating the graphical variation of porosity log curve, such as the sonic log, according to the resistivity log curve by which assigns a value to the crossover, named Dlog R method (Passey et al., 1990). The r Dlog R is calibrated against TOC with respect to LOM (Level of Maturity, estimated from R_o.

Equations (4-3 to 4-5) are used to estimate TOC content for only one well to compare between the TOC obtained from the AI and the TOC obtained from Passey's method. Figure 4-5 compares the measured TOC content with the AI and Passey's methods from Kockatea shale of Redback-2 well. The TOC obtained from the AI is found to be very close to the measured TOC contents.

$$\Delta\text{LogR} = Log_{10}\left(\frac{R}{R_{baseline}}\right) + (\text{P} * (\Delta\text{t} - \Delta t_{baseline})) \qquad \text{Equation 4-3}$$

$$LOM = 5.9462R_O^2 + 16.653R_o + 0.3281 \quad \text{Equation 4-4}$$

$$TOC\ (wt\%) = \Delta LogR * 10^{(2.297-0.1688*LOM)} \quad \text{Equation 4-5}$$

Where, P is Resistivity logarithmic cycle over transit time cycle. R_o is Vitrinite reflectance measurement.

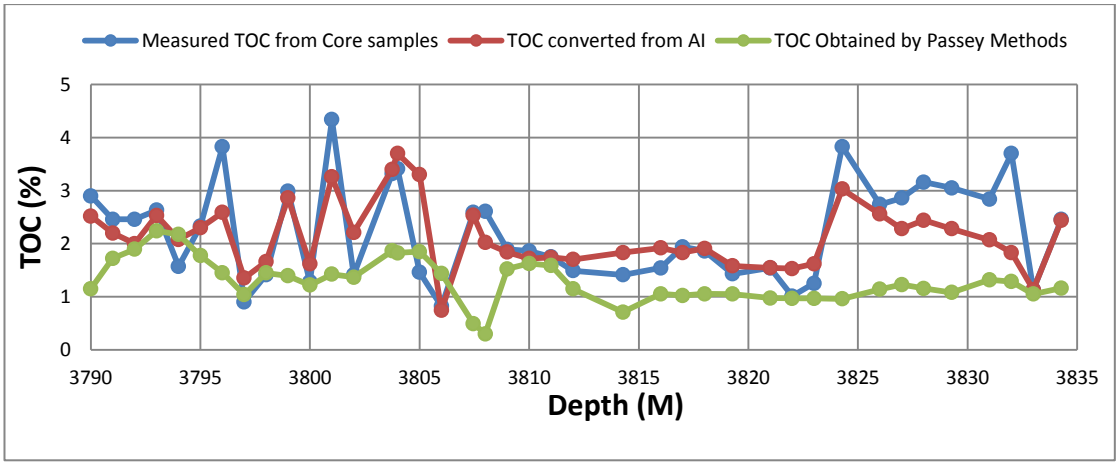

Figure 4-5: A comparison between TOC derived from the AI and Passey's methods with measured TOC.

4.3 Results and analysis

4.3.1 Poststack seismic inversion

Poststack (model-based) inversion, which is used to generate AI volume, involves a series of steps to be followed after the wells and 3D seismic data are loaded and the horizon is imported. The first step is to extract the wavelet. There are two methods that can be used to achieve this. One process uses the well data and can provide a good evaluation of both the amplitude and phase spectra of the wavelet. The second process involves the use of a statistical wavelet, which uses seismic data to extract the actual wavelet. Both processes were used to produce the best correlation between the log and seismic data. The next step is to tie each well to the seismic data that will be used to build the inversion model. Thirty wells are used in this study to control the model. The aim of the process is to correlate the wells to the seismic data, allowing a

seismic interpretation of the horizons of interest. The availability of the check-shot data in some wells is sufficient for the time/ depth relationships to be established. The main point is to compare the real seismic data to the synthetic traces, the same event in both traces should be matched (Figure 4-6). The blue traces, associated with the synthetic traces that are generated from the density and velocity well-logs, are zero-phase wavelets and the red traces characterise the average of the traces around the well. The main events on the blue and red traces are matched and correlated many times to obtain the best correlation coefficient. The correlation ranges from 0.55 to 0.75 for all the wells that are used to control the inversion model. The next step is to generate the initial model (low frequency) using the control wells and the selected horizons.

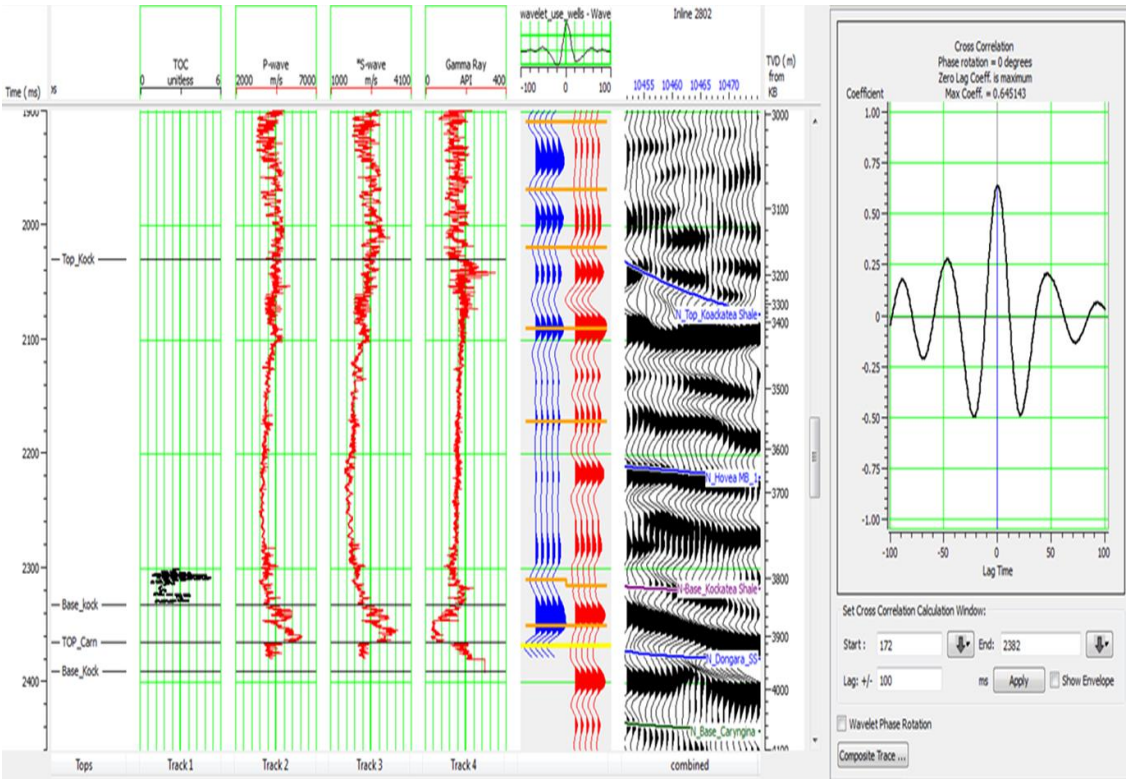

Figure 4-6: RedBack-2 well tied to seismic data and the correlation between the synthetic trace and real seismic, which is 0.65 for the well.

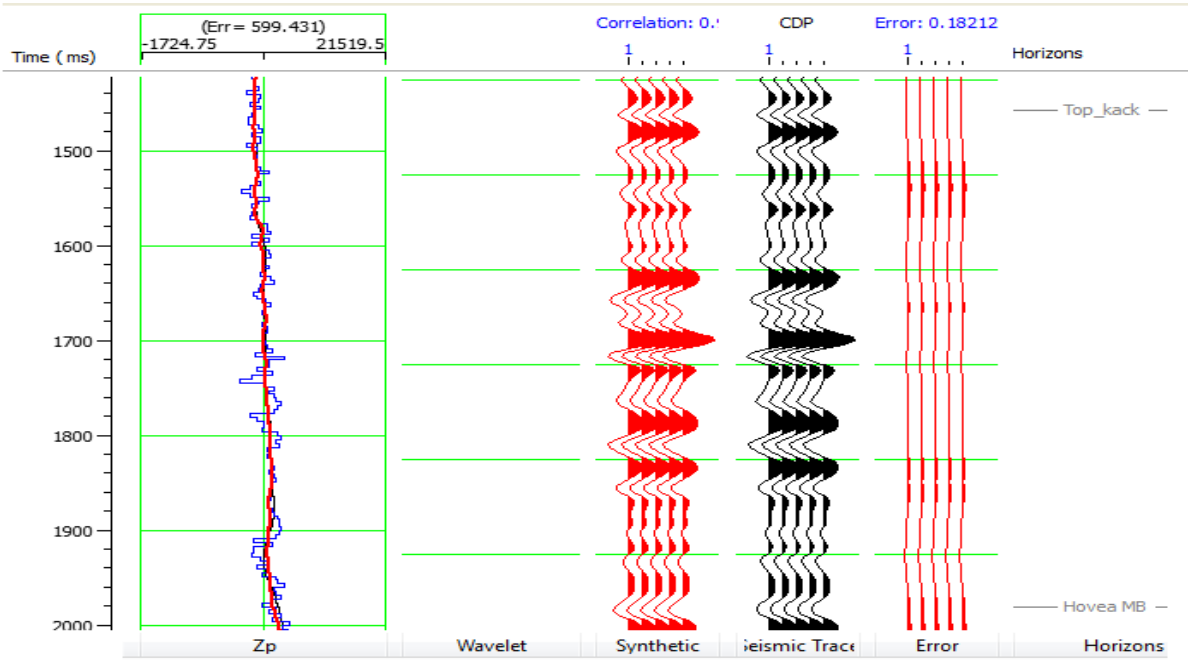

Figure 4-7: Example of the P-impedance inversion analysis of one well for the Kockatea Shale. The inverted synthetic correlation is 0.89. The blue curve is P-impedance, the red curve is the synthetic seismogram and the black curve is the seismic trace.

The next step is to perform the inversion analysis, which depends to some extent on the control wells (and in particular their location), to optimise the inversion parameters. Figure 4-7 shows the result of the inversion analysis at different well locations, with the correlation error map and a profile plot. It can be seen that the inverted trace agrees with the actual log and the correlation between the synthetic and seismic trace is acceptable. The inversion analysis applies AI inversion for the Kockatea Shale using 30 wells, resulting in the inverted synthetic correlation of 0.89. The second inversion analysis applies S-impedance (SI) inversion, (as assumption from the relationship between the P-wave and S-wave), for the same formation, which results in an inverted synthetic correlation of approximately 0.8 based on the 30 wells; the AI and SI inversion results for the seismic section are shown in Figure 4-8 (A) and (B). In this slice (Figure 4-9 (A) and (B)), it can be seen from the resultant seismic data that the area of the base of the Hovea Member is composed of lower AI materials.

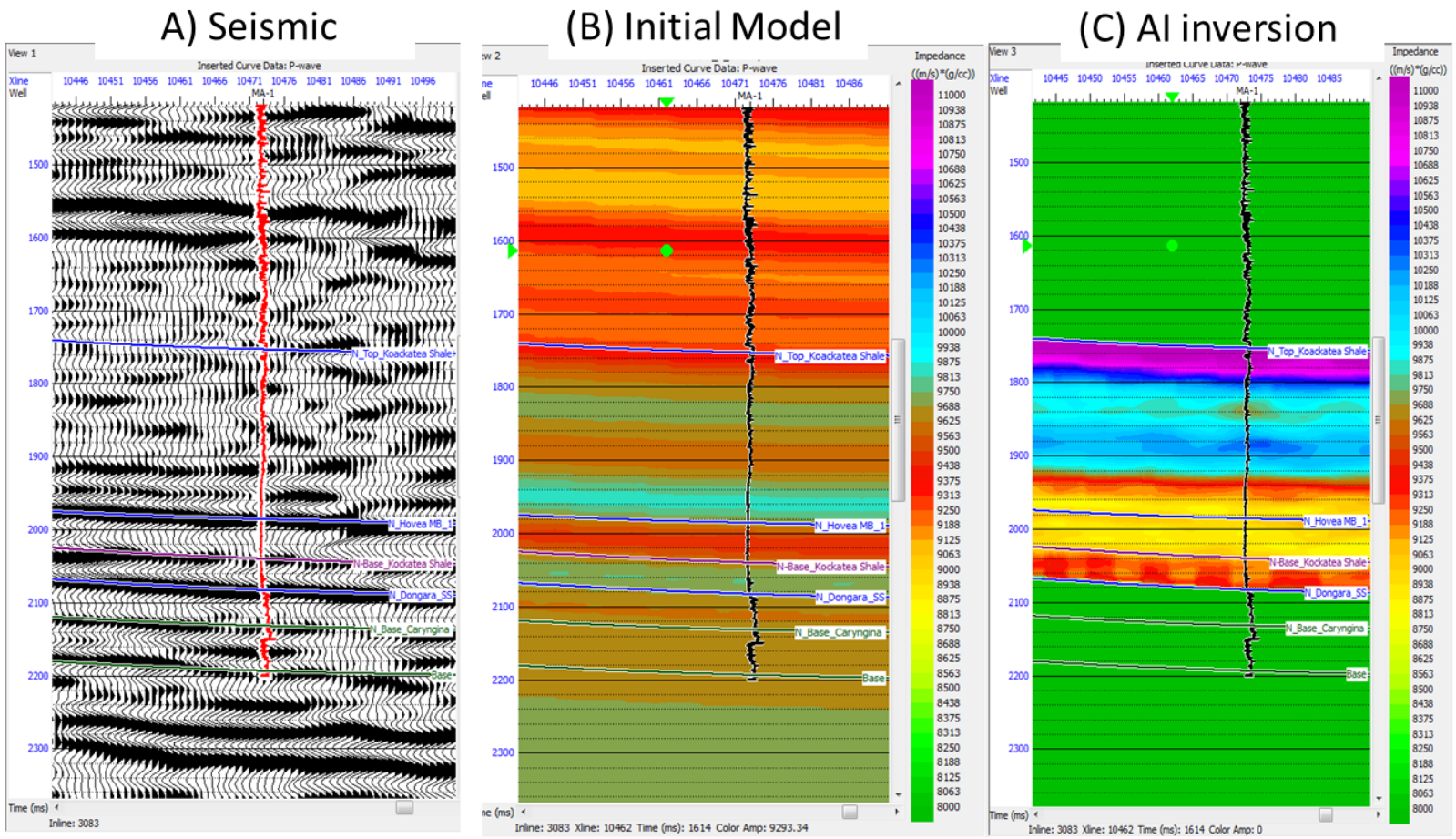

Figure 4-8: The AI (A) and SI (B) inversion results for a seismic section, showing low values of both impedances in the Hovea Member.

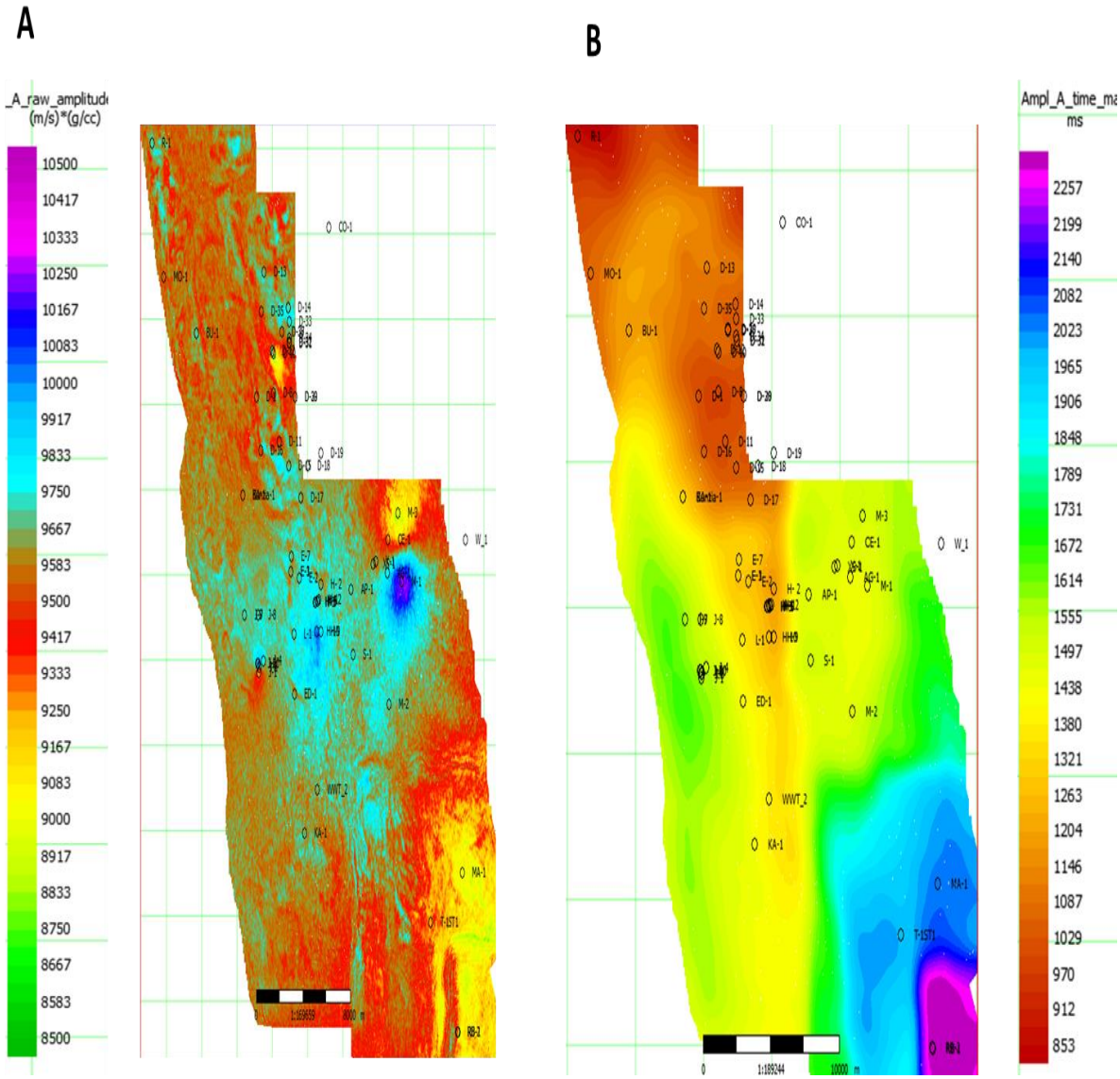

Figure 4-9:(A) An interval maps of seismic data show the area of the base of Hovea Member composed of lower AI materials compared with (B) the structure map (time interval) for Hovea Member over all the seismic data.

4.3.2 AVO modelling and analysis of an organic shale formation

I have applied two AVO models from Redback-2 well at different parameters. The first model contains an organic shale rock with 5 wt% TOC. The organic content layer is removed in the second log model, now making it a non-source shale rock (TOC is about 0 wt%). In the organic shale example, the P-wave, S-wave and density

are presented with lower values than in the inorganic shale. Poisson's ratio in the organic shale is also lower (0.25–0.27) than in the inorganic shale, which is around 0.33 – 0.36 (Figure 4-10). The AVO analysis shows that the amplitude is increasing with an increased offset for the organic shale, which generates a Class 1 AVO anomaly. On the other hand, there is less amplitude with the non-source shale rock compared to the organic shale.

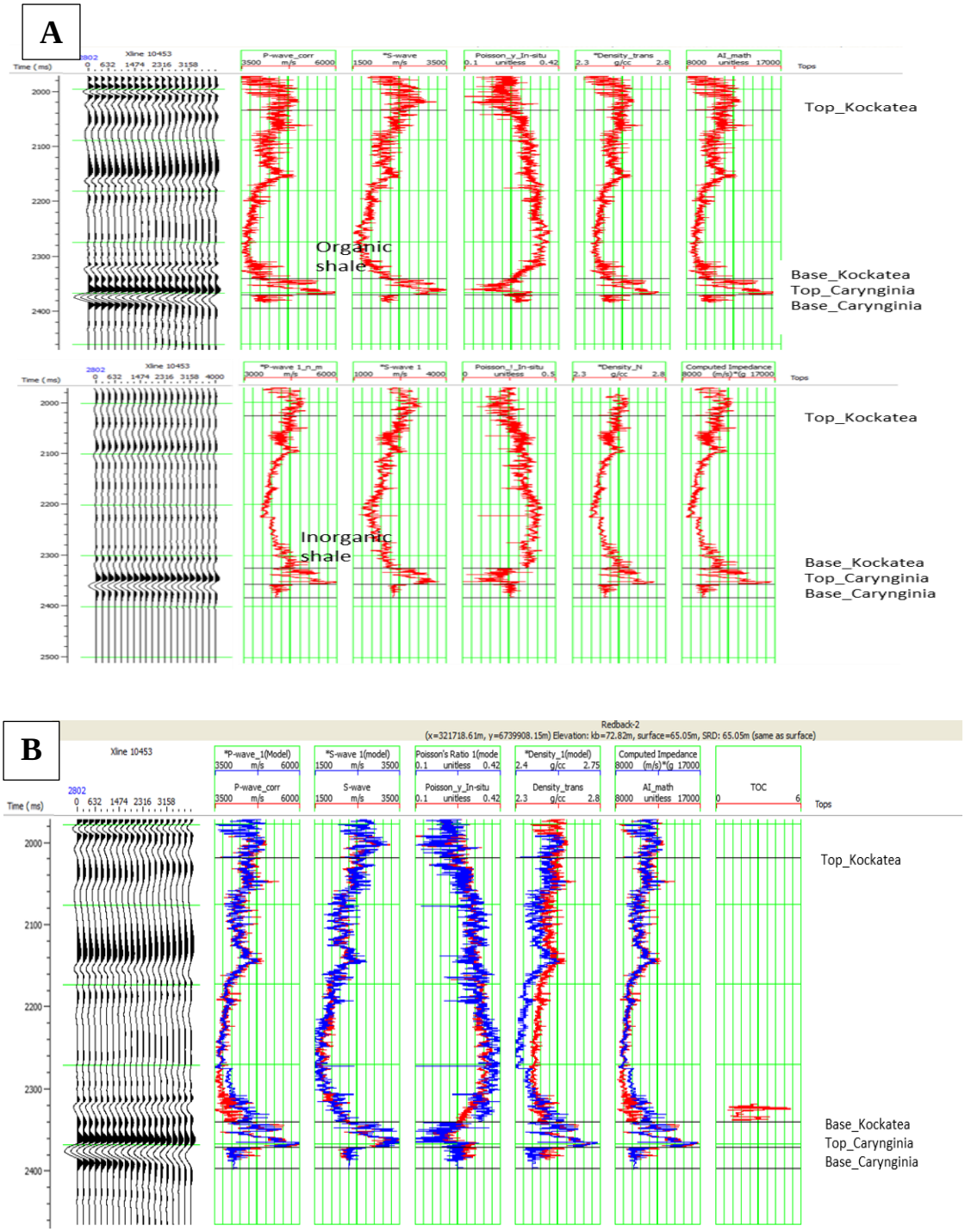

Figure 4-10: (A) AVO modelling and response of two log models, the first log model contains an organic shale rock while the second log model contains a non-source shale rock. The AVO analysis shows that the amplitude is increasing with an increased offset for organic shales. (B) A log view for with both logs superimposed on each other.

Synthetic CDP gathers are modelled for the organic shale using the elastic wave algorithm to predict the AVO behaviour. The AVO gradient analysis is performed to analyse the AVO behaviour of the organic shale layer at 2,300 ms. Figure 4-11 shows the Class 1 AVO anomaly with amplitudes increasing for the base of the top

of the organic shale layer, as well as the peak at the base of the organic shale layer. As the organic content increases, the AI decreases and this is shown in the organic shale example. This increases the magnitude of the AVO intercept. Zhu et al. (2011) noted that there is no difference on physical properties between the source shale and the insource shale rock, if the TOC is low in the source rock. In general, our study shows that the organic shale and clay minerals have an impact on P-waves, S-waves and density, which suggests that the TOC affects the analysis of the geophysical data.

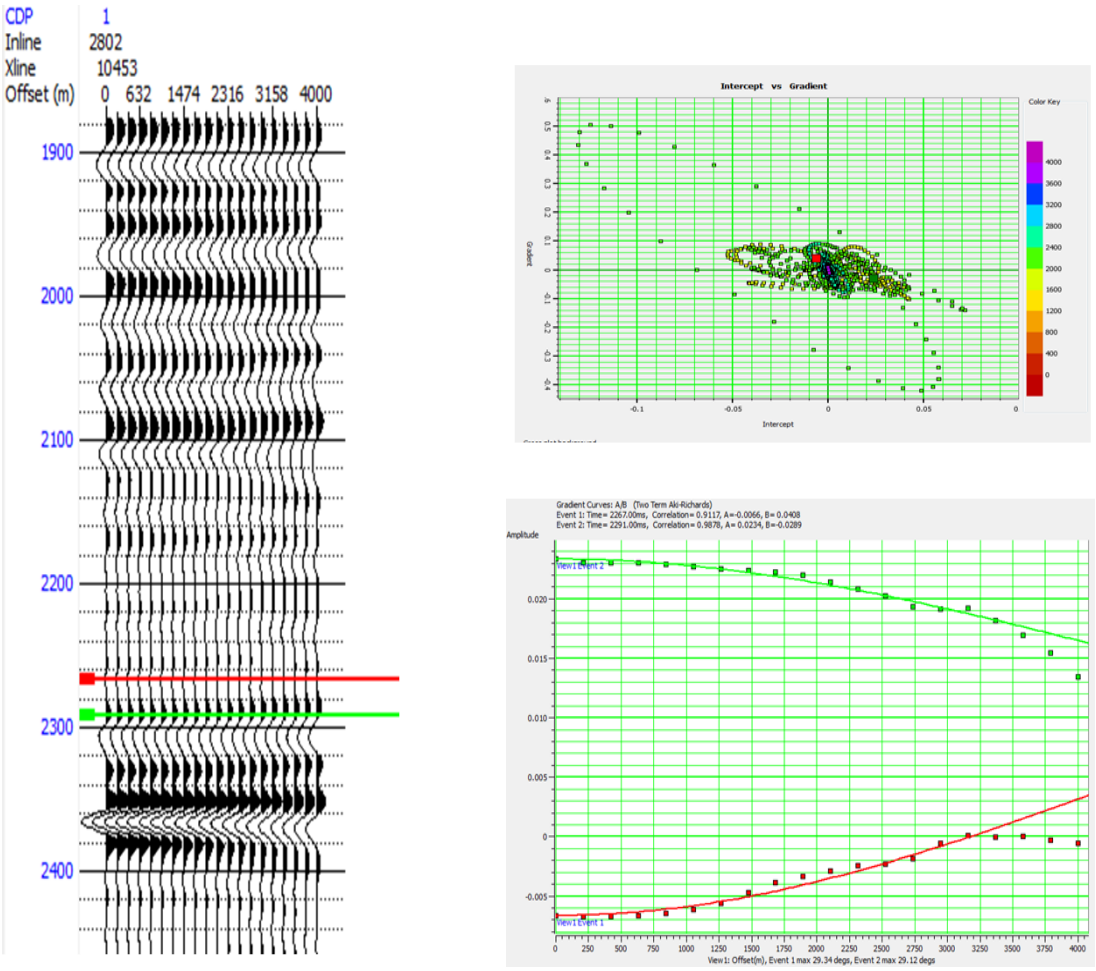

Figure 4-11: A Class 1 AVO anomaly with amplitudes increasing for both the trough at the base top of the organic shale layer and the peak at the base of the organic shale layer.

4.3.3 Elastic Impedance inversion for near and far offsets

EI was used in this project to extend the study of the AVO response. This inversion process was used to generate an EI volume for both near- and far-offsets using the same method of AI workflow. We have used the angle of 5^{o} for near offset and 30^{o} for far offset. From the 30^{o} and 5^{o} elastic impedance logs, EI 30^{o} is a broadly similar transformation to the EI 5^{o} log but with lower absolute values; it is a property of the EI that the level decreases with an increasing angle. EI inversion involves a series of steps to be followed, similar to the AI inversion, using the poststack inversion algorithms. The only difference in the elastic inversion setup when building the initial models is the EI equation configuration, which applies an incidence angle of 5^{o} for the near offset and 30^{o} for the far offset, based on the use of 30 control wells. The correlation ranges from 0.55 - 0.75 for all the wells that are used to control the inversion model. The inversion analysis applies that for the EI 30^{o} inversion to the Kockatea Shale data using 30 wells, the inverted synthetic correlation was 0.91. The second inversion analysis that applies the EI 5^{o} inversion to the same formation resulted in an inverted synthetic correlation of approximately 0.89 based on 30 wells. In Figure 4-12, the comparison can be seen between the near and far elastic impedance inversion. The overall EI 30^{o} inversion shows higher amplitude at 30^{o} than at 5^{o}, but the EI 5^{o} inversion shows a higher absolute value than the EI 30^{o} inversion. Both impedances show that the area of the Hovea Member is composed of lower EI materials when compared with the top of the Kockatea Shale.

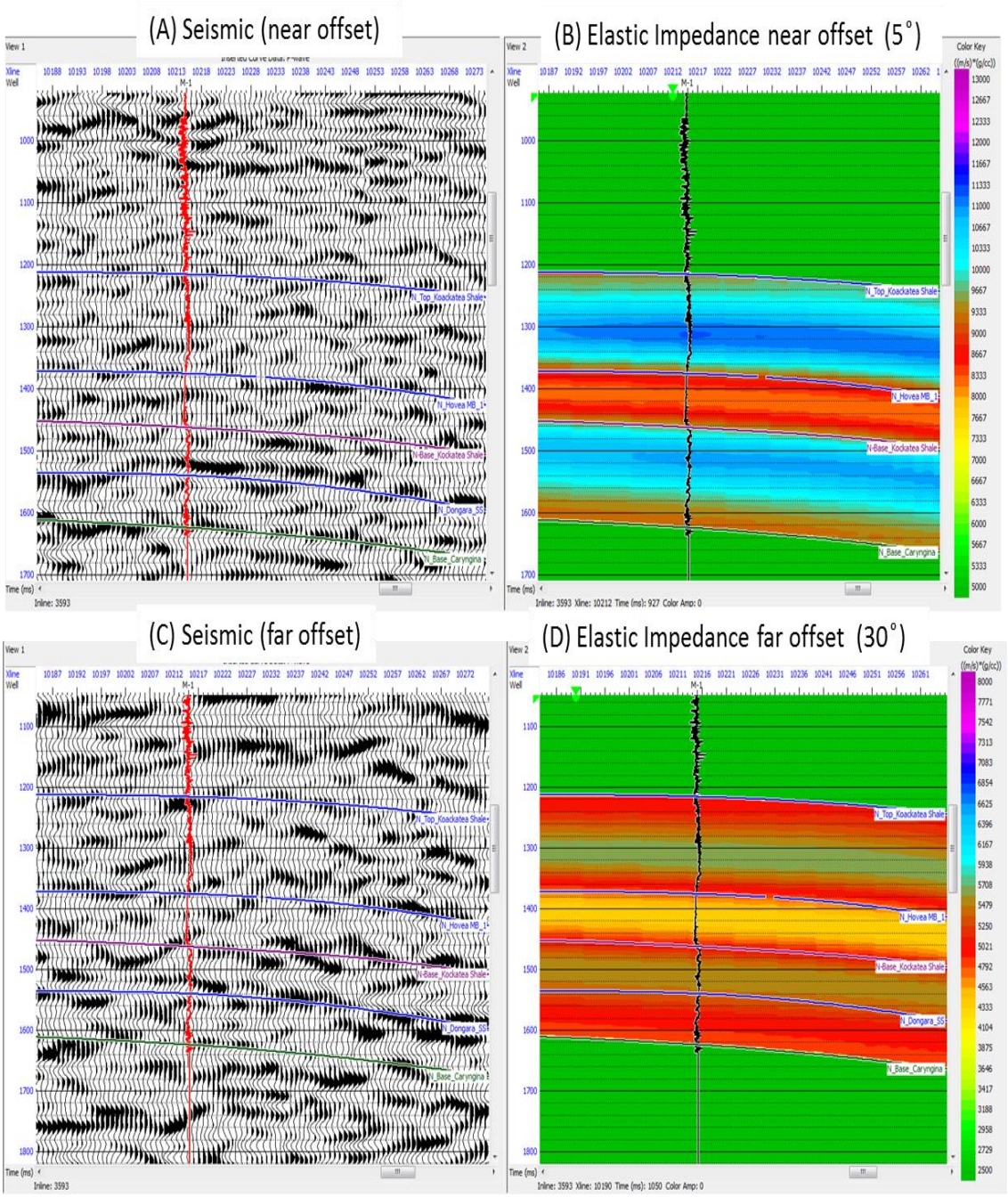

Figure 4-12: A comparison between the near and far offset of the EI inversion. The El **30°** inversion shows higher amplitude than the EI **5°** inversion, but the EI **5°** inversion shows a higher absolute number. Both EI inversions are composed by lower values in Hovea Member.

4.3.4 TOC estimation using multi-attribute analysis

The final step is to predict the TOC percentage from the seismic AI using the rock physics linear relationship equation between TOC and AI for the Kockatea Shale and the Carynginia Formation. The first stage in the seismic multi-attribute analysis is to select applicable seismic attributes that will be used by employing a stepwise regression approach in the analysis process (Hampson et al., 2001). There are two types of seismic attributes: (1) sample based, which is calculated from the trace on a sample-by-sample basis, such as the amplitude envelope, and (2) a horizon-based attribute, which is calculated as averages within a window of a seismic section. The Emerge software is used in this project to apply the seismic attributes using sample-based attribute types. The application of multi-attribute analysis is useful for predicting the target log by choosing the combinations of attributes. This program uses a process called step-wise regression. "The first step is to find the single best attribute by trial and error and then to calculate the prediction error. The attribute with the lowest prediction error is the best attribute. The second step is to find the best attribute pair, which is also the one with the lowest prediction error. The final step is to find the best triplet of attributes" (Hampson et al., 2001).

Multi-attribute analysis using a convolutional operator was applied to estimate the TOC percentage. Using the convolutional operator is likely to add more attributes; however, it will also improve the prediction error (Hampson et al., 2001). The nominated attributes are used to produce a linear equation that can be applied to estimate a target prediction. A summary of the different types of inversions with respect to the TOC prediction for the Kockatea Shale using seismic attributes analysis is shown in Table 4-1. The application of different approaches using the seismic inversion and multi-attribute analyses helps us pick the best inversion method to predict the TOC. Multi-attribute analysis applied to each inversion shows similar seismic attributes but with a different correlation coefficient and error.

Table 4-1: Seismic multi-attribute analysis table that is applied to the Kockatea Shale.

Type of the inversion	**Seismic attribute**	
(Model Based) P- Impedance	Quadrature Trace, Average Frequency, Instantaneous phase, Filter 15/20-25/30, AI*2, 1/AI, Dominant Frequency, Derivative Instantaneous Amplitude	0.87 by using 8 attributes Error = 0.9%
Elastic Impedance (near offset)	Dominant Frequency, Derivative Instantaneous Amplitude, Apparent Polarity, Instantaneous phase, Instantaneous Frequency, EI*2, 1/EI, Integrate.	0.82 by using 8 attributes Error = 1.14%
Elastic Impedance (far offset)	Apparent Polarity, Integrate, Instantaneous Phase, Second Derivative, 1/EI, Integrated Absolute Amplitude, Average Frequency, Instantaneous Frequency, Derivative Instantaneous Amplitude.	0.84 by using 8 attributes Error = 1.3%

For example, multi-attribute analysis is applied to predict the TOC from a model-based inversion and uses the AI as external attribute as this study is based on the relationship between the TOC and the AI. A total of eight seismic attributes were applied for the Kockatea Shale using the convolution operator. The correlation is approximately 0.87 with a five point convolutional operator. This produces an error lower than 0.99 for the training; the validation error is also lower than 1.06. The validation error is the absolute prediction error in units of the TOC, which is wt%. One way of measuring the correlation between the target and an attribute is to crossplot the two parameters. Figure 4-13 shows the predicted and actual TOC from 10 wells using eight attributes with a correlation of 0.87 and an error of 0.99.

All the information in the table is shown graphically in Figure 4-14 (A) in which the validation results are also shown. The lower black curve is the estimation error when all the wells are used in the analysis and the upper red curve shows the average validation error. Figure 4-14 (B) shows the plot of the average error between the predicated TOC and the number of the attributes used as the number of attribute increase, the error decreases.

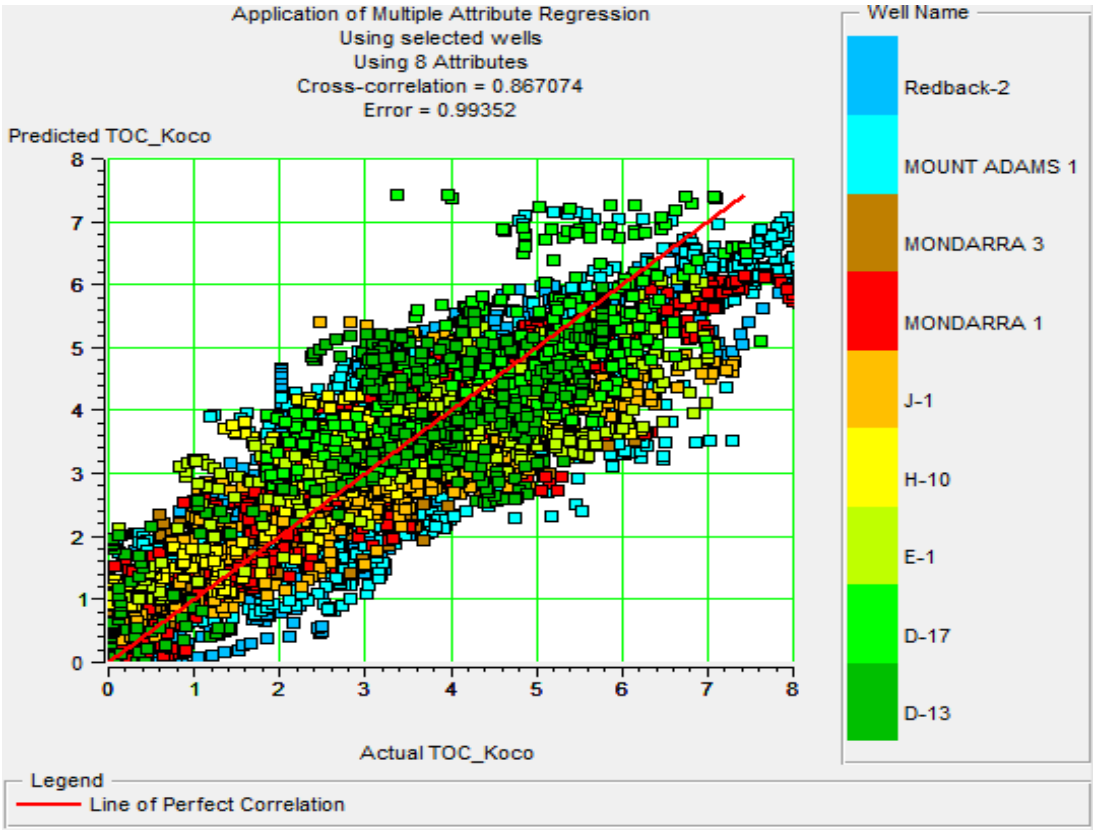

Figure 4-13: Crossplot of predicted TOC and actual TOC using eight attributes of the Kockatea Shale based on 10 wells with a correlation of 0.87 and an error of 0.99.

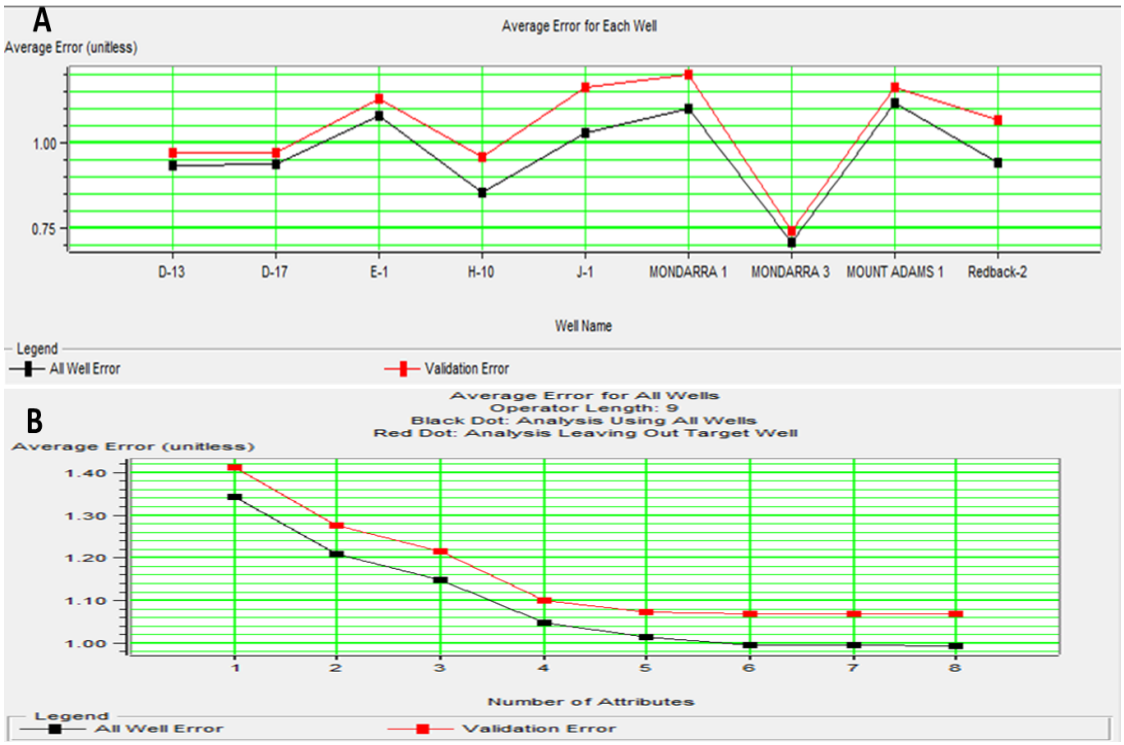

Figure 4-14: (A) Average error for each well of the Kockatea Shale. (B) The plot of the average error between the predicated TOC and the number of the attributes used; as the number of the attributes increases, the error decrease.

The results show that the poststack seismic inversion with multi-attribute analysis is effective in defining the TOC percentage in the Kockatea Shale. Figure 4-15 shows the conversion section of the TOC and the section of the seismic AI inversion. The TOC profile, following the application of multiple attributes across the wells in the Perth Basin, shows different TOC values, which are represented by different colours. For example, the gold colour shows the TOC percentage of the Hovea Member as 3.25 wt% and is associated with a low AI of 8,700 ((m/s)* (g/cc)). The measured TOC of the core samples from the RedBack-2 well is displayed in the TOC profile and compared with our results. The comparison shows that the values of the TOC in the core sample are close to 3.4 wt% at the base of Kockatea Shale. This is close to the predicted TOC values from the seismic data with approximately 3.25 wt% after converting the AI values to TOC values and applying them to the seismic data.

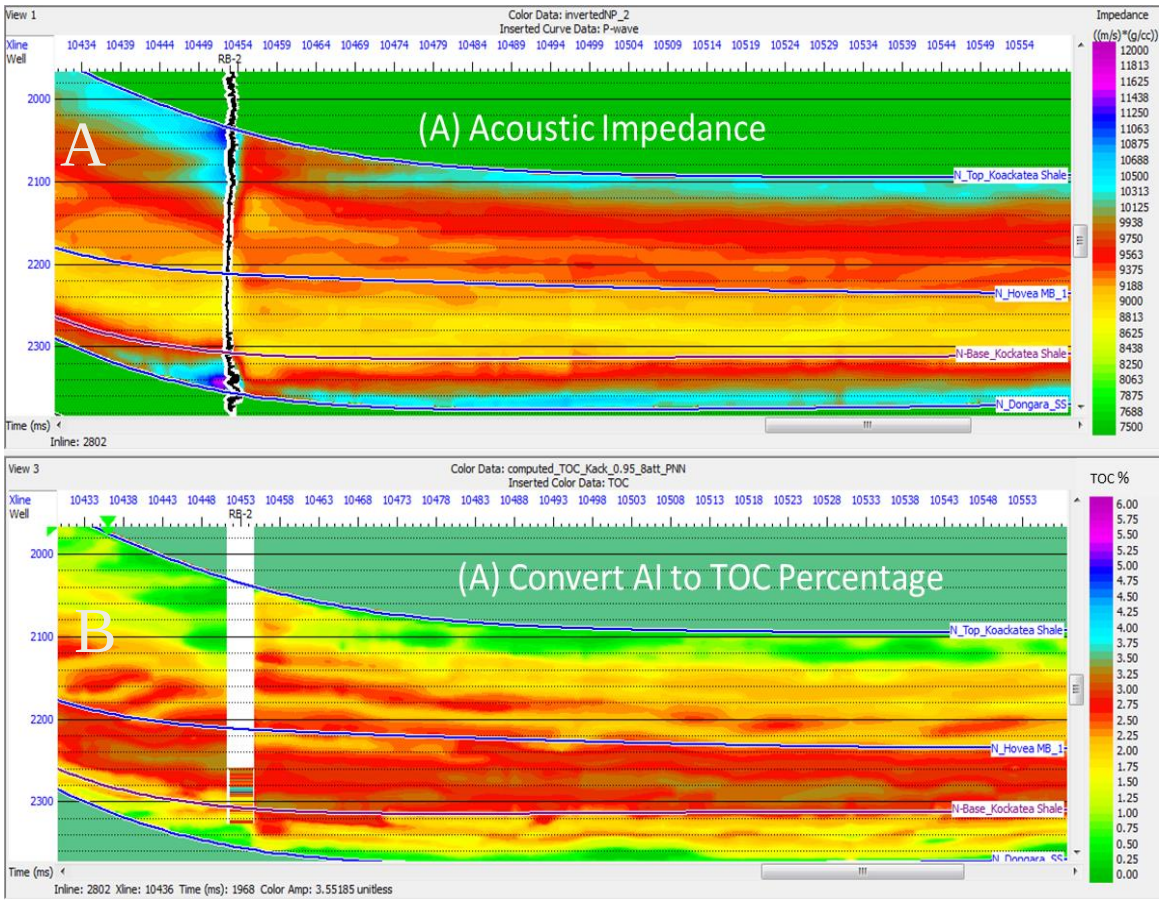

Figure 4-15: (A) AI inversion in the Kockatea Shale. (B) The TOC percentage after converting the AI values to the TOC percentage, the actual TOC from well is applied with the same colour bar of the predicted TOC, for comparison.

Table 4-2: Comparison between the actual TOC and the predicted TOC of different wells.

Well name	Actual TOC	Prediction TOC from inversion	Estimation Error %
Redback-2	**2.24 wt%**	**2.06 wt%**	**2.9%**
MA-1	**0.87 wt%**	**1.11 wt%**	**5.4%**
Mondarra-1	**1.16 wt%**	**2.11% wt%**	**19%**
Jingemia-1	**1.12 wt%**	**1.41 wt%**	**8.5%**

4.3.5 Estimation of shale brittleness by using LMR approach

The crossplots of LR versus MR are most beneficial when defining the fundamental properties of gas shale. Goodway et al. (2010) and Perez et al. (2011) developed LMR interpretation templates for the gas shale (assumed the shale is isotopic) using

rock physics trends. The comparison values of the LR and MR logs calculated from measured compressional and shear sonic logs, together with the density log, show a correlation between these geophysical parameters and more traditional petrophysical properties. The crossplot of LR versus MR of the RedBack-2 well-log in Figure 4- 16 shows all the data from the Kockatea Shale with changing rock composition. Clay-rich rocks are displayed with high LR and lower MR values, while quartz-rich rocks are displayed with high LR and even higher MR values. Qualitatively, the changes in rock composition are related to the brittleness of the rock, with quartz-rich rocks described as brittle and better for hydraulic fracturing and clay-rich rocks described as ductile and less able to fracture. The definition of a sweet spot in the reservoir zone is characterised by low LR and higher MR values.

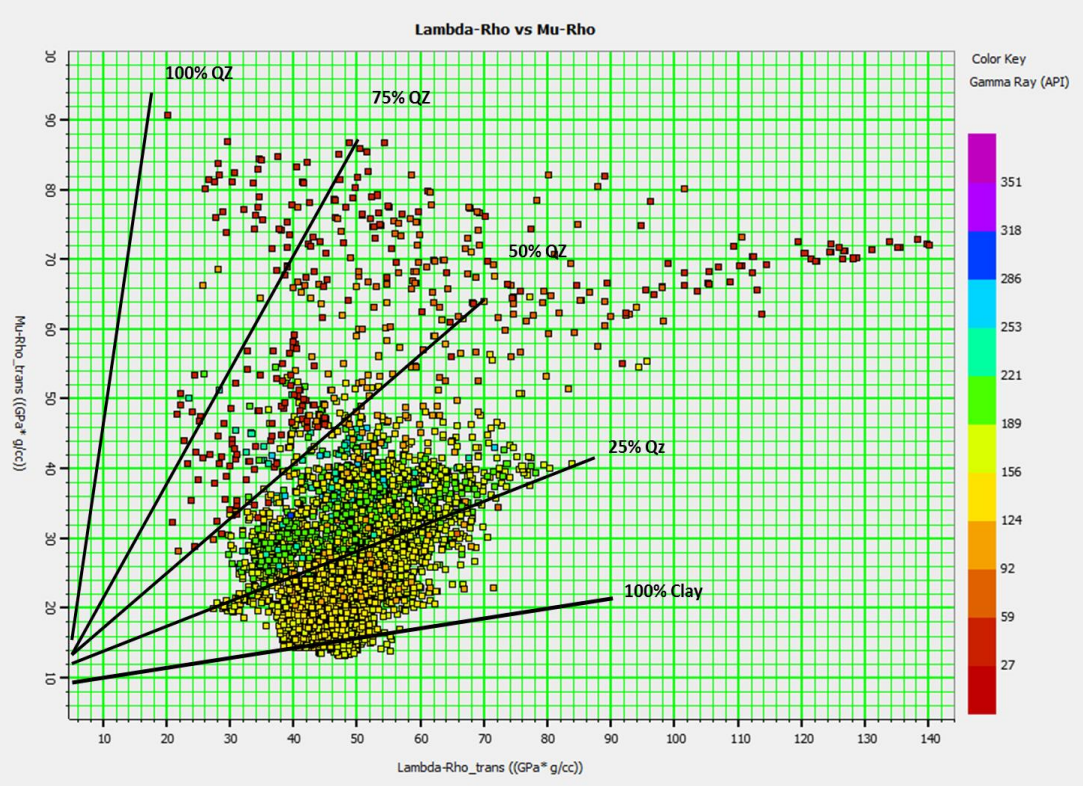

Figure 4-16: All data from the Redback-2 for the Kockatea Shale with changes in rock composition; clay-rich rocks are displayed with high LR and lower MR values, while the quartz-rich rocks are displayed with high LR and higher MR values.

The relationship between the elastic properties, such as Young's modulus and Poisson's ratio, as well as the reservoir quality properties, such as TOC, is important in identifying the brittleness of the rock (Alzate and Davedowda, 2013). Figures 4-17

(A) and (B) and Figure 4-18 show the crossplot from Redbac-2 well of LR versus MR having similar values but are displayed for each plot by Poisson's ratio, Young's modulus and TOC%. The higher values of Poisson's ratio are associated with high LR and lower MR in more ductile rocks. The lower values of Young's modulus are associated with high LR and lower MR indicates more ductile rocks. Figure 4-18 shows the crossplot of LR versus MR, which is obtained by combining Figure 4-17 (A) and (B). Group 1 highlights the brittle shale with a rich TOC percentage found in areas of the Kockatea Shale that have low Poisson's ratio values, low Young's modulus values and high TOC percentage. Group 2 highlights the ductile shale with a high TOC percentage, which is the area of the shale play represented by high values of Poisson's ratio, low Young's modulus values and high TOC percentages. Group 3 highlights the brittle shale with a poor TOC percentage and include the areas of the shale play represented by low values of Poisson's ratio, high values of Young's modulus and a high TOC percentage. Group 4 highlights the ductile shale with a poor TOC percentage and are the portions of the shale play represented by high values of Poisson's ratio, high values of Young's modulus and a low TOC percentage. To extend this analysis to 3D seismic data and to locate the brittle shale of the Kockatea Shale, the cross-plot of LR versus MR from the seismic data has been applied. This is shown in Figure 4-19. The brittle shale is located at the base of Kockatea Shale (the base of Hovea Member) and the ductile shale is located on the top of the Hovea Member.

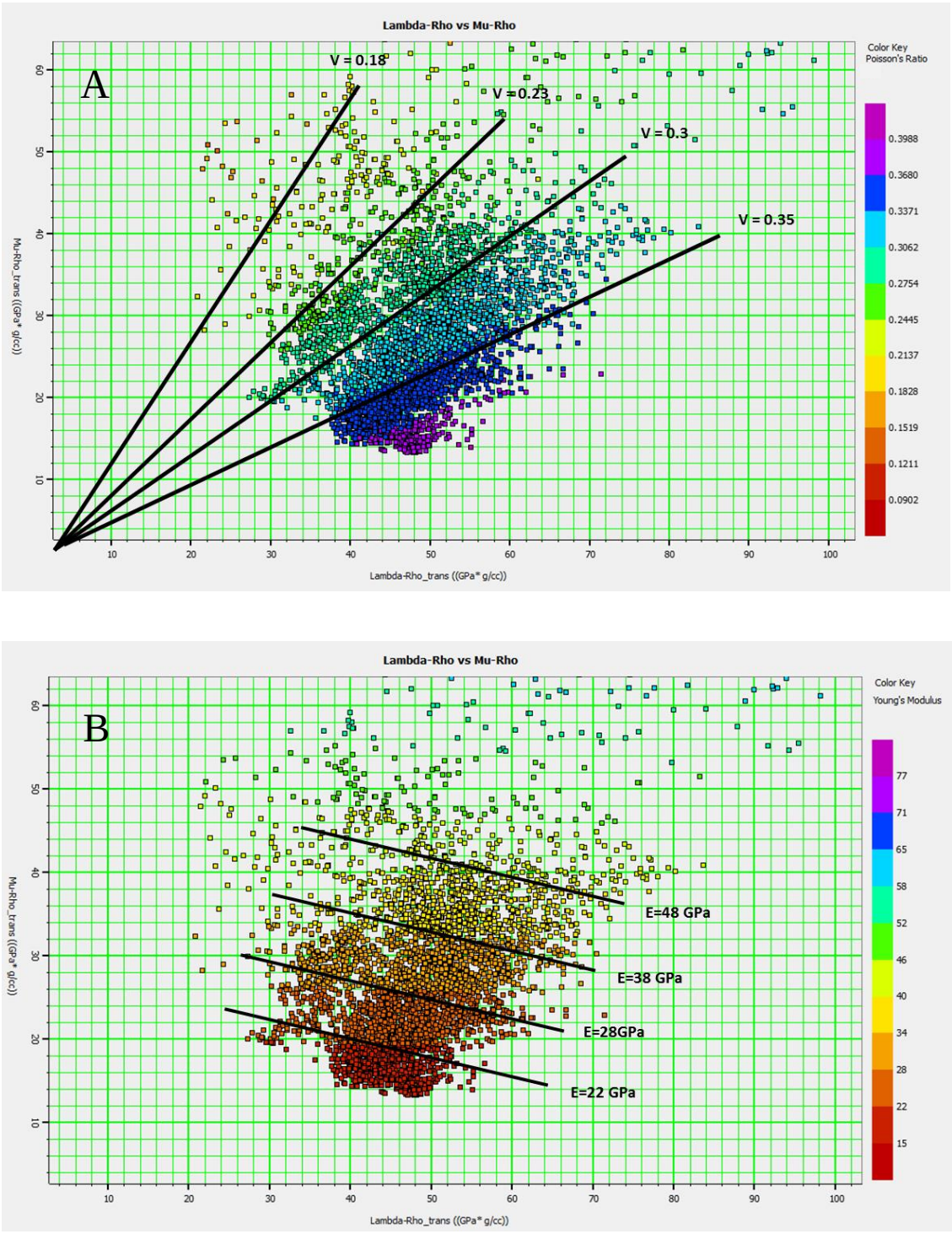

Figure 4-17: (A) and (B) show the crossplots of LR versus MR having similar values and are displayed for each plot by Poisson's ratio and Young's modulus

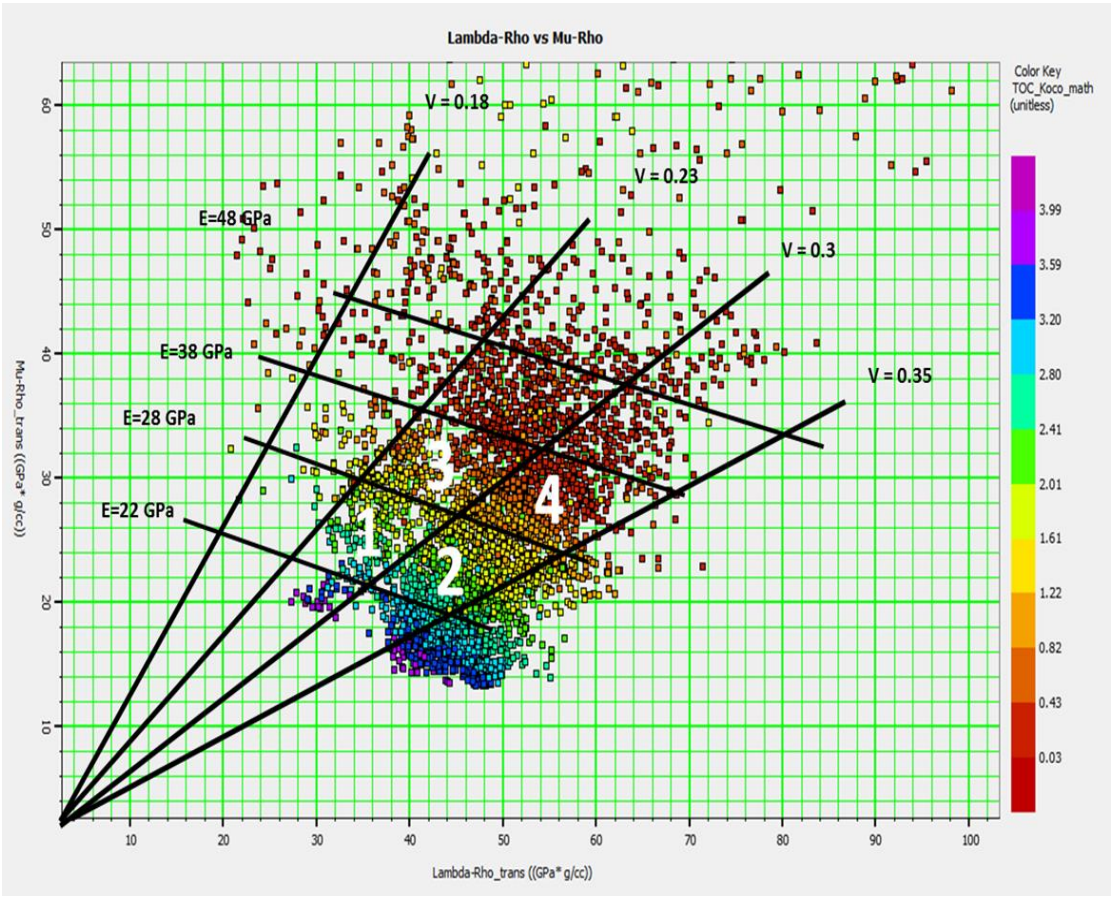

Figure 4-18: Crossplot of LR versus MR obtained by combining Figure 19 A and B. Group 1 is shown to be brittle shale with a rich TOC percentage while Group 2 is shown to be ductile shale with a rich TOC percentage.

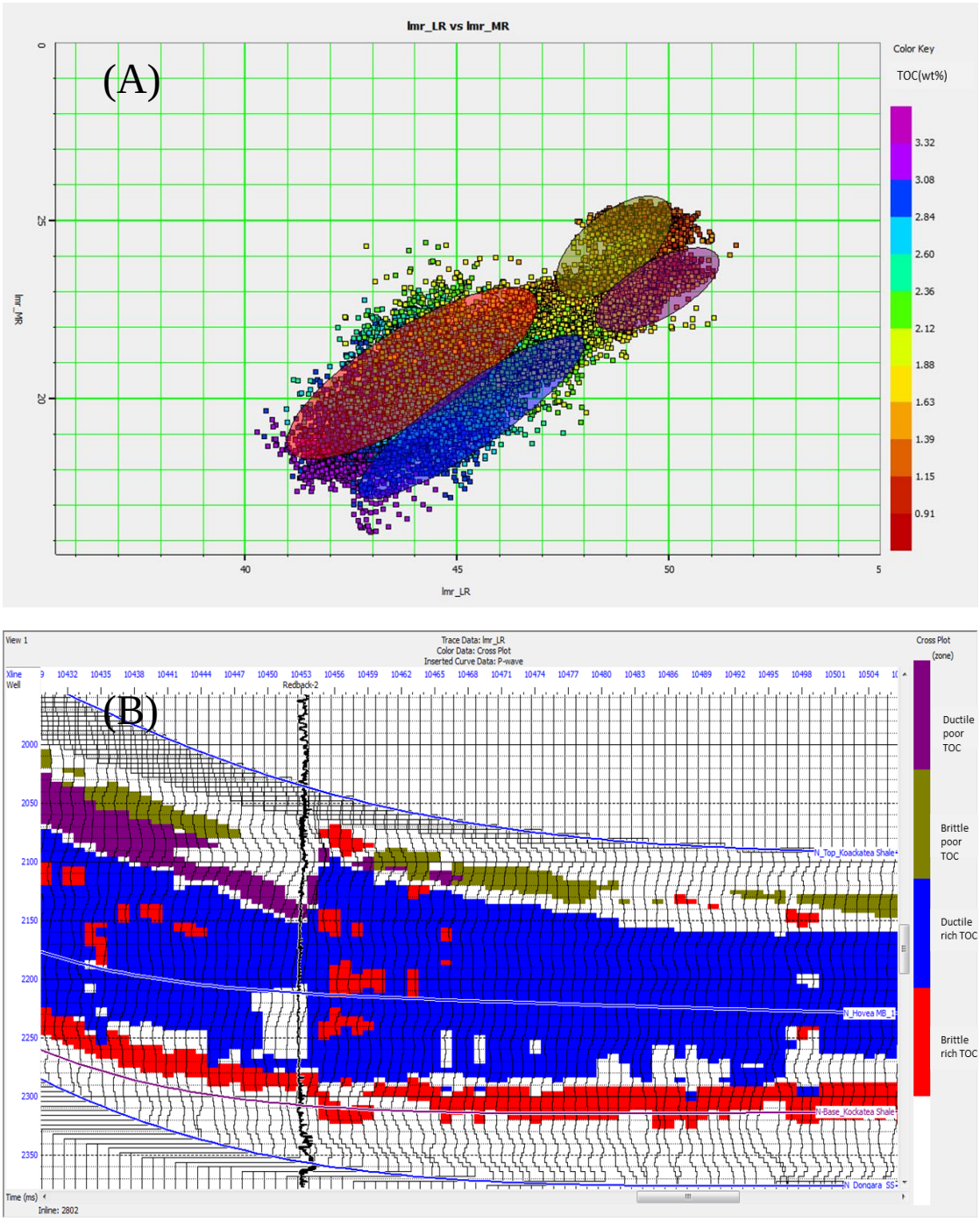

Figure 4-19: Crossplot of LR versus MR (A) applied to the seismic data, (B) displaying the TOC percentage. It shows the brittle shale, which is located at the base of the Kockatea Shale (the base of the Hovea Member) and the ductile shale, which is located at the top of the Hovea Member.

4.4 Discussion

This study covers the interesting potential gas shale formations of north Perth, which are associated with different 3D seismic surveys in the area. Figure 4-20 and Figure 4-21 show the depth of the top and base of the Kockatea Shale. Also, Figure 4-22 shows the isopach map of the Kockatea Shale. There are five areas of interest that have the potential gas shale as future gas fields as shown in Table 4-3, with the most important being the Beharra Springs, which is located in the southern part of the seismic survey. The depth of the Beharra Springs for the Kockatea Shale is between 3200 to 3800 m and the thickness is around 600 m. The TOC content is between 1.30 - 6.11 wt% and the average porosity is around 2.4%. The base of the Kockatea Shale is richer in TOC and is more brittle. The Dongara Gas Field is located in the north of the surveyed area. The depth of the Kockatea Shale is between 1040 to 1250 m and the thickness is around 200 m. The TOC content is between 0.14 - 4.04 wt%. The average porosity is about 18%, which is estimated by using the density log. Note that the variation in porosity of kockatea shale in Beharra Spring field and Dongarra gas filed due to many factors such as the variation of clay minerals, depth, and density.

Table 4-4 shows the gas shale potential of different areas in the Carynginia Formation. The most important area is the Woodada Gas Field, which is located in the south east of the Perth Basin. The depth of the Carynginia Formation in this field starts from 2720 to 2911m, and the thickness is around 169 m. The average TOC content is about 1.45 wt%, and the average porosity is about 5.7%, which is measured by the DMP from different core samples. The Dongara Gas Field is also an important area for gas shale potential, the depth of this formation is between 1609 – 1646 m and the thickness is around 37 m. The TOC content is between 2.13 - 11.0 wt%. The average porosity is about 14%, which is estimated by using the density log and 6.20 % measured from the core samples.

In general, the results show that in different 3D seismic survey studies of the Perth Basin, the poststack seismic inversion (AI and SI) with multi-attribute analysis is effective in defining the TOC volume in both formations. The results of poststack seismic inversion, after all the methods have been completed, show that when we have a low AI anomaly in the Kockatea and Carynginia Formations, this is the response of high TOC with values of between 2 – 4 wt%.

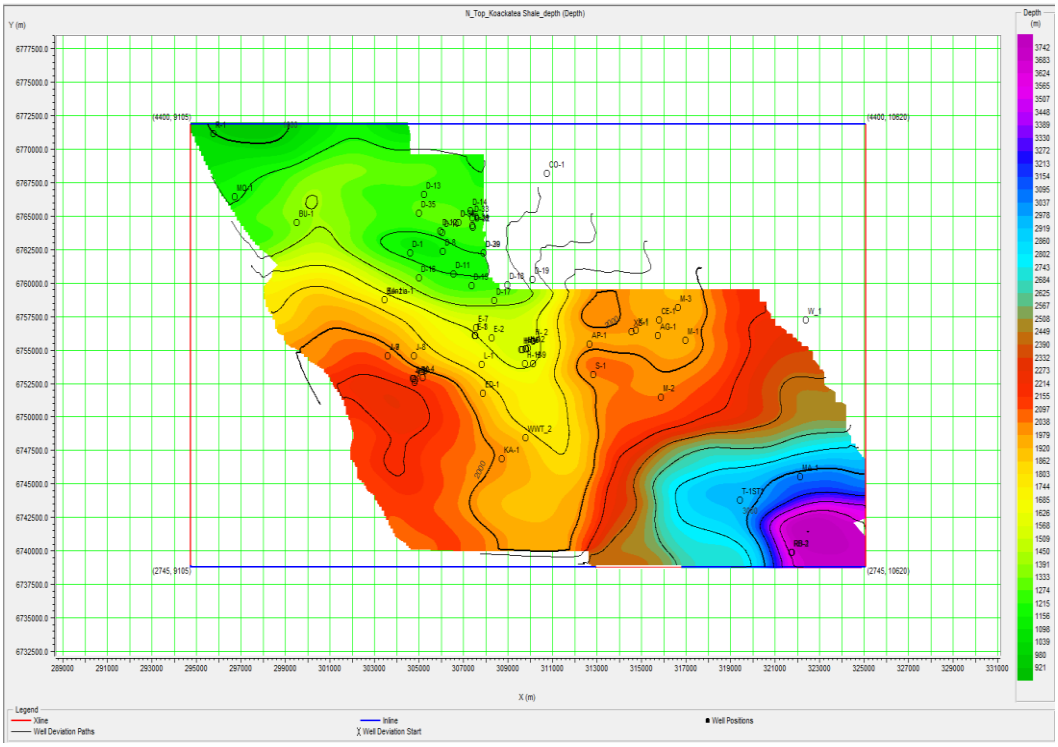

Figure 4-20: Structural contour map of the Kockatea Shale based on the top depth.

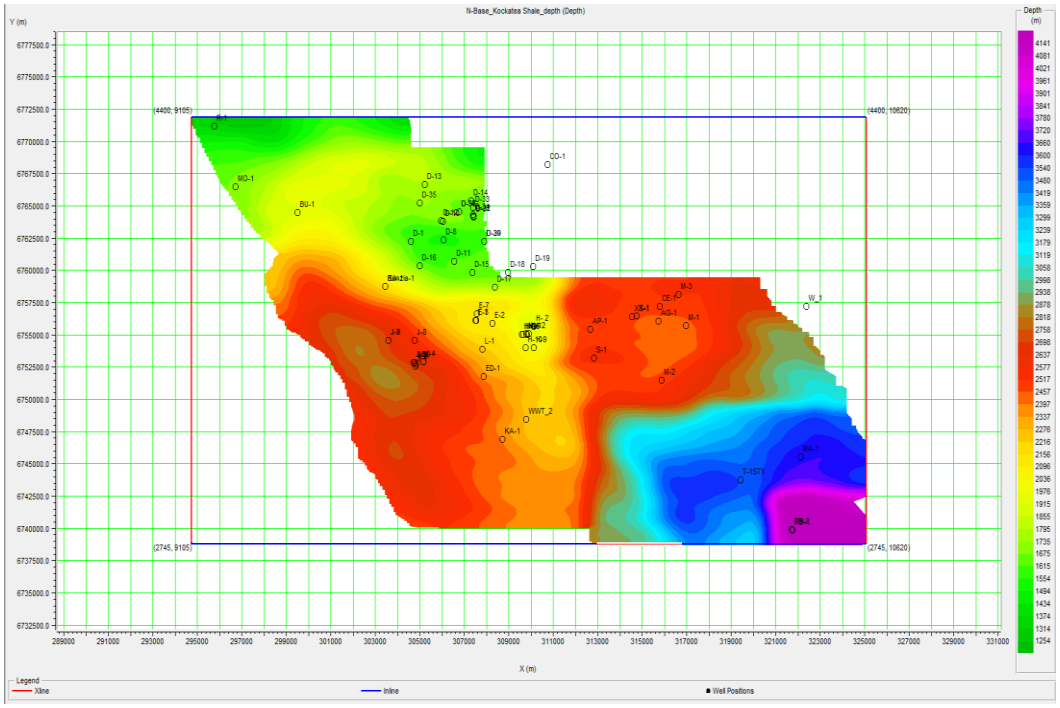

Figure 4-21: Structural contour map of the Kockatea Shale based on the bottom depth.

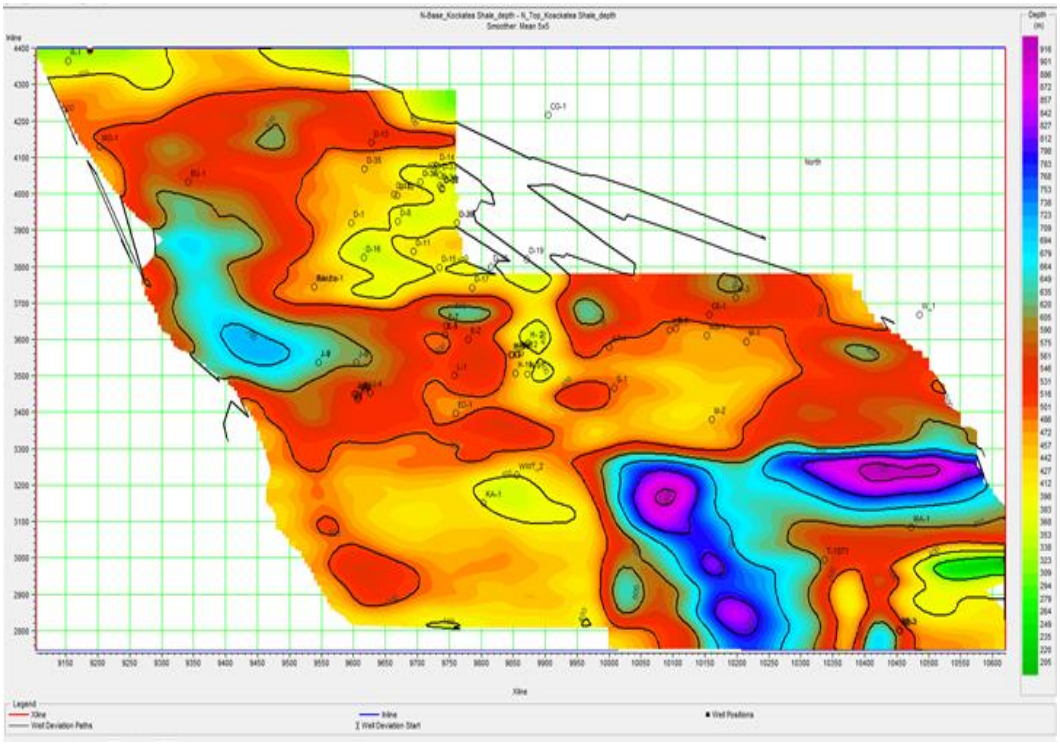

Figure 4-22: Isopach map of the Kockatea Shale.

Table 4-3: Sweet spot information in the Perth Basin (some of the information comes from our studies while others are from different sources namely the DMP, Origin Energy LTD and C. D'Ercole et al., 2003).

	Age	Depth of Kockatea Shale	Thickness	TOC (wt%)	Brittleness Ratio	Porosity (%)
Bahharra Spring Field	Lower Triassic	3200m-3800m	600m	1.30-6.11 (3.04)	0.29-0.71 (0.45)	2.40%(core) 4.15%(log)
Mondarra Gase Field	Lower Triassic	2100m-2500m	400m	0.14-4.04 (2.09)	0.1-0.49 (0.29)	16% (log) 7.4(core)
Dongara Gas Field	Lower Triassic	1039m-1250m	210m	0.04-5.4 (2.72)	0.25-0.74 (0.46)	18% (log)
Hovea Field	Lower Triassic	1650m-2000m	350M	0.8-4.06 (2.2)	0.22-0.75 (0.57)	7.34% (log)
Jingemia Field	Lower Triassic	1980m-2450m	470m	0.2-2.29 (1.24)	0.17-0.65 (0.32)	4.27% (log)

Table 4-4: Sweet spot information in Perth Basin (some of the information posted from our studies while other are from different sources namely the DMP, Origin Energy LTD and C. D'Ercole et al., 2003).

	Age	Depth of Carynginia	Thickness	TOC (wt%)	Brittleness Ratio	Porosity (%)
Bahharra Spring Field	Early Permian	3750m-3796m	46m	1.33-2.41 (1.07)	0.35-0.47 (0.41)	**21.7%(core)**
Mondarra Gase Field	Early Permian	2466m-2527m	61m	0.7-4.06 (2.38))	0.2-0.65 (0.43)	**12.2%(log)**
Dongara Gas Field	Early Permian	1609m-1646m	37m	2.13-11.0 (7.0)	0.21-0.46 (0.31)	**6.20%(core)** **14%(log)**
Hovea Field	Early Permian	1734m-1781m	47m	0.35-4.42 (2.9)	0.18-0.72 (0.42)	**5.21% (log)**
Jingemia Field	Early Permian	2626m-2680m	54m	1.40-2.42 (2.08)	0.2-0.68 (0.42)	**13% (core)** **12.2%(logs)**
Woodada Gas field	Early Permian	2250-2419	169m	0.6-3.33 (1.96)	0.19-0.53	**5.7%(core)**
Arrowsmith-2 well	Early Permian	2720m-2911m	191m	0.6-3.75 (1.45)	0.27-0.61 (0.42)	**2.72(core)**

Chapter 5. Shale elastic property relationships for the TOC content using real and synthetic shale samples

5.1 Ultrasonic measurements of real gas shale samples

In the previous chapter, we have presented some results of estimation the TOC content based on seismic inversion and rock physics relationships. However, more parameters need to be introduced to support the relationship, due to the elastic properties of organic shale, which varies significantly within and across such reservoirs due to variable mineral compositions and fabric anisotropy exhibited by these organic rich shales (Zhu et al., 2011). The laboratory experiment is the key to studying the characterisation of gas shale properties more thoroughly using core samples. This chapter presents laboratory core measurements on the elastic properties of gas shale reservoir rocks collected from the Arrowsmith-2 and Redback-2 wells in the Perth Basin. The shale samples used were selected based on the TOC content, enabling a study of the impact of TOC on the elastic and mechanical properties. The depth and density of these samples are closer together to avoid any impact of the physical properties on the elastic properties. The in-situ effective stress is calculated from the overburden stress at the depth of 3,000 m. Effective stress is about 34 MPa for the Arrowsmith-2 well and for the Redback-2 well at depth of 4,000 m it is calculated to be 60 MPa. This section will focus on the static/ dynamic elastic properties and anisotropy as well as to define the key parameters that control the gas shale properties. This will help us to understand the link between the elastic and deformational properties of these rocks. Some of the presented result and analysis in this chapter have been published before (Altowairqi et al., 2013; Altowairqi et al., 2015).

5.1.1 Shale composition and microstructure of gas shale formations

The samples used in our experiments come from two different gas shale formations: the Kockatea Shale and the Carynginia Formation from the Redback-2 and Arrowsmith-2 wells in the Perth Basin. The mineralogy and geochemical analysis data were provided by the DMP. The composition of the whole rock mineralogy for

the Arrowsmith-2 and Redback-2 wells for different shale formations in the Perth Basin are displayed in a ternary plot in Figure 5-1.

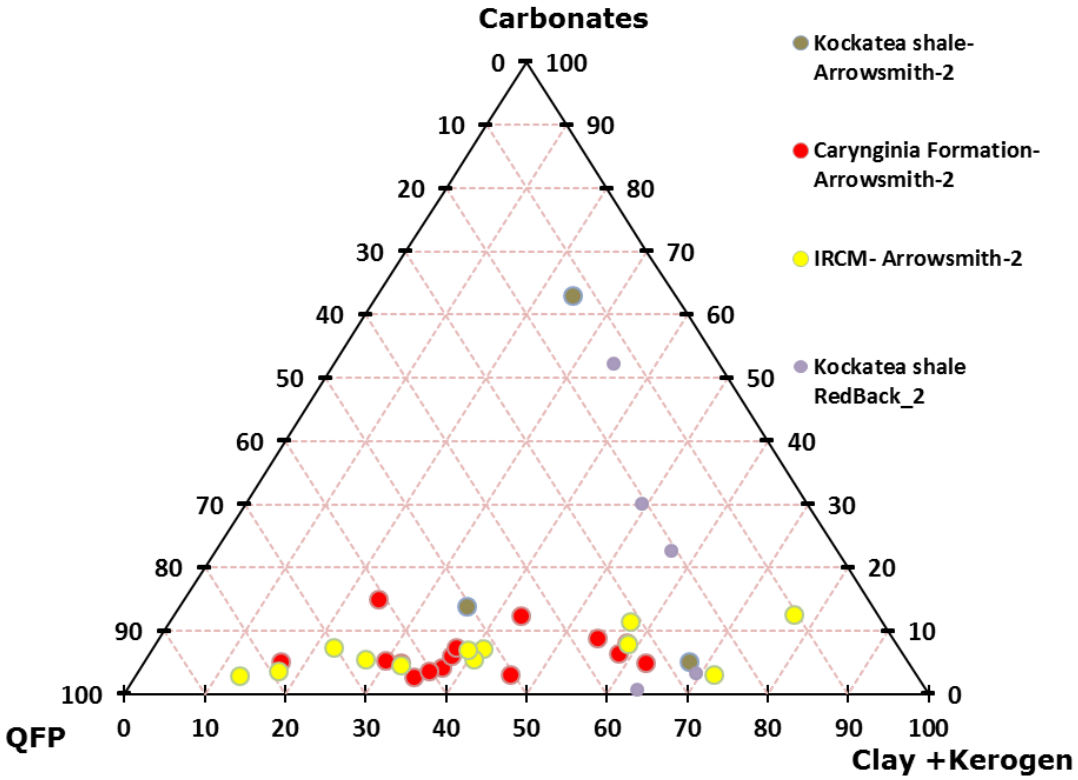

Figure 5-1: Ternary plot is a representation of the sample material compositions for different shale formation: Quartz, Feldspar and Pyrite (QFP) (most of the data are from the DMP and Origin Energy LTD, Shale reservoir evaluation report).

Figure 5-2 shows a secondary electron SEM image of A.C.01 sample from the Carynginia Formation (the TOC percentage is 3.03 wt% and the clay minerals are around 56% by the weight). A fabric anisotropy creating the bedding planes is described by the combination of the following: the preferred orientations of the matrix clay, the shape/ distribution of organics and the preferred alignment of elongated fossils. Aggregates of aligned clay minerals are permanently observed in the local samples when tested under the SEM. The shale is composed of aligned layers of clay, quartz-rich and fine-grained material displaying vast heterogeneity in terms of the mineralogical content. Some porosity can be seen at the grain contacts within the aligned layers of clay.

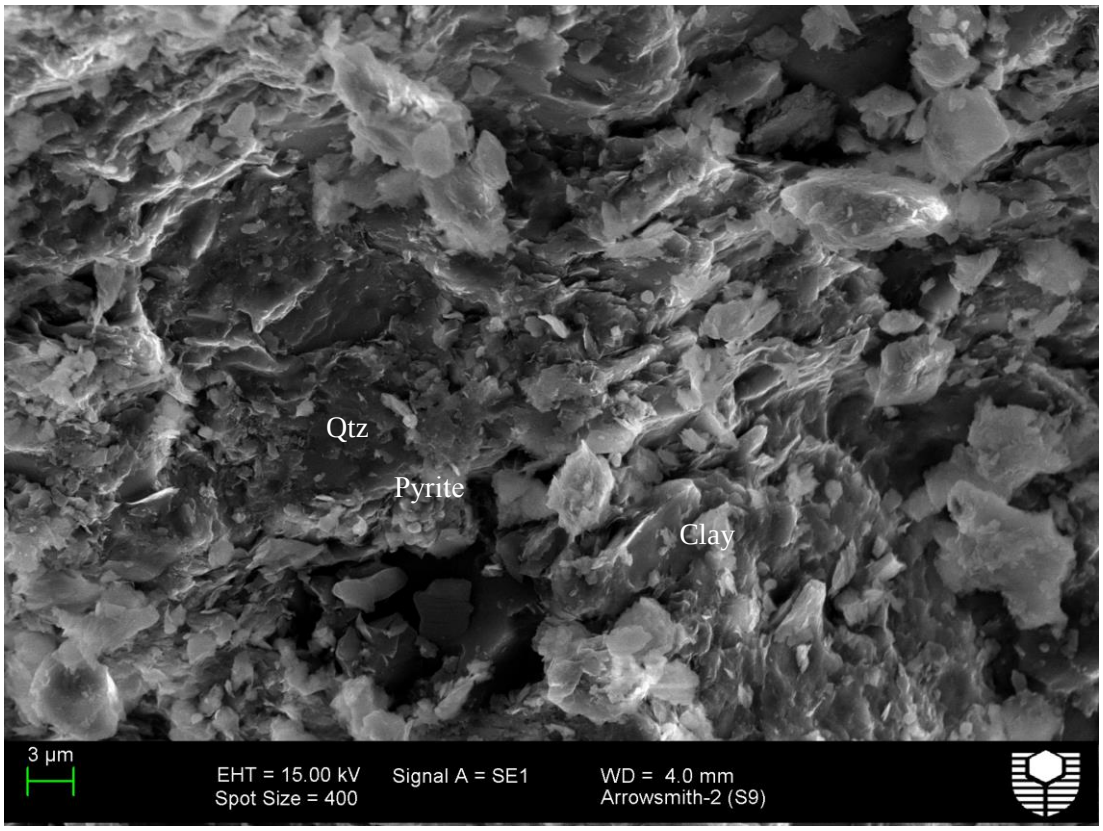

Figure 5-2: SEM image on the core shale sample of the Carynginia Formation.

5.1.2 Petrophysical properties

The petrophysical properties of the Arrowsmith–2 well are shown in Table 2. The bulk density ranges from 2.619 to 2.648 g/cc. The grain density ranged from 2.630 to 2.674 g/cc. The effective porosity percentages range from 2.67 to 3.23%. Three shale samples used in this research were selected based on the TOC content, enabling a study of the impact of the TOC on the physical properties and ultrasonic velocities. The highest percentage of the TOC was 3.03%, by weight (found in A.C.01) and the lowest percentage was about 0.23%, by weight (found in A.C. 10).

Table 5-1: Physical properties from the Arrowsmith–2 well of different shale samples.

Sample ID	Depth (m)	Bulk Density ($^{g}/_{cc}$)	Grain Density ($^{g}/_{cc}$)	Effective Porosity (%)	TOC (WT %)	Clay (%)	Non Clay (%)	Carbonate (%)
A.C.1	2780.32	2.619	2.63	5.98	3.03	56	38	6
A.C.2	2793.7	2.619	2.662	5.67	0.64	31	67	2
A.C.3	2802.94	2.616	2.647	5.46	0.86	33	62	5
A.C.8	2806	2.619	2.632	3.01	1.8	41	54	5
A.C.9	2812.62	2.615	2.653	5.09	1.08	28	68	4
A.C.5	2816.59	2.623	2.665	5.47	1.36	33	61	5
A.C.6	2829.28	2.543	2.654	6.88	0.17	15	81	4
A.C.10	2831.15	2.648	2.674	2.93	0.23	33	60	7

Figure 5-3 (A) shows the TOC content plotted against clay minerals volume for eight samples from the Carynginia Formation, the Arrowsmith-2 well. There is a positive correlation between them and it is clear that as the clay mineral volume increases, the TOC content also increases. Figure 5-3 (B) shows the measured porosity plotted against the TOC with clay mineral volume. Also, the relation between the grain density against clay volume and TOC wt% are shown in Figure 5-3 (C) and (D) respectively. The correlations are positive; as the volume of clay or the percentage of TOC content increases, the density becomes lower. These results shows similar correlations, confirming the observations made in previous studies with organic matter and clay mineral in gas shale samples (Loucks et al., 2009; Sondergeld et al., 2010).

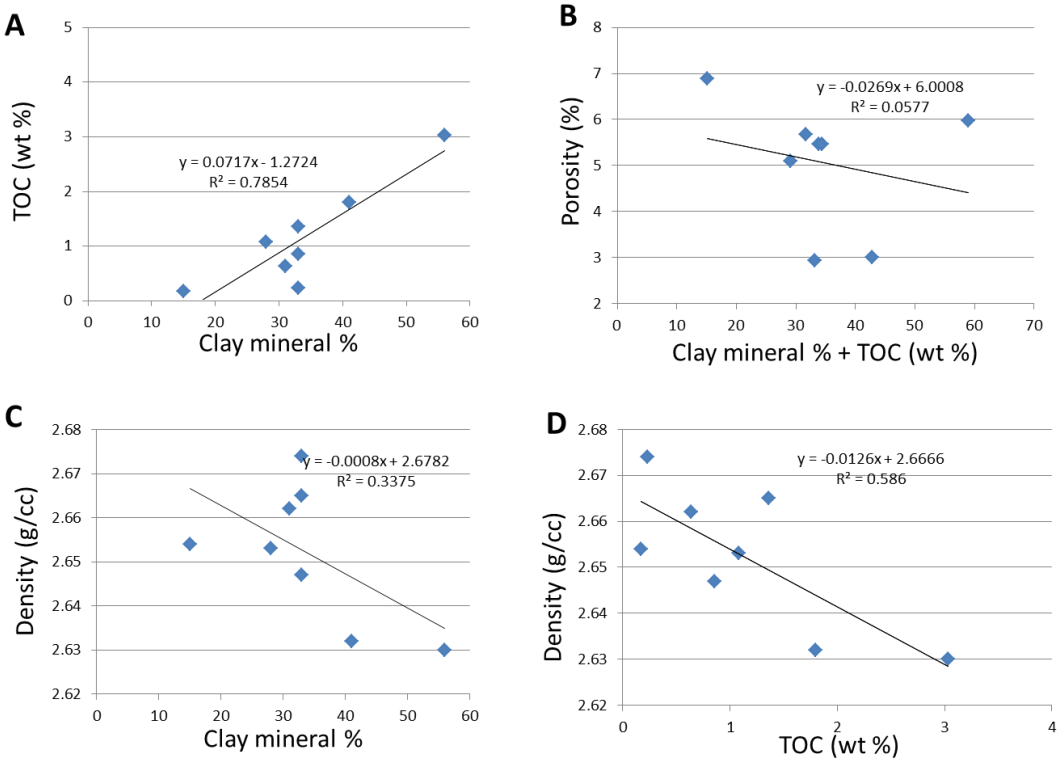

Figure 5-3: Relationships, of some core samples from the Arrowsmith-2 well, between (A) the TOC content vs Clay volume. (B) Porosity vs. Clay volume+ the TOC content. (C) Density vs Clay volume. (D) Density vs theTOC content.

The petrophysical properties of the Redback–2 well are shown in Table 3. Three shale samples used from the Redback-2 well were selected based on the TOC content (4.34, 2.25 and 1.94 wt%). The depths of those three samples are 3801.45, 3810.6 and 3794.25 m respectively.

Table 5-2: Petrophysical properties from the Redback–2 well of different shale core samples.

Sample ID	Depth (m)	Bulk Density ($^{g}/_{cc}$)	Grain Density ($^{g}/_{cc}$)	Effective Porosity (%)	TOC (wt%)	Clay (%)	Non Clay (%)	Carbonate (%)
R.B.1	3789.91	2.647	2.681	3.50	2.25	66	30.9	3
R.B.2	3794.60	2.653	2.685	2.77	1.94	48.2	22.9	21.9
R.B.3	3795.81	2.634	2.671	2.95	2.94	48.2	22.4	29.4
R.B.4	3797.91	2.590	2.635	3.49	4.31			
R.B.5	3800.46	2.558	2.582	2.54	4.71	61.3	38.1	0.5
R.B.6	3805.92	2.665	2.688	2.69	0.61	34	14.95	51.1
R.B.7	3807.53	2.598	2.618	3.33	2.13			
R.B.8	3814.76	2.624	2.647	2.98	1.38			
R.B.9	3818.66	2.625	2.644	2.72	1.55			
R.B.11	3821.36	2.640	2.655	1.77	1.02	16.4	51.3	32
R.B.12	3825.28	2.644	2.661	2.02	2.03			
R.B.13	3827.93	2.598	2.619	2.49	2.81			
R.B.14	3834.86	2.608	2.632	2.64	2.88			

Figure 5-4 (A, B, C, and D) show some correlation physical properties and the TOC and clay mineral from different core samples from the Kockatea Shale, the Redback-2 well. In general, the density became lower whereas the porosity became larger with an increase in TOC or clay minerals.

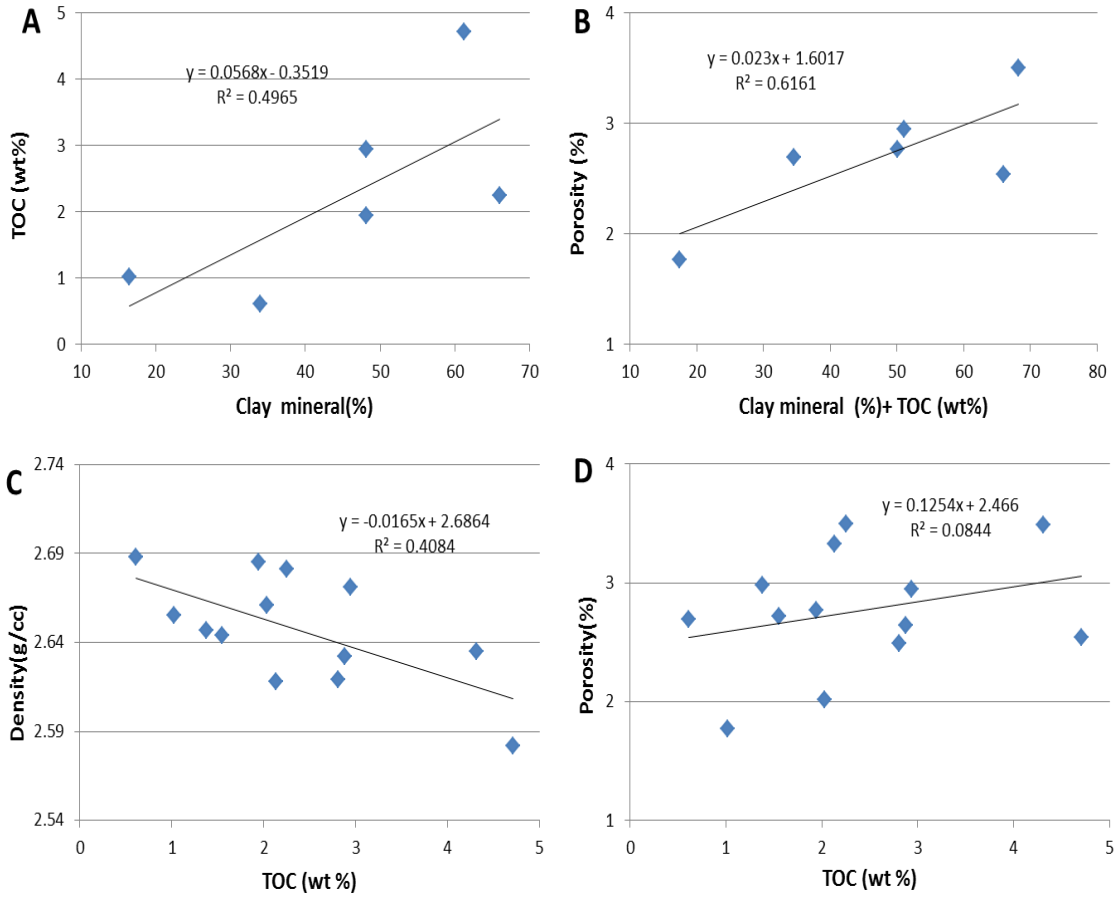

Figure 5-4: Relationships , of some core samples from the Redback-2 well, between (A) the TOC content vs Clay volume; (B) Porosity vs Clay volume + The TOC content; (C) Density vs The TOC content and (D) Porosity (%) vs the TOC content from the Redback-2 well.

5.1.3 Results and analysis

5.1.3.1 Elastic wave velocities measurement

The aim of the laboratory measurement was to test the elastic wave velocities and their anisotropy with varying stress levels. This part will present the results of two core samples out of six, one from the Arrowsmith-2 and one from the Redback-2, while the rest will be presented in Appendix 3. The impact of the mean effective stress on the ultrasonic wave velocity in the Arrowsmith–2 shale samples is presented in Figure 5-5 A and B. The first test was conducted using a horizontal core plug from A.C.08, with a TOC content of 1.8 wt%; the velocity of V_{Ph} increased from 4,171 to 4,575 m/s as the mean effective stress increased from 0.7 to 38 MPa. The velocity of V_{Pv} increased from 3,290 to 4,293 m/s over the same stress range. The quasi-P velocity increased from 3,707 to 4,392 m/s over the range of 0.7 – 38

MPa and was therefore between the range of V_{Ph} and V_{Pv}. The V_{Sh} increased from 2,500 to 2,624 m/s, while the V_{Sv} increased from 2,229 to 2,346 m/s as the mean effective stress increased from 0.7 – 38 MPa. The V_{Ph} / V_{Sh} ratio increased slightly from 1.7 to 1.77 by increasing the mean effective stress within the same stress range, as shown in the Appendix 3 (Figure C-2 (A)). The V_{Pv} / V_{SV} ratio also increased from 1.5 to 1.85 over the same stress range.

The impact of the mean effective stress on the ultrasonic velocity in shale core sample studied from the Redback-2 well is presented in Figure 5-5 (B). In general, all the wave velocities are increased as the stress increased, V_{Ph} is slightly higher than V_{Pv} and V_{Sh} is almost higher than V_{SV}. The first test of the shale was conducted using core plug from R.B.21, with a TOC content of 1.94%, by weight and from a depth 3,794m; the velocity of V_{Ph} increased from 5,300 to 5,414 m/s as the mean effective stress increased from 10 to 90 MPa. The velocity of V_{Pv} increased from 4,000 to 4,400 m/s over the same stress range. The quasi-P velocity increased from 4,500 to 4,940 m/s over the same range of stress and was therefore, between the range of V_{Ph} and V_{Pv}. The V_{Sh} is stable around 3040 m/s as the stress increased, while V_{Sv} increased from 2,220 to 2400 m/s as the mean effective stress increased to 90 MPa. The V_{Ph} / V_{Sh} ratio increased slightly from 1.74 to 1.79 by increasing the mean effective stress within the same stress range. The V_{Pv} /V_{SV} ratio also increased from 1.78 to 1.90 over the same stress range.

These results suggest that the velocity increased as the stress level increased, while the errors decreased with rising stress levels. The errors in the S-wave velocity were approximately 7% at lower stress levels. P-wave errors were small at all stress levels.

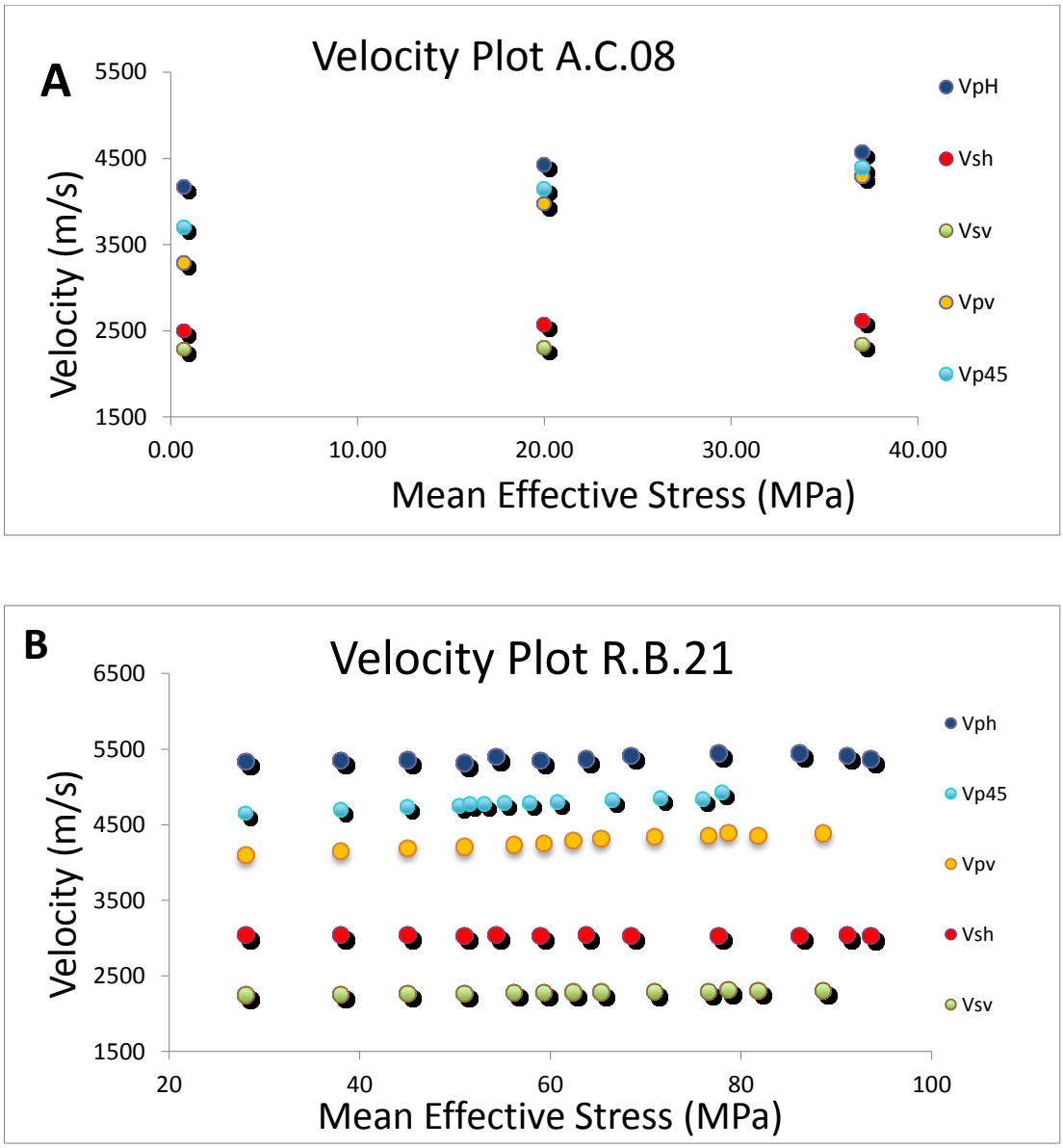

Figure 5-5: Relationship between the velocities and mean effective stress for the Arrowsmith-2 well sample (A) A.C.08, and for the Reback-2 well sample. (B) R.B.21, the velocities increase as the mean effective stress increases.

5.1.3.2 Elastic coefficient calculation

The responses of the elastic coefficients of the samples from A.C.08 are shown in Figure 5-6 (A). The C11 increased from 45.5 to 54.7 GPa, while C33 increased from 28.3 to 48.2 GPa as the mean effective stress increased from 0.7 to 38 MPa. Both C44 and C66 increased over the same stress range from 13.7 to 14.1 GPa and 16.4 to 17.9 GPa, respectively. C12 increased from 12.8 to 18.8 GPa, C13 increased from 5.7 to 20.4 GPa as the mean effective stress increased from 0.7 to 38 MPa. Figure 5-6 (B) shows the result of R.B.21 sample reports that, the C11 increased from 75.6 to 77.8 GPa, while C33 increased from 44.7 to 51.4 GPa as the mean effective stress increased from 10 to 90 MPa. Both C44 and C66 increased over the same stress range from 13.4 to 14.2 GPa and 24.4 to 24.6 GPa, respectively. C12 increased from 26.5 to 28.7 GPa and C13 increased from 25.1 to 3.46 GPa as the mean effective stress increased from 10 to 90 MPa.

The errors of calculation of the elastic constants were around 1 to 2% in this experiment, while errors in the anisotropy parameters were higher due to the use of the ratios of the elastic constants. “Using these ratios, errors in ε and γ can be up to 2%, while δ has the least accuracy, with errors of typically ±13%” (Dewhurst and Siggins, 2006).

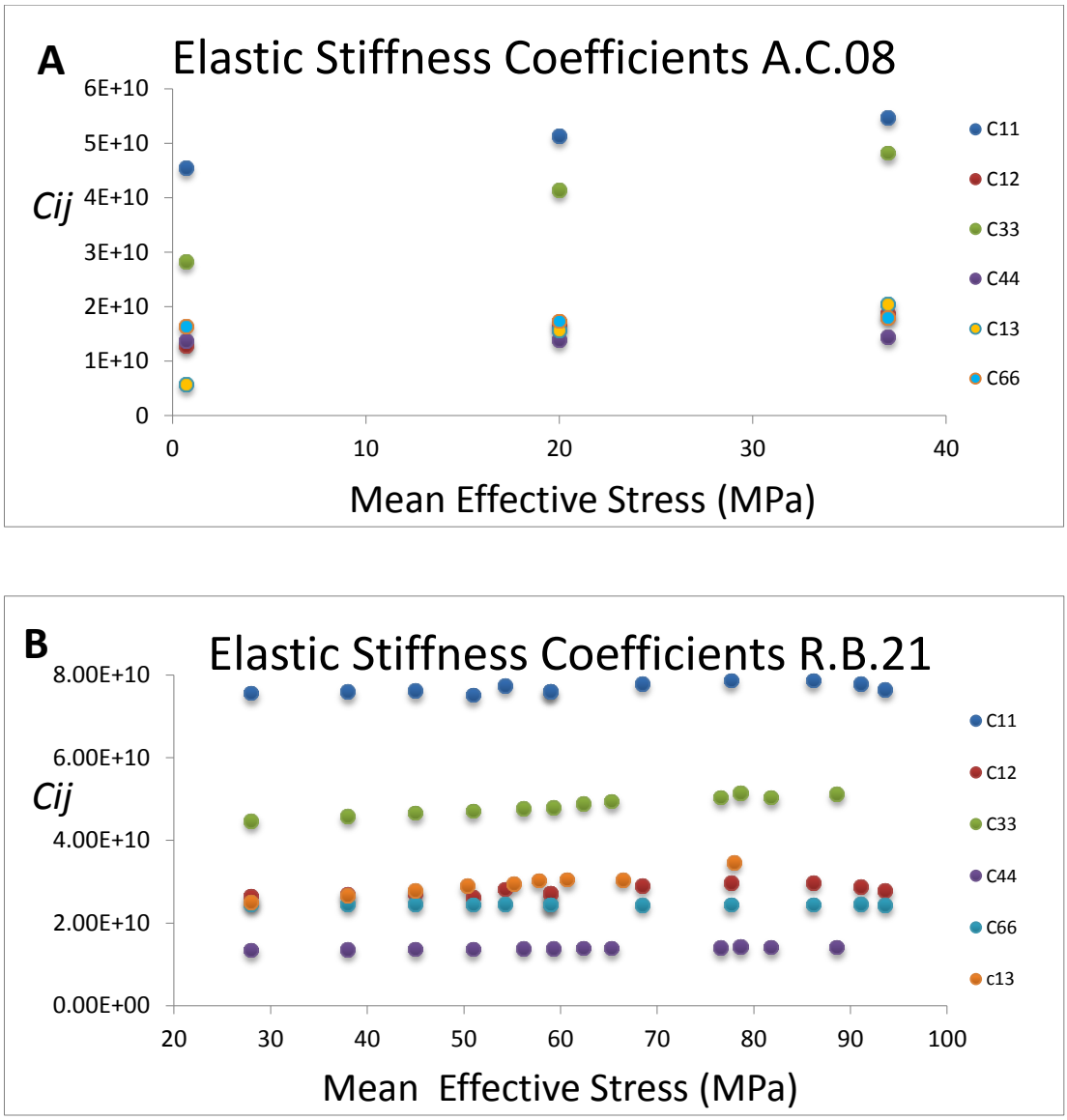

Figure 5-6: The responses of the elastic constants to increase the mean effective stress for (A) shale sample A.C.08 and (B) shale sample R.B.21.

5.2.3.3 Thomsen parameters estimation

The elastic coefficients calculated were used to derive the Thomsen's anisotropy parameters (Thomsen, 1986). The impacts of mean effective stress on P-wave (ε) and S-wave (γ) anisotropy factors, as well as the elasticity factor (δ), are shown in Figure 5-7. For example for sample A.C08 the initial anisotropy at a low stress level is displayed with large values (0.30 for P-wave, 0.10 for S-wave) and varies with changing mean effective stress. ε decreased from 0.3 to 0.07 as the mean effective stress increased from 0.7 to 38 MPa. Initially, γ was stable around 0.13 as the stress

increased. However, δ dropped from 0.19 to 0.02, as the mean effective stress increased from 0.7 to 38 MPa.

Three shale core plug samples from the Arrowsmith–2 well were tested, which were moderately anisotropic and loaded parallel to the bedding. The anisotropy parameters were sensitive to the changes in confining pressures. Velocity anisotropy (A), as described in Dewhurst et al, (2011), is shown in Figure 5-7(A), (B) and (C); ε (epsilon) in sample A.C.08 decreased as the confining pressure increased. This was also reported in the samples A.C.01. Over the entire range of stress levels in the samples A.C.08 and A.C.01 however, γ (gamma) was stable. In the third shale sample A.C.10, ε and γ were stable over the entire range of stress levels. However, there is an increase in (delta) as the stress levels increased. This could be a possible mistake when measuring the P-wave velocity for 45^{o}.

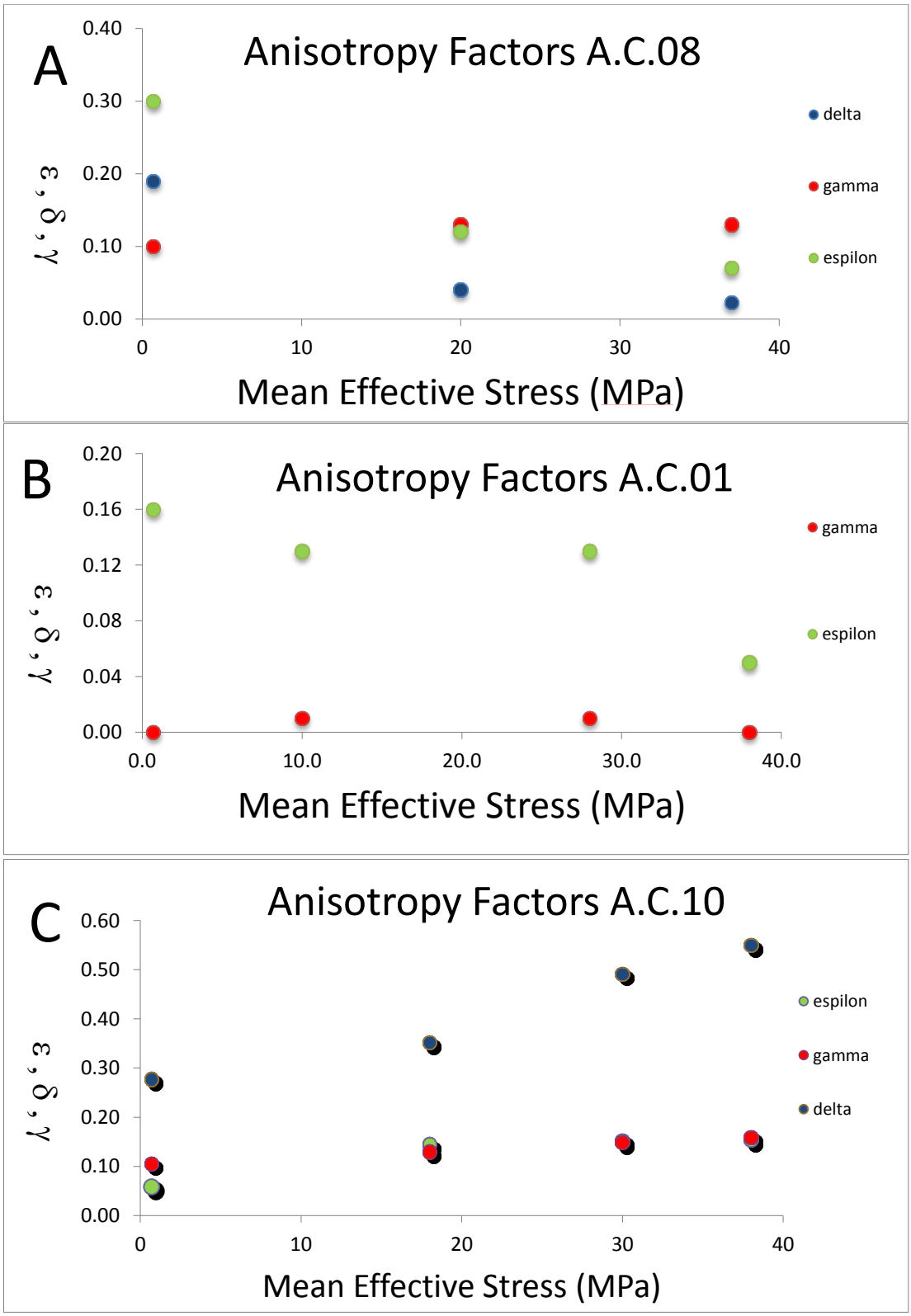

Figure 5-7: Influence of mean effective stress of shale sample (A) A.C.08, (B) A.C.01 and (C) A.C.10 on ε, γ and δ for Arrowsmith–2 .

5.2.4 Discussions

The key controls on the elastic properties of the organic shale were effective stress, the TOC content, porosity, density and clay mineral. High TOC shales are generally characterised by strong velocity anisotropy and low velocity in the beddings normal direction and relatively low density and porosity (e.g., Vernik, and Nur, 1992; Vernik and Liu, 1997; Sondergeld et al., 2000). The intrinsic anisotropy increased with rising TOC (Tutuncu, 2010). Therefore, the velocities of organic-rich shales decreased with increasing TOC. Loseth et al. (2012) studied the relationships between the TOC of organic rich claystones and AI. The studies show that AI decreases nonlinearly with increasing TOC.

Figure 5-8 (A) shows the relationships between different TOCs (0.23, 1.8 and 3.03%) and the velocities of shale samples from the Arrowsmith-2 well. In this study, we have selected the velocities at 38 MPa in-situ effective stress values as the reservoir condition. It is clear from the results that all of the velocities decrease with increasing TOC content. The V_{Ph} of three samples (A.C.10, A.C.08 and A.C01) decreases from 4,908.9 to 4,385.3 m/s as the TOC percentage increases. Furthermore, the velocity of V_{pv} decreases from 4,490 to 4,191 m/s over all the three samples, while the TOC percentage increases. The last two waves, V_{Sh} and V_{Sv}, decreases as the TOC percentage rises. Figure 5-8 (B) compares the velocities from the DT log data of the Arrowsmith-2 well and the measured velocities of core samples from the same well. It shows the same correlation as the TOC content increases, the velocities decrease.

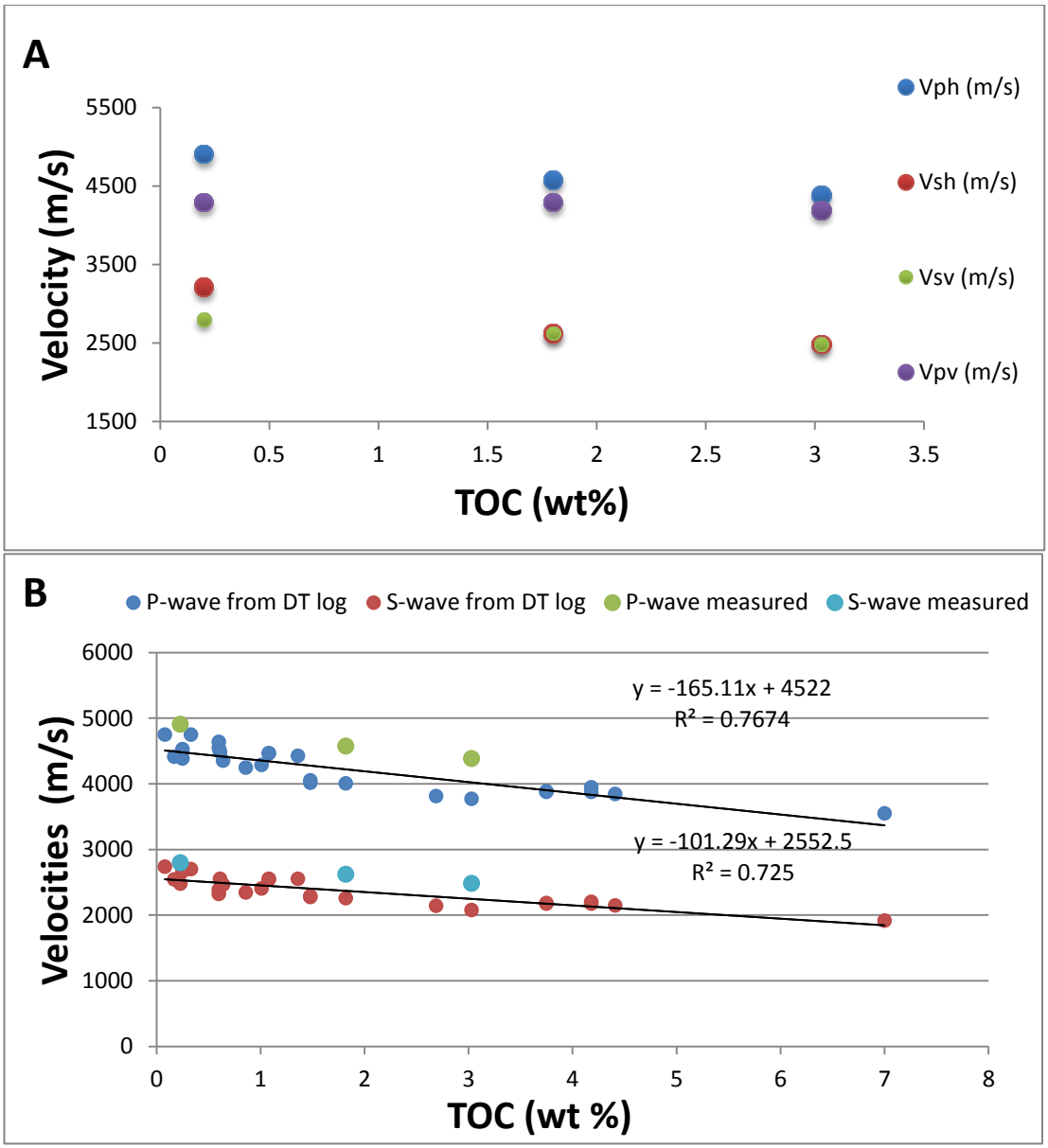

Figure 5-8: (A) Impact on the velocities from different percentages of TOC in the Arrowsmith-2 well. (B) The comparison between the velocities from the DT log data of Arrowsmith-2 well and the measured velocities of core samples.

Figure 5-9 (A) shows the relationships between different TOCs (1.94, 4.34 and 2.25%) and the velocities of shale samples from the Redback-2 well. For these samples we have selected the velocities at 60 MPa in-situ effective stress values as the reservoir condition. It is clear from the results that all of the velocities decrease with increasing TOC content. The V_{Ph} of three samples (R.B.21, R.B.22 and R.B.23) decreases from 5,413 to 4,480 m/s as the TOC percentage increases. Furthermore, the velocity of V_{pv} decreases from 4,316 to 3,703 m/s over all the three samples, while the TOC percentage increases. The V_{p45} decreases from 4,830 to 4,170 m/s as the TOC content increases. Also, the last two waves, V_{Sh} and V_{Sv}, decrease as the

TOC percent increase from 3,032 m/s to 2,8030 m/s and from 2,363 m/s to 1,760 m/s. Figure 5-9 (B) shows the comparison between the velocities from the DT log data from the Redback-2 well and the measured velocities of core samples from the same well. It shows the same correlation; as the TOC content increases, the velocities decrease.

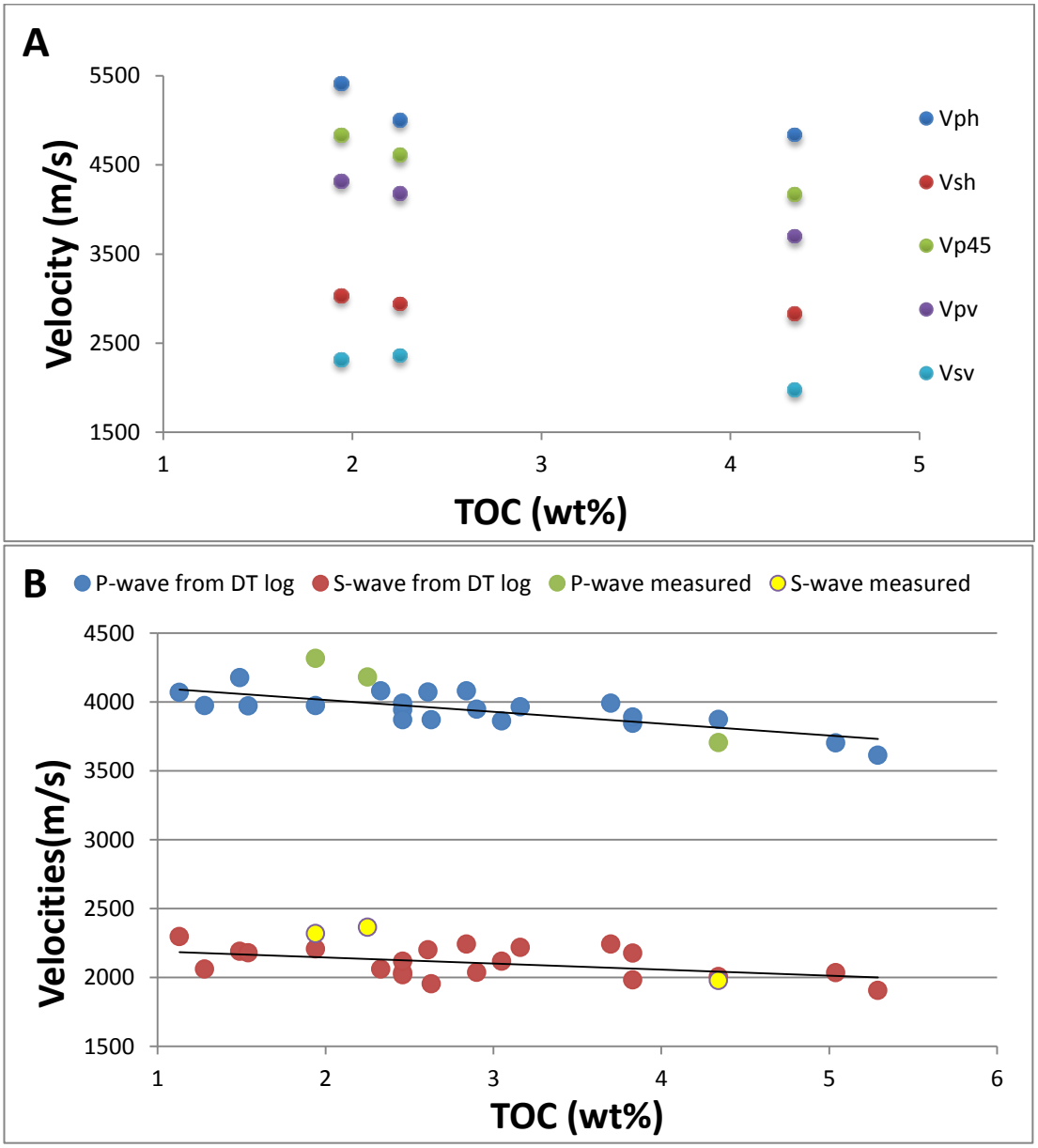

Figure 5-9: (A) Impact on the velocities from different percentages of the TOC in the Redback-2 well. (B) Comparison between the velocities from the DT log data from the Redback-2 well and the measured velocities of core samples.

There are many studies of anisotropy in organic shales including alignment of clay platelets, organic matter, stresses and fractures. A study by Hornby (1998) suggested that compaction results increased the clay particle alignment as that increased anisotropy. Sayers (2008) suggested that the deformation and shape of pore space in shales control the anisotropy. Sondergeld et al. (2000) considered that the anisotropy increased with organic matter content. On the other hand, density can be decreased with increased organic matter in shales, as shown in Figure 5-10 and can also produce an effect opposite to compaction. In addition, the porosity will increase with an increase of organic matter, as shown in Figure 5-11.

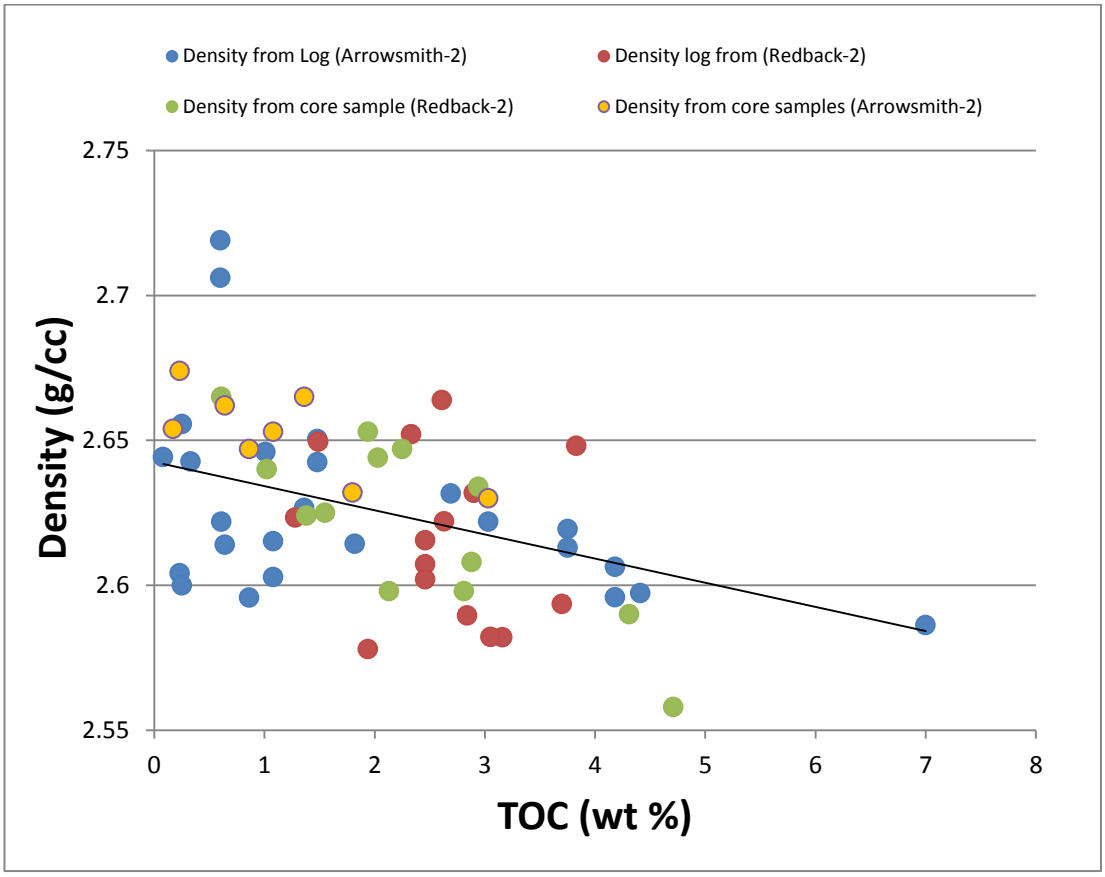

Figure 5-10: Impact on the densities from the core samples and density log of both wells, are displayed with different percentages of TOC.

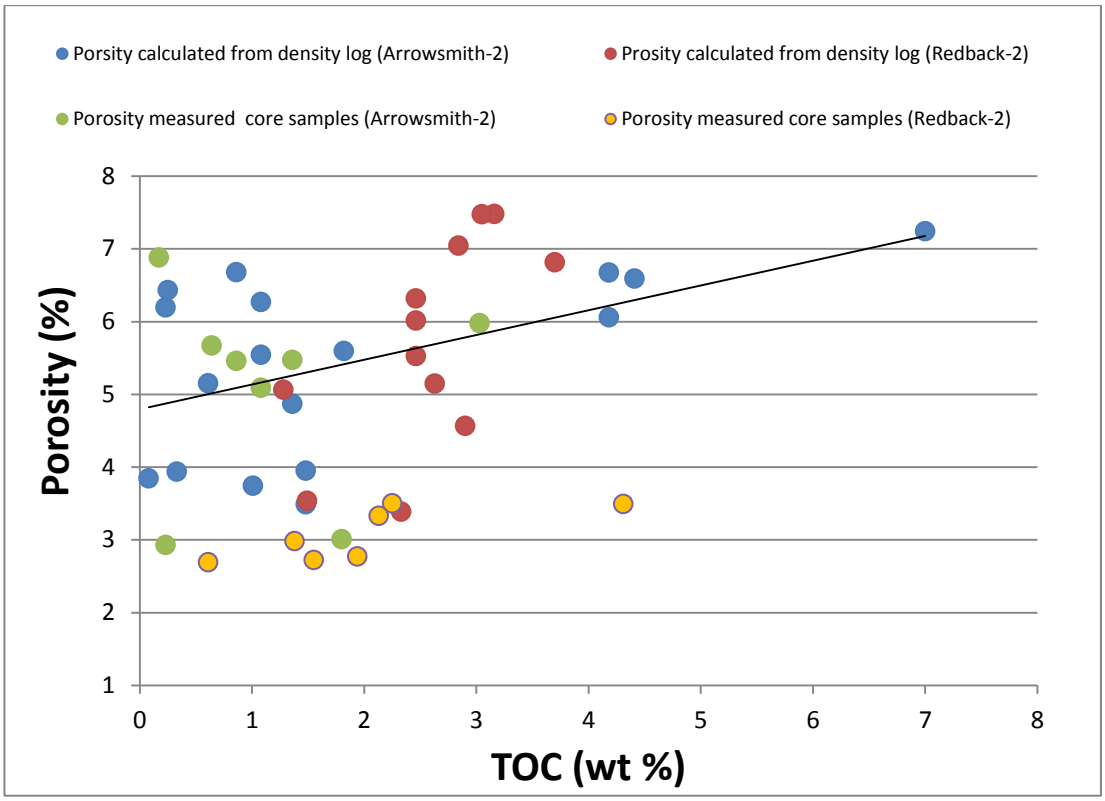

Figure 5-11: Impact on the porosities measured from core samples and porosities calculated from the density log of both wells, displayed with different percentages of TOC.

The key finding from this chapter is that the velocities in the shale sample P and S waves and the elastic stiffness coefficients responded in similar ways with changes in the stress levels. Equations (5-1 and 5-2) were used for anisotropy calculation.

$$A_{vp} = \frac{(V_{Ph} - V_{Pv})}{(V_{Ph})} * 100 \qquad \text{Equation 5-1}$$

$$A_{vs} = \frac{(V_{sh} - V_{sv})}{(V_{sh})} * 100 \qquad \text{Equation 5-2}$$

The results show that velocities increase with the mean effective stress across the whole stress range. This is also found in previous work on ultrasonic characterisation on shale under the same conditions (Dewhurst and Siggins, 2006; Dodds et al., 2007; Delle Piane et al., 2011; Dewhurst et al., 2011). "Changes in ultrasonic anisotropy occurred mainly as a result of changes in the magnitude of the mean effective stress, as well as the orientation and degree of anisotropy of the stress field". Increasing the TOC content increased the P and S-wave anisotropy (%) as shown in Figure 5-12 (A) and (B); however, the effect on ultrasonic anisotropy is possibly dependent on the degree of stress anisotropy or clay mineral. A comparison between the samples from the Redback-2 and Arrowsmith-2 wells, found that the anisotropy (%) is higher in

the Redback-2 well than in the Arrowsmith-2 well. This is attributed to the clay mineral composition in the Redback-2 well, as the clay mineral content is higher as shown in Tables 5-1 and 5-2.

Tutuncu (2010) found that "the anisotropy drop with increasing mean effective stress at low stresses implies that the high degree of anisotropy is closely associated with the presence of fractures. The increase of the stress results in the closure of most of the fractures reducing the degree of the anisotropy." Dewhurst et al. (2011) noted the ultrasonic anisotropy decreases in a changing isotropy stress field, rather than a changing anisotropic stress field. The results show that there is stress sensitivity and researchers should be careful when using isotopic approaches when dealing with compacted organic shales because of their highly anisotropic nature and possible compositional impacts on velocity.

Figure 5-13 (A) shows the relationship between the elastic moduli and different percentage of the TOC content of six core samples with log data from the Redback-2 and Arrowsmith-2 well. The graph shows that bulk, shear and Young's modulus are affected by the TOC content; as the TOC content increases, the elastic moduli decreases. Figure 5-13(B) also shows the relationship between Poisson's ratio and TOC of core samples and log data; the graph shows that the TOC content increases as the Poisson's ratio is increased. The Poisson's ratio of organic shale is around 0.25 to 0.29 as described in literature (Crain, 2000).

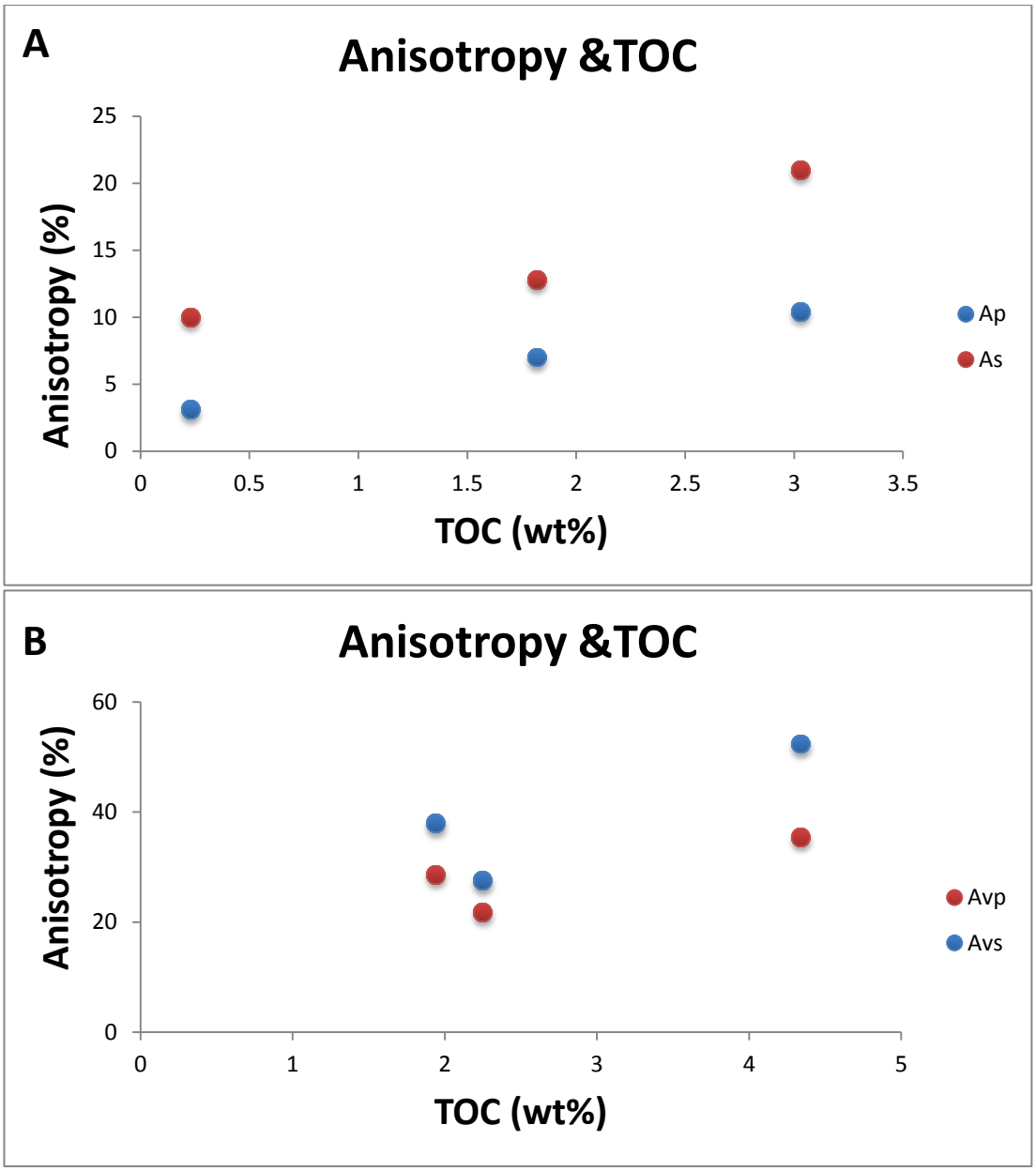

Figure 5-12: Impact on the Anisotropy velocities between different of TOC contents for (A) the Arrowsmith-2 well and (B) the Redback-2 well.

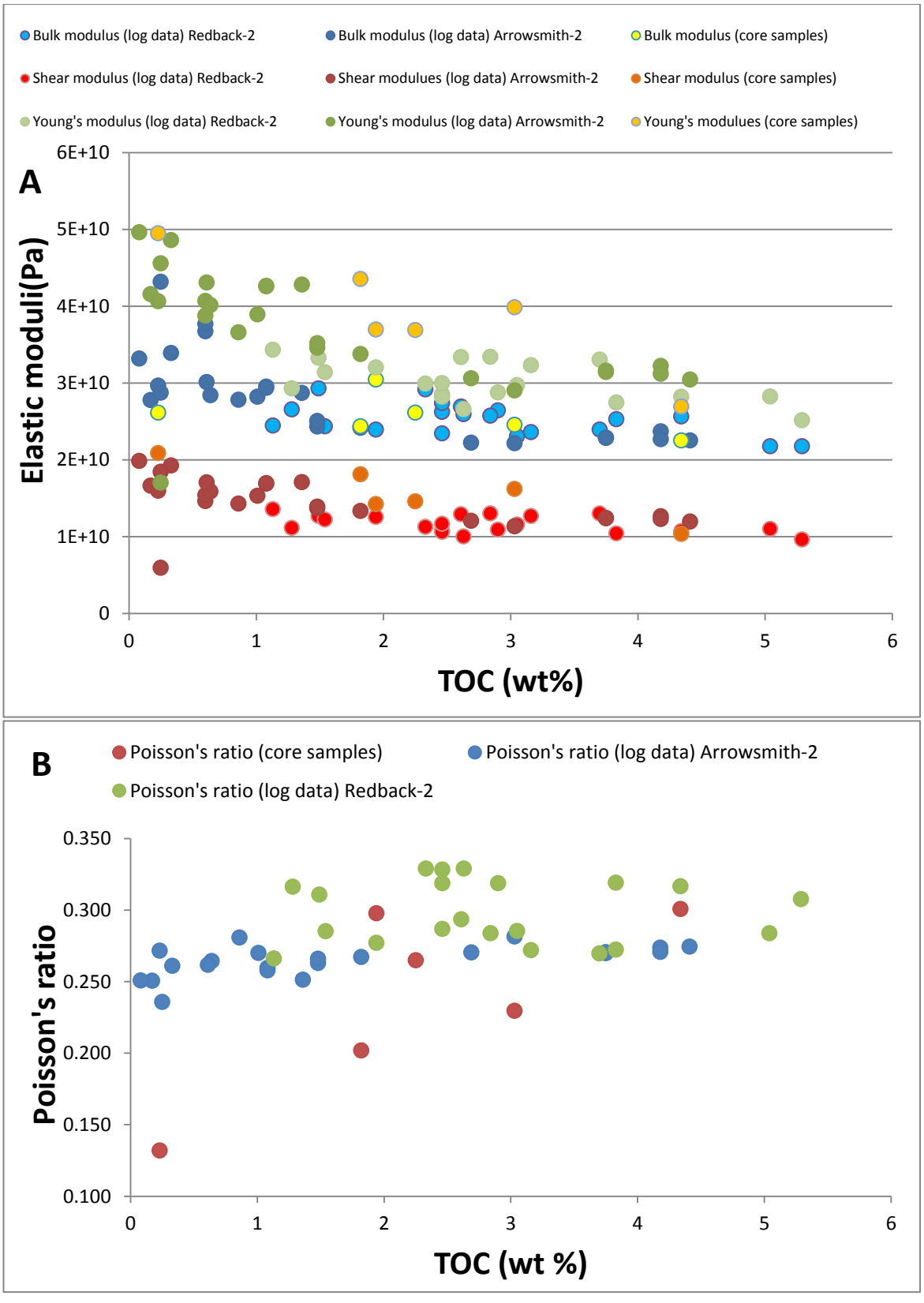

Figure 5-13: Impact of the elastic moduli with different percentages of the TOC of core samples and log data.

In addition, in Figure 5-14, the results of this research show that as the clay mineral content increased in the shale, the velocity decreased. Also, the density decreased and the porosity increased, as clay minerals increased over all of the core plug shale samples. Figure 5-15 (A) and (B) show the relationship between the elastic moduli and the different percentages of the TOC content of core samples with log data from the Arrowsmith-2 well. The graph shows that bulk, shear and Young's modulus are affected by clay minerals; the clay mineral increases as the elastic moduli decreases. In the relationship between Poisson's ratio and the clay minerals of core samples and log data, the graph also shows that as the TOC content increases, Poisson's ratio increases.

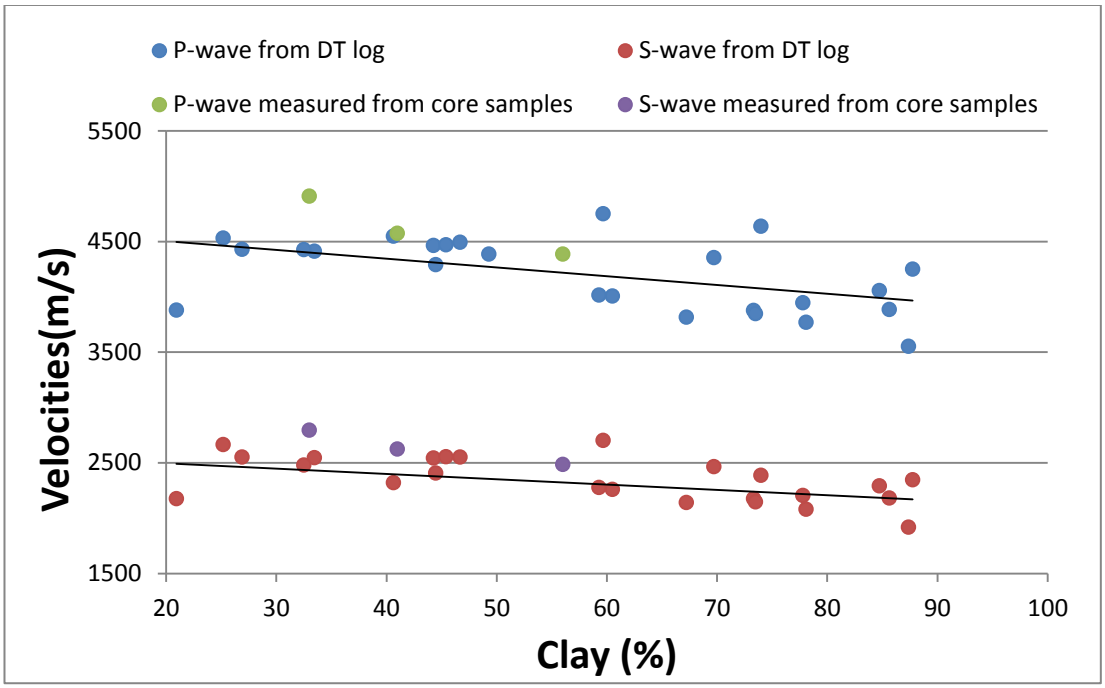

Figure 5-14: Impacts of the velocities from the DT log data from the Arrowsmith-2 well and the measured velocities of core samples, which are displayed with different percentages of clay minerals.

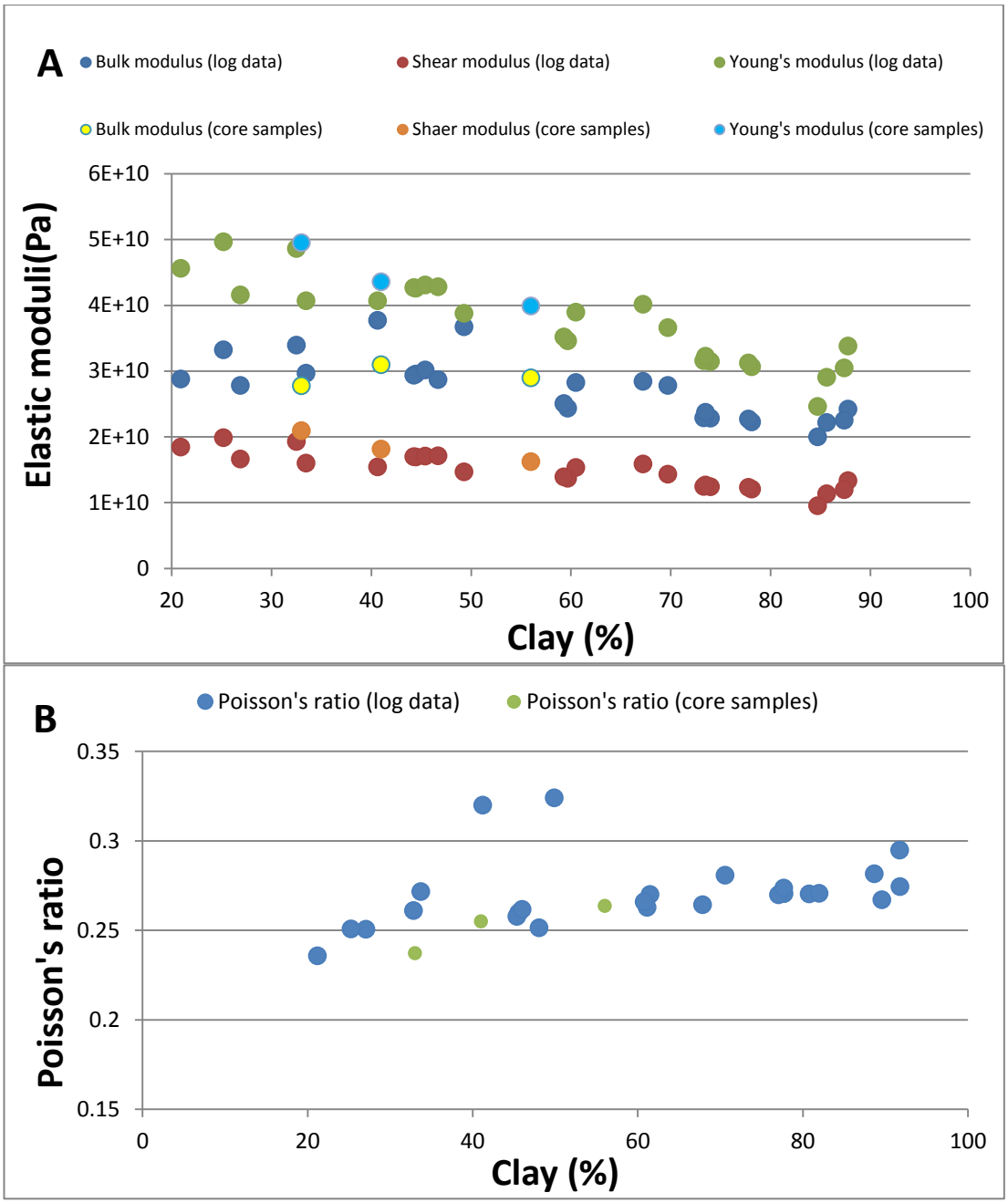

Figure 5-15: Impact of the (A) elastic moduli with different percentages of clay minerals from core samples and (B) log data from the Arrowsmith-2 well.

5.2 Ultrasonic measurement of synthetic shale samples

Previous laboratory experiments have studied the effects of stress, lithology and the TOC content on wave velocities using natural shale core samples from the Perth Basin (Altowariqi et al., 2013). The results showed that the velocities increased with the stress levels and decreased as the TOC percentage increased. To further extend our understanding, 40 synthetic shale samples were manufactured under typical geological stress conditions with similar mineral compositions but different TOC percentages resembling those found in the field. Also, this study presents the variations of ultrasonic wave velocities for shale samples with different TOC contents. This approach enables us to estimate the organic material richness of potential gas shale reservoirs using P-wave and density. In this part of the chapter of 17 synthetic samples will be presented, while the rest will be presented in Appendix 4.

5.2.1 Shale composition and microstructure

In general, gas shale usually consists of different types of minerals such as clay, quartz, calcite, dolomite and pyrite, which generally form intricate and perhaps an anisotropic matrix of rocks (Zhu et al., 2011). The composition of synthetic shale samples used in our experiment had the same composition of a typical gas shale formation found in the Perth Basin wells, the Arrowsmith-2 (Well Completion Report- Arrowsmith-2, 2011) and the Redback-2 (Well completion report- Redback-2, 2011). The first part of this study presents the effect of organic matter on the elastic wave velocities on the synthetic shale sample; 12 samples that were manufactured, had the mineral composition of 45% clay mineral (kaolinite), 40% non-clay (quartz), and 15% cement. Organic matter was added to the mixer minerals with different percentages for each sample. The second part of this study presents the effect of clay mineral on the elastic wave velocities in the synthetic shale sample, the minerals composition for five samples applied different clay content and non-clay mineral but with the same TOC content of 5 wt% and 15% cement were manufactured.

5.2.2 Physical properties

The petrophysical properties of the first group of synthetic shale samples are shown in Table 5-3. The clay mineral and non-clay mineral are the same with all the samples, but with different TOC percentages. The bulk density ranges from 2.30 to 2.02 g/cc. The calculated porosity percentages from density data range from 23to 29%. The 12 synthetic shale samples used in this research were selected based on different TOC percentages, enabling a study of the impact of the TOC on the physical properties and ultrasonic velocities. The highest percentage of the TOC was 20 wt%, whereas the lowest percentage was about 0 wt%.

Table 5-3: Physical properties for synthetic shale samples studied.

Sample ID	Mass (g)	Volume (^{CC})	Bulk Density ($^{g}/_{cc}$)	Porosity	TOC (WT %)	Clay (%)	Non Clay (%)	Carbonate (%)
S.S.01	145	63.3	2.30	23.16	0	45	40	15
S.S.02	143	62.7	2.28	23.19	1	45	40	15
S.S.03	141	63.9	2.27	23.25	2	45	40	15
S.S.04	139	63.3	2.26	23.39	3	45	40	15
S.S.05	131	61.0	2.24	24.39	4	45	40	15
S.S.06	107	50.1	2.20	25.83	5	45	40	15
S.S.07	116	54.0	2.17	27.10	7	45	40	15
S.S.08	109	52.0	2.13	27.70	10	45	40	15
S.S.09	130	62.0	2.12	27.75	12	45	40	15
S.S.10	113	55.2	2.09	27.70	15	45	40	15
S.S.11	105	52.1	2.04	28.92	18	45	40	15
S.S.12	117	60.2	2.02	29.23	20	45	40	15

The petrophysical properties of the second group of the synthetic shale samples are shown in Table 5-4. The clay minerals and non-clay minerals are different for each sample, while the TOC and the cement percentages are the same. The bulk density ranges from 2.24 to 2.20 g/cc. The calculated porosity percentages from density data range from 22% to 30%. Five synthetic shale samples used in this part of the research were created based on different clay mineral percentages, enabling a study of the impact of clay minerals on the physical properties and ultrasonic velocities.

The highest percentage of clay minerals was 60 % by weight while, the lowest percentage was about 30% by weight.

Table 5-4: Physical properties for synthetic shale samples

Sample ID	Mass (g)	Volume (^{CC})	Bulk Density ($^{g}/_{cc}$)	Porosity	TOC (WT %)	Clay (%)	Non Clay (%)	Carbonate (%)
S.C.01	105	48.3	2.20	30.5	5	60	20	15
S.C.02	110	50.4	2.21	30.3	5	50	30	15
S.C.03	132	60.2	2.22	29.1	5	45	40	15
S.C.04	105	56.6	2.23	27.8	5	40	40	15
S.C.05	108	50.1	2.24	22.6	5	30	50	15

5.2.3 Results and analysis

5.2.3.1 Elastic properties of synthetic shale based on TOC

The experimental technique was chosen to investigate the variations of P- and S-wave velocities as a function of the TOC content for 12 samples under varying stress levels. Figure 5-16 (A) and (B) show graphs of P- and S-wave velocities versus confining stress for 12 synthetic shale samples. For all samples, the P- and S-wave velocities smoothly increased from 0 to 3,000 psi (0 to 20 MPa) as the stress increased, but there was a relatively sharp increase in the values at higher pressures, 3,000 and 5,000 psi (20 MPa to 34 MPa). Thereafter, further increases in velocities occurred with increasing stress levels.

The Vp/Vs ratio increased slightly from 1.59 to 1.63 by increasing the stress level within the same stress range, as shown in Figure 5-17. A comparison between the ultrasonic waves and the total organic matter percentages suggested that at high TOC, all synthetic shale samples showed a decrease in their P- and S-wave velocities. Figure 5-18 shows graphs of P- and S-wave velocities versus the TOC content for 12 measured samples using the ultrasonic data at both atmospheric and steady pressures of up to 5,000 psi (34 MPa), this is the average effective pressure of our gas shale formation in the Perth Basin at around 3,000m depth of burial (Well completion report- Redback-2, 2011). A comparison between the pressurised and unpressurised samples clearly shows, as can be expected, an increase in the P- and S-

wave velocities. It showed an increase in P-wave velocities of more than 240 m/s, while there was an increase of about 100 m/s for the S-wave velocity. The velocities of the P- and S-waves showed a smooth decrease, as the amount of TOC weight percentage of the synthetic shale increases over the stress level.

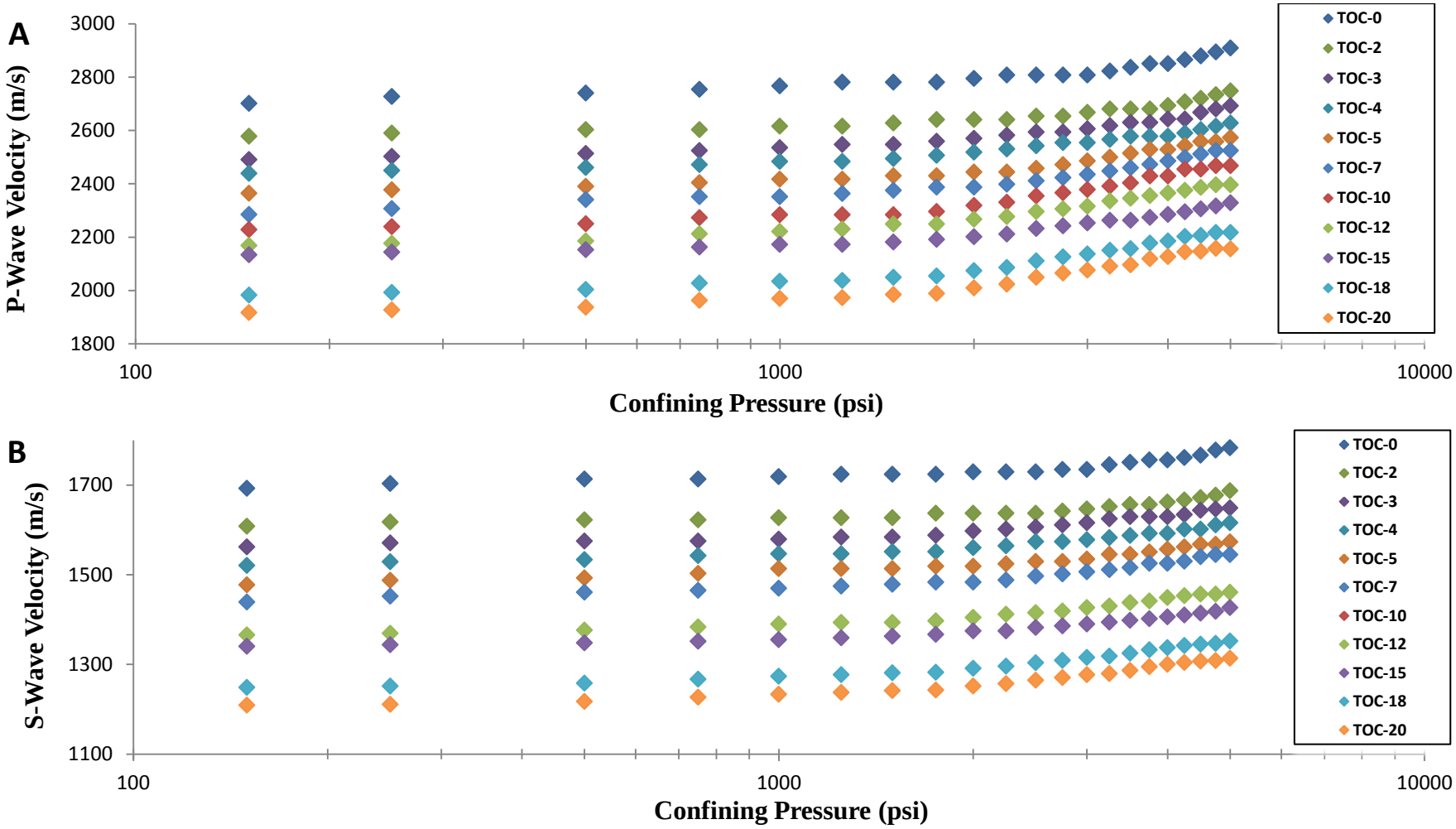

Figure 5-16: (A)Vp and (B) Vs versus stress for a number of synthetic shale cores as the stress increased, the velocities increased.

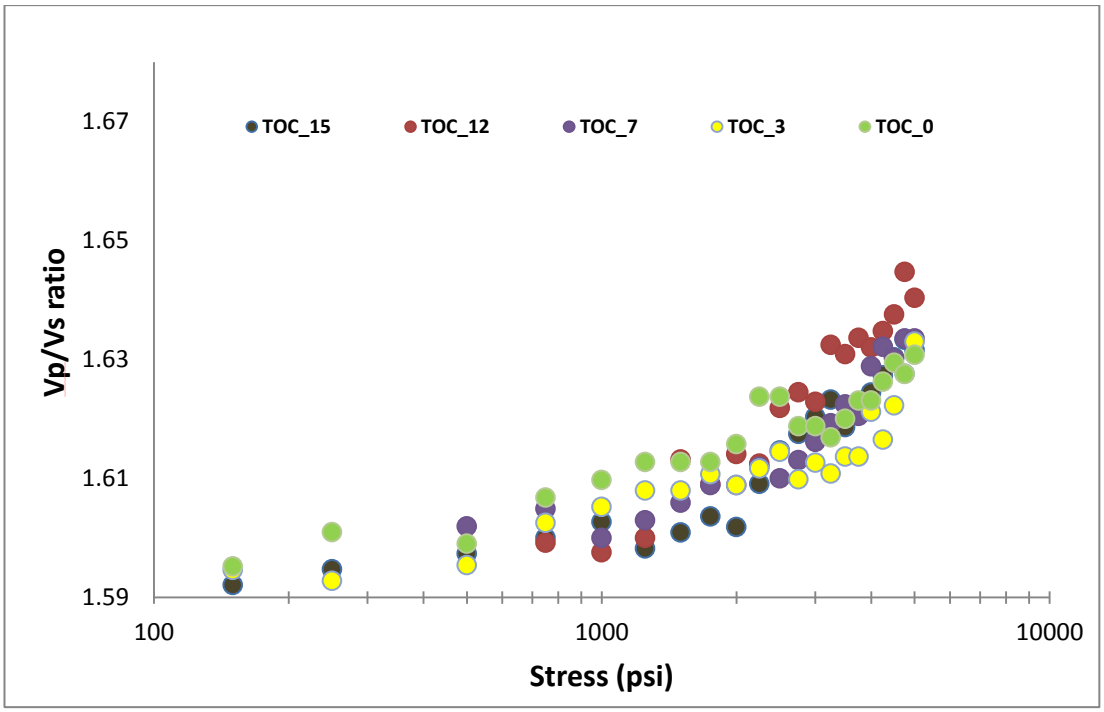

Figure 5-17: Vp/ Vs ratio increased slightly from 1.59 to 1.63 by increasing the stress level.

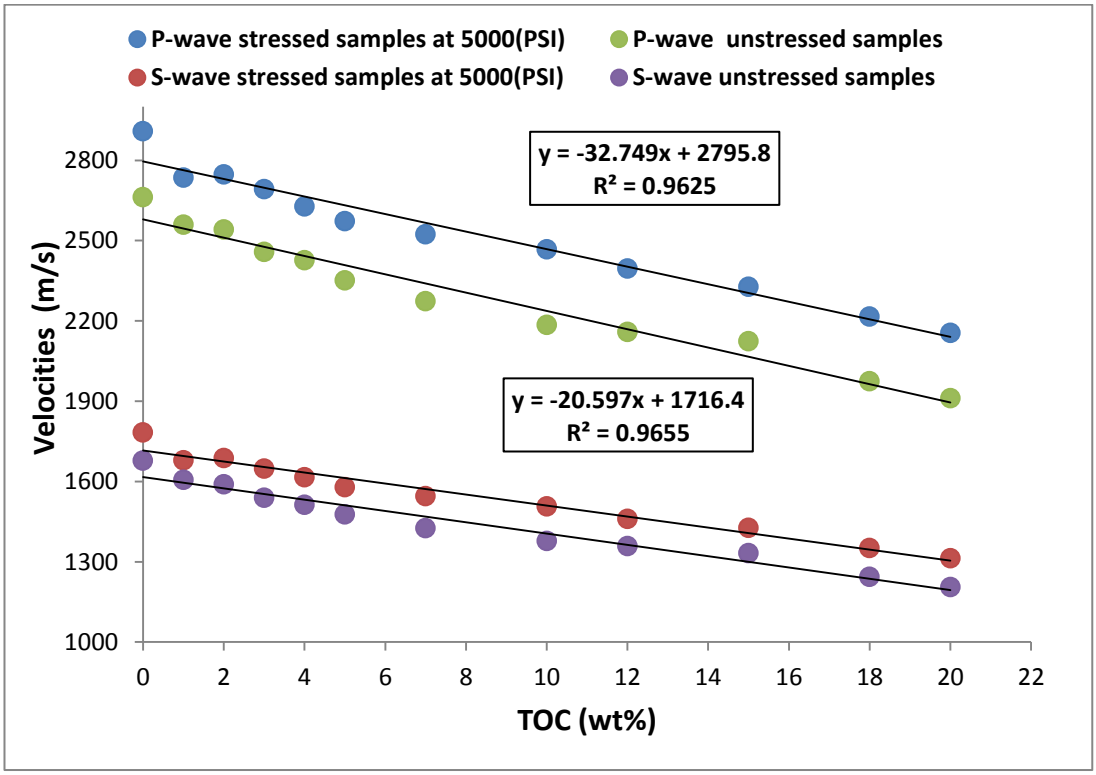

Figure 5-18: Vp and Vs versus TOC% for unpressurised samples and pressurised samples for a number of synthetic shale samples as the TOC percentage increased, the velocities decreased.

The increase in the TOC content corresponds to a linear decrease in density from 2.32 g/cc to 2.05 g/cc as shown in Figure 5-19 (A). Figure 5-19 (B) shows a Vp/ Vs ratio increase with an increase in TOC wt% from 1.61 to 1.64. Also, the porosity of the synthetic shale samples is in the range of 20 to 30% as the TOC percentage changed as shown in Figure 5-19 (C). In addition, Figure 5-19 (D) shows a relationship between the P-wave and the porosity, the P-wave increased with a decrease in the porosity.

Vernik and Mlivaco (2011) showed a similar relationship between the bulk density and the TOC content of cores sampled from organic shale formations worldwide superimposed for different models of 5% and 10% porosity. When the TOC weight percentage increases the density reduces.

The ratio of Vp/ Vs for all samples was approximately stable in the range of 1.6 for unpressurised samples and 1.63 for pressurised samples. The dynamic Poisson's ratios were calculated from these synthetic shale samples of around 0.17 to 0.18 for unpressurised samples, while for pressurised samples, the dynamic Poisson's ratios were calculated around 0.2. In the literature, core measurements have reported that the presence of high TOC content on the organic shale reduces both the velocity and density, while increasing velocity anisotropy. The organic shale also affects the effective Vp/Vs of the rock (Altowairqi et al., 2013; Vernik and Mlivac, 2011). Table 5-5 shows measured ultrasonic wave velocities with different TOC contents, as well as the calculation of the elastic properties of those respective samples without stress applied.

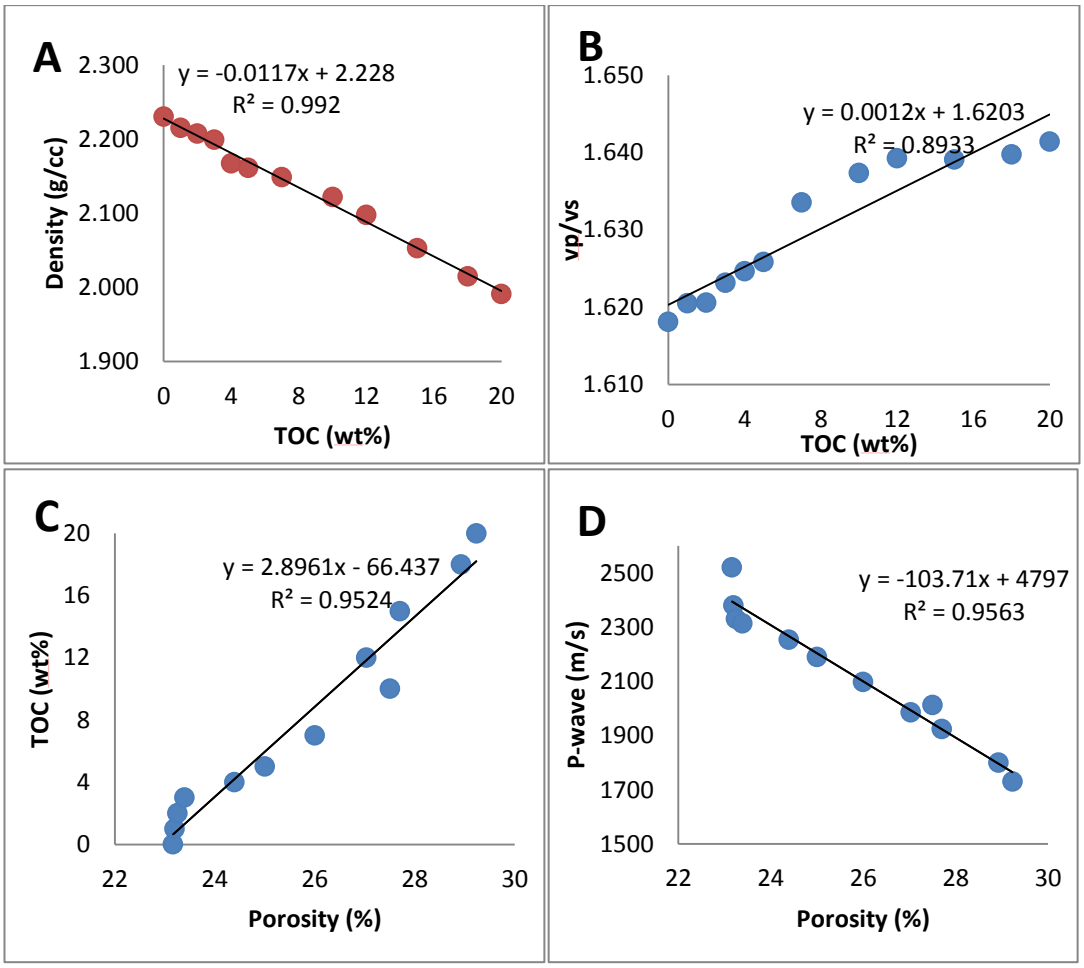

Figure 5-19: (A) The density reduced with an increase in TOC wt% from 2.4 to 2.18 g/cc. (B) Vp/ Vs ratio increased with an increase in TOC wt% from 1.61 to 1.64. (C) The porosity increased as the TOC increased wt% from 0.27 to 0.31. (D) The relationship between P-wave velocity and the porosity.

Table 5-5: Measured ultrasonic wave velocities and elastic properties without stress applied, with different TOC contents.

TOC (wt%)	Vp (m/s)	Vs(h) (m/s)	Vs(v) (m/s)	Vp/Vs	Poisson's ratio	Lame constant λ (GPa)	Shear modulus μ (GPa)	Bulk modulus K (GPa)	P-wave modulus (Gpa)	Young's modulus E (Gpa)
0	2908	1798	1690	1.618	0.191	4.45	7.21	9.26	18.9	17.2
1	2755	1705	1620	1.620	0.192	4.01	6.40	8.28	16.8	15.3
2	2748	1696	1611	1.621	0.193	3.97	6.35	8.20	16.7	15.1
3	2692	1659	1581	1.623	0.194	3.84	6.05	7.87	15.9	14.4
4	2628	1618	1542	1.625	0.195	3.62	5.67	7.40	15.0	13.6
5	2573	1583	1513	1.626	0.196	3.48	5.41	7.09	14.3	12.9
7	2524	1545	1484	1.634	0.200	3.43	5.13	6.85	13.7	12.3
10	2468	1507	1454	1.637	0.203	3.28	4.82	6.49	12.9	11.6
12	2396	1462	1421	1.639	0.204	3.08	4.48	6.07	12.0	10.8
15	2328	1420	1386	1.639	0.204	2.84	4.14	5.60	11.1	9.96
18	2217	1352	1321	1.640	0.204	2.54	3.68	4.99	9.90	8.86
20	2156	1313	1289	1.641	0.205	2.38	3.43	4.67	9.25	8.28

5.2.3.2 Clay type and elastic wave velocities

In addition to the previous samples, five synthetic shale samples with different clay contents but the same TOC content were manufactured to study the impact of the clay mineral (kaolinite) content on the ultrasonic wave with varying stress levels. The velocities of P- and S-waves show a smooth increase as the stress level increased from 0 psi to 5,000 psi (0 to 34 MPa). Figures 5-20 (A) and (B) shows graphs of P- and S-wave velocities versus confining stress for four synthetic samples. For all samples, P- as well as S-wave velocities increase as the stress increases and there is a significant increase in the velocity values between 3,000 – 5,000 psi (20 to 34 MPa) where the compaction begins for each sample. The increase in the velocities started to be smooth during the stress changes. The Vp/ Vs ratio increased slightly from 1.59 to 1.63 for all the samples with increasing stress level. A comparison between the ultrasonic waves and the clay mineral percentages suggested that when increasing the percentage of clay minerals, all synthetic samples showed a decrease in their P- and S-wave velocities. A comparison between the pressurised samples and unpressurised

samples suggests that at a steady pressure, all the samples show an increase in their P- and S-wave velocities as shown in Figures 5-21 (A) and (B). The samples containing a high percentage of clay minerals show an increase in P-wave of more than 150 m/sand 80 m/s for S-wave velocity. Indeed, the sample containing a lesser percentage of clay minerals was more compacted than the samples containing high percentages of clay minerals, which had an increase in P-wave velocity of more than 300 m/s and 180 m/s for S-wave velocity.

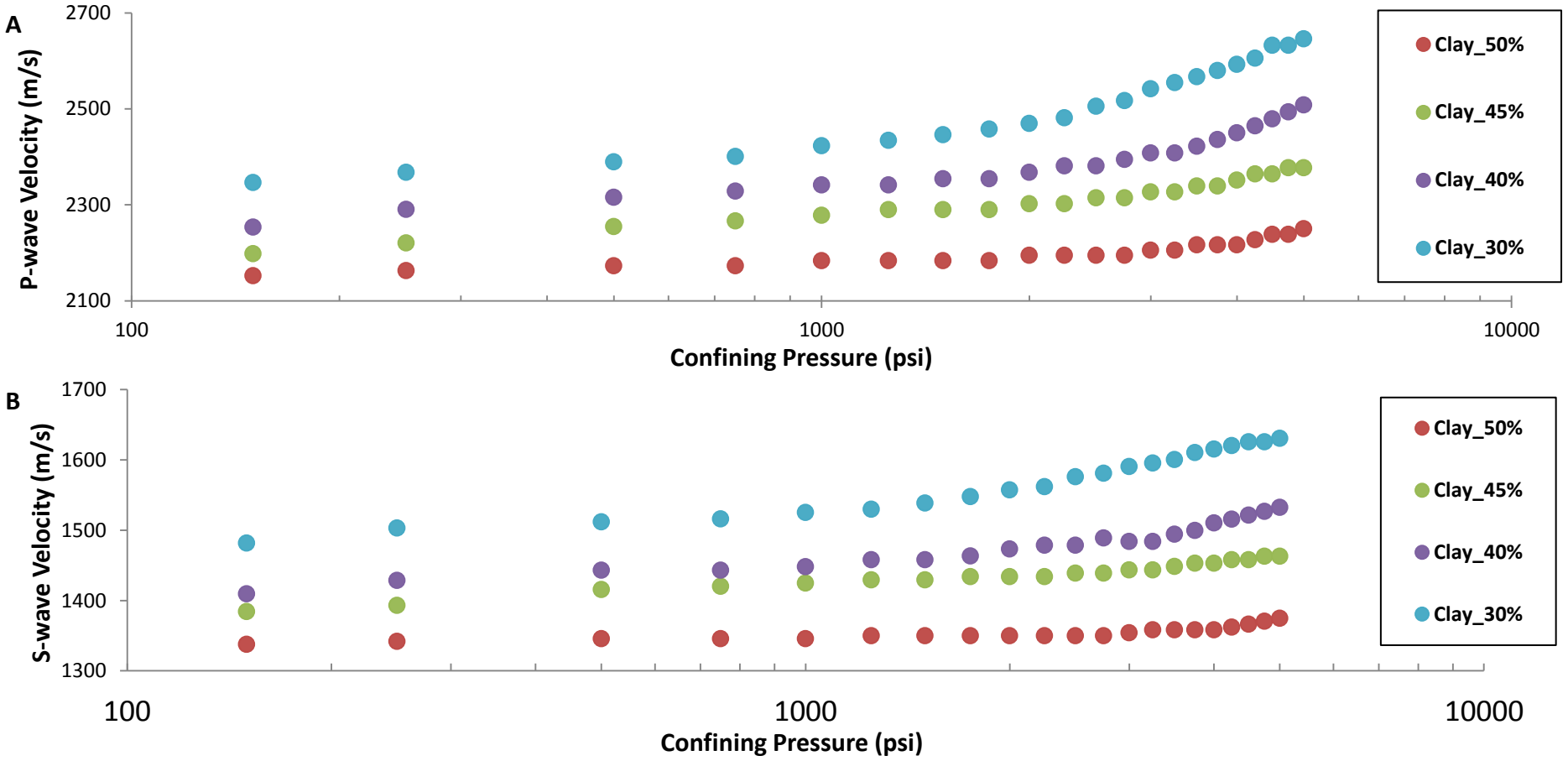

Figure 5-20: Vp (A) and Vs (B) versus stress for a number of synthetic shale cores- as the stress increased, the velocities increased.

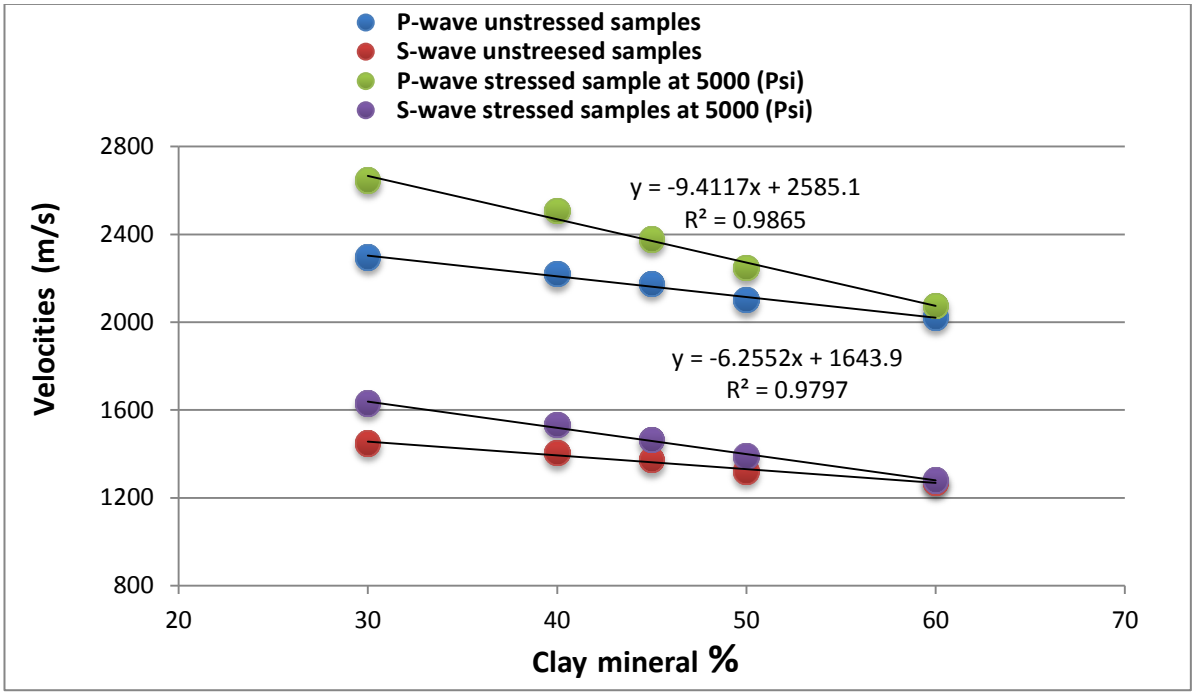

Figure 5-21: Vp and Vs versus Clay mineral for (A) unpressurised samples and (B) pressurised samples for synthetic shale samples- as the clay mineral percentage increased, the velocities decreased.

In Figure 5-22(A), the increase in the clay mineral correspond to a linear decrease in density from 2.3 to 2.17 g/cc. Figure 5-22 (B) shows that the porosity of the synthetic shale samples was in the range of 20 to 30 %, as the clay mineral percentage changed. Figure 5-22 (C) shows a relationship between the P-wave velocity and the porosity; the velocity increased with a decrease in the porosity. Figure 5-22 (D) shows a relationship between the density and porosity, the porosity, of the samples decreased as the density of the rock increased. The ratio of Vp/ Vs increased for all samples from approximately 1.58 to 1.6 over the 30 to 60% for the clay mineral percentages for unpressurised samples, while for pressurised samples, the ratio of Vp/ Vs slightly increased from 1.61 to 1.63 over the 30 to 60% of the clay mineral percentages. The dynamic Poisson's Ratios calculated from these synthetic shale samples decreased from approximately 0.20 to 0.165 as the clay mineral percentage increased from 30% to 60%.

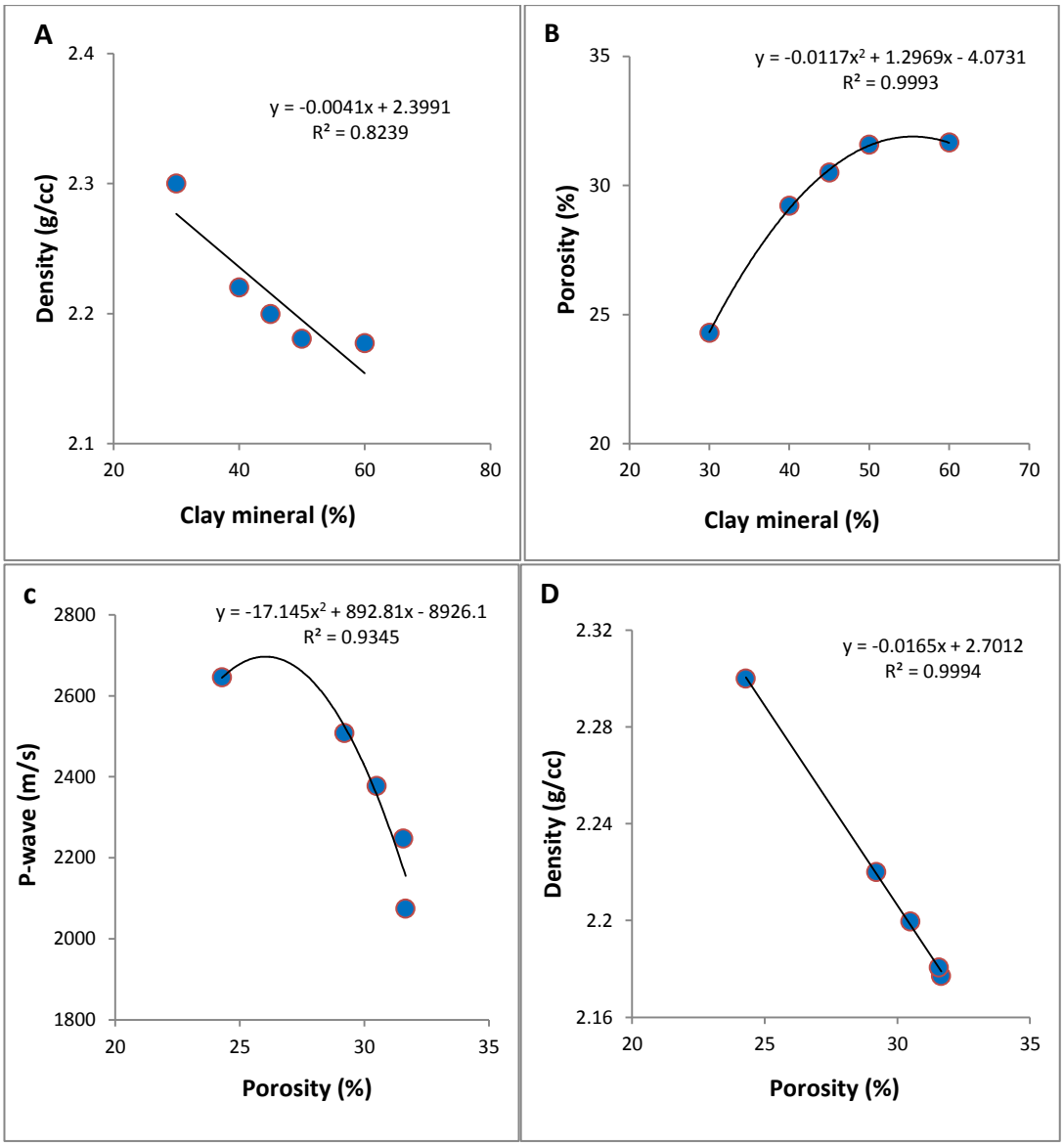

Figure 5-22: (A) the density reduced with an increase in clay mineral (%) from 2.3 to 2.17 (g/cc). (B) The porosity increased as the clay mineral increased from 22 to 32%. (C) The relationship between P-wave velocity and porosity. (D) The relationship between density and porosity.

5.2.4 Discussions (Practical application to field data)

There are several fundamental quantitative methods for the prediction of the TOC contents from well-logs and core samples, such as using regression equations of core TOC versus acoustic impedance (Altowairqi et al., 2013), or using sonic and resistivity log data (Passey et al., 1990). The Passey method was the most common approach used to predict TOC in gas shale formations, using the DT and resistivity logs (Passey et al., 1990). The application of this method to other shale formations requires having similar clays and conductive minerals such as pyrite in the

calibration intervals, as well as available LOM data to predict TOC (Sondergeld et al., 2010).

The results of the study reported here demonstrate that synthetic shale rocks having controlled levels of TOC, clay minerals and non-clay minerals are suitable for testing some of the fundamental geophysical relationships between physical properties in a controlled and systematic manner, without the scatter that is inherent in measurements with natural gas shale rock.

This study presents equations that enable us to estimate shale TOC content using compressional and shear wave velocities. The equations are listed in Table 5-6. The equations have been tested using real data from shale formations of the Perth Basin from the Redback-2 well.

Table 5-6: Table of geophysical relationships at depth of 3000 m.

Geophysical Relationships	Equations
Vp versus TOC%	Vp = 2411.9m/s - 35.08*TOC%
Vs versus TOC%	Vs = 1530.2m.s - 18.92*TOC%
Vp versus clay mineral content	Vp = 2772.2m/s - 10.93*TOC%
Vs versus clay mineral content	Vs = 2120.9m.s - 14.37*TOC%
Vp/Vs versus TOC%	Vp/Vs = 1.58 - 0.0046*TOC%
Vp/Vs versus clay mineral content	Vp/Vs = 1.202 + 0.0079*TOC%
Density versus TOC%	D = 2.29g/cc – (0.0185*TOC%) + (0.0002*TOC%^2)
Density versus clay mineral content	D = 2.75g/cc – (0.0206*TOC%) + (0.0002*TOC%^2)

Based on our equations from the synthetic shale samples for prediction of the P-and S-wave velocities and bulk density, we calculated P-wave and bulk density, then we compared the real core samples data from the Redback-2 well and synthetic shale samples (Figure 5-23). The difference of the P-wave velocity between real and synthetic samples is obvious. In fact, the 40% velocity difference between synthetic and the natural samples can be attributed to the compactions effect. As a result, the bulk densities of the synthetic shale samples are much less than the shale sample from the Redback-2. As such, it was necessary to apply a factor to the equations to make the equations applicable to a natural shale formation.

The factor used for the P-wave was estimated by calculating the average P-wave velocity using the natural shale formation values from the data base in the Perth Basin and the average P- wave velocity of the synthetic shale samples, and then calculating the difference between them. The same process was applied to estimate the density factor. Then we used multi-regression analysis to develop the following equation (5-1) that enabled us to predict the TOC content from P-wave velocity and bulk density:

$$TOC\ (\%) = 17.46 - \left(2.410 * Vp\left(\frac{km}{s}\right)\right) - (2.11 * bulk\ density(g/cc)) \qquad \text{Equation 5-1}$$

Moreover, TOC variations were computed from the sonic and resistivity logs by using the ΔlogR method (Passey et al., 1990) for the same well, to compare between the TOC for our equation and Passey's and Schmoker's methods. Figure 5-24 compares these two methods with measured TOC from core samples. It is obvious that, the TOC obtained from our method is close to the measured TOC when compared with Passey's method. The error percentage of ours compared to the real data is less than 8%.

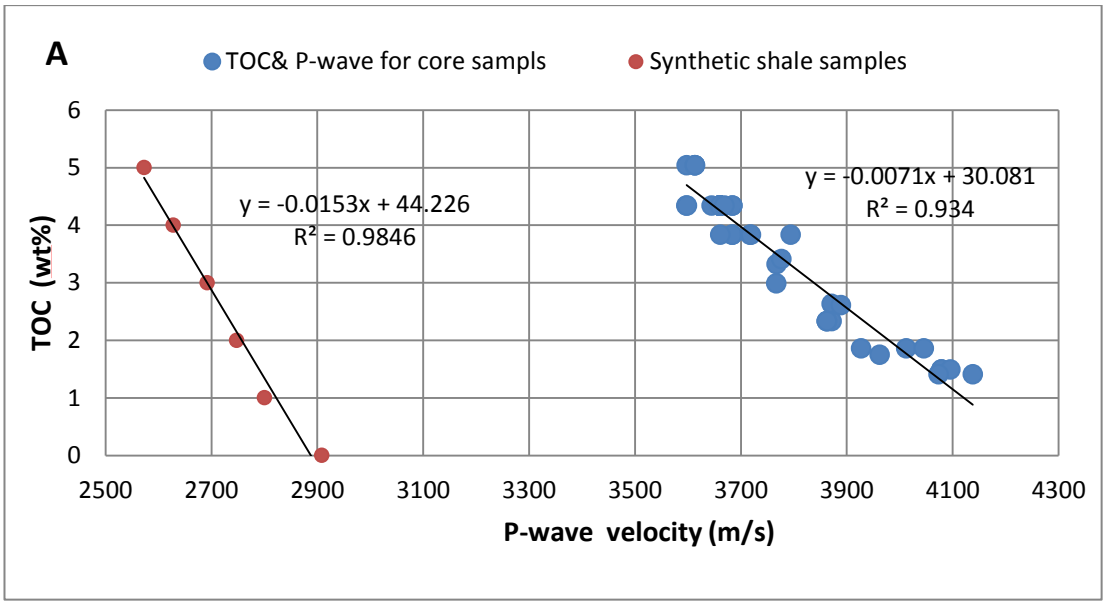

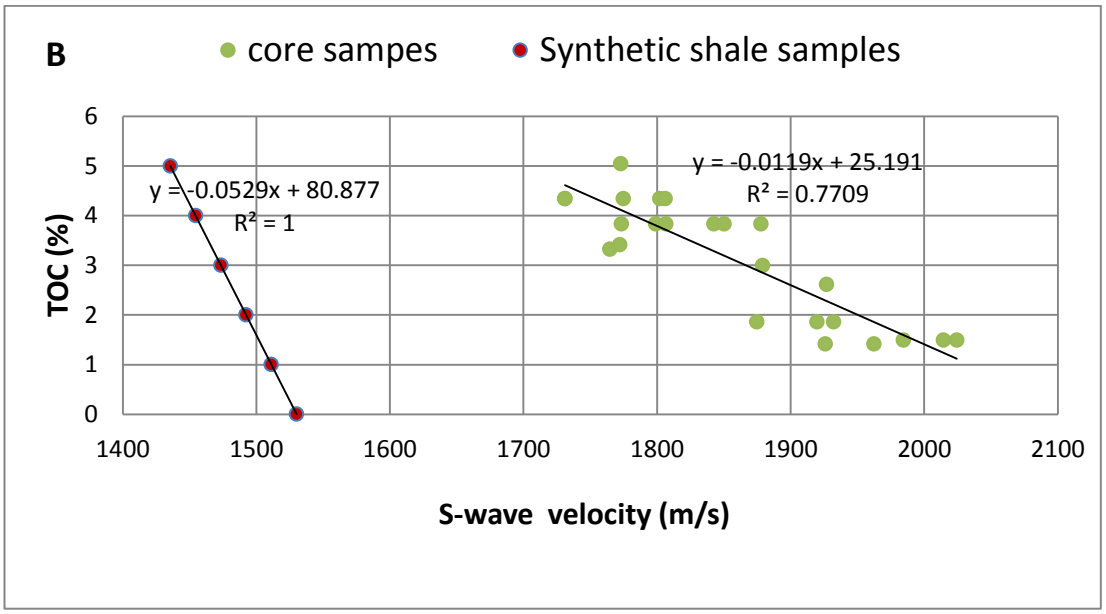

Figure 5-23: Relationship between TOC (wt%) and P-wave velocity (A) and TOC (wt%) and S-wave velocity applied to both synthetic shale samples and real core samples from the shale formation.

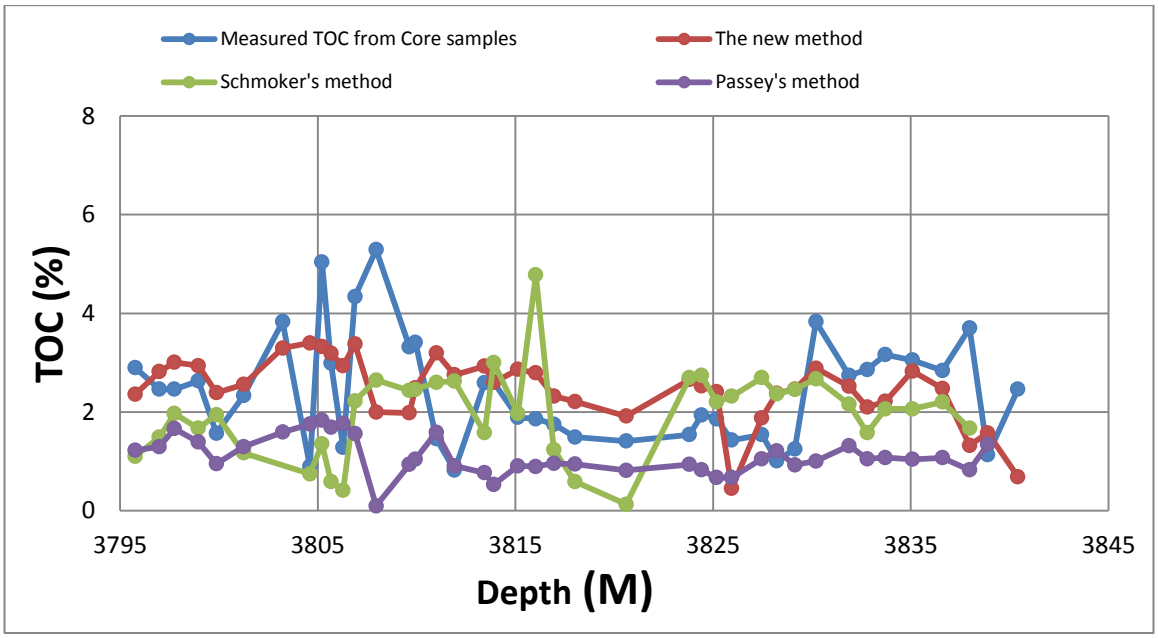

Figure 5-24: A comparison between Passey's and Schmoker's methods and our equation to estimate the TOC content and the measured TOC from the core samples. The TOC obtained from our equation shows a good agreement with the measured TOC.

Chapter 6. The AVO response of organic gas shale based on laboratory testing

6.1 Introduction

AVO measures the variations in the seismic reflection amplitude with changes in the distance between the source and the receiver and indicates differences in lithologies and fluid contents. This is based on the relationship between the reflection coefficient and the angle of incidence. AVO response analysis is important and can be used to predict the change in reservoir properties as well as help identify the optimal locations and distribution of hydrocarbon resources (Goodway et al., 2010). However, many factors can significantly affect the AVO analysis in shales, such as the TOC contents and mineral compositions, which affect the rock physics of shales, include density, velocity and Passion's ratio (Zhu et al., 2011). This study helps to define the AVO response of gas shale due to the changes in TOC contents and mineral compositions.

In general, the P- and S-wave velocities, as well as density decrease in organic shales with high TOC contents, due to the decrease in the reflection coefficient (Vernik and Nur 1992; Vernik and Liu 1997). The reflection coefficient describes how much energy is reflected and these changes are due to different media and reflection angles. At a normal incidence, a zero degree offset, the reflection coefficient values can range from -1 to 1; -1 means that nearly all of the energy was reflected and not transmitted. Non-normal incidence becomes slightly more complicated. The ratio of amplitudes depends on other factors, including the S-wave velocity and the incident angle.

It is important to understand that every shale formation can be different and some "sweet spots" may actually exhibit a decreasing AVO. It is important to know the background trend of the rock and locate data that differs from this trend. The objective is to measure the AVO effect on organic and inorganic shale using well-log and seismic data and then compare the results to experimental studies by measuring the AVO from different synthetic shale samples. We have presented some studies and results of AVO modelling and analysis in Chapter 4. The study used two

different AVO modelling experiments which were conducted using the amplitude/ incident angle crossplot methods from the Redback-2 well in the Perth Basin. The first model contains an organic shale rock with 5 wt% of TOC. In the second log model, the rich organic content layer is removed, making that layer a non-source shale rock (TOC is about 0 wt %). This chapter will extend the AVO response of testing the organic synthetic shale sample and inorganic shale sample by measuring the AVO rays in the laboratory.

6.2 Creation of synthetic block samples

Several steps and equipment were involved in creating a single sample. Each synthetic sample was formed under high pressure using a hydraulic compressor, to produce a cubic block sample (Figure 6-1). A hydraulic compressor contains the control system and digital displays, which can help to control a force at a constant rate or at constant pressure. Almost 7000 psi of hydraulic pressure is applied using an oil-driven hydraulic pump.

The first stage in preparing the samples was to measure and mix the appropriate amount of fine-powdered mineral material using a mixer machine for several hours until it becomes consistent. The mix was composed of 45% clay minerals (kaolinite), 40% non-clay minerals (25% quartz and 15% feldspar) and 15% cement with some water. Organic matter was then added to the mixed minerals in different percentages for each sample, and was distributed in the mixed minerals. Petrographic analysis result for the organic material indicated a mixture of vitrinite (71%) and semi-fusinte (13%) as well as some other minor components. The density of the organic material was about 1.4 g/cc. The composition of the synthetic shale samples used in the experiment had the same composition as a typical gas shale formation found in the Perth Basin Redback-2 well (Well Completion Report- Redback-2, 2011). The AVO modelling and analysis was then applied to the same well, to understand the difference between the natural shale and the synthetic shale samples.

The next step was to add saline water to the mixed minerals until they become clay-like and press and compact the mix into a steel frame (20 cm x 20 cm). The frame, with the material inside was placed between several 19.5 cm x 19.5 cm steel blocks, along with a hydraulic pressure jack, which was then all placed under the hydraulic compressor. This machine stabilises the blocks and jack during the compaction

process. The pressure was applied at a constant flow rate of hydraulic oil, (0.5 ml/min) until it reached 4,500 psi. Once this pressure was reached, the sample was left at this constant pressure overnight to ensure it was fully compacted. In the last stage, the sample was removed from the steel frame and the weight and volumes were measured. The bulk density and porosity for both sample compositions were in the range of 2.2 to 2.4 g/cc and 16to 20% respectively. The thickness of the samples was around 4 to 6 cm.

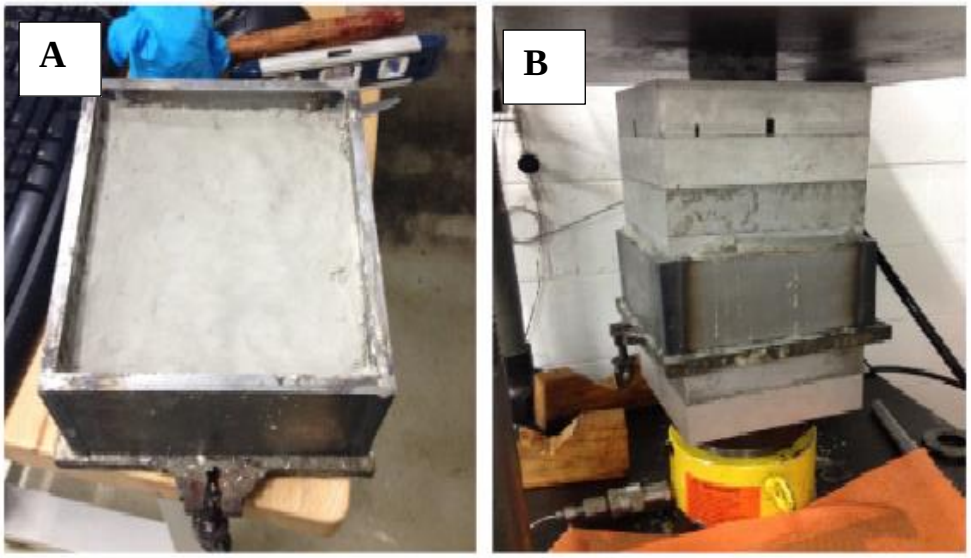

Figure 6-1: (A) Shows the material in steel frame after combining with water. (B) Compaction of material using the hydraulic pressure jack in yellow at the bottom of the steel.

6.3 AVO set-up

The first step was to sand and smooth the synthetic block so that any minor fractures in the samples were removed, the sides were level so that the block was of the required thickness. It is difficult to see if there are any internal fractures in the sample so transducers were moved around the top and the base surface of the block to test which area shows the best signal; the goal was to obtain a clean, first arrival P-wave. The second step was to place the transducers in several holes that have been carved out of a steel plate, as shown in Figure 6-2 (A). This allows the transducers to be arranged in many different patterns. The sample was then placed on the top of the steel block, as shown in Figure 6-2 (B), ensuring that there is good surface contact with the transducers. One source and seven receivers were placed into the holes in

the steel block. A piece of plastic was put underneath the source transducer at an angle of 45 degrees towards the receivers, so it rested in a tilted position and directed the source energy towards the receivers. This method was found to improve the signal.

The next step was to use the True Triaxial Stress Cell (TTSC) for testing the samples. This allows both axial and confining pressures to be applied to the sample, as seen in Figure 6-2 (D) and (C). The TTSC is manufactured for geomechanics testing and simulations. There are four plates that apply confining pressures on the sides of the samples and a hydraulic jack located on top, which applies axial pressures. The four plates are spread 30 cm apart and the samples are around 20 cm in length. Spacers were constructed to fill in the gaps between the sides of the sample and the plates. Once the sample, steel blocks and the transducers were correctly set up, confining and axial pressure were applied equally. The sample was kept under isotropic stress to avoid any fracturing and was tested while both the axial and confining pressures were increased equally, from 0 to 2,000 psi. The highset pressure used in this test is 2,000 psi due the ability and safety reasons of the (TTSC). At each pressure point, 14 volts of energy from the source transducers was directed into the sample, which was then received by the seven receivers. Ten traces were recorded and stacked for each receiver at each pressure. Once the maximum stress was reached, the pressure was released and the first dry media test was complete. The same test process was repeated three times using different fluid medias. For the second test, a thin piece of mesh was inserted between the sample and the top steel plate; the holes in the mesh represented an air or gas layer in the media. In the third and fourth test, the mesh was covered with water and then oil. The objective was to understand the change in amplitude when different fluids were set on the reflection boundary of the sample. Two synthetic shale samples with the same compositions but different TOC content (one with 0% of TOC and the other with 5% of TOC) were tested using different fluids media (dry, water, gas and oil) to study the impact on the TOC.

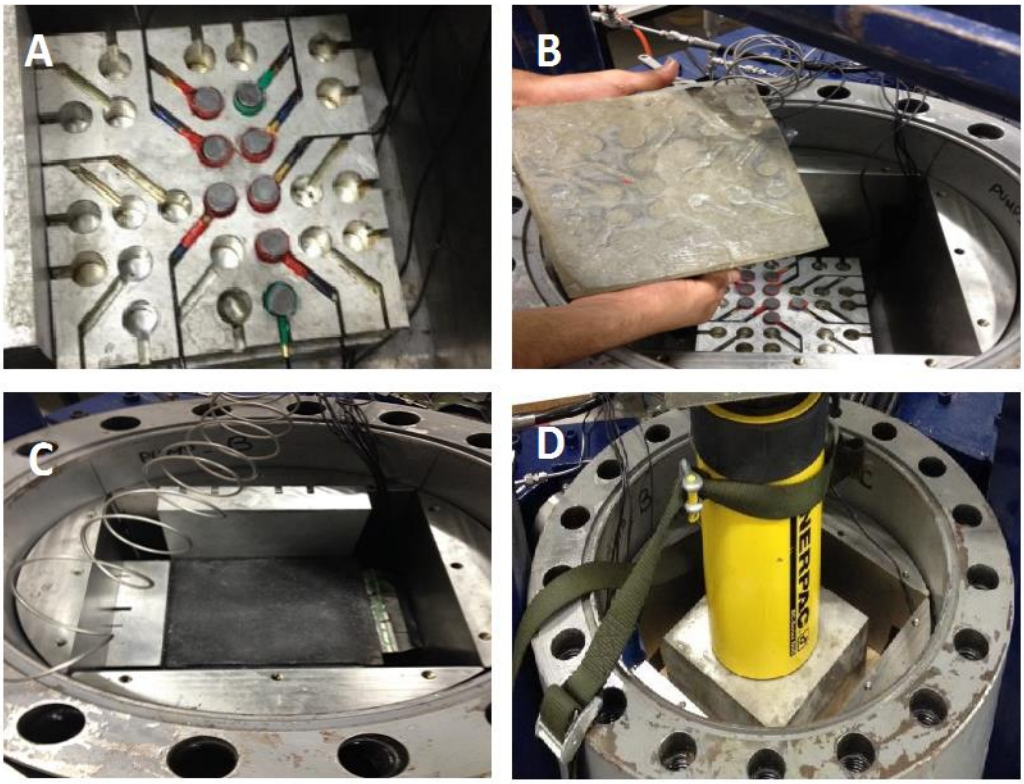

Figure 6-2: (A) An example of the receiver arrangement in the lower steel block. (B) The synthetic shale sample before the test. (C) The sample located into the TTSC, using the steel spacers to fill the gap between the sample and the walls of the TTSC. (D) The TTSC ready for testing.

6.4 Results and analysis

6.4.1 Steel measurement

Before the synthetic samples test starts, it is important to understand the AVO measurement and analysis on the steel block as a guide. The source energy with the steel sample is greater than the synthetic samples because the steel medium is homogeneous, which allows us to better understand the AVO analysis. A steel block was placed in the same position as the shale sample block in this experiment. One source transmitter and eight receivers were placed into the holes of the steel block, as shown in Figure 6-3. The steel sample was tested at different pressure points, from 0 to 3000 psi, using different fluids media (Dry, water, gas and oil). At each pressure point, one source transducer was transmitted into the sample and received by the eight receivers.

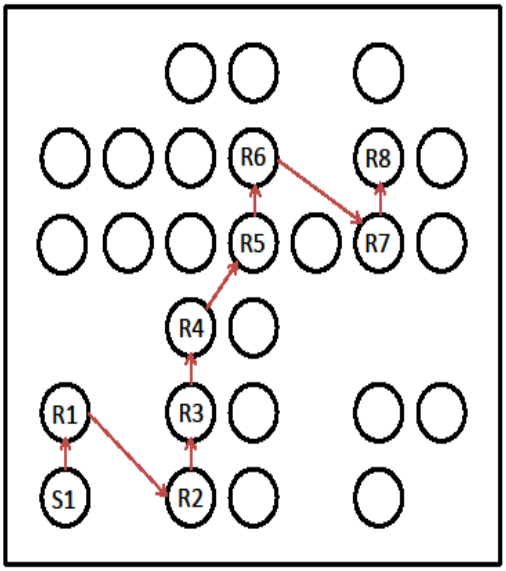

	R1	R2	R3	R4	R5	R6	R7	R8
offset	30.4	52.4	60.56	80.26	116.43	144.74	156.61	178.67
angle	8.64	14.68	16.85	21.87	30.2	35.89	38.1	41.78

Figure 6-3: An example of source and receivers arrangement for the steel test.

The objective was to observe the change in the amplitude with pressure when different fluid layers exist. In general the trend found in this experiment is that the amplitude values increased smoothly as the pressure increased and then decreased slightly when higher pressures are reached for each receiver (Figure 6-4). For example, during the dry test the amplitude drops when the pressure reaches between 400 and 500 psi depending on the receiver location. Moreover, during the water and oil tests, the amplitude decreases when the pressure reaches between 2,000 to 3,000 psi. However, in the gas test, the amplitude in some receivers are stable while others show a decrease when the pressure reaches 3,200 psi. In receiver number eight, the amplitude increases smoothly as the pressure increases for all the fluid media types except for the dry sample, where it shows a decrease with increasing pressure. There are amplitude differences when comparing each fluid type. The dry test shows a lower amplitude as compared to than the water, oil and gas layer tests.

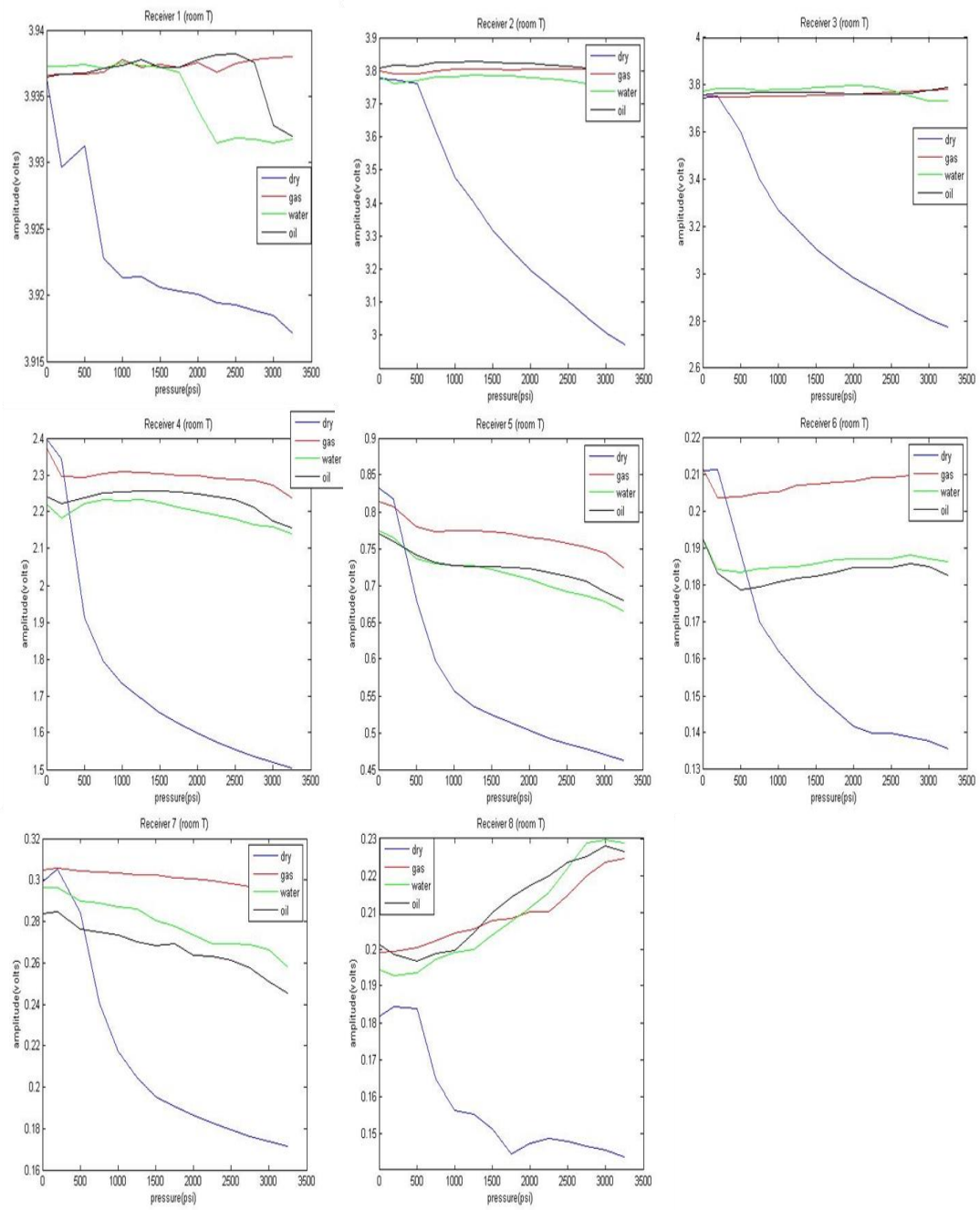

Figure 6-4: Amplitude versus pressure for each receiver using different fluids media.

Figure 6-5 shows the amplitude versus offset measured with different pressure points (0, 500, 1000, 1500, 2500 and 3000 psi). The amplitude drops as the offset/angle is increased. Among the three fluids, gas normally has the highest amplitude, followed by oil and then water. When inserting a fluid layer at the reflection boundary, the medium is changed. This means that the wave of energy moving through the material will hit an area of slightly different velocity. The larger the difference in elastic property values between two media across an interface, the greater the ratio of the

reflected wave to the incident wave. A large positive or negative reflection coefficient coincides with a greater amplitude. With the addition of a non-steel medium, the acoustic impedance changes and the amplitude values visibly increase.

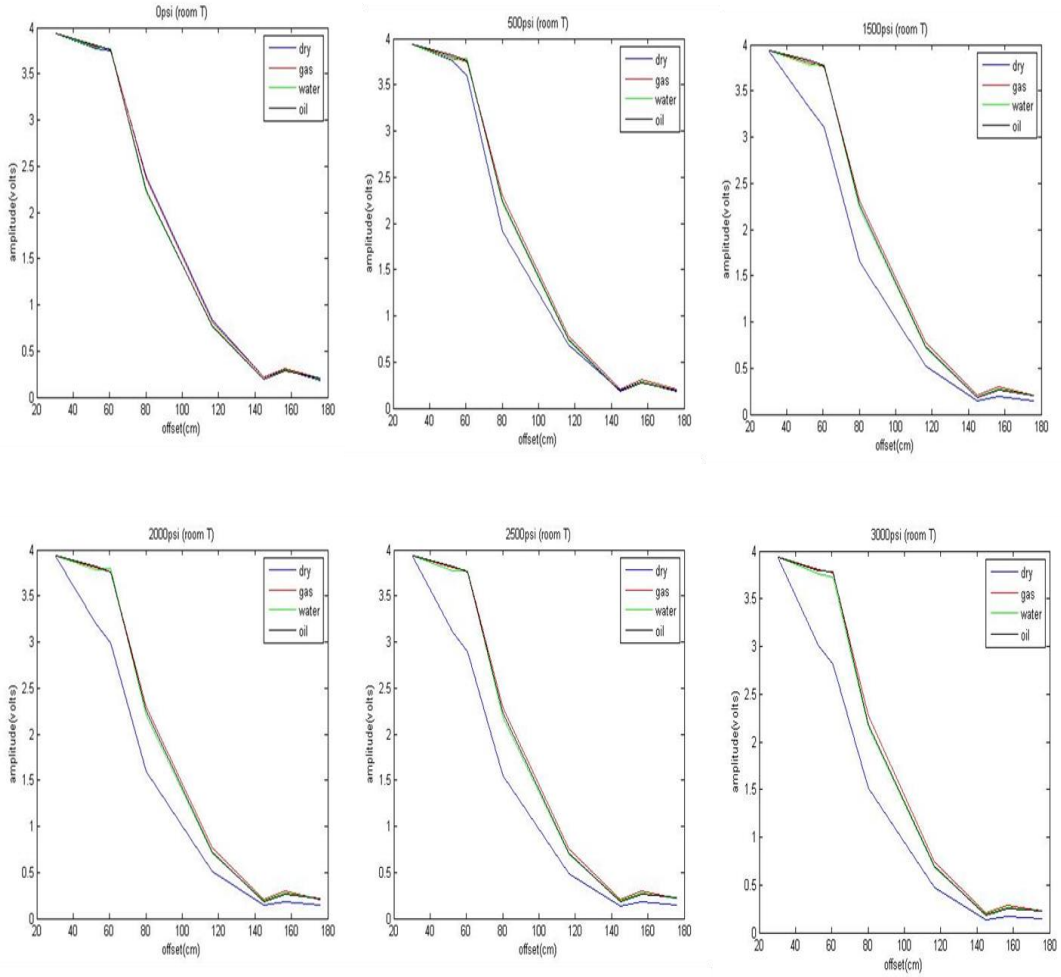

Figure 6-5: The amplitude versus offset measured at different pressure points.

6.4.2 Inorganic shale measurement

The results from both the synthetic tests were similar, the amplitude decreases as the offset increases. The dry test should show lower amplitude values than the fluid test and the amplitude should increase overall with an increasing pressure. At normal atmospheric conditions, the velocity of the steel was 5,000 m/s and the shale block, with 0 wt% TOC, was 2,500 m/s. The bulk density of shale block was 2.4 g/cc. As the pressure increased, the shale block compacted and the velocities increased to 2,800 m/s under a pressure of 5,000 psi—as we have tested the velocities with core

samples of the same composition in Chapter 5 (Altowairqi et al., 2015 (A)). One source transmitter and seven receivers were placed into the holes of the inorganic block, as shown in Figure 6-6. As pressure increases, the acoustic impedance of the shale also increases. The reflection coefficient at the shale-steel boundary will decrease, thus, presenting a decrease in amplitude. Comparing the different fluid layers showed similar results to the previous test; the dry test should have lower amplitude values than in the water, oil and gas test. The data collected for the first block of shale included the amplitudes and frequencies recorded from seven receivers at axial and confining stresses (from 150 to 2,000 psi). The average maximum amplitudes were plotted against the pressure for each receiver. The plots of amplitudes versus offset and angle for each pressure are also made (Figure 6-7). The amplitude slightly decreased with pressure for all fluid types for the first block with 0 wt% TOC. The far offset receiver showed low values of amplitude with pressure, while in the near offset, the amplitude was higher when compared to the far offset. The dry curve had the lowest amplitude values, followed by water and then oil and gas.

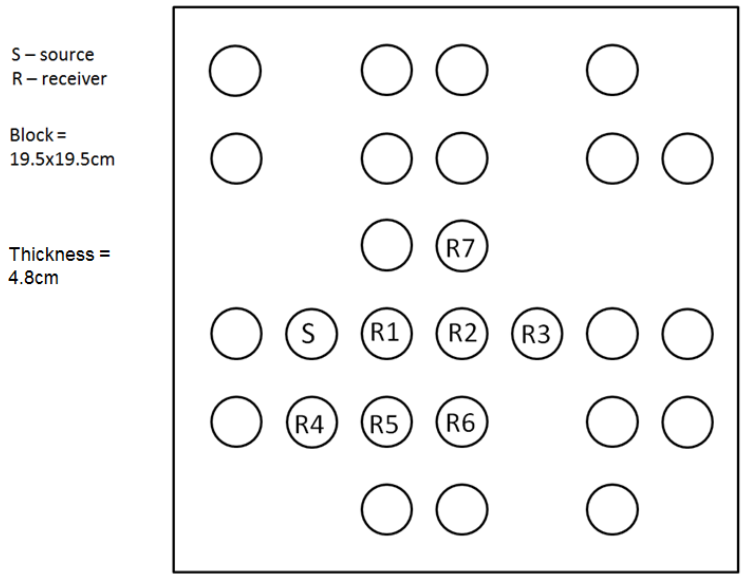

	R1	R2	R3	R4	R5	R6	R7
offset (cm)	2.62	5.24	7.87	3.04	4.01	6.06	6.06
angle (deg)	15	29	40	18	23	32	32

Figure 6-6: Source and receiver arrangements for the inorganic shale experiment.

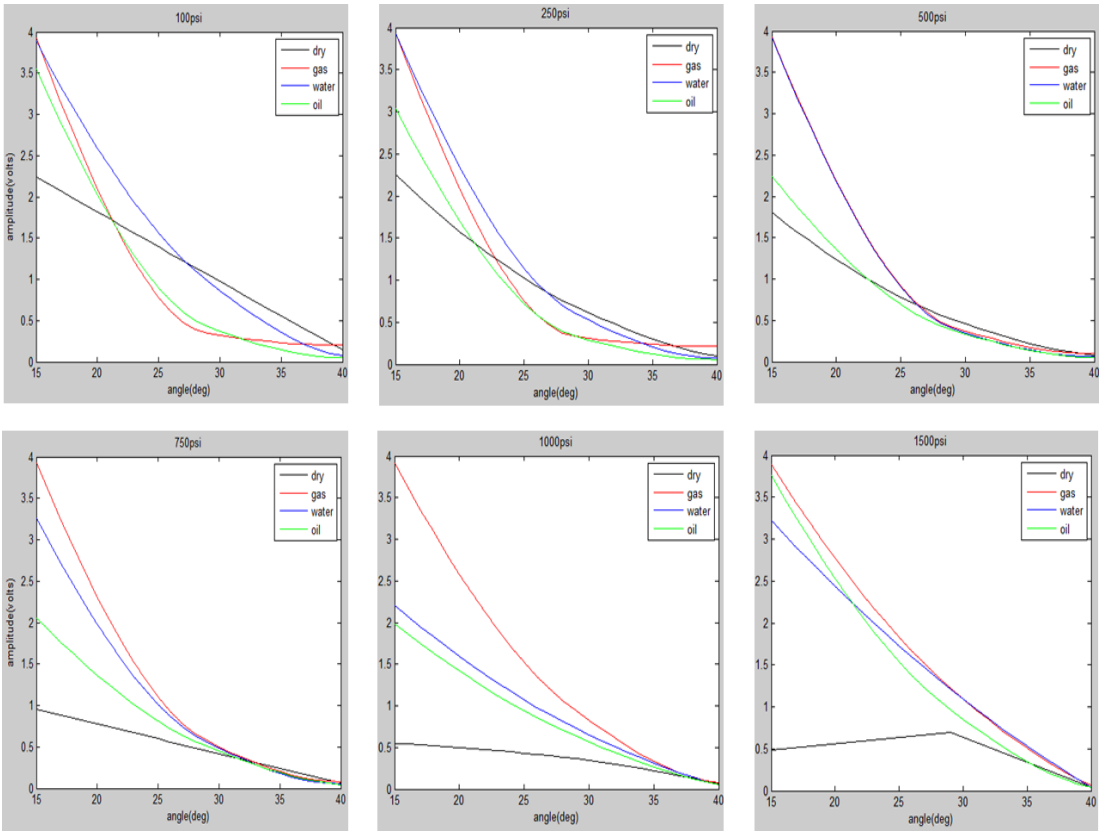

Figure 6-7: Amplitude versus angle measured at different pressure points and with different fluids media for the inorganic shale sample.

6.4.3 Organic shale measurement

The second test was conducted using the same method but the synthetic shale block was composed of 5 wt% TOC and was also slightly thicker. At normal atmospheric conditions, the velocity of the shale block, with 5 wt% TOC, was 2,300 m/s. The density was 2.2 g/cc. As the pressure increased, the shale block compacted and the velocities increased to 2,600 m/s under a pressure of 5,000 psi (Altowairqi et al., 2014). One source transmitter and seven receivers were placed into the holes of the organic block, as shown in Figure 6-8. Due to the increased thickness of this sample, some amplitude adjustments needed to be fixed, before the analysis could be carried out. Although the same incident angles are able to be plotted for both synthetic blocks, the travel path is longer for the second block and absorption becomes an issue. Absorption is when a wave eventually disappears into a medium, as the elastic energy that is associated with the wave is gradually absorbed by that material. Therefore, the amplitude values would be larger for the second test if the sample had a thickness equal to that of the first test sample. The difference in travel path distances needed to be determined for both synthetic blocks at every receiver to correct the amplitude values. Based on the percentage difference, a multiplication factor was assigned to each receiver's amplitude value. For instance, the values from receiver 1 for the second sample are multiplied by 1.1897. This increases the amplitudes by 19% and displays roughly what the amplitudes should be if the second sample is the same thickness as the first. To determine a more exact multiplication factor, the absorption coefficient of the medium needs to be calculated (Mitchell, 2013). In the interest of time, the "back of the envelope" calculation was used to give a general comparison of the two blocks. Table 6-1 listed the travel path distances along with the calculated multiplication factors. The fluid curve trends prove to be the same as in the first sample; the dry sample has consistently lower amplitude values than the gas, water and oil samples. The amplitude versus pressure trend is different though. In general, the amplitudes increase with pressure and the amplitude values themselves are higher than in the inorganic sample at higher pressures. The organic content impacts on the density and velocities for the organic sample, therefore increasing the amplitude values. Figure 6-9 shows the amplitude versus offset for the organic shale sample.

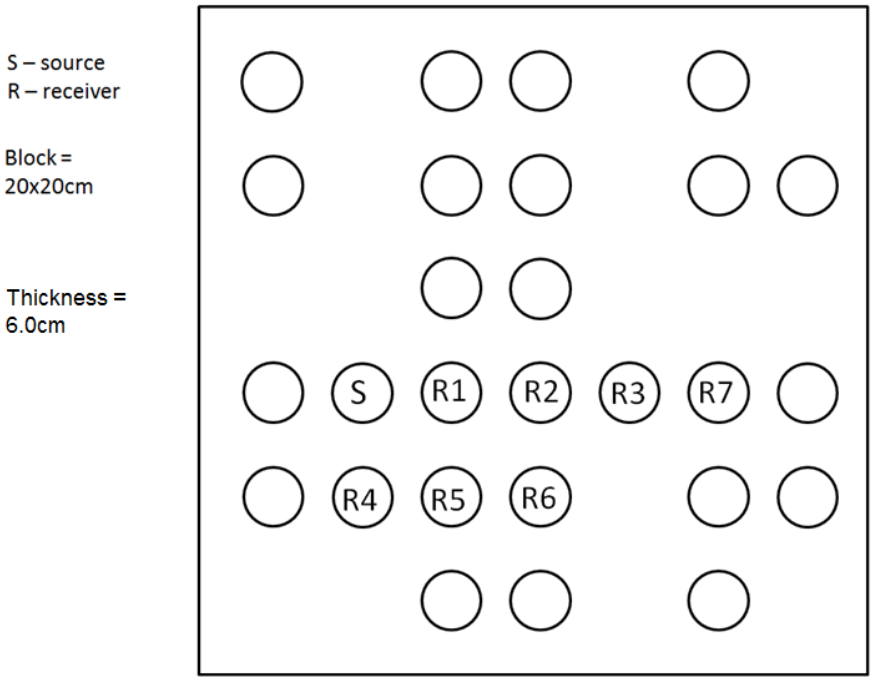

	R1	R2	R3	R4	R5	R6	R7
offset (cm)	2.62	5.24	7.87	3.04	4.01	6.06	10.5
angle (deg)	12	24	33	14	18	27	41

Figure 6-8: One source transmitter and seven receivers were placed into the holes of the inorganic block.

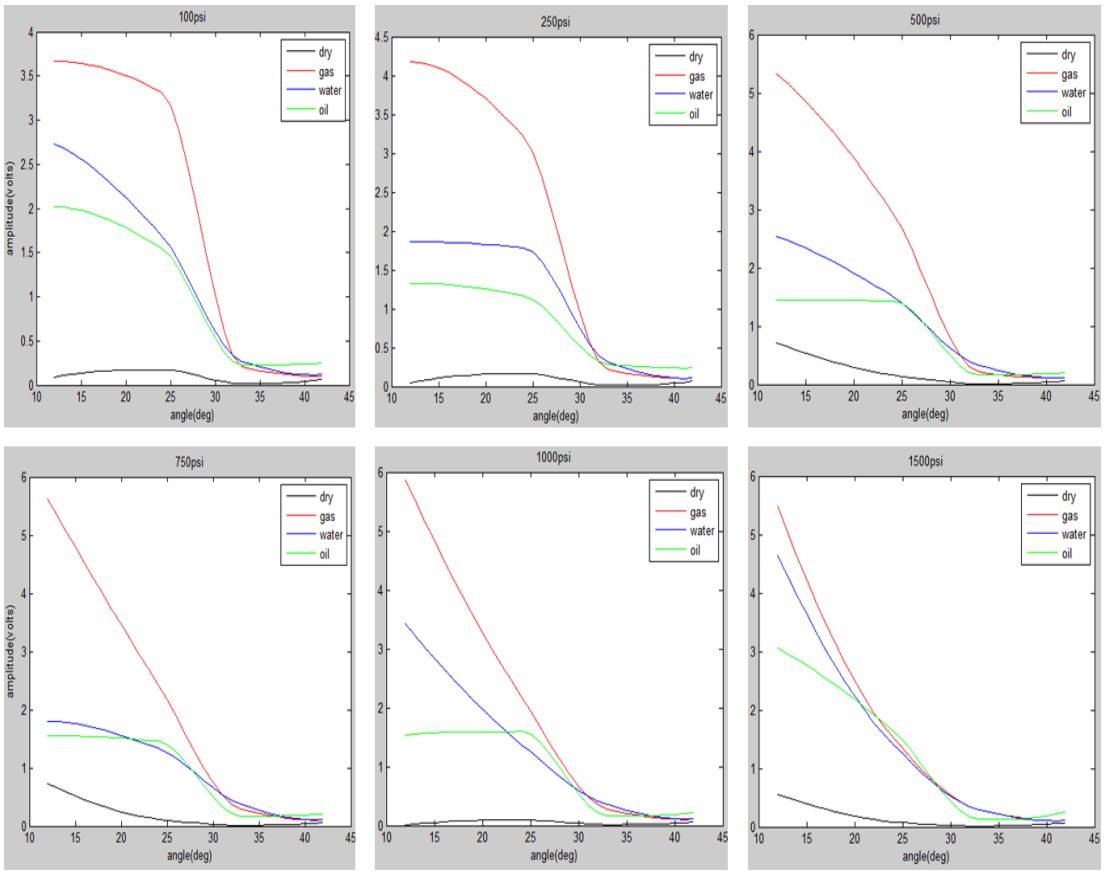

Figure 6-9: Amplitude versus angel measured at different pressure points and with different fluids media for the organic shale sample.

6.4.4 Comparison of inorganic and organic measurements

The same tests were performed on both samples. The difference was that the percentage of the TOC in second sample is 5 wt%, and the second sample is also slightly thicker. The source to receiver offsets range from 25 to 105 mm with a corresponding angle of incidence range of 12 to 42 degrees. The angle of incidence is the angle where a ray path intersects a line perpendicular to an interface. Refraction is the change in the wave-fronts, direction as it moves from one material to another, with a change in velocity. When moving through this interface, there is a reflected and transmitted P-wave, along with the partial conversion and reflection of a P-wave to an S-wave. Snell's Law describes the refraction index of two medias, depending on the angle of incidence. Based on the velocities of the steel block and the shale samples, the first critical angle was approximately 30 degrees. After this angle, the P-wave energy decreased due to an increased in the reflection of S-waves. After this

point, the amplitude values may be lower or more difficult to interpret due to the splitting of shear waves.

The AVO trend for the first sample with zero wt% of TOC was a sharp decrease for near offsets followed by a gradual decrease in amplitude for the farther offsets. As the angle of incidence increased, the ratio of reflected waves to incident waves decreased. Moreover, the source energy scatters with the distance and the same amount of energy will not be able to travel to the far offsets. On the other hand, the AVO trend for the second sample with 5 wt% of TOC seems to mimic the first sample result, except that the amplitude values were slightly higher at high pressures and that the slope of the initial decrease is sharper. A decrease in amplitude with offset was expected due to absorption, but overall amplitude values should be increased with increased in the clay mineral compositions. The organic content in the shale sample increased amplitude values and show a “sweet spot” in the seismic data. This is important; however, more information is needed when interpreting the data. Looking closely at the amplitude could help determine the amount of organic content in a shale formation, which is critical from a production stand point. Based on both tests, amplitude values will be higher with an increase in the TOC. Figures 6-10 and 6-11 show the two blocks (the organic sample and the inorganic sample) plotted against each other for each receiver, with respective gas, oil, water and dry curves.

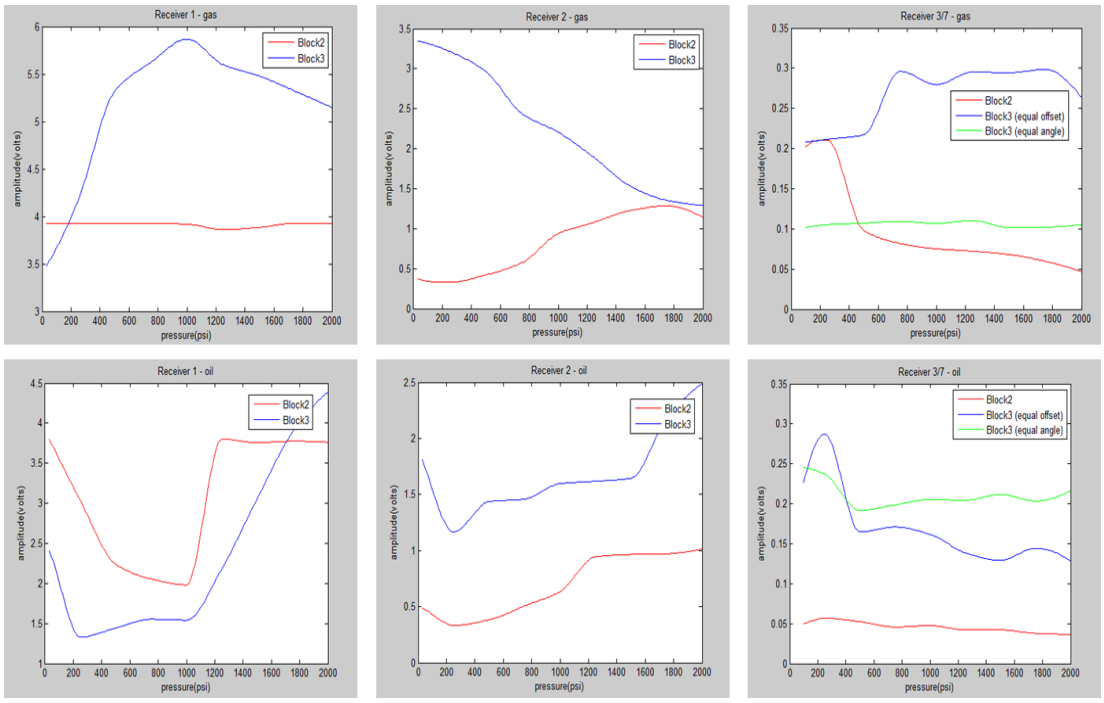

Figure 6-10: Shows the two blocks plotted against each other for each receiver with gas and oil curves.

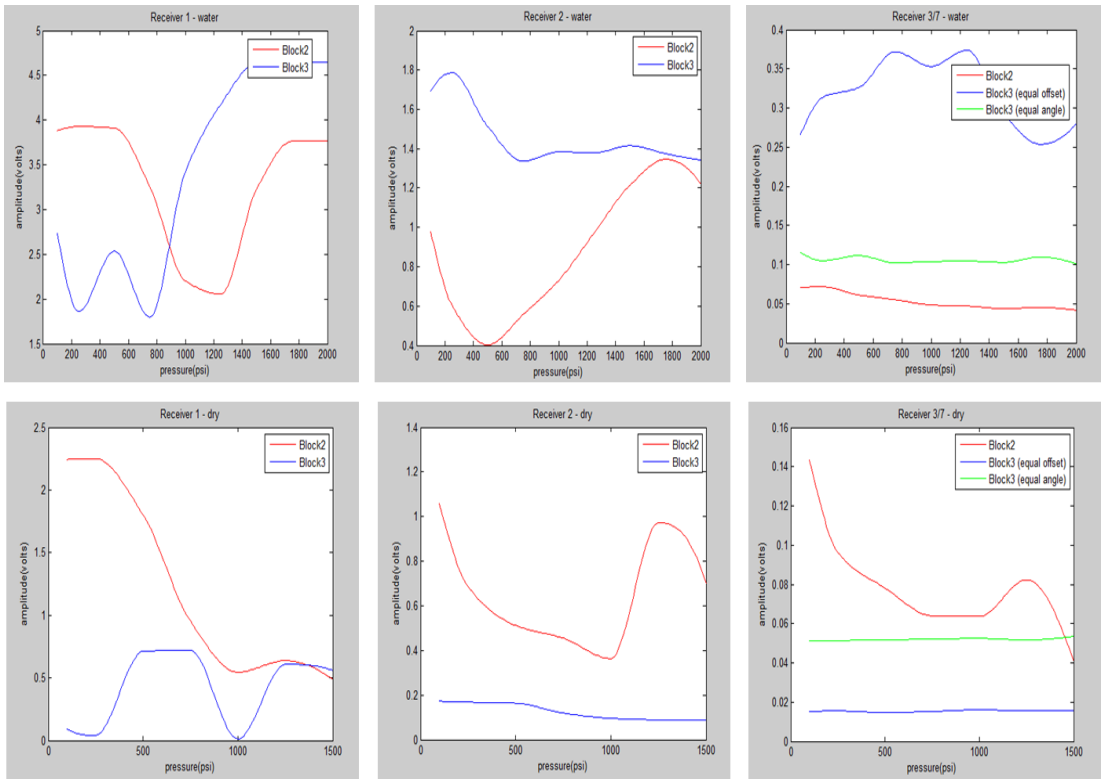

Figure 6-11: Shows the two blocks plotted against each other for each receiver with water and dry curves.

The next step was to determine exactly how much of an amplitude increase exists between inorganic and organic shale samples. For this comparison, the highest pressure was needed in the experiment to attempt to match actual reservoir

conditions. Theoretically, once very high pressures are reached, amplitude values should level off. After a certain point a formation will be fully compacted and its thickness and density should stay relatively constant. Tables 6-1, 6-2 and 6-3 list the amplitude values at maximum pressure for each block and the differences between the two. Table 6-4 lists the percentage increases in the amplitude values from the inorganic sample to the organic sample for all four curves at each receiver. As shown in the tables, it is found for all curves (gas, oil, water and dry), the percentage amplitude increase between the inorganic and organic sample is greater at large offsets. The amplitude values at the far offsets are smaller in magnitude, but the amount by which they increase is much larger. Figure 6-12 plots amplitude increases (%) versus angles of incidence for all the curves and includes the trend lines and slopes assigned to each curve.

The practical application for these trend lines would be the possibility of determining the TOC wt% of a survey area in an exploration project. To further this study, more samples should be created with larger amounts of organic content to test this trend. The dry curve slope with theoretical lines should also be plotted. The slopes of the lines should increase with an increase in organic content. By knowing the amplitude values of a “bright spot” versus the “background shale”, these trends could in fact be a good estimation of the amount of organic content in the formation of interest. It is interesting to see that for all curves the percentages increase with offset. Of course this is only a small data set and many more samples would be needed to confirm this trend.

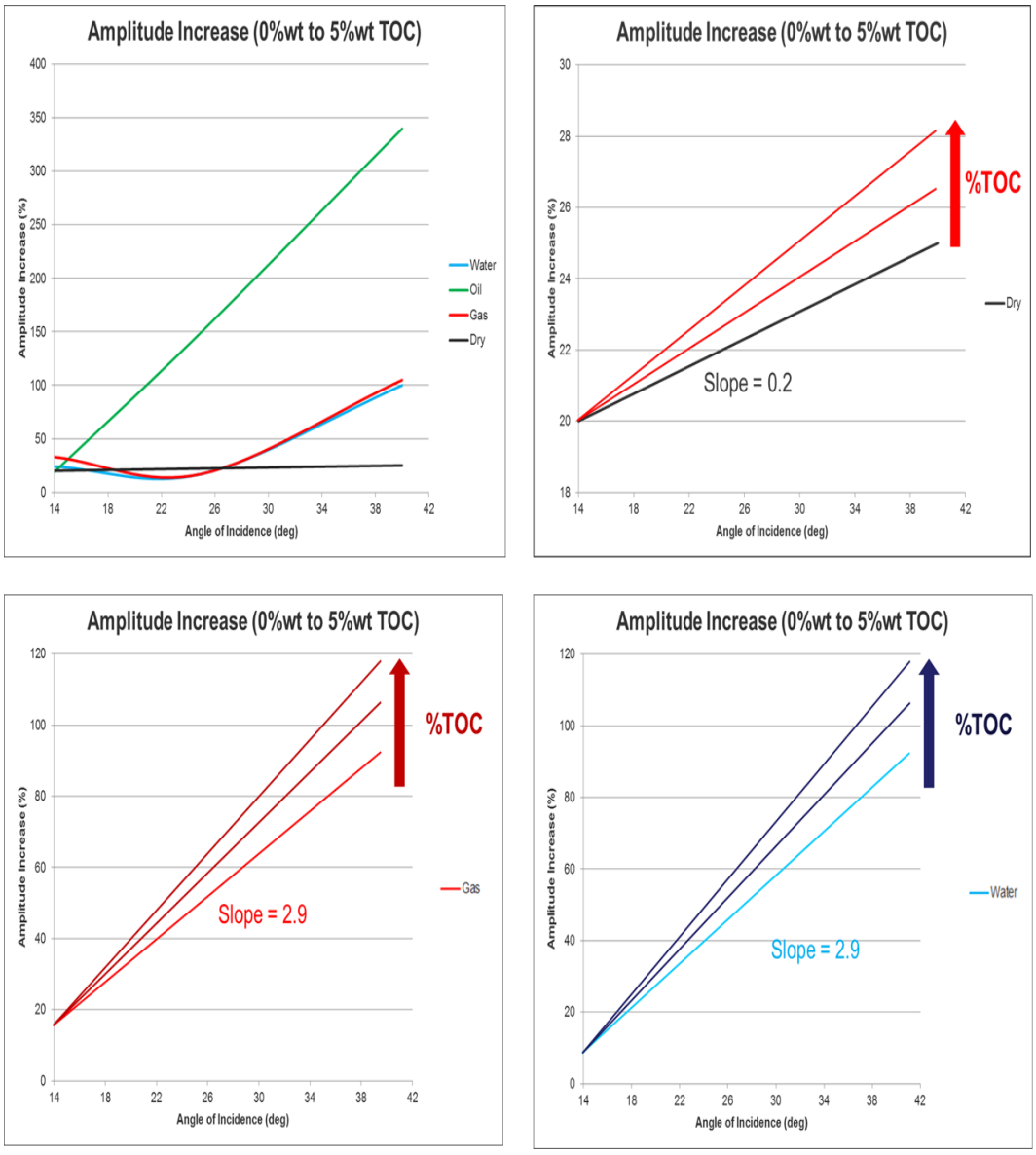

Figure 6-12: Amplitude increase verses angle of incidence. The plot shows that amplitude values increase more with a larger offset/angle.

Table 6-1: Block 0 wt% of TOC and Block 5 wt% of TOC amplitude values at maximum pressure (Receiver 1).

R1	Block (0 wt%%) TOC	Block (5 wt%%)TOC	Difference (%)
Water	3.7	4.6	0.9
Oil	3.7	4.4	0.7
Gas	3.9	5.2	1.3
Dry	0.5	0.6	0.1

Table 6-2: Block 0 wt% of TOC and Block 5 wt% of TOC amplitude values at maximum pressure (Receiver 2).

R2	Block (0 wt%) TOC	Block (5 wt%)TOC	Difference (%)
Water	1.2	1.4	0.2
Oil	1.0	2.5	1.5
Gas	1.2	1.4	0.2
Dry	0.7	0.1	-0.6

Table 6-3: Block 0 wt% of TOC and Block 5 wt% of TOC amplitude values at maximum pressure (Receiver 3).

R3/7	Block (0 wt%) TOC	Block (5 wt%)TOC	Difference (%)
Water	0.05	0.1	0.05
Oil	0.05	0.22	0.17
Gas	0.05	0.1	0.05
Dry	0.04	0.05	0.01

Table 6-4: Percentage increase of amplitude value from Block (0) wt% of TOC to Block (5) wt% of TOC.

	R1	**R2**	**R3/7**
Water	24%	17%	100%
Oil	19%	150%	340%
Gas	33%	17%	100%
Dry	20%		25%

6.5 Discussions

There were many difficulties with testing the synthetic shale blocks. The main issue was the soft material of the samples. Often the corners of the blocks were chipped or broken. The blocks were sanded to help smooth out any fracturing areas, but many irregular edges still remained. There was always the possibility of internal fractures that could affect the signal or obstruct wave propagation. Shale is a heterogeneous medium and simulating its formation in just several hours can definitely introduce errors.

It was also difficult to see the signal from the far offset receivers. This is mainly due to the amount of energy from the source, but also potentially any internal fractures that could have diffracted the waveform. To help with coupling, the source transducer was tilted. This made its surface contact with the shale block angle towards the receivers. This seemed to help reduce noise but still the far offsets could not be reached. The maximum offset with good signal was about 100 mm; approximately 40 – 45 degrees angle of incidence. Another factor to take into consideration was the pattern in which the energy radiates from the source transducer and the fact that the energy was not projected evenly in all directions. This is why the majority of receivers are aligned together. One long, straight line was ideal but as the farthest offsets could not be reached, two straight lines of receivers were positioned closer to the source. However, only one of these lines was used in the plots and analysis. The testing equipment also seemed to be quite sensitive, where a small amount of wire movement could affect the signal; therefore, the equipment had to be used very carefully in order to obtain accurate results.

Chapter 7. Conclusions

7.1 Estimation of the TOC and predictions of sweet spot locations

The poststack seismic inversions, with multi-attribute analysis, are effective in defining the TOC volume in both formations. The rock physic relationships between AI and TOC were applied for two shale Formations in Perth Basin, to predict the TOC content, there was a good correlation between them, the AI decreased as the TOC content increased. These correlations are used to map variations in the TOC profile with well-calibration by converting seismic AI data to TOC content. After all the methods have been applied the results showed a low acoustic impedance anomaly in the Kockatea and Carynginia Formations. This irregular anomaly was the response of high TOC with values between 2 – 4 wt %. As a result, the measured TOC log from the core samples of different wells was applied, in the TOC profile (converted from AI), which was displayed on the seismic data. The result was quite similar with generated TOC values after converting AI values to the TOC percentage using the seismic and rock physics linear relationships by comparing it to the TCO content measured from core samples. The investigations show the high TOC content are characterised with low AI, and the shale sweet spot is characterised by high TOC and relatively high acoustic impedance which is found in the base of Hovea Formation, where the TOC is around 4%. The application of the AVO analysis shows that the amplitude increases with an increasing offset for organic shale, which generates a Class 2 AVO anomaly. The relationship between the LMR approach and the elastic properties helps in predicting the change of gas shale properties such as lithology, porosity and stiffness of the rock.

7.2 Ultrasonic measurements

Ultrasonic wave velocities are measured in a changing stress field simulated under reservoir conditions using six natural shale core samples from the Redback-2 and Arrowsmith-2 wells in the Perth Basin. The laboratory results of the organic shale samples indicated evidence of stress sensitivity and that there were challenges when dealing with compacted organic shales due to their highly anisotropic nature and likely compositional effects on velocity. The increase in velocities with mean

effective stress levels signify a progressive increase in the stiffness of the samples and possibly associated with the micro-crack closure Also, the results of the research showed that the velocities dropped when there are high TOC percentages. In addition, other factors including porosity, concentration of clay minerals and density have an effect on the elastic waves of organic shale.

This study supports the concept that organic matter content and clay minerals have a significant impact on the elastic properties of synthetic shale samples. Organic matter, as well as shale mineralogy strongly affects the strength of the rock for hydraulic fracturing applications and this is reflected in the fact that Young's Modulus, Poisson's ratio and Vp/ Vs are strongly affected by in-situ rock parameters. This study also shows that the ratio of Vp\Vs increased as the isotropic stress increased (all the stresses applied in all the directions equally on the samples), which means that the P-wave is affected by the stress more than the S-wave.

This approach of preparing synthetic shale samples with different proportions of organic content enabled us to introduce an equation that can be used to estimate the TOC content of shale formations, as the TOC content is a very important parameter to define sweet spots for shale plays.

7.3 AVO analysis and measurements

AVO modelling and analysis of log data with the laboratory experiments are good techniques to understand the dynamics of shale. The main objective of this project was to understand the influence of the TOC shale on the AVO response. Knowing the percentage of the organic content in a prospective reservoir was one of the most important factors when looking at exploration and production of a shale formation. In general, a shale formation will not produce well if it has less than 2.5% TOC content. The experiments conducted have been able to determine several things: TOC has a direct effect on amplitude response, the more the TOC present, the slower the acoustic impedance and thus the reflection co-efficient increases and the fluid may impact the amplitude response. It is shown that isotropic stress significantly impacts the amplitude. In addition, fluid in the shale changes the amplitude response. Generally, the trend of the amplitude values increase smoothly as the pressure is increased and then dropped suddenly when higher pressures are reached; the dropping values are different dependent on the fluid media. The dry amplitude values

are significantly lower than the gas, oil and water values. It is also important to understand the amplitude background trend of the formation of interest. This way, amplitude anomalies are able to be interpreted accurately. In most cases, as shown in these experiments, increasing amplitude is evident among formations with higher levels of TOC.

7.4 Recommendations

In the seismic inversion study, a bigger database of core samples for testing of the TOC content is recommended for better correlation. Vertical seismic profile will also play an important role to understand the gas shale more deeply. In addition, it will be beneficial to compare this study of the Perth Basin to an example of US shale formations.

In the laboratory study, it is recommended to have more shale samples, so as to have better understanding of the rock properties and its impact on the elastic properties. Moreover, a good number of synthetic shale with different clay mineral compositions should have been created. For further work of the AVO study, more samples should be created with larger amounts of organic content to test the AVO trend. By knowing the amplitude values of a “bright spot” versus the “background shale”, these trends could in fact be a good estimation of the amount of organic content in the formation of interest.

References

Altowairqi, Y., R. Rezaee., B. Evans, and M. Urosevic, 2015 (B), Shale elastic property relationship as function of total organic carbon using synthetic samples: 3rd International Workshop on Rock Physics, 2015.

Altowairqi, Y., R. Rezaee., B. Evans, and M. Urosevic, 2015 (A), Measuring Elastic Properties to determine the influence of TOC on Synthetic Shale Samples: ASEG Extended Abstracts, 2015(**1**), 1-5.

Altowairqi, Y., R. Rezaee, and M. Urosevic, 2014, Quantitative application of post stack inversion of organic-rich based on rock physics linear relationship and 3D seismic data, Perth Basin, Western Australia: Australian Petroleum Production and Exploration Association Extended Abstracts, 2014.

Altowairqi, Y., R. Rezaee, M. Urosevic, and C. Delle Piane, 2013, Measuring ultrasonic characterisation to determine the impact of TOC and the stress field on shale gas anisotropy: Australian Petroleum Production and Exploration Association, 2013.

Alzate, J, H., and D. Devegowda, 2013, Integration of surface seismic, microseismic, and production logs for shale gas characterization: Methodology and field application. Interpretations for unconventional resources, **1**, no.2, SB37-SB49.

Avseth, P., T. Mukerji, and G. Mavko, 2005, Quantitative seismic interpretation: Cambridge University Press.

Bayuk, I., M. Ammerman and E. Chesnokov, 2007, Elastic moduli of anisotropic clay: Geophysics, **72**, D107–D117.

Bohacs, K.M., G. J. Grabowahi, A. R. Carroll, P. J. Mankiewicz, K. J. Miskell-Grahardt, J. R. Schwalbach, M. B. Wegner, and J. A. Simo, 2005, Production, destruction, and dilution—the many paths to source-rock development, the Deposition of Organic-Carbon-Rich Sediments: Models, Mechanisms, and Consequences; SEPM Special Publications, **82**, 61–102.

Borham, C. J., J. M. Hope, and B. Hartung-Kangi, 2001a, Understanding source, distribution and preservation of Australian natural gas: a geochemical perspective: APPEA Journal, **41**, 523–547.

Borham, C. J., J. M. Hope, and Hartung-Kangi, B., and B. J. K. van Aarssen, 2001b, More sources for gas and oil in Perth Basin: Study highlights potential for multiple

petroleum systems: Australian Geological Survey Organisation, Research Newsletter, December 2000, p. 5–9.

Boyer, C., J. Kieschnick, R. Suarez-Rivera, R. E. Lewis, and G. Waters, 2006, Reducing gas from its source: Oilfield Review, Autumn, 36-49.

Brevik, I., G. R. Ahmadi, T. Hatteland, and M. A. Rojas, 2007, Documentation and quantification of velocity anisotropy in shales using wireline log measurements: The Leading Edge, **26**, 272 – 277.

Cadman, S. J., L. Pain, and V. Vuckovic, 1994, Australian Petroleum Accumulations: Report 10.

CGG Veritas., 2012, Starta Workshop.

Ciz, R., and S. A. Shapiro, 2009, Stress-dependent anisotropy in transversely isotropic rocks: Comparison between theory and laboratory experiment on shale: Geophysics, **74**, D7-D12.

Connolly, P., 1999, Elastic impedance: The Leading Edge, **18,** no. 4, 438-452.

Crain, E. R., 2000, Crian's petrophysical handbook, Spectrum.

Crostella, A., 1995, An evaluation of the hydrocarbon potential of the onshore northern Perth Basin, Western Australia: Geological Survey of Western Australia.

Close, D., S. Stirlings, D. Cho, and F. Horn, 2010, An integrated workflow for shale-gas in the Western Canadian sedimentary basin: Surface seismic to stimulation, AAPG 2010 Annual Convention, New Orleans, Louisiana, 11–14, April, 40569.

Chesnokov, E., I. O. Bayuk, and M. Ammerman, 2010, Determination of shale stiffness tensor from standard logs: Geophysical Prospecting, **58**, 1063–1082.

Dodds, K.J., D. N. Dewhurst, A. F. Siggins, R. Ciz, M. Urosevic, B. Gurevich, and D. H. Sherlock, 2007, Experimental and theoretical rock physics research with application to reservoirs, seals and fluid processes: Journal of Petroleum Science and Engineering, **57,** 16–36.

Department of Mines and Petroleum, 2014, Summary of Petroleum Prospectively: Perth Basin, Geological Survey of Western Australian , Report 41.

D'Ercole, C. A. Pitchford., and A. J. Mory., 2003, Lenads and prospects within tenements of the northern Perth Basin, Western Australia,2002 : Western Australia Geological Survey, Record 2003/4, P.126.

Delle-Piane, C., D. Dewhurst, A. Siggins, and M. Raven, 2011, Stress-induced anisotropy in brine saturated shale: Geophysical Journal International, **184**, no. 2, 897–906.

Dewhurst, D. N., A. F. Siggins, J. Sarout, M. D. Raven, H. M. Nordg ård -Bol ås, 2011, Geomechanical ultrasonic characterization of a Norwegian sea shale: Geophysics, **76**, no. 3, Special section—seismic anisotropy.

Dewhurst, D. N., A. F. Siggins, 2006, Impact of fabric, microcracks and stress field on shale anisotropy: Geophysical Journal International, **165**, no. 1, 135–148.

Dewhurst, D. N., A. C. Aplin, J. P. Sarda, and Y. Yang, 1998, Compaction-driven evolution for porosity and permeability in natural mudstones: An experimental study: Journal of Geophysical Research: Solid Earth **103**, (B1), 651–661.

Goodway, W., M. Perez, J. Varsek, and C. Abaco, 2010, Seismic petrophysics and isotropic-anisotropic AVO methods for unconventional gas exploration: The Leading Edge, **29**, no. 12, 1500–1508.

Goodway, W., J. Varsek, and Abaco, 2006, Practical applications of P-wave AVO for unconventional gas resources plays. Part 2: Detraction of fracture prone zones with azimuthal AVO and coherence discontinuity: CSEG Recorder, **31**, no. 4, 53-65.

Goodway, W., T. Chen, and J. Downton, 1997, Improved AVO fluid detection and lithology discrimination using Lamé petrophysical parameters: 67th Ann. Internat. Mtg: SEG, 183–186.

Gupta, N., S. Sarkar, and K. J. Marfurt, 2013, Seismic attribute driven integrated characterization of the Woodford shale in west-central Oklahoma: Interpretation for Unconventional Resources, **1**, no. 2, pp.SB85–SB96.

Filippova, K., A. Kozhenkov., and A. Alabushin, 2011, Seismic inversion techniques: choice and benefits: First break, **29**.

Hampson, D., J. Schuelke, and J. Quirein, 2001, Use of multiattribute transforms to predict log properties from seismic data: Geophysics, **66**, no. 1, 220–236, doi: 10.1190/ 1.1444899.

Han, De-hua, 2002, Introduction of reservoir rock and hydrocarbon: Foundation for reservoir exploration and exploitation.

Harris, L. B., 1994, Structural and Tectonic Synthesis for the Perth Basin, Western Australia: Journal of Petroleum Geology **17,** no. 2, 129–56.

Horsrud, P., E. F. SØnstebØ, and R. BØe, 1998, Mechanical and petrophysical properties of North Sea shales: International Journal of Rock Mechanics and Mining Sciences, **35**, no. 8, 1009–1020.

Hornby, B.E., 1998*, Experimental laboratory determination of the dynamic elastic properties of wet, drained shales*, Journal of Geophysical Research: Solid Earth, **103** (B12), 29945–29964.

Johnson, C. L., T. J. Greene, D. A. Zinniker, J. M. Moldowan, M. S. Hendrix, A. R. Carroll, 2003, Geochemical characteristics and correlation of oil and nonmarine source rocks from Mongolia: AAPG Bulletin, **87**, no. 5, 817–846.

Kennet, B., 1980, Seismic waves in stratified half space- II. Theoretical seismograms: Geophysical Journal of Royal Astronomical Society, **61**, P1–10.

Lebedev, M., A. Bona, R. Pevzner, and B, Gurevich, 2011, Elastic ansotropy estimation from laboratory measurements of velocity and polarization of quasi-P-wave uing laser interferometry: Geophysics, **76**, WA83–WA89.

Løseth, H., L. Wensaas, M. Gading, K. Duffaut, and M. Springer, 2012, Can hydrocarbon source rocks be identified on seismic data?: Geology, **39**, no. 12, 1167–1170.

Loucks, R. G., R. M. Reed., S. C. Ruppel., and D. M., Jarvie., 2009, Morphology, Genesis, and Distribution of Nanometer-Scale Pores in Siliceous Mudstones of the Mississippian Barnett Shale: Journal of Sedimentary Research, **79**, 848-861.

Magoon, L.B., W. G. Dow, 1994, The petroleum system from source to trap: AAPG Memoir, **60**, 3–24.

Mavko, G., T. Mukerji, and J. Dvorkin, 1998, The rock physics handbook: Tools for seismic analysis in porous media, Cambridge: Cambridge University Press.

Mavko, G., T. Mukerji, and J. Dvorkin, 2009, The Rock Physics Handbook: Tools For Seismic Analysis In Porous Media – 2nd Edition: Cambridge University Press, Cambridge, UK.

Millheim, K., 1972, Exploration report for 1972: Oil Permit, E.P 69, Western Australia, Sunningdale Oils Pty. Ltd.

Mory, A. J., and R. P. Iasky, 1996, Stratigraphy and Structure of the Onshore Northern Perth Basin: Western Australia:Geological Survey of Western Australia, 46.

Ogiesoba, O. C., and R. Eastwood, 2013, Seismic multi-attribute analysis for shale gas/oil within the Austin Chalk and Eagle Ford shale in a submarine volcanic terrain, Maverick basin, South Texas: Interpretation for Unconventional Resources, **1**, no. 2, pp, SB21–SB83.

Origin Energy LTD, Shale reservoir evaluation, Perth Basin, Australia: DMP.

Owad-Jones, D. L., and G. K. Ellis., 2000, Western Australia atlas of petroleum fields, Onshore Perth Basin: Petroleum Division, DMEWA, **1**.

Passey, Q. R., S. Creaney, J. B. Kulla, F. J. Moretti, and J. B. Stroud, 1990, Practical model for organic richness from porosity and resistivity logs: AAPG Bulletin, 74, 1777–1794.

Passey, Q.R., K. M. Bohacs, W. L. Esch, R. Klimentidis, and S. Sinha, 2010, From oil-prone source rock to gas-producing shale reservoir - Geologic and petrophysical characterization of unconventional shale gas reservoirs: International Oil and Gas Conference and Exhibition, Beijing, China, 8-10 June, 131350-MS.

Prasad, M., A. Pal-Bathija, M. Johnston, M. Rydzy, and M. Batzle, 2009, Rock physics of the unconventional: The Leading Edge, **28**, no. 1, 34–38, doi:10.1190/1.3064144.

Rokosh, C., J. Pawlowicz, H. Berhane, S. Anderson, and A. Beaton, 2009, What is Shale Gas? An Introduction to Shale-Gas Geology in Alberta: Alberta Geological Survey Open File Report, 2008-08, Alberta, Canada.

Perez, M ., B. Good, and G. Purdue, 2012, Integrated workflows for shale gas and case study results for the horn river basin, British Columbia, Canada: The Leading Edge, **31**, no. 5, 556–569.

Perez, M., D. Close, B. Goodway, and D. Monk, 2011, Workflows for integrated seismic interpretation of rock properties and geomechanical data: Part 1–principles and theory: CSEG Convention Abstracts.

Playford, P. E., A. E. Cockbain, and G. H. Low, 1976, Geology of the Perth Basin Western Australia: Geological Survey of Western Australia, Bulletin, 124.

Ross, D. J. K., and R. M. Bustin, 2009, The importance of shale composition and pore structure upon gas storage potential of shale-gas reservoirs: Marine and Petroleum Geology, **26**, no.6, 916–927.

Sarout, J., and Y. Gueguen, 2008, Anisotropy of elastic wave velocities in deformed shales, part 1: experimental results: Geophysics, **73,** D75–D89.

Sarout, J., L. Molez, Y. Gue´guen, and N. Hoteit, 2006, Shale dynamic properties and anisotropy under triaxial loading, Experimental and theoretical investigations: Physics and Chemistry of the Earth, **32**, 896–906.

Sayers, C.M., 2005, Seismic anisotropy of shales: Geophysical Prospecting, **53**, 667–676.

Sayers, C. M., 2008, The effect of low aspect ratio pores on the seismic anisotropy of shales: 78th Annual International Meeting, SEG, Extended Abstracts, 2606–2611.

Schmoker, J., 1979, Determination of organic content of Appalachian Devonian shales from Formation-density logs, American Association of Petroleum Geologists, P.127-134.

Sherlock, D., and A. Siggins, 2003, The development of synthetic CIPS sandstones for geophysical research: ASEG 16th Geophysical Conference and Exhibition, Adelaide, Australia.

Sena, A., G. Castillo, K. Chesser, S. Voisey, J. Estrada, J. Carcuz, E. Carmona, and P. Hodgkins, 2011, Seismic reservoir characterization in resource shale plays: Stress analysis and sweet spot discrimination: The Leading Edge, **30**, no.7, 758–764.

Singleton, S., and R. Keirstead, 2011, Calibration of prestack simultaneous impedance inversion using rock physics: The Leading Edge, **30**, no.3, 70–78.

Singleton, S., 2008, The use of seismic attenuation to aid simultaneous impedance inversion in geophysical reservoir characterization: The Leading Edge, **27**, no. 3, 398–407.

Singleton, S., 2009, The effects of seismic data conditioning on prestack simultaneous impedance inversion: The Leading Edge, **28**, no. 7, 772–781.

Sena, A., G. Castillo, K. Chesser, S. Voisey, J. Estrada, J. Carcuz, E. Carmona, and P. Hodgkins, 2011, Seismic reservoir characterization in resource shale plays: Stress analysis and sweet spot discrimination: The Leading Edge, **30**, no.7, 758–764.

Song,T., and P. A. Cawood, 2000, Structural styles in the Perth Basin associated with the Mesozoic break-up of Greater India and Australia: Tectonophysic, no.1–2, **317**, 55–72.

Sone, H., 2012, Mechanical properties of shale-gas reservoir rocks and its relation to the in situ stress variation observed in shale-gas reservoirs: Stanford University, SRB, **128**.

Sondergeld, C. H., and C. S. Rai, 2011, Elastic anisotropy of shales: The Leading Edge, **30**, 324–331.

Sondergeld, C. H., K. E. Newsham, J. T. Comisky, and M. C. Rice, 2010, Petrophysical considerations in evaluating and producing shale gas resources: the Society of Petroleum Engineers (SPE) 131768, 23–25, Pittsburgh.

Sondergeld, C.H., C. S. Rai, R. W. Margesson, and K. J. Whidden, 2000, Ultrasonic measurements of anisotropy on Kimmeridge shale: 70th Annual International. Meeting, SEG, Expanded Abstracts, 1858–1861.

Storvoll, V., I. Brevik, 2008, Identifying time, temperature and mineralogical effects on chemical compaction in shales by rock physics relations: The Leading Edge, **27**, 750–756.

Spikes, K. T., 2008, Probabilistic seismic inversion based on rock physics models for reservoir characterization: Stanford University.

Thomsen, L., 1986, Weak elastic anisotropy, Geophysics, **51**(10), 1954–1966.

Thomas, B. M., and C. J. Barber, 2004, A Re-Evaluation of the Hydrocarbon Habitat of the Northern Perth Basin: APPEA Journal **44**, 59-92.

Triche, N., 2012, Wave of the future? Petroleum Geologist Resources Branch, Shale gas in Western Australia: Petroleum in Western Australia, Western Australia's digests of petroleum exploration, development and production, pp 20.

Tupper, N. P., 1992, Source potential of the onshore Perth Basin: Sagasco resources limited.

Tutuncu, , A.N., 2010, Anistropy, compaction and dispersion characteristics of reservoir and seal shales: 44th U.S. Rock Mechanics Symposium and 5th U.S.-Canada Rock Mechanics Symposium, June 27–30, Salt Lake City, Utah,10–344.

Vernik, L., and M. Kachanov, 2010, Modeling elastic properties of siliclastic rocks: Geophysics, **75**, no. 6, 171–182.

Vernik, L., and X. Liu, 1997, Velocity anisotropy in shales: A petrophysical study: Geophysics, **62**, no. 2, 521–532.

Vernik, L., and J. Milovac, 2011, Rock physics of organic shales: The Leading Edge, **30**, no. 3, 318–323.

Vernik, L., and A. Nur, 1992, Ultrasonic velocity and anisotropy of hydrocarbon source rocks: Geophysics, **57**, no. 5, 727–735.

Veritas DGO Asia Pacific LTD, 2006, 3D land seismic data processing Denison, Hibbertia, Hovea and Beharra springs Perth Basin: Onshore Australia seismic data processing report for ARC Energy Limited.

Volk, H., C. Simon, C. Boreham, and R. Kempton, 2004, Geochemical and compound specific carbon isotropic characterization of fluid inclusion oils from the offshore Perth Basin (Western Australia): implications for recognizing effective oil source rocks: APPEA,

Well completion report—Arrowsmith-2, 2011, Department of Mines and Petroleum, Perth, Australia.

Well completion report—RedBack-2, 2011, Department of Mines and Petroleum, Perth, Australia.

Wang, Z., 2001, Fundamentals of seismic rock physics: Geophysics, **66**, 398-412.

Yang, Y. T., B. M. Zhang, C. Y. Zhao, T. G. Xu, 2004, Mesozoic source rocks and petroleum systems of the northeastern Qaidam basin, northwest China: AAPG Bulletin, **88**, no. 1, 115–125.

Zhu, Y., E. Liu, A. Martinez, M. A. Payne, C. E. Harris, 2011, Understanding geophysical responses of shale-gas plays: The Leading Edge, **30**, no. 3, 332–338.

'Every reasonable effort has been made to acknowledge the owners of copyright material. I would be pleased to hear from any copyright owner who has been omitted or incorrectly acknowledged.'

Appendixes

Appendix A.
Denison 3D Seismic Inversion and multi-attribute analysis of Carynginia Formation

This study was discussed in chapter 4 for the Kockatea Formation, but here this part will show Carynginia formation with the same seismic data (Denison Survey) as located in the Perth Basin. The model based inversion was applied with the same workflow presses as explained before. The inversion analysis was applied for both P and S impedances for the Carynginia formation using 15 control wells. The inverted synthetic correlations were 0.9 and 0.7 respectively. Figure A-1 shows acoustic and shear impedance inversions for the Carynginia formations with low values of P and S impedances.

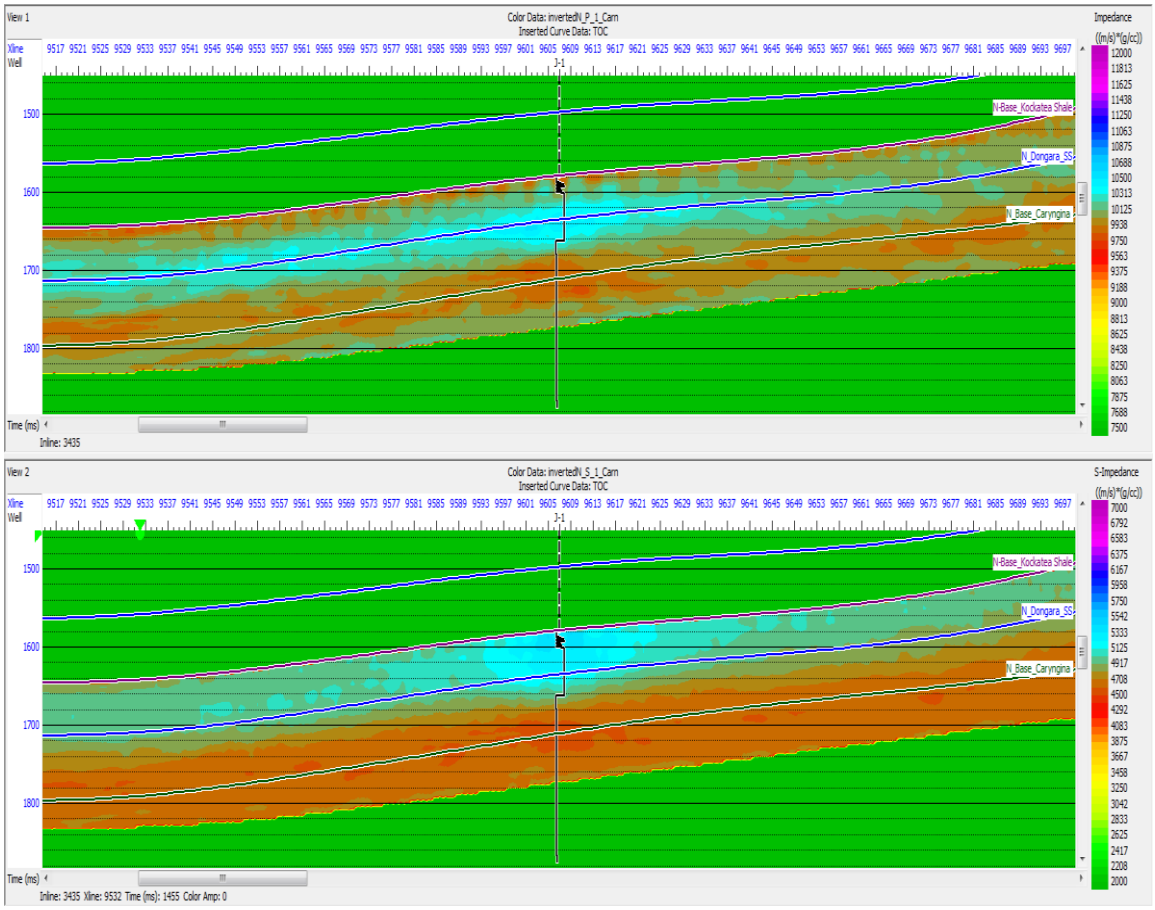

Figure A-1: Acoustic and shear impedance inversions for Caeynginia formation.

The multi-attribute analysis was also applied to the Carynginia formation, and 6 seismic attributes were used (Table A-1) with the Convolution operator. Which is effects of estimate TOC percentage, and it increases the correlation between the predicted TOC and the actual TOC. The correlation increased to 0.71 with a seven point convolutional operator, which gives an expectation error lower than 0.76% for training, and less than 0.8% for validation. (This error is the absolute prediction error in the units of TOC, which is Wt %).

Table A-1: The Multi-attribute analysis applied for Caryngina formation**.**

	Target	Final Attribute	Training Error	Validation Error
1	(TOC)	(inverted-P-Impedance)**2	0.790123	0.800854
2	(TOC)	Integrate	0.778476	0.790797
3	(TOC)	Average Frequency	0.773434	0.793491
4	(TOC)	Dominant Frequency	0.771142	0.794996
5	(TOC)	Cosine Instantaneous Phase	0.766627	0.798038
6	(TOC)	Filter 25/30-35/40	0.767796	0.791592

One way of measuring the correlation between the target and attribute is to cross-plot the predicted TOC estimated from the attribute and the actual TOC. A cross plot showing the correlation between predicted TOC and actual TOC using 15 wells and 6 seismic attributes is shown in (Figure A-2). The correlation was approximately 0.71 with less than 0.76% error.

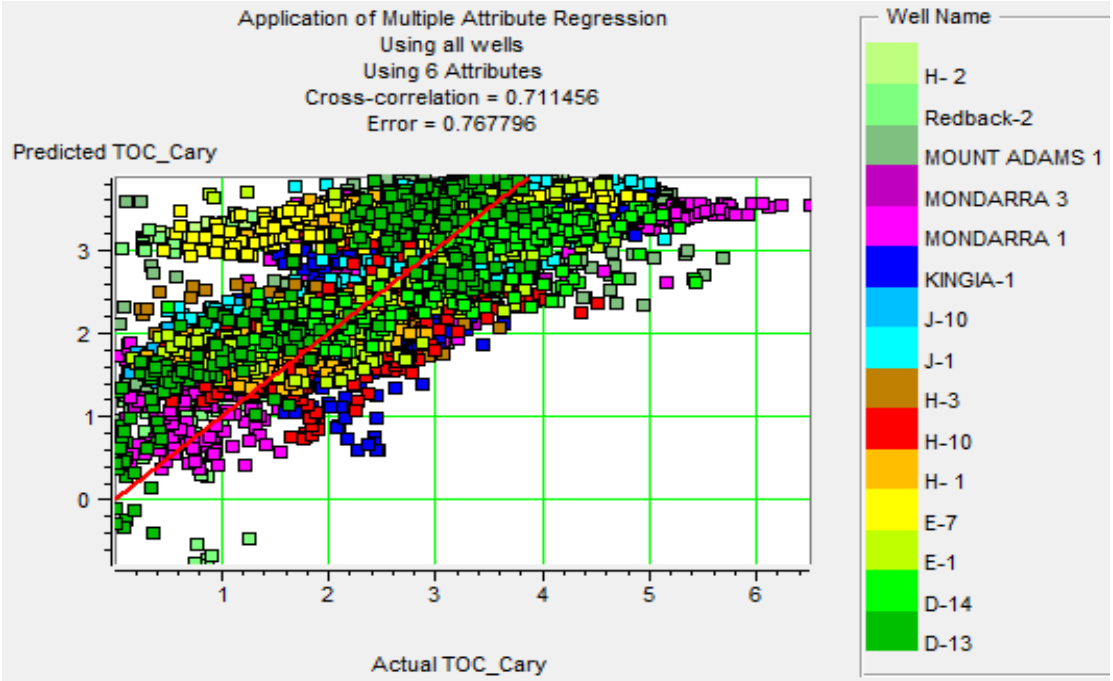

Figure A-2: Cross-plot of Predicted TOC and Actual TOC using 6 Attributes of Carynginia Formation.

All the information in the table is shown graphically in Figure A-3, which shows the validation results. The lower curve in black is the estimation error when all the wells are used in the analysis and the upper (red) curve shows the average validation error.

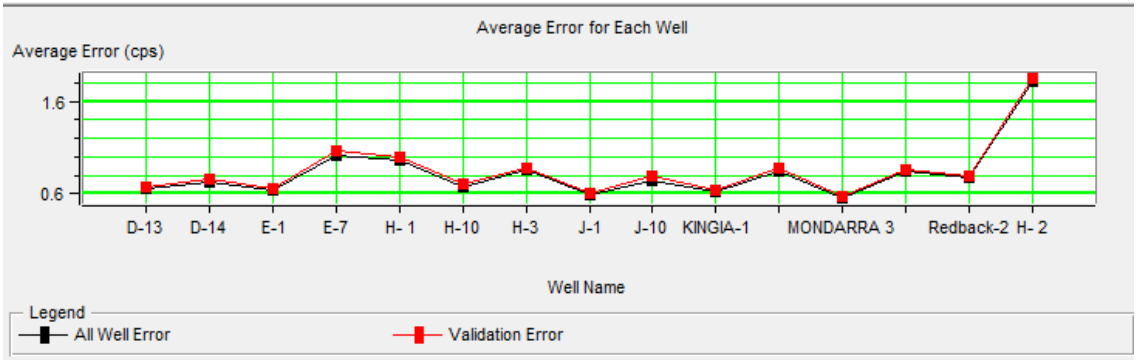

Figure A-3: Average Error for each well of the Carynginia formation.

The multi-attribute transformation using 6 different attributes were applied to the seismic inversion model to estimate TOC distribution in the Carynginia formation. The results showed that the post stack seismic inversion with multi-attribute analysis was effective in defining the TOC volume in the Carynginia formation. Figure A-4shows the conversion section of TOC and the section of seismic acoustic impedance inversion, the profile of TOC

after the multi-attribute is applied crossing the wells in Perth basin, shows the that different colors in the TOC section represent different TOC values. For example, the red shows the highest of TOC values in the Carynginia formation between 2.1 to 2.3wt % and is associated with low acoustic impedance between 9667 to 10333 ((m/s)* (g/cc)). As a result of the comparison between the measured TOC from the core sample of Jingemia-1 well displayed in the TOC profile to and the results with the real measured TOC and it showed that the values of TOC were around 2.2 wt% in the Carynginia formation. Which has a close percentage of generated TOC values from the seismic data with approximately 2.1 wt% after converting Acoustic impedance values.

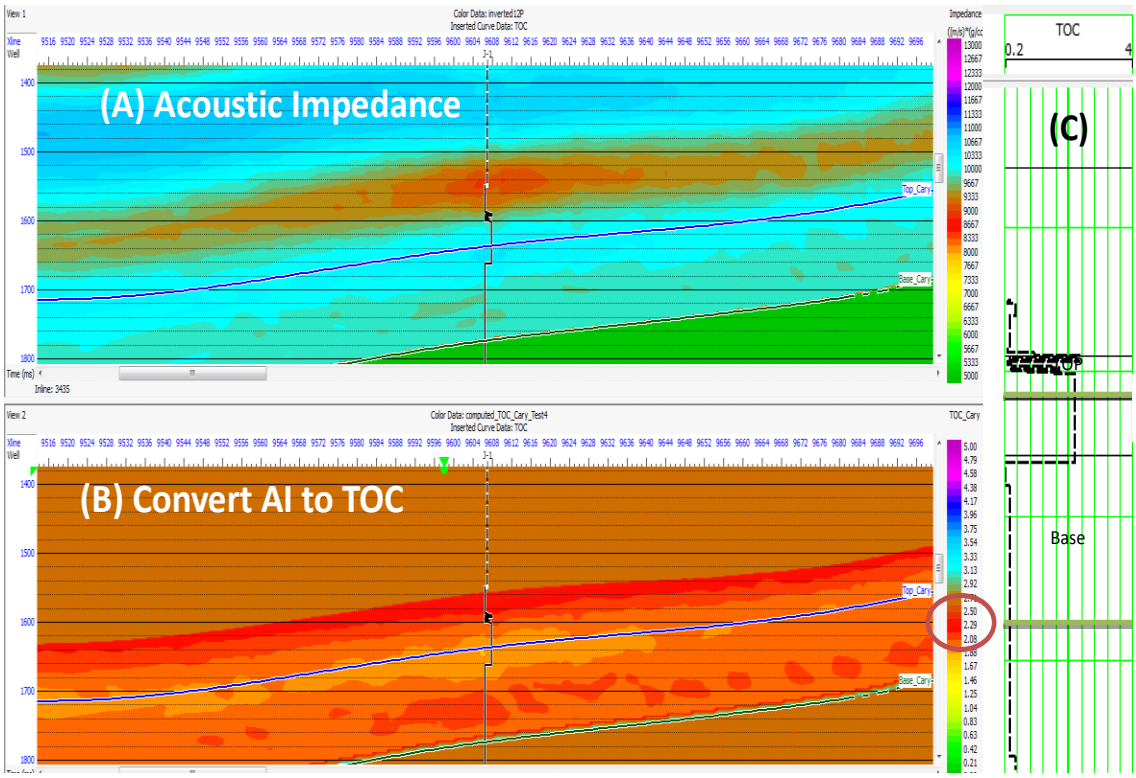

Figure A-4: (A) Acoustic Impedance Inversion in the Caryngina Formations, (B) The TOC percentage after converting AI values to TOC percentage in the Caryngina Fm Caryngina Formations with lower values (C) The Measured TOC from core sample

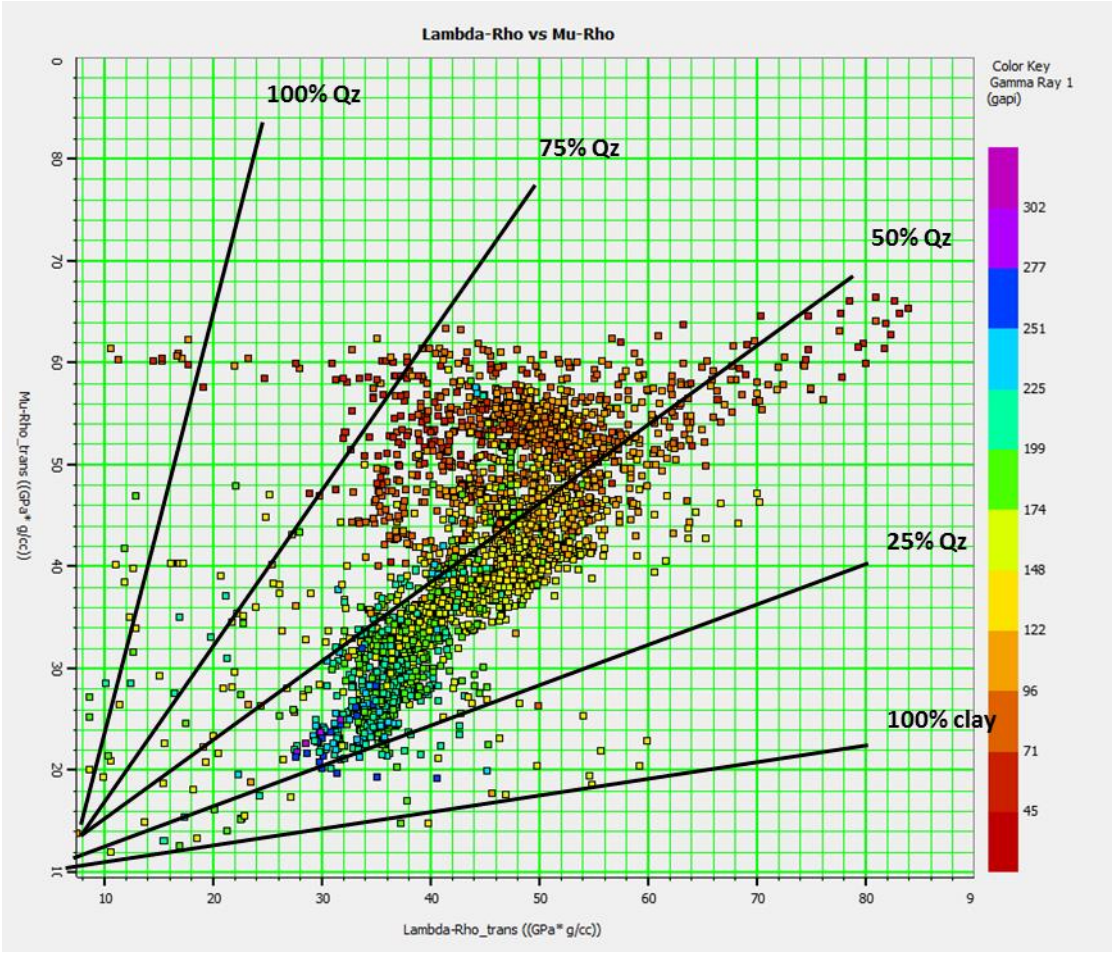

Figure A-5: All data from the Arrowsmith-2 well for the Carynginia formation and IRCM with changes in rock composition; clay-rich rocks are displayed with high LR and lower MR values, while the quartz-rich rocks are displayed with high LR and higher MR values.

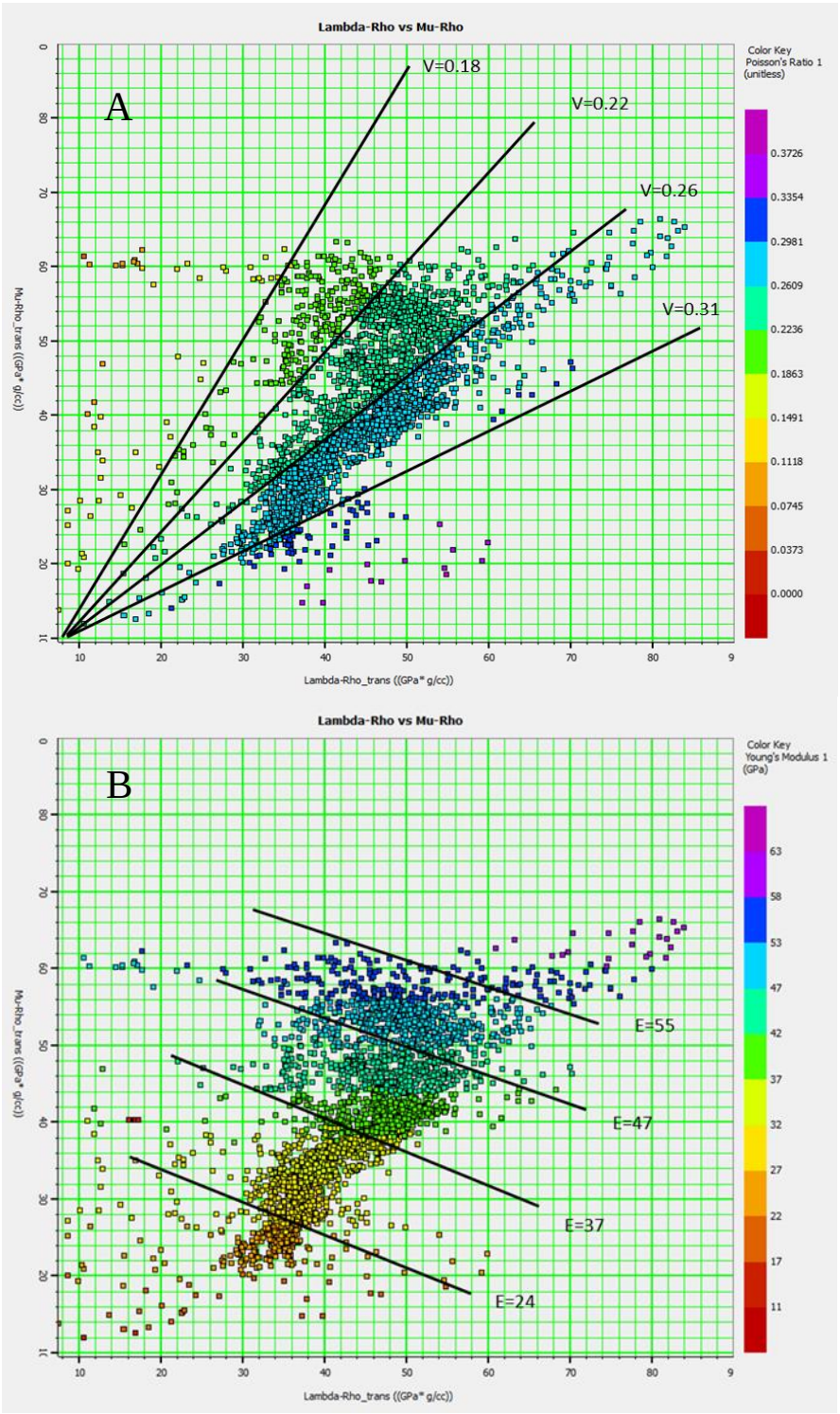

Figure A-6: (A) and (B) show the crossplots of LR versus MR for the Arrowsmith-2 well having similar values and are displayed for each plot by Poisson's ratio and Young's modulus.

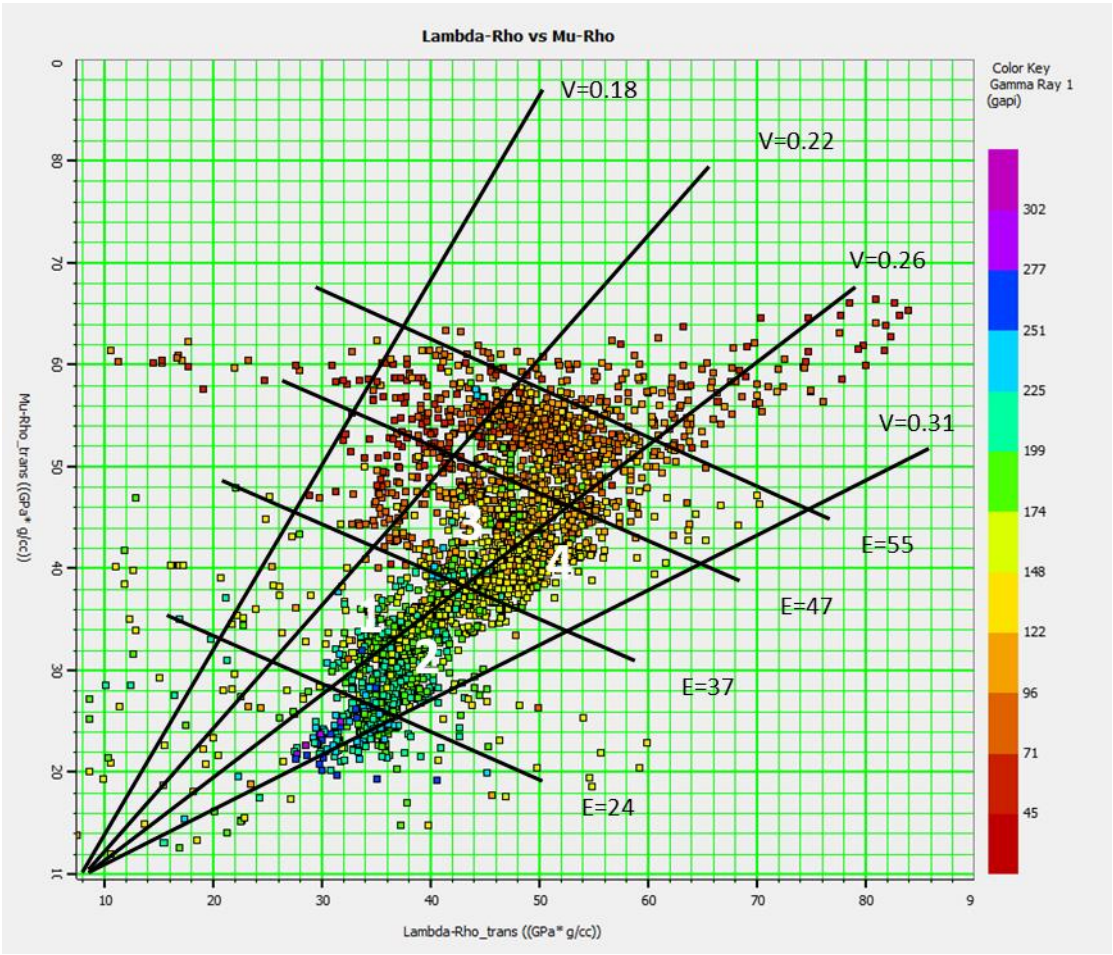

Figure A-7: Crossplot of LR versus MR obtained by combining Figure A8 A and B. Group 1 is shown to be brittle shale with a rich TOC percentage while Group 2 is shown to be ductile shale with a rich TOC percentage.

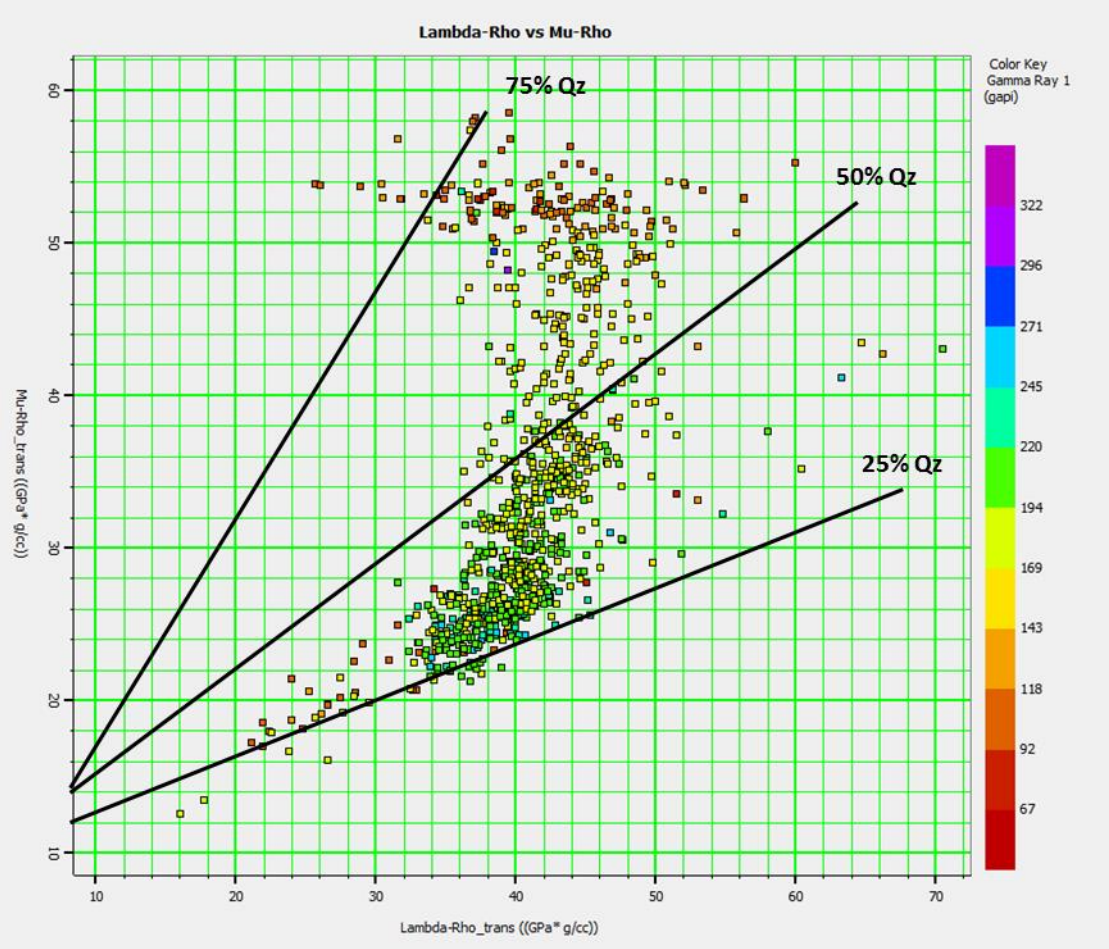

Figure A-8: All data from the Woodada deep-1 well for the Carynginia formation with changes in rock composition; clay-rich rocks are displayed with high LR and lower MR values, while the quartz-rich rocks are displayed with high LR and higher MR values.

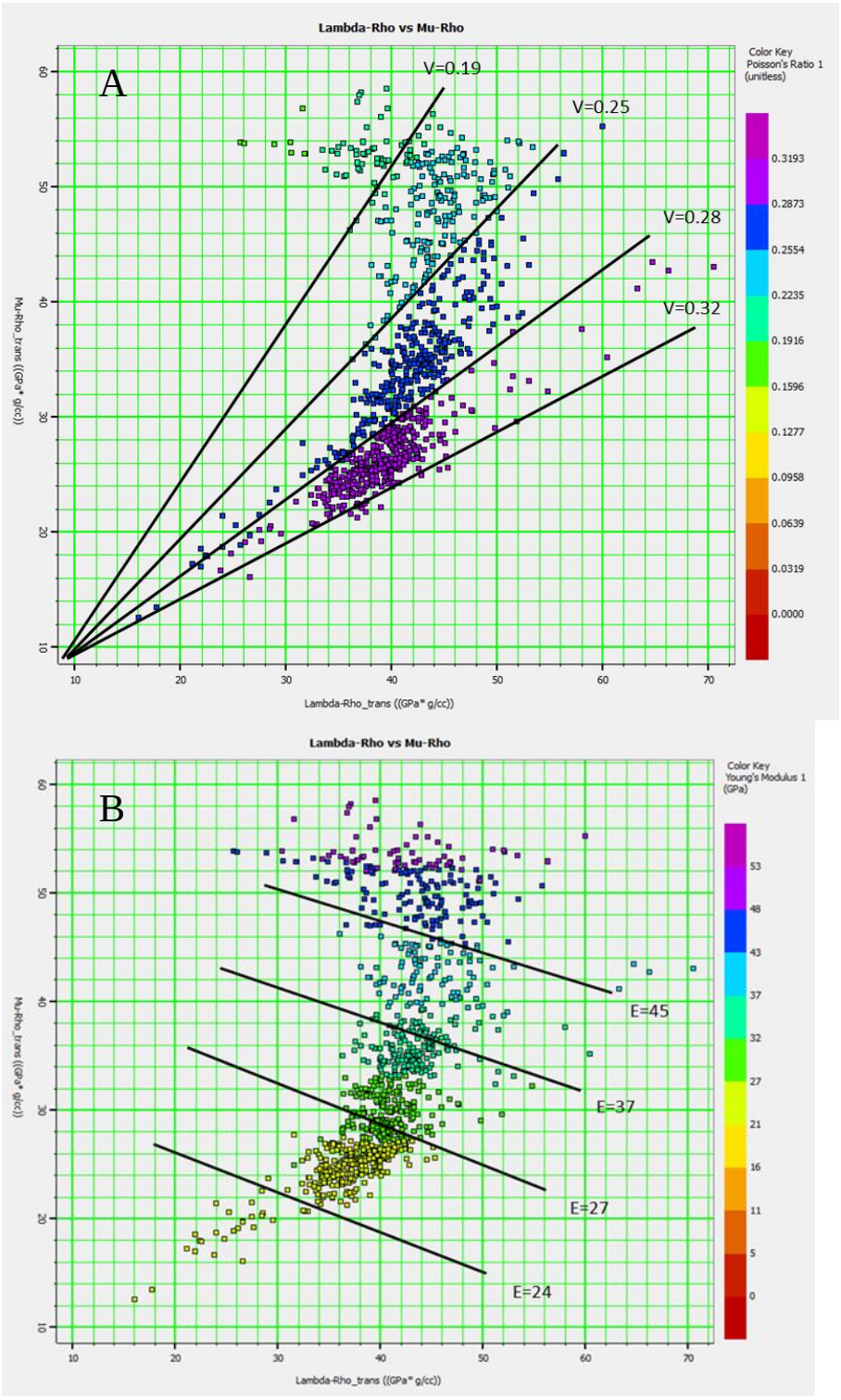

Figure A-9: (A) and (B) show the crossplots of LR versus MR for the Arrowsmith-2 well having similar values and are displayed for each plot by Poisson's ratio and Young's modulus.

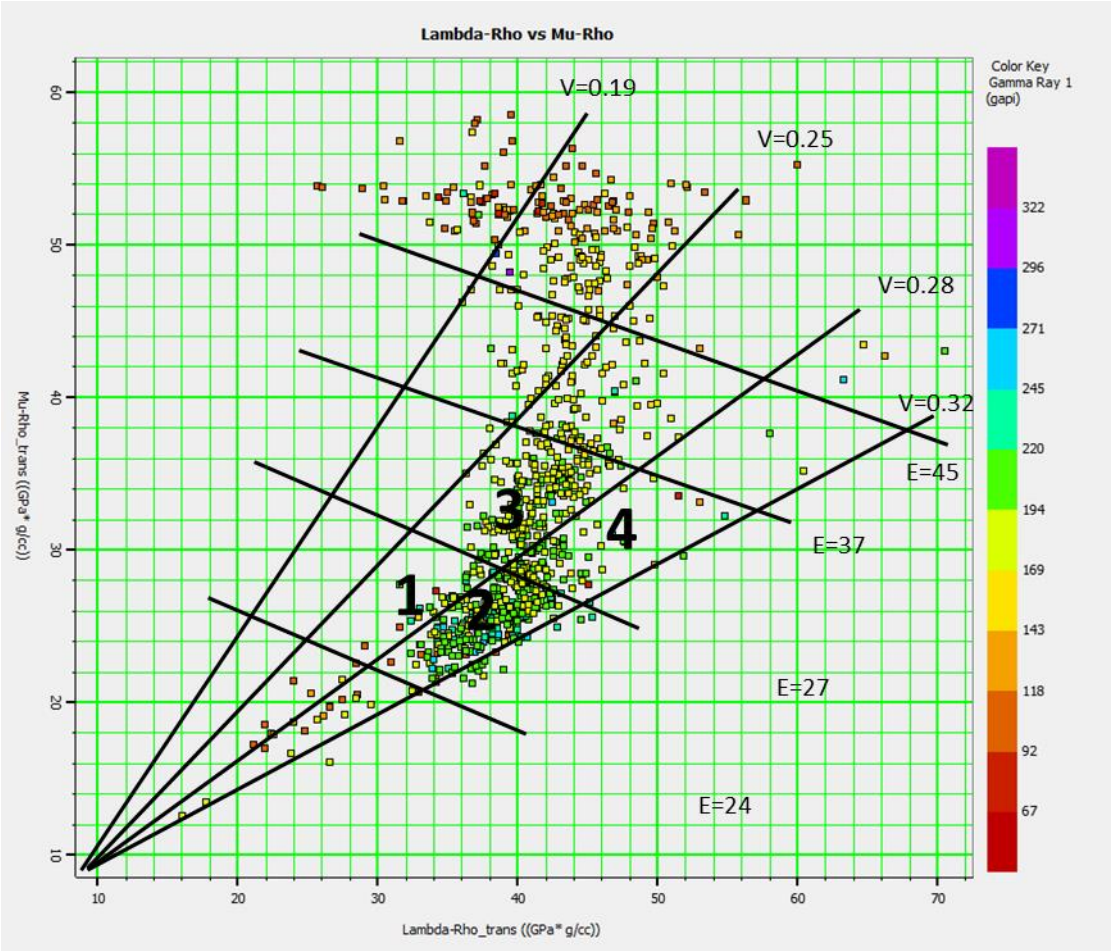

Figure A-10: Crossplot of LR versus MR obtained by combining Figure A9 A and B. Group 1 is shown to be brittle shale with a rich TOC percentage, while Group 2 is shown to be ductile shale with a rich TOC percentage.

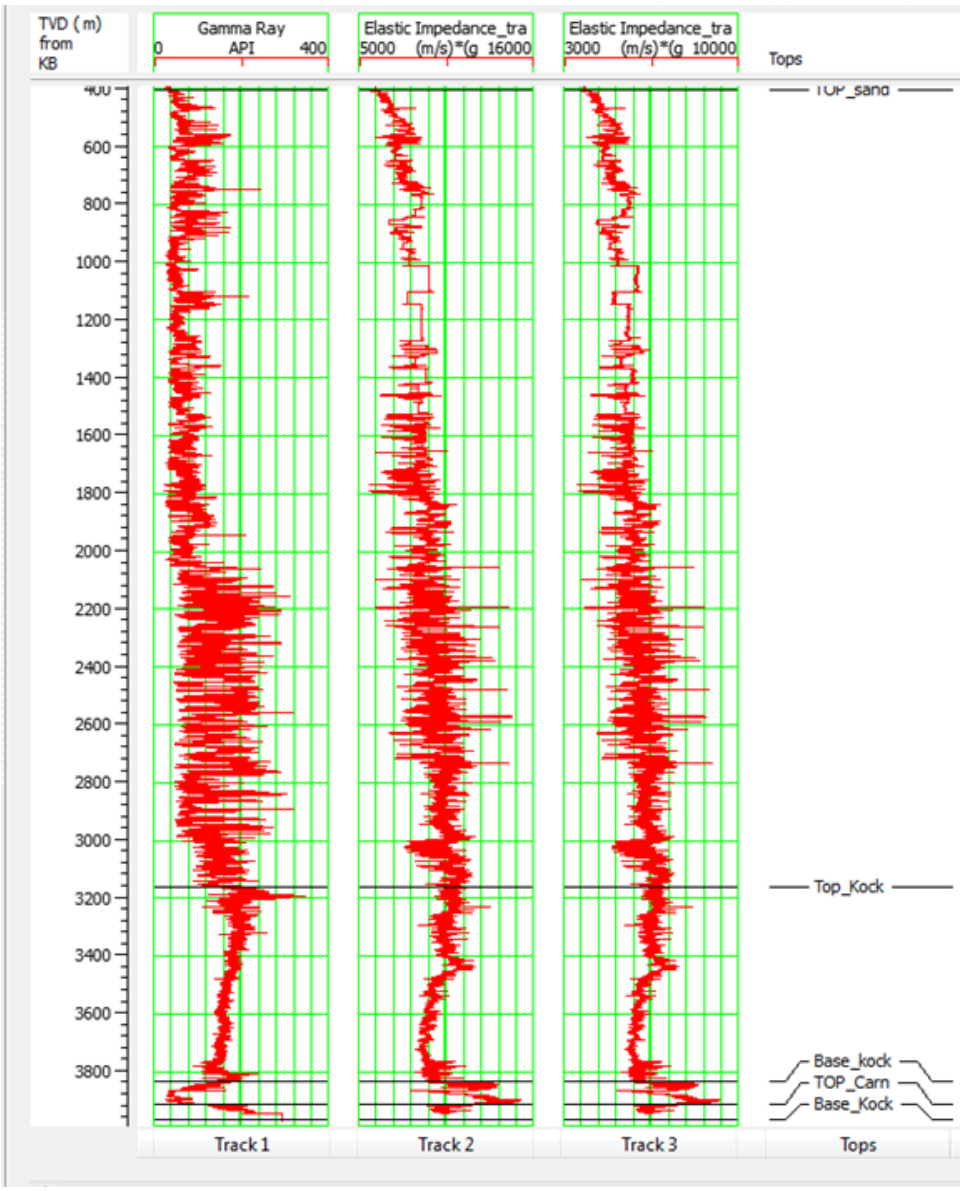

Figure A-11: EI models from log data for near offset 5and far offset 30 with gamma ray log.

Appendix B.
Cliff Head 3D Marine Seismic Inversion and multi-attribute analysis of Kockatea Formation

The Cliff Head survey is located offshore in the Perth Basin, Western Australia (Figure B-1). A 3D seismic survey was conducted by Exploration Consultants Australia Pty Ltdin 2003. The offshore 3D survey covered approximately 367.17 $km^{2.}$ The data was acquired using a single vessel in signal source mode and towing 2 streamers separated by nominal distance of 50.0 meters. The streamer length being 1,050 m, with a group interval of 12.5 m, and a

shotpoint interval of 12.5 m, meant that the fold achieved was 42 maximum acquisition techniques with a vibrator source and 1,152 receivers. The dataset was processed using a 3D post-stack time migration by (Veritas DGC Australia Pty Ltd). In the study area, more than 14 wells were used in the seismic interpretation to pick the target formations. Only 8 control wells were used to build the poststack inversion and inversion. Most of the control wells had the requisite log suites (i.e., gamma ray, sonic, density, resistivity, neutron porosity, etc.)

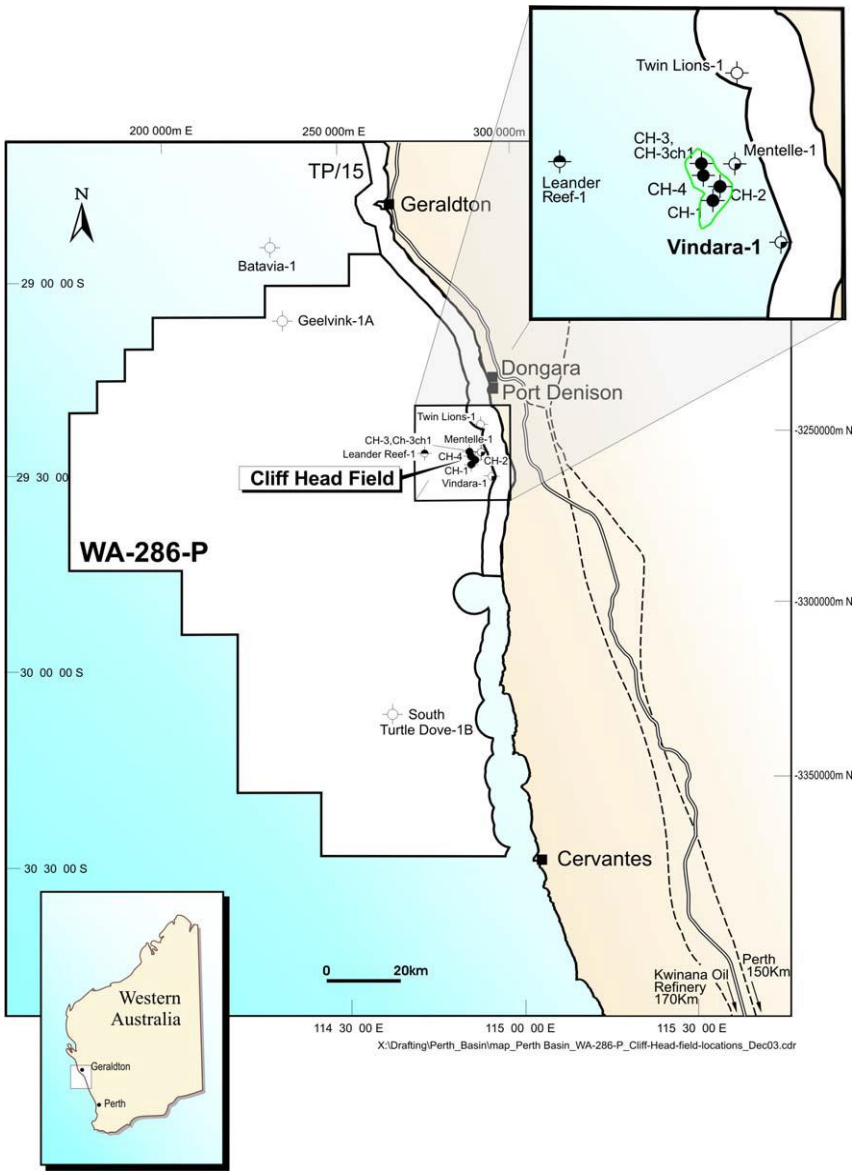

Figure B-1: Location map of Cliff Head 3D Marine Seismic Survey.

The cliff Head structure is complex by faulting in four discrete segments: the Main Horst, the East Ridge, the SE Lobe, and the CH-3 Area (Figure B-2). In total, five horizons were

interpreted including the Kockatea Shale (Top and Base of the Kockatea shale Foramtion), Top Cadda Formation, Top Eneabba Formation and Top Woodada Formation as shown in Figure B-3.

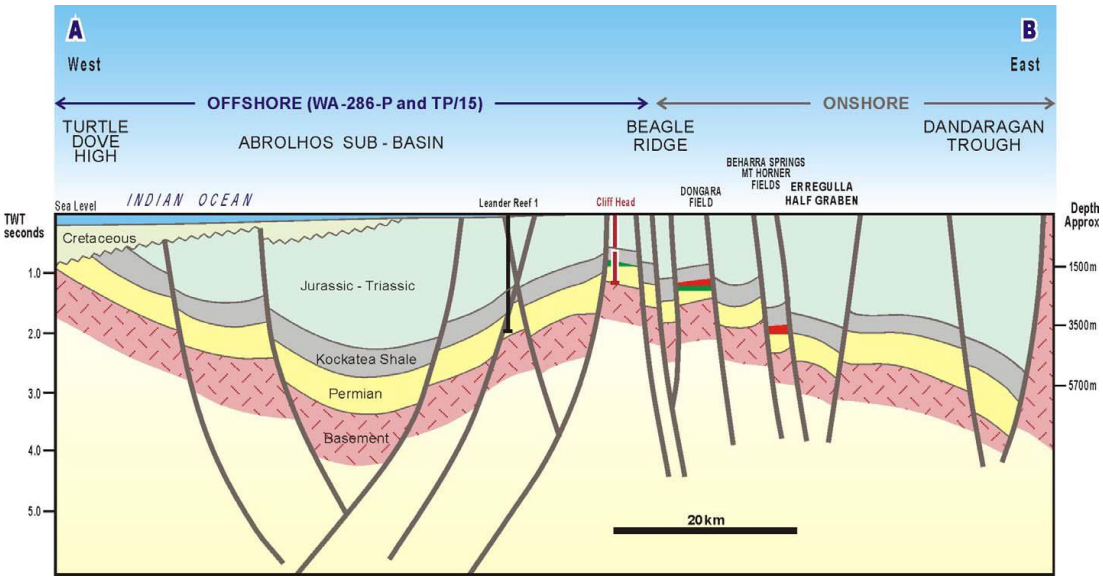

Figure B-2: Structure Mapping.

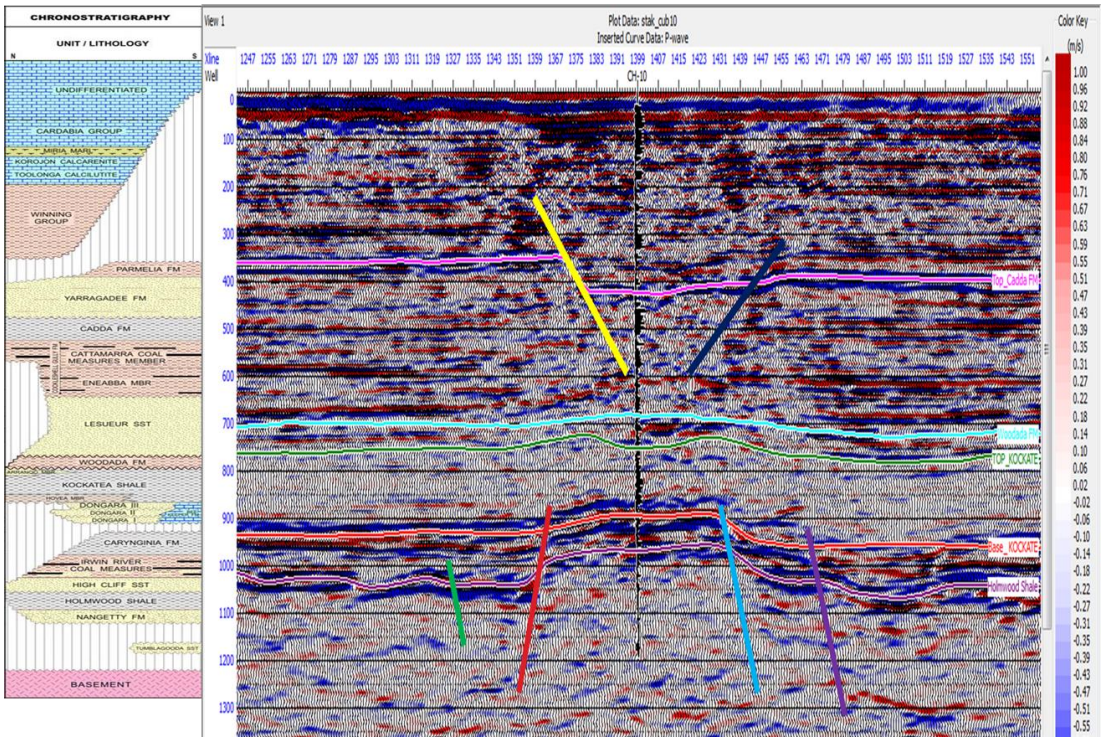

Figure B-3: Seismic horizons and faults.

The TOC analysis is displayed in Figure B-4 for Cliff Head-1, the TOC content is high in the base of the Kockate Shale and in the IRCM Formation. In this study the aims were to pick the top and base of the Kockatea shale, and to define the depth and the thickness of the target formation, so ad to generate isopach and isochore maps. The isopach and isochore maps were applied in order to determine the thickness distribution of the Kockatea. Post-stack inversion involves a series of steps to be followed with the same workflow presses explained before in Chapter 4.The first step was to find the relationship between TOC content and AI as shown in Figure B-5.

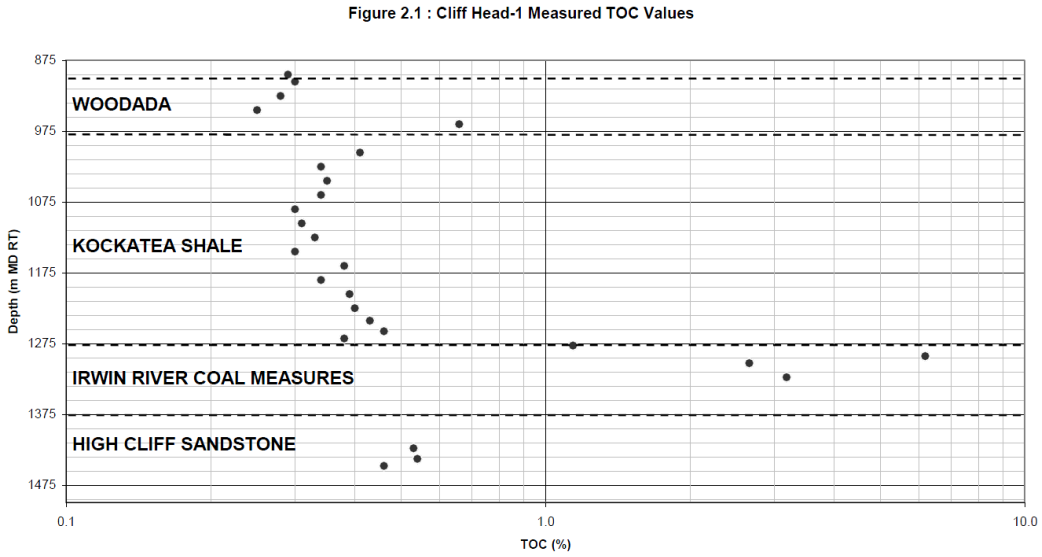

Figure B-4: Cliff Head-1 Measured TOC content.

Based on 50 samples collected from 14 wells at depths of 870–4,000 m, the TOC present in the Kockatea shale varies from 0.3 to 5wt%. There is a good correlation between TOC and AI for both the Kockatea Shale; as the TOC percentage increases the AI decreases. The next step is to correlate each well used to build the inversion model. The initial model by using the control wells and the selected horizons, then running the inversion analysis with a correlation of 0.9 (Figure B-6). The AI inversion and the initial model results for the seismic section are shown in Figure B-7. It can be seen from the resultant seismic data that the area of the base of Kockatea Shale is composed of lower AI materials.

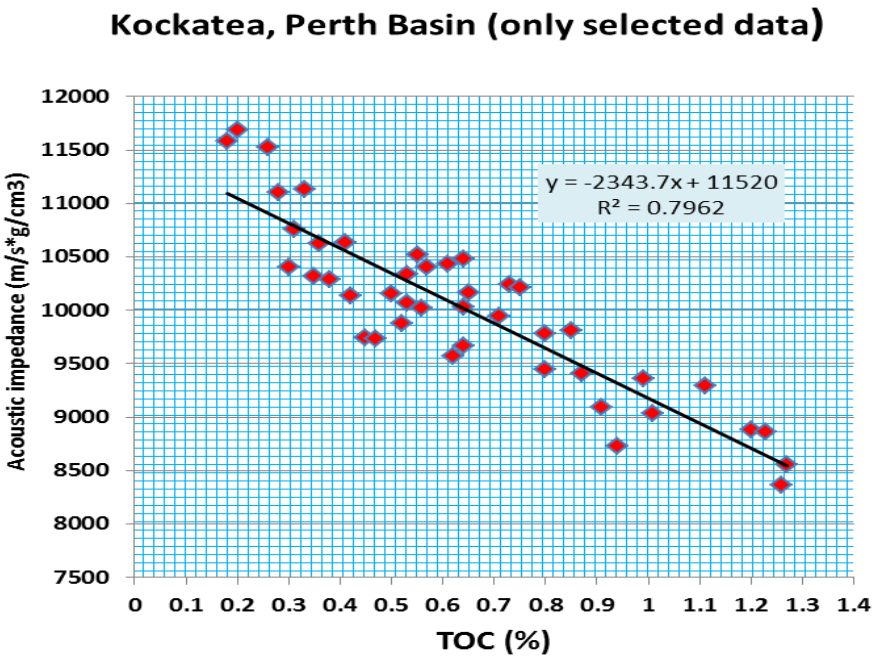

Figure B-5: The relationship between TOC and AI for the Kockatea Shale.

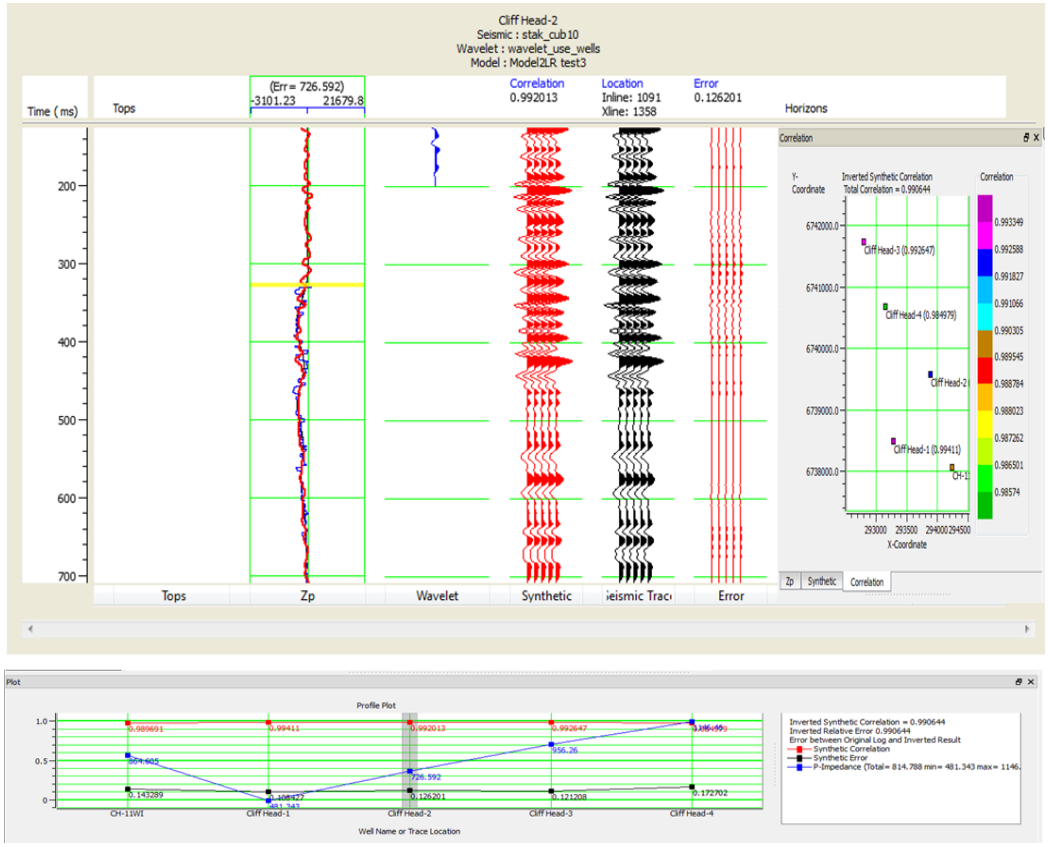

Figure B-6: P-Impedance inversion for the Kockatea Shale with 5 control wells. The inverted synthetic correlation was 0.9.

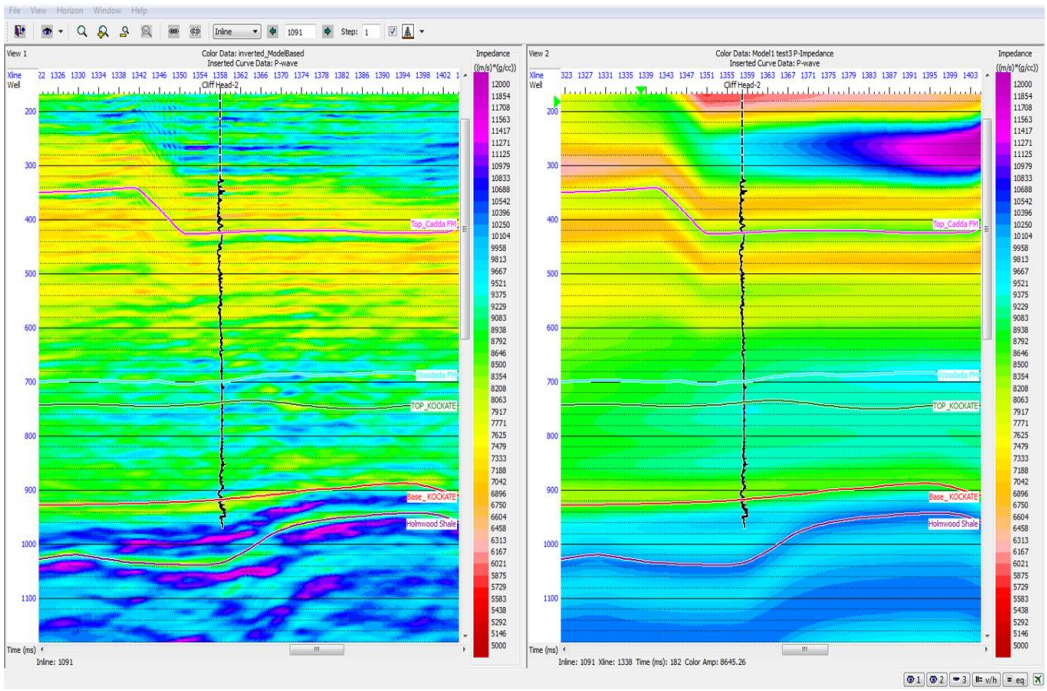

Figure B-7: The initial model and Acoustic impedance inversions for the Kockatea Shale.

The final step is to predict the TOC percentage from the seismic acoustic impedance using the rock physics linear relationships equation between TOC and AI for the Kockatea Shale. Multi-attribute analysis is applied to predict TOC from a model-based inversion and uses the acoustic impedances as external attribute. A total of four seismic attributes were applied for the Kockatea Shale using the convolution operator. The correlation is approximately 0.86 with a five point convolutional operator as shown in (Table B-1). This produces an error lower than 0.19 for the training; the validation error was also lower than 0.197. One way of measuring the correlation between the target and an attribute is to crossplot the two parameters. Figure B-8 shows the predicted and actual TOC from 5 wells using four attributes with a correlation of 86% and an error of 19%.

All the information in the table is shown graphically in Figure B-9 in which the validation results are also shown. The lower curve (black) is the estimation error when all the wells are used in the analysis and the upper curve (red) shows the average validation error. Figure B-10 shows the application plot between the predicted logs from the multi-attribute transform overlain on the actual target log. The correlation is better when we used multi-attribute analysis with convolutional operator.

Table B-1: The multi-attribute table applied to predict TOC content**.**

	Target	Final Attribute	Training Error	Validation Error
1	Sqrt(TOC)	inverted_ModelBased	0.196263	0.197224
2	Sqrt(TOC)	Amplitude Weighted Cosine Phase	0.180823	0.185263
3	Sqrt(TOC)	Filter 5/10-15/20	0.174904	0.182593
4	Sqrt(TOC)	Instantaneous Phase	0.173793	0.181592

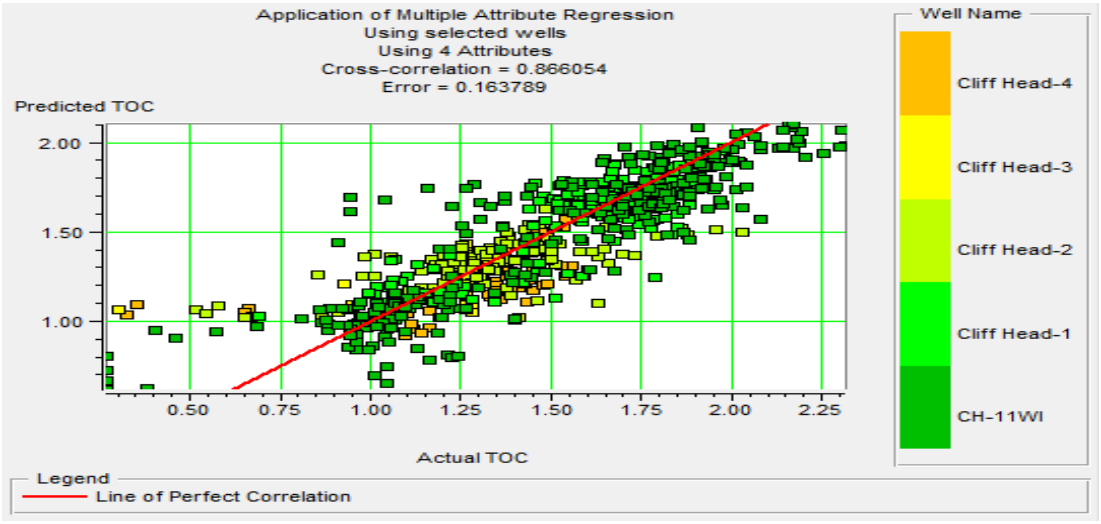

Figure B-8: The actual correlation and error are printed at the top by using four attributes with a correlation of 89%.

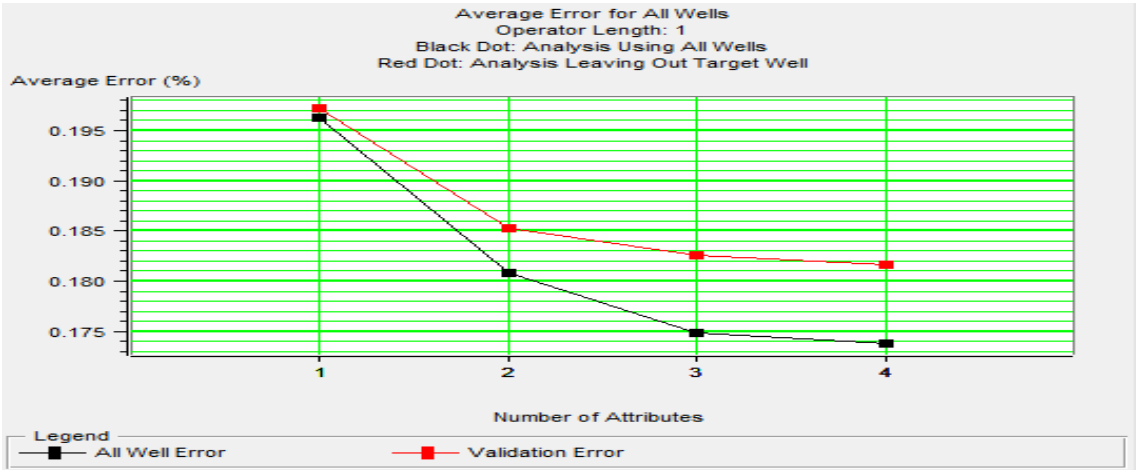

Figure B-9: The plot of validation and training errors plot for the seven point convolutional operator.

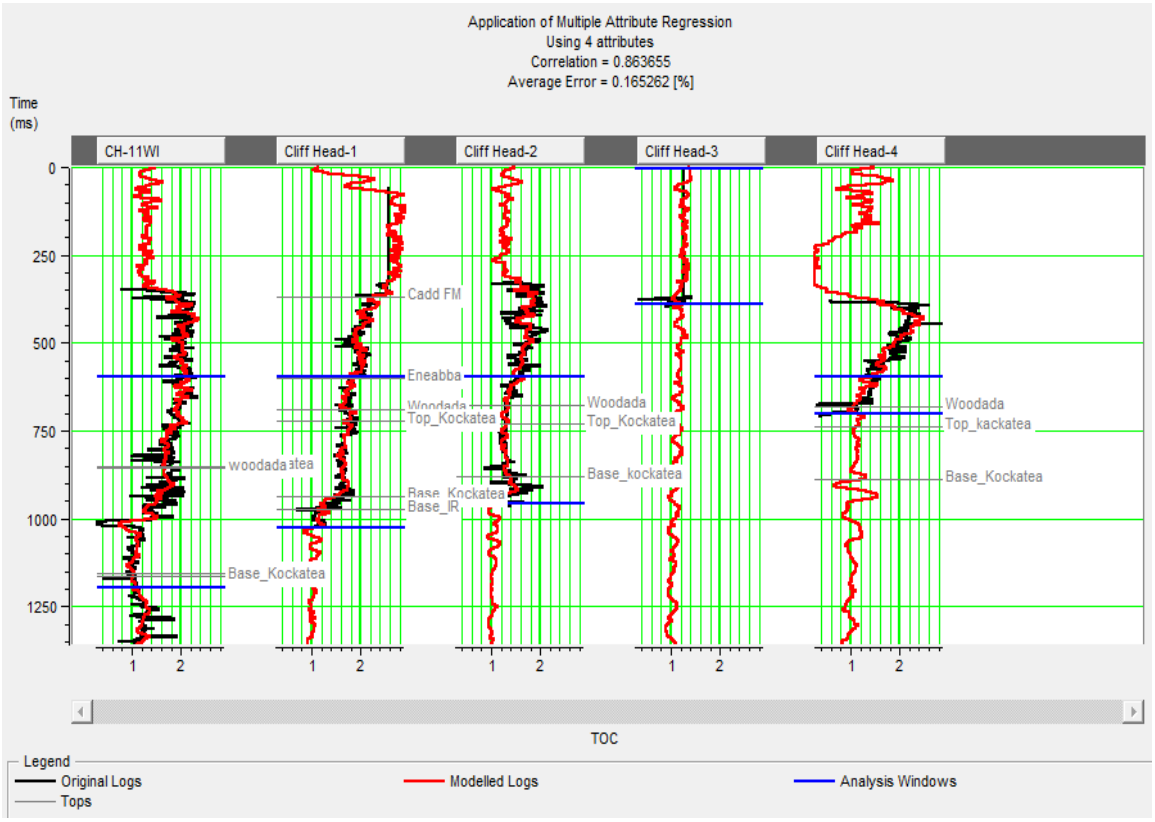

Figure B-10: The window that shows the predicted log from this multi-attribute transform overlain on the actual target log.

Figure B-11 shows the conversion section of TOC and the section of the seismic AI inversion. The TOC profile, following the application of multiple attributes across the wells in the Cliff Head area, shows different TOC values, which are represented by different colors.

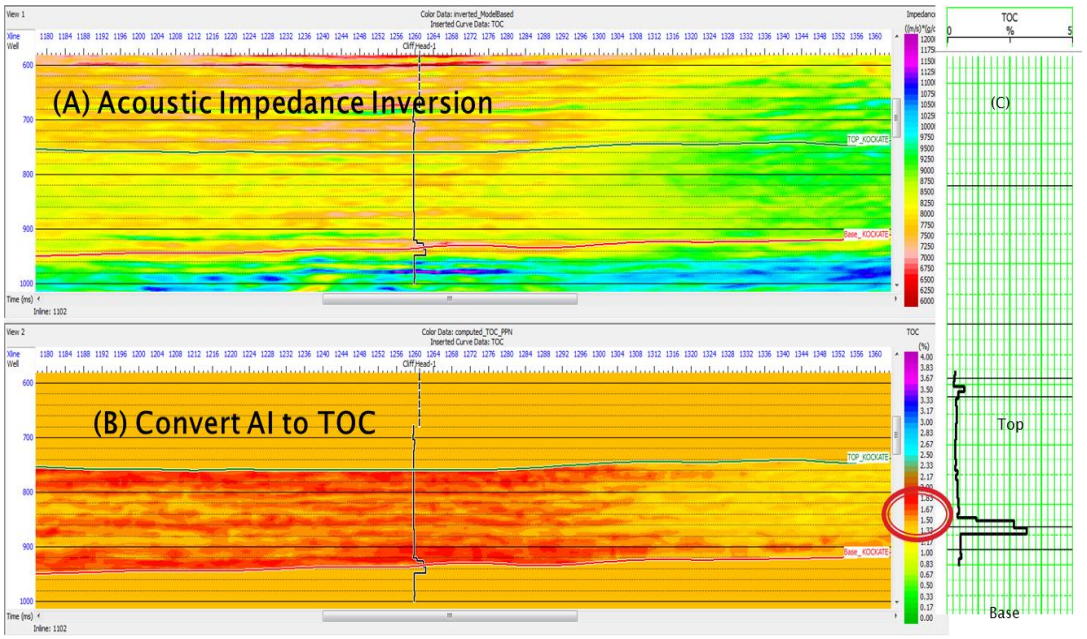

Figure B-11: (A) Shows the Acoustic Impedance Inversion in the Kockatea Formation. (B) Shows the TOC percentage after convert AI values to TOC percentage in the Kockatea Formation with lower values. (C) The Measured TOC from Core Sample in Cliff Head-1.

Appendix C.
Elastic wave velocities measurement

This part is presented as an extension of results in Chapter 5

The laboratory measurement tests the elastic wave velocities and their anisotropy with varying stress levels for three samples from the Carynginia Formation, Arrowsmith-2 well. The first test was conducted using a vertical cut core plug from A.C.01, with a TOC of 3.03%, as reported in Figure C-1 (A). The velocity of V_{Ph} increased from 4,237 to 4,385 m/s as the mean effective stress increased from 0.7 to 38 MPa, while V_{Pv} increased from 3,682 to 4,191 m/s over the same stress range. The V_{Sh} increased from 2,420 to 2,484 m/s, while V_{Sv} increased from 2,414 to 2,483 m/s as the mean effective stress increased from 0.7 to 38MPa. Unfortunately, the electrical connection for the quasi-P velocity was lost early in the experimental cycle and therefore, these waveforms were not recorded. Figure C-2) shows that the V_{Ph} /V_{Sh} ratio also increased from 1.7 to 1.78 over the same stress range. The V_{Pv} /V_{Sv} ratio increased slightly from 1.52 to 1.8 when the mean effective stress increased in the range of 0.7 to 38 MPa. The second test was conducted on A.C.10 (a horizontal cut), with a TOC of 0.23%. The velocity of V_{Ph} increased from 4,502.6 to 4,909 m/s as the mean effective stress increased from 0.7 to 38 MPa (Figure C-1 B). The V_{Pv} increased from 4,259.5 to 4,293 m/s over the same stress range. The quasi-P velocity increased from 4,283.5 to 4,443.7 m/s over the same stress range and was, therefore, between V_{Ph} and V_{Pv}. The V_{Sh} increased from 2,905 to 3,208 m/s, while V_{Sv} increased from 2,639 to 4,293 m/s as the mean effective stress increased from 0.7 to 38MPa.

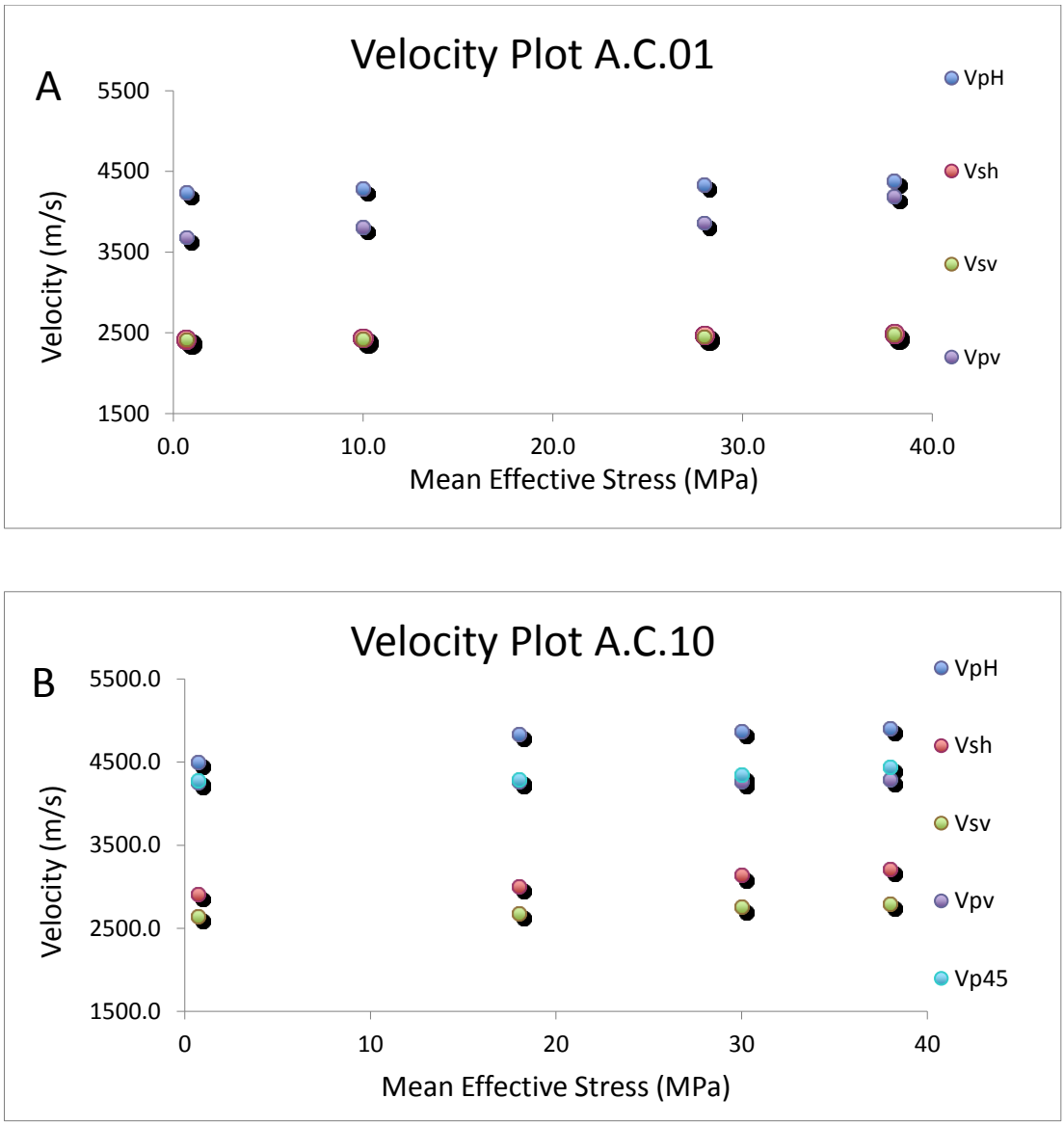

Figure C-1: The influence of the mean effective stress on Vp/Vs ratios for shale sample A.C.01 and A.C.10 samples.

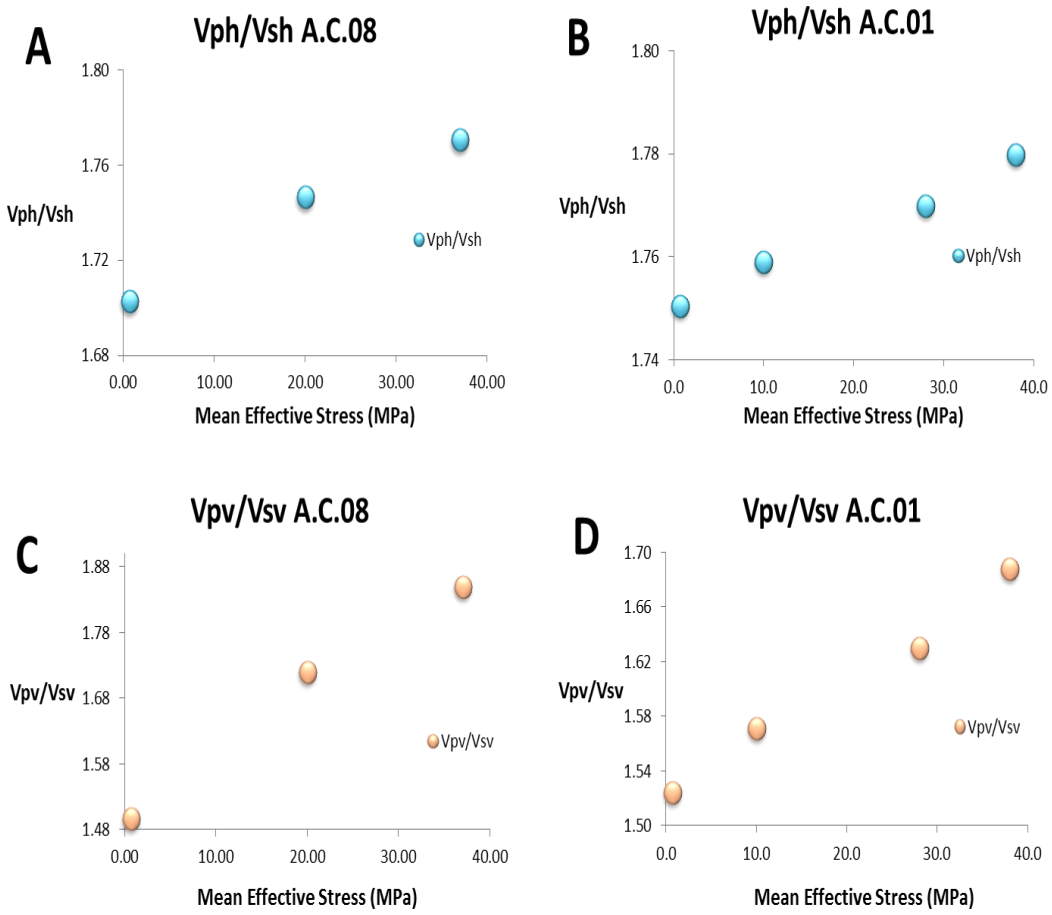

Figure C-2: The influence of the mean effective stress on Vp/Vs ratios for shale sample A.C01 and A.C08 samples.

The laboratory measurement tests the elastic wave velocities and their anisotropy with varying stress levels for three samples from the Kockatea Shale, Redback-2 well. The impact of the mean effective stress on the ultrasonic velocity in shale core samples studied is presented in Figure C-3 (A) and (B). In general, all the wave velocities are increased as the stress increased, V_{Ph} is slightly higher than V_{Pv} and V_{Sh} is almost higher than V_{SV}.

The first test was conducted using the core plug from R.B.22, with a TOC of 4.34% with depth of 3,801m, reported in Figure C-3 (A). The velocity of V_{Ph} increases from 4,650 to 4,900 m/s as the mean over the mean effective stress range was measured between 10 to 90MPa, while V_{Pv} increased from 3,400 to 3,800 m/s over the same stress range. The quasi-P velocity increased from 4,400 to 4,420 m/s over the same range of stress. The V_{Sh} is stable at around 2,820 m/s, while V_{Sv} increased from 1,900 to 2,020 m/s as the mean effective

stress increased. The V_{Ph} /V_{Sh} ratio also increased from 1.7 to 1.74 over the same stress range. The V_{Pv} /V_{Sv} ratio increased slightly from 1.80 to 1.9 when the mean effective stress increased in the range of 10 to 90 MPa.

The second test was conducted on R.B.23, with a TOC of 2.25 wt%; the depth is about 3,810 m. The velocity of V_{Ph} increased from 4,900 to 5,034 m/s as the mean effective stress increased from 10 to 90 MPa as shown in Figure C-3 (B). The V_{Pv} increased from 4,000 to 4,230 m/s over the same stress range. The quasi-P velocity increased from 4,500 to 4,640 m/s over the same stress range. The V_{Sh} increased from 2,800 to 2,950 m/s, while V_{Sv} increased from 2,300 to 4,390 m/s as the mean effective stress increased from 0.7 to 38MPa.

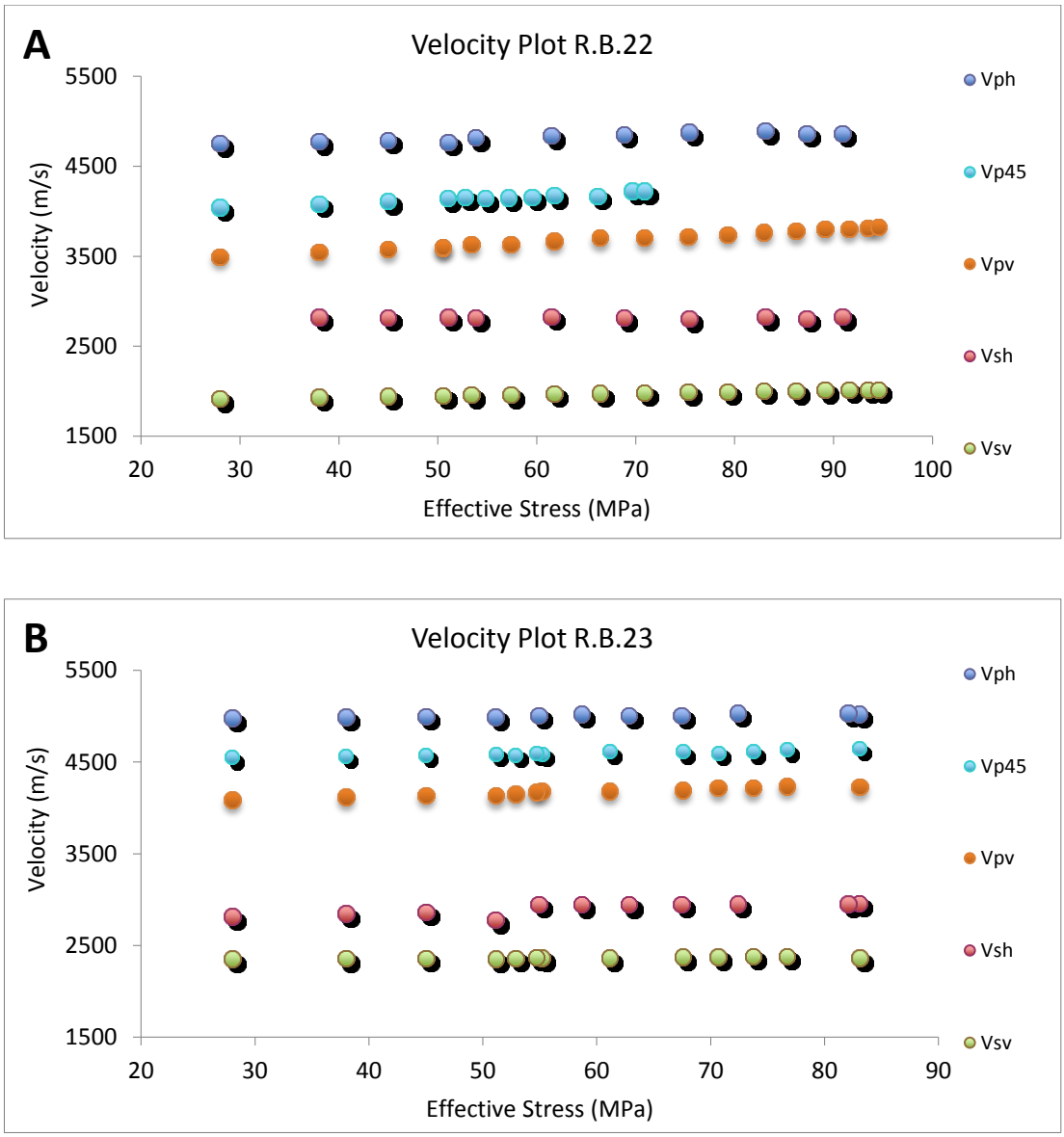

Figure C-3: The relationship between velocities and mean effective stress for the Redback-2 well samples (A) R.B.22 and (B) R.B.23, the velocities increase as the mean effective increases.

Elastic coefficient calculation

The responses of the elastic coefficients of the samples of the three samples from Arrowsmith and RedBack-2 wells are shown in Figures C-4 (A), (B) and (C). In general all the elastic coefficients increased as the stress increased.

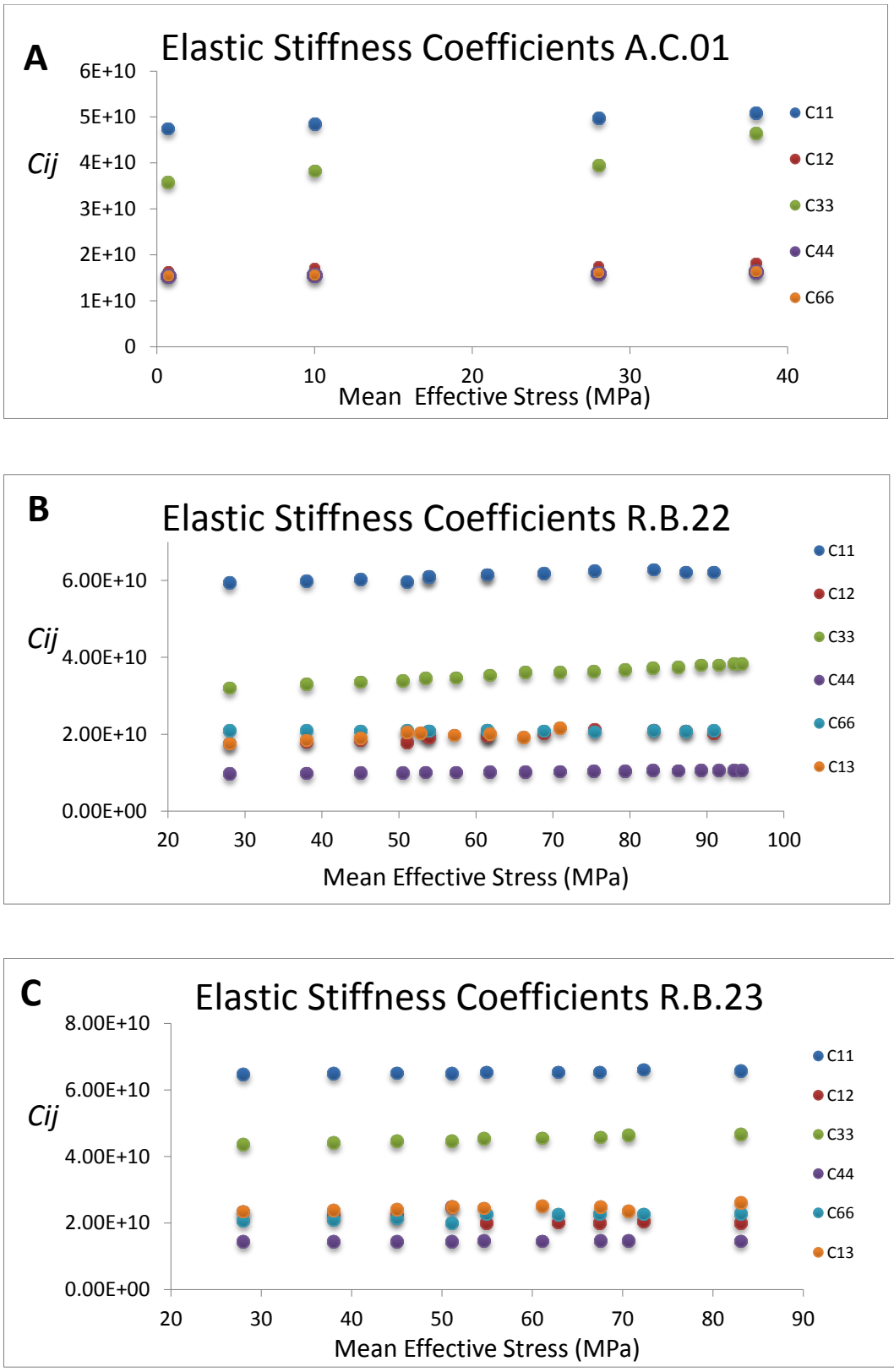

Figure C-4: The responses of elastic constants to increase the mean effective stress for (A) shale sample A.C.01, (B) sample R.B.22 and (C) R.B.23.

Thomsen parameters estimation

Three shale core plug samples were tested from the Redback–2 well and the anisotropy parameters were sensitive to changes in confining pressures. The impacts of mean effective stress on P-wave (ε) and S-wave (γ) anisotropy factors, as well as the wave front an elasticity factor (δ), are shown in Figure C-5 (A), (B) and (C) for the three sample. In the first sample with TOC content of 1.94 wt%, the initial anisotropy at low stress is seen to be large (0.35 for P-waves, 0.4 for S-waves) and variable with changing mean effective stress and ε decreased from 0.35 to 0.25 as the mean effective stress increased from 28 to 80 MPa. Initially, γ decreased from 0.41 to 0.36 as the stress increased; however, δ increased from 0.18 to 0.28 as mean effective stress increased.

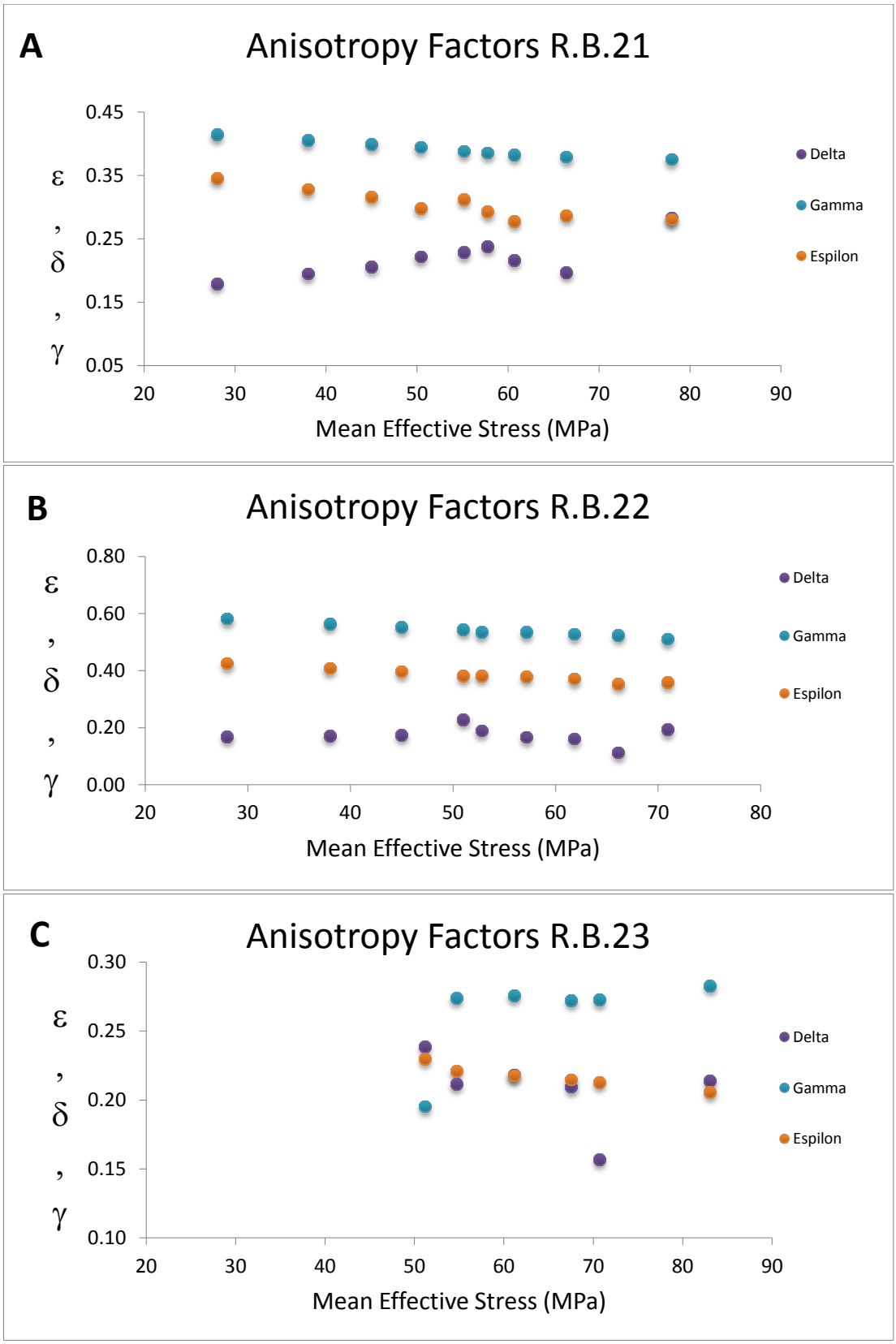

Figure C-5: Influence of mean effective stress on ε, γ and δ for Redback–2 shale sample (A) R.B.21, (B) R.B.22 and (C) R.B.23.

Appendix D.
Measuring elastic properties to determine the influence of TOC on synthetic shale samples

Synthetic samples were prepared with pre-defined properties to enable systematic investigations of their elastic properties as a function of TOC or other factors such as mineral composition. We have produce two groups of samples with different mineral completions: the first group involved 12 samples composed of 45% clay minerals (kaolinite), 40% non-clay minerals (quartz), and 15% cement with some water, each sample had different percentage of organic matter. In addition, we have created another group of synthetic samples using the same preparation, but with different composition combined with a mix of 40 % of clay minerals and 30 % of non-clay minerals, as well as 30% of cement plus water. Organic matter was added to the mixer minerals with different percentages for each sample. All the samples were tested ultrasonically to obtain the elastic properties.

The velocities of the P- and S-waves show a smooth decrease as the amount of TOC weight percentage of the synthetic shale was increased in Figure D-1. The S-wave decreased from 1650 to 1165 m/s as the TOC percentages increased. In the second composition is mixed with 40% clay minerals (kaolinite), 30% non-clay minerals (quartz) and 30% cement. The velocities of the P- and S-waves show a smooth decrease as the amount of TOC weight percentage of the synthetic shale was increased in Figure D-2. P-wave decreased from 2020 m/s in the sample having 0.0 wt% of TOC to 1800 m/s in the sample having 20 wt% of TOC. The S-wave decreased from 1100 to 850 m/s as the TOC parentages increased.

A comparison between the ultrasonic waves and the total organic matter percentages suggested that at high TOC, all synthetic shale samples showed a decrease in their P- and S-wave velocities. In the both compositions, the increase in the TOC corresponds to a polynomial decrease in density from 2.32 to 2.05 g/cc, and from 2.4 to 2.15 g/cc as shown in Figure D-3 The ratio of Vp/Vs decreased for both compositions, from approximately 1.6 to 1.5 over the 0% to 20% of the TOC percentages used in the first composition, and decreased

from 1.8 to 1.5 over the 0to 20% of the TOC percentages in the second composition as shown in Figure D-4.

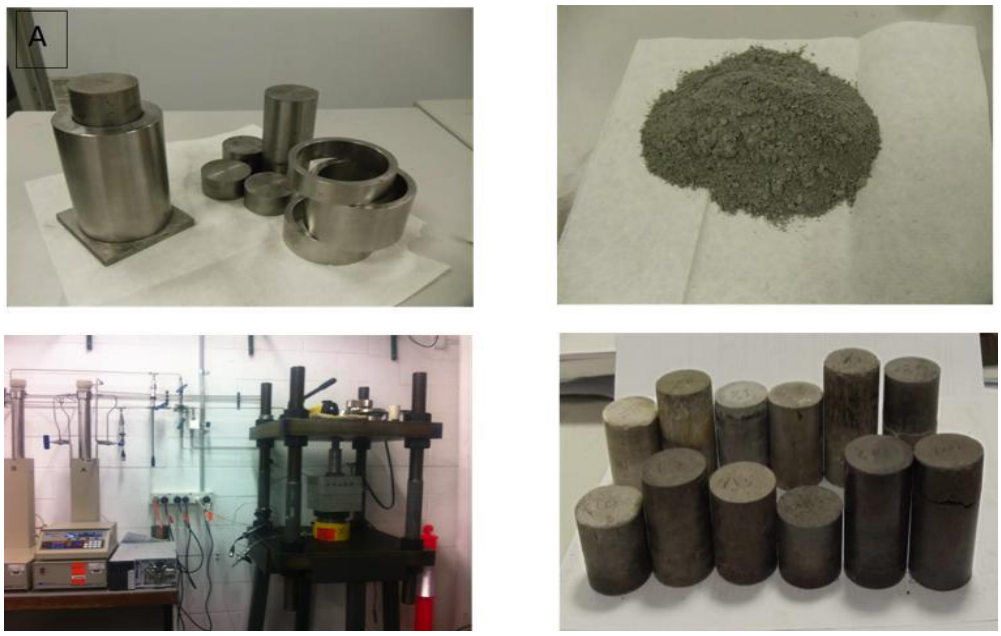

Figure D-1: Steel cylinder casts designed for high pressure use, the mineral mix as a fine powder and synthetic shale core samples with different percentages of TOC.

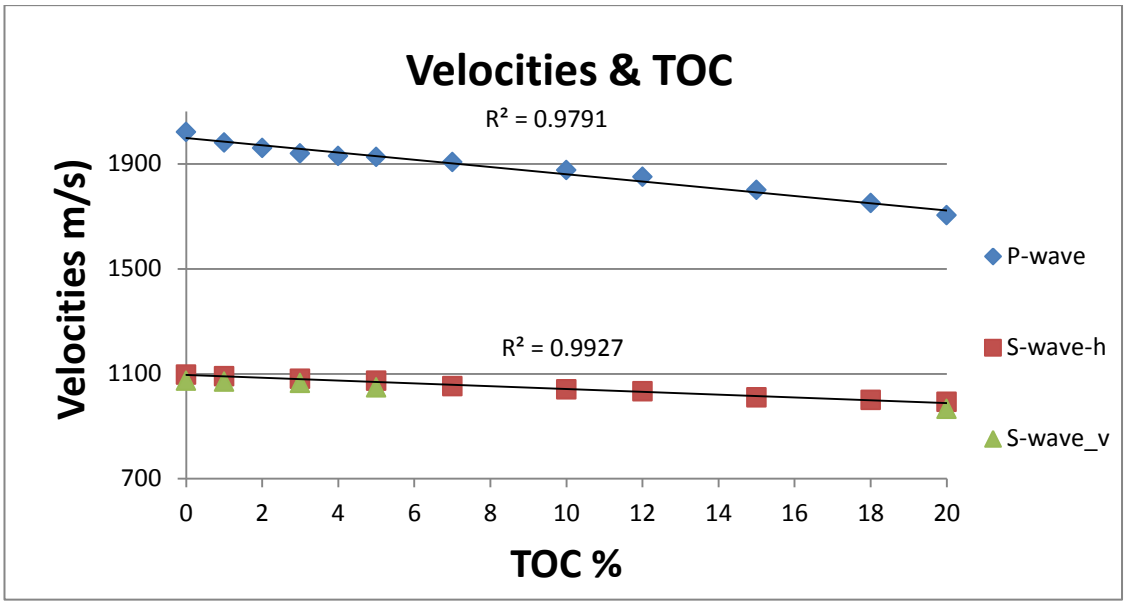

Figure D-2: Vp and Vs versus TOC% for a number of synthetic shale cores, as the TOC percentage increased, the velocities decreased.

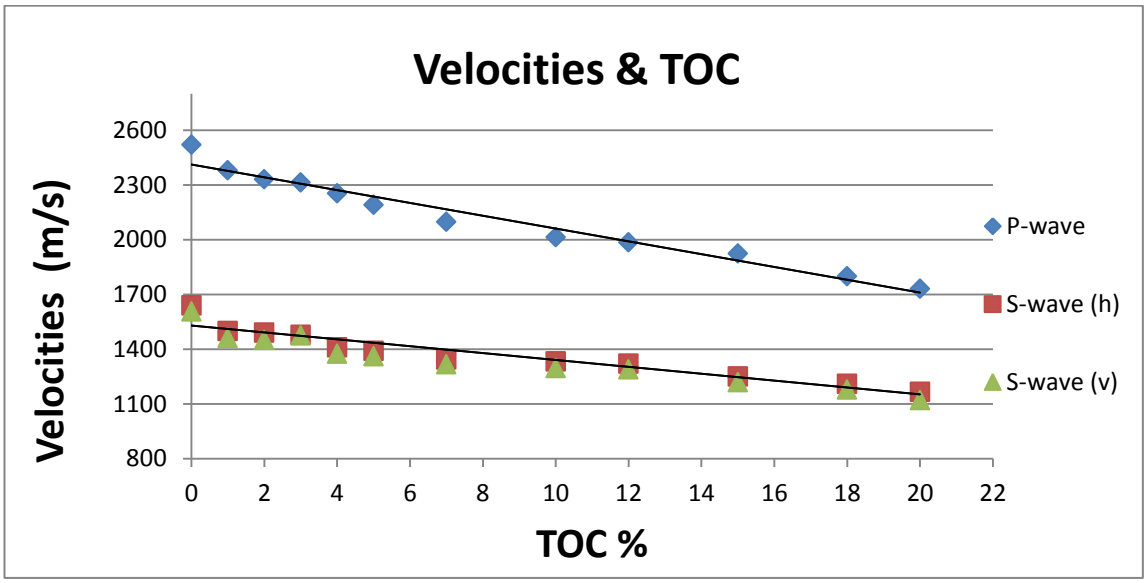

Figure D-3: Vp and Vs versus TOC% for a number of synthetic shale cores, as the TOC percentage increased, the velocities decreased.

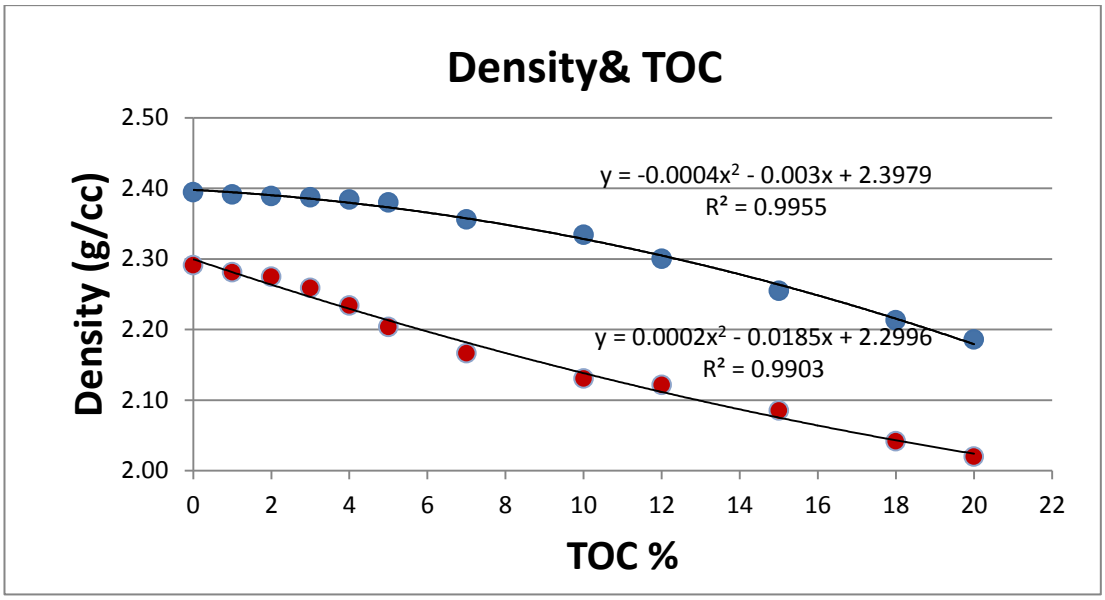

Figure D-4: Density reduced with an increase in TOC wt%.The first composition (red) reduced from 2.3 to 2.05 (g/cc) and the second composition (blue) reduced from 2.4 to 2.15.

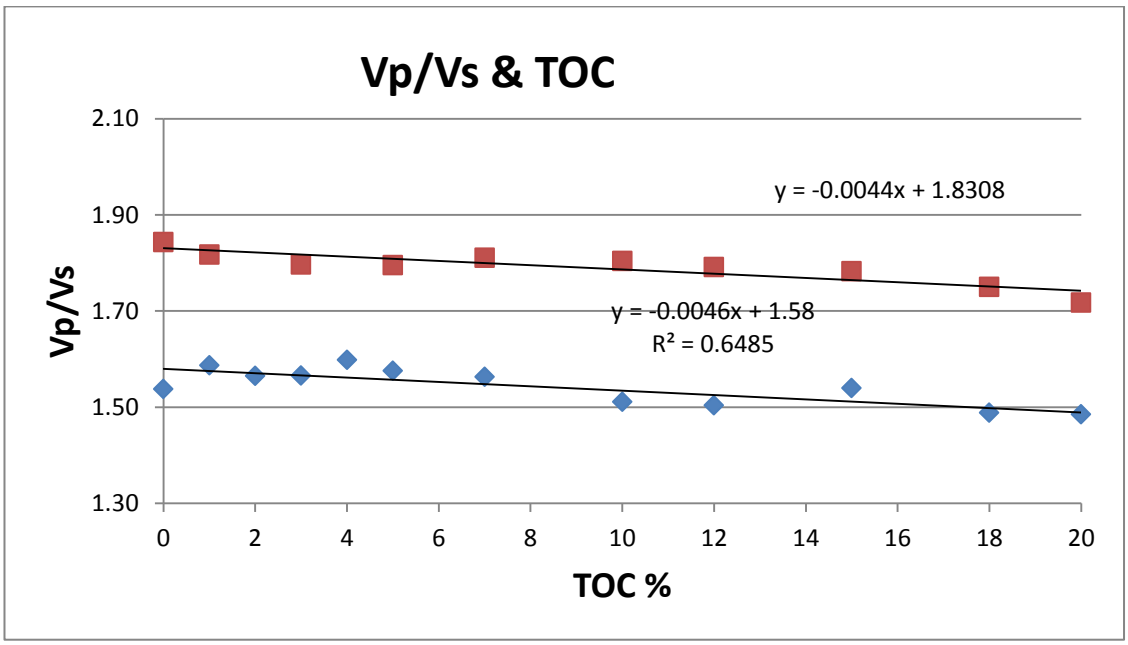

Figure D-5: Vp/Vs ratio reduced with increasing TOC%.